Theoretical Calculations in Photoelectron Spectroscopy

by

John Joseph Delaney, B.Sc.

A thesis submitted to the
VICTORIA UNIVERSITY OF MANCHESTER
for the degree of
DOCTOR OF PHILOSOPHY
in the
FACULTY OF SCIENCE

October 1985

Acknowledgements

I wish to thank Professor I.H. Hillier for his supervision during this research; the SERC for financial support; Dr.V.R.Saunders for making available the Tchebycheff moment imaging program and many fruitful discussions; Monika Stifter for typing this thesis, and all others who made its submission possible.

This thesis was produced using the TEX computer typsetting system.

Declaration

No portion of the work referred to in this thesis has been submitted in support of an application for another degree or qualification of this or any other university or other institution of learning.

Abstract

Methods of calculating bound state molecular electronic wavefunctions are discussed, and applied to MoO_4^{2-}, $Rh_2(O_2CH)_4$, $MnCl_2$, and $CrCl_2$. The Stieltjes Tchebycheff moment imaging technique for calculating photoionization cross sections using conventional LCAO-MO programmes is described.

These methods are applied to calculating the partial channel photoionization cross sections of the open shell diatomic molecules NO and O_2, and to the closed shell systems H_2O, C_2H_2, and N_2O. These results are compared to reported Xα calculations, and found to be in considerably superior agreement with experiment.

Contents

Chapter 1

Molecular Orbital Theory

The purpose of this chapter is to give a brief outline of the methods used in this research to calculate molecular wave functions. More detailed expositions may be found in many standard text books [1,2].

1.1 The Schrödinger Equation

The fundamental equation of quantum chemistry is the time independent Schrödinger equation [3], given here in the nonrelativistic form.

$$\hat{H}\Psi(1,2,3,\ldots n) = E\Psi(1,2,3,\ldots n) \tag{1.1}$$

$\hat{H}$ is the Hamiltonian operator for the system and E the total energy. Within the Born-Oppenheimer approximation [4], in which the nuclear and electronic wave functions are assumed to be separable and the nuclei fixed in space, the Hamiltonian operator can be written in atomic units as

$$\hat{H} = \sum_i -\frac{\nabla_i^2}{2} + \sum_{i,j,j>i} \frac{1}{r_{ij}} - \sum_{M,i} \frac{Z_M}{R_{Mi}} + \sum_{L,M,M>L} \frac{Z_L Z_M}{R_{LM}} \tag{1.2}$$

∇_i = the Laplacian operator for electron i

Z_M = the atomic number or nucleus M

r_{ij} = the distance between electrons i and j

R_{Mi} = the distance between nucleus M and electron i

R_{LM} = the distance between nucleus L and nucleus M

and the sums i,j run over all the electrons in the system, and M,L over all nuclei. This is an eigenvalue equation where Ψ, the molecular wave function, is the

eigenfunction of $\hat{H}$ and E its eigenvalue. Complete solution of the Schrödinger equation, because of the interaction term between the electrons, presents an intractable problem for systems of any complexity. In order to obtain approximate solutions the orbital approximation, in which the electrons move independently of one another in one electron spin orbitals, is employed. The wave function may then be written as

$$\Psi = MA[\phi_1(1)\phi_2(2)\phi_3(3)\phi_4(4)\ldots\phi_n(n)] \tag{1.3}$$

where A is the antisymmetrizer with respect to electron interchange, M is a normalization factor and the ϕ_i's are the one electron orbitals. A convenient way of writing the antisymmetrized wave function is in the form of a Slater determinant.

$$\Psi = \frac{1}{\sqrt{n!}} \begin{vmatrix} \phi_1(1) & \phi_2(1) & \ldots & \phi_n(1) \\ \phi_1(2) & \phi_2(2) & \ldots & \phi_n(2) \\ & \vdots & & \\ \phi_1(n) & \phi_2(n) & \ldots & \phi_n(n) \end{vmatrix} \tag{1.4}$$

which is often written as

$$\Psi = \left| \; \phi_1(1)\phi_2(2)\ldots\phi_n(n) \; \right| \tag{1.5}$$

or in the closed shell case

$$\Psi = \left| \; \phi_1(1)\bar{\phi}_1(2) \quad \ldots \quad \phi_{\frac{n}{2}}(n-1)\bar{\phi}_{\frac{n}{2}}(n) \right| \tag{1.6}$$

where

$$\phi_1(1) = \psi_1(r_1)\alpha(1) \tag{1.7a}$$

and

$$\bar{\phi}_1(2) = \psi_1(r_2)\beta(2) \qquad [1.7b]$$

α and β being the one electron spin functions with eigenvalues $M_S = 1/2$ and $M_S = -1/2$ respectively, and the ψ_i describe the spatial distribution of an electrons in the spin orbital ϕ_i.

Provided that the orbitals in 1.6 are orthonormal the electronic energy of the system is given by

$$E = 2\sum_{i=1}^{n/2} h_{ii} + \sum_{i,j=1}^{n/2} (2J_{ij} - K_{ij}) \qquad [1.8]$$

where, in atomic units

$$h_{ii} = \int \psi_i^*(1)\hat{h}(1)\psi_i(1)dV_1 \qquad [1.9a]$$

$$J_{ij} = \int \psi_i^*(1)\psi_i(1)\frac{1}{r_{12}}\psi_j^*(2)\psi_j(2)dV_1 dV_2 \qquad [1.9b]$$

$$K_{ij} = \int \psi_i^*(1)\psi_j(1)\frac{1}{r_{12}}\psi_i(2)\psi_j^*(2)dV_i dV_2 \qquad [1.9c]$$

and $\hat{h}$ is the one electron part of the Hamiltonian

$$\hat{h}(i) = -\frac{\nabla_i^2}{2} + \sum_M \frac{Z_M}{R_{Mi}} \qquad [1.9d]$$

1.2 The Hartree Fock Method [5,6]

The variation theorem states that the best approximate wave function is that which produces the minimum energy. In order to optimize the n electron wave function, Ψ, the total wave function must be minimized with respect to an arbitrary variation in the wave function. This requirement together with the requirement that one electron orbitals remain orthonormal leads to the Hartree Fock equations, given here for a closed shell system.

$$\hat{F}_i\psi_i = \epsilon_i\psi_i \qquad [1.10]$$

where the Fock operator $\hat{F}$ is defined by

$$\hat{F}_i = h(i) + \sum_{i=1}^{n/2}(2\hat{J}_i - \hat{K}_i) \qquad [1.11a]$$

$$\hat{J}_i\psi_j(1) = \int \psi_i^*(2)\frac{1}{r_{12}}\psi_i(2)dV_2\psi_j(1) \qquad [1.11b]$$

$$\hat{K}_i\psi_j(1) = \int \psi_i^*(2)\frac{1}{r_{12}}\psi_j(2)dV_2\psi_i(1) \qquad [1.11c]$$

This is a pseudo eigenvalue equation where the Fock operator depends on its own eigenfunctions, because of the Coulomb ($\hat{J}_i$) and exchange ($\hat{K}_i$) operators. Thus the equations must be solved iteratively until self consistency is achieved. As a result of their spherical symmetry the equations may be solved numerically for atomic systems but for molecular systems this is difficult computationally.

1.3 The Roothaan Equations [7,8]

Roothaan and Hall independently suggested expanding the molecular orbitals as a sum over basis functions

$$\psi_i = \sum_\mu C_{\mu i} \chi_\mu \qquad [1.12]$$

By a similar method to that used above (1.2) this leads to the best orbitals, of this form, which are solutions of equation (1.13).

$$\sum_\rho C_{\rho i}(F_{\mu\rho} - \epsilon_i S_{\mu\rho}) = 0 \qquad [1.13]$$

where

$$F_{\mu\rho} = \int \chi_\mu^*(1) F \chi_\rho(1) dV_1 \qquad [1.14a]$$

and

$$S_{\mu\rho} = \int \chi_\mu^*(1) \chi_\rho(1) dV_1 \qquad [1.14b]$$

$$|F_{\mu\rho} - \epsilon_i S_{\mu\rho}| = 0 \qquad [1.15]$$

In order for these equations to have non-trivial solutions the secular determinant must be zero. This gives the eigenvalues which on substitution into equation [1.13] yield the basis function coefficients. These equations must also be solved iteratively. With a set of m basis functions m molecular orbitals are defined. In the closed shell case with 2n electrons the n lowest roots of the

secular determinant correspond to the occupied orbitals. The remaining (m-n) are unoccupied (or virtual) orbitals which describe the motion of an electron moving in the field of the 2n electrons in the n doubly occupied molecular orbitals, whereas the first n orbitals describe the motion of an electron in the field of 2n-1 electrons.

In the limit of a complete basis the Roothaan orbitals are identical to those obtained by numerical solution of the Hartree Fock equations, the Hartree Fock limit.

The development outlined above applies only to closed shell molecules. Much work has been done on the method of extending this treatment to open shell molecules, whose wave functions usually cannot be expressed in terms of a single determinant. These methods usually involve constraining the molecular wave function to transform as a representation in the molecular point group and often also involve an equivalence restriction. This makes the singlet paired electrons of the molecular core occupy orbitals with the same spatial form, although electrons of different spin experience different potentials due to the presence of the open shell. This is known as the Restricted Hartree Fock method (RHF). Removal of this restriction is known as the Unrestricted Hartree Fock (UHF) method and is computationally more expensive.

By a suitable modification of the Hartree Fock operator over which the (n-

m) unoccupied orbitals are constructed or canonicalized, these orbitals may be made to describe an electron excited from one of the ground state orbitals to an orbital higher in energy, without any change on the orbitals describing the remaining (2n-1) electrons. Such orbitals are described as improved virtual orbitals (IVO's).

1.4 Basis Functions and Basis Sets.

There are two kinds of basis functions in general use, Slater type functions (STF's) [9] and Gaussian type functions (GTF's) [10]. STF's vary as $exp(-\xi r)$, where ξ is the orbital exponent, and r the radial distance from the centre on which the function is based. Integrals involving STF's on two or more centres have to be solved numerically, a process which is computationally very expensive for functions of this type.

The use of Gaussian type functions was originally suggested by Boys [10]. These functions vary as $exp(-\xi r^2)$ and have the advantage that the product of two functions on different centres can be expressed as another Gaussian on the line connecting the two centres. Integrals involving only this type of function are much quicker to evaluate than similar integrals involving STF's and so the use of GTF's is computationally advantageous. However, these functions do not

describe the motion of an electron very well. STF's have a cusp at the nucleus where the derivative is non-zero, whereas GTF's have a derivative of zero at the nucleus. This cusp is essential for a good description of the wave function in this region. GTF's also decay asymptotically, whereas the wave function decays exponentially, as do STF's. Hence many more GTF's have to be employed than STF's in order to give results of the same quality.

The resulting increase in basis set size has been overcome by contraction of the large number of original GTF's (primitives) into a smaller set of Gaussian type orbitals (GTO's). Within each GTO the coefficients of each GTF is fixed but the coefficient of each GTO in an MO is variationally determined. Care must be taken in the contraction process so as not to lose variational flexibility.

Two major schemes have been used to determine the contraction coefficients. In the first a set of GTF's are contracted to fit an STO [27], usually by a least squares fit to the STO, and in the second the coefficients are varied so as to give the lowest total energy while retaining flexibility in the valence region [28].

1.5 The Core-Valence Method

The exact Hartree Fock procedure demands the evaluation of a large number of integrals, of the order of the number of basis functions raised to the fourth power, which demands large amounts of computer time. The reduction of this number without a loss of accuracy in the final results would give a considerable computational advantage. One such method suggested by Campbell, Hillier and Saunders [11] is the use of the core-valence approximation. This approximation is based on the recognition that there are basically two kinds of basis functions used in the construction of molecular orbitals, core and valence basis functions. Core basis functions are localized near a nucleus whereas valence basis functions extend over the whole molecule.

As the core basis functions change so rapidly over a small region where valence basis functions on a different centre are approximately constant the charge density, $(p^A a^B)$, involving a core basis function p, on centre A, and a valence basis function a, on another centre B, depends mainly on the core basis function. In the core valence approximation core valence overlap distributions are expanded in terms of a mono-centric basis centred at the core.

The basis set for each core valence distribution is a function of the core orbital only. The zeroth order generator, p^0, for a given core basis function is

spherically symmetric and is a sum of Gaussian's for a Gaussian basis set. It is related to the core orbital by eqn 1.16.

$$p = p^0 x^i y^j z^k \qquad [1.16]$$

A first order basis consists of the set p^0, xp^0,yp^0 and zp^0. The second order basis set consists of the first order terms supplemented with additional quadratic terms. The core valence distribution is then approximated by (1.17), where $A_{p\sigma}$ is determined by requiring that the lower moments of the core valence distribution and the approximation be equal.

$$[p\sigma] = \sum_{\sigma} A^{\sigma}_{p\sigma}[p^{\sigma}] \qquad [1.17]$$

In the calculations reported in this thesis $p^A a^B$ are only approximated if $A \neq B$. Integrals involving $p^A a^B$ are evaluated exactly if the second charge distribution in the integral $[p^A a^B|p^C b^D]$ involves a core or a valence orbital on A. Integrals involving an overlap charge density arising from core orbitals on different centres $p^A q^B$ are set to zero. So two electron integrals involving core basis functions p and q and valence basis functions a,b and c are approximated

as ;

$$[p^A a^B|q^C b^D] = \sum_{\sigma i} A^{\sigma}_{pa} A^{i}_{qb} [p^{\sigma}|q^{i}] \qquad [1.18a]$$

$$[p^A a^B|b^D c^E] = \sum_{\sigma} A^{\sigma}_{ap} [p^{\sigma}|bc] \qquad [1.18b]$$

Thus as well as the normal four function integrals a new class of integrals involving $[p^{\sigma}|q^{i}]$ and $[p^{\sigma}|bc]$ must be evaluated. However in a large system the total number of integrals and thus the computational time varies as $N^4_{valence}$. So a substantial saving at the integral stage, and also during the iteration process owing to the reduction in the length of the integral tape, which has to be read at each iteration, is achieved by the use of this approximation.

1.6 The Correlation Problem and Configuration Interaction

The Hartree Fock method is based on the assumption that each electron moves independently of the instantaneous positions of all the other electrons in the molecular system, and the best orbitals constructed using this assumption are used to construct the wave function. These orbitals describe the motion of an electron in the average field of all the other electrons in the system. This produces an energy which is higher than the exact energy owing to neglect of the

instantaneous interactions between the electron pairs. The correlation energy is defined as the difference between the solution of the non-relativistic Schrödinger equation and the restricted Hartree Fock limit.

The correlation energy is small compared to the total energy of the system but, as the energy of most chemical processes is the difference between the energies of two states of quite similar energy, it is of similar magnitude to most reaction energies and so is not negligible. For example, different states of a molecular system may have different amounts of correlation energy. Thus the experimental ordering of these states may be different to the Hartree Fock predicted ordering (ionization potentials etc.), a point which has to be considered when using the Hartree Fock method to interpret experimental results.

An expensive computational technique exists which permits the calculation of correlation energies. This is the Configuration Interaction method [12], in which the wave function, Ψ, is written as the sum of a series of configurations, $\tilde{\Phi}_i$, including the ground state HF determinant, which are generally taken as linear combinations of Slater determinants, constructed by replacing occupied orbitals in the ground state RHF wavefunction with virtual orbitals.

$$\Psi = \sum_i C_i \tilde{\Phi}_i \qquad [1.19]$$

Since a large number of configurations can be generated from a moderately

sized basis set the number of configurations contributing to the series must be restricted. It is thus important to select those configurations which make a large contribution to the correlation energy.

1.7 Koopman's Theorem [13]

Koopman's theorem states that the binding energy of an electron in a closed shell molecule may be approximated to by the negative of its Hartree Fock ground state orbital energy. This very useful theorem means that it is possible to obtain estimates of the ionization potentials of a molecule from its ground state wave function without any calculation of the wave functions for the various ionized states of the system. As a result of this great saving in computational labour it is widely used, though such estimates must be treated with some caution. An assumption involved in its proof requires that the molecular orbitals in the ion be the same as those in the molecular ground state, the sudden approximation.

This is clearly not the case. Upon ionization, if there are 2n electrons initially, the remaining electrons move in the field of (2n-2) electrons, rather than (2n-1) as in the ground state, and reorganize, or relax, so as to minimize the energy of the ionic system. This will tend to make Koopman's theorem ionization potentials greater than experiment. Upon ionization there is also usually a de-

crease in the correlation energy of the system, as the number of electrons within the molecular system decreases. This increases the magnitude of the ionization potential. The fact that the two errors, relaxation and correlation, are of opposite sign and so tend to cancel out explains the often startlingly good agreement of Koopman's theorem estimates and the experimental ionization potentials.

Allowance for relaxation effects may be made by use of the ΔSCF Method. This involves calculating ionic state wave functions of equal quality to the ground state wave function, and the IP's may then be obtained from the difference between the ground state energy and the energies of the various ionic states, thus accounting for much of the relaxation energy. In cases where relaxation is very great the ΔSCF Method and Koopman's theorem can produce different orderings of the ionization potentials.

1.8 Rydberg States and Quantum Defects.

A photon may not be sufficiently energetic to ionize an electron from a given orbital but may be of the correct energy to excite an electron to a Rydberg orbital, yielding a Rydberg state [14]. Such orbitals are very diffuse and extend far from the molecular core. At such distances the molecular potential is effectively that of a unipositive centre, as the remaining electrons, in comparatively

constricted ground state orbitals, shield the nuclear charges. The spacing of the energy levels of the hydrogen atom bears similarities to such a molecular situation, as in both cases the electron under consideration is, in effect, moving in the electric field of a unipositive centre.

The energy required to excite the atomic hydrogen electron into a given Rydberg orbital is

$$E_n = IP_i - R/n^2 \qquad [1.19]$$

where R is the Rydberg constant, n the principal number of the Rydberg orbital under consideration and IP_i the ionization potential of the atomic orbital i from which the electron is excited. Thus there exists a series of states, progressively more closely spaced in energy, and the energy required to excite an electron to one of these states converges onto the ionization potential of the orbital from which the electron is excited as n increases.

The energy required to excite an electron from molecular orbital i to a given Rydberg orbital with principal quantum number, n, is given by a modification of Eqn. 1.19.

$$E_n = IP_i - R/(n - \delta_{n,x})^2 \qquad [1.20]$$

$\delta_{n,x}$ is the quantum defect [15] and arises from the interaction of the Ry-

dberg electron with the other electrons in the system and with the molecular framework. The quantum defect is a function of several variables. As the principal quantum number, n, increases the orbital becomes more diffuse. Thus the quantum defect must be dependent on the principal quantum number n, but this dependence has been found to be small and is mostly ignored. Other factors, x, which affect the quantum defect include the angular momentum of the excited electron and the direction in which the Rydberg orbital is oriented with respect to the molecular framework. Thus ns, np and nd orbitals all have different quantum defects and the quantum defects for $np\sigma$ and $np\pi$ orbitals are significantly different, as are those for $nd\sigma$, $nd\pi$ and $nd\delta$ orbitals.

Knowledge of the ionization potentials and quantum defects make it possible to estimate excitation energies for transitions which have not been measured experimentally. Such estimates will be compared with IVO values and the available experimental values for several small molecules in this thesis.

The values of the quantum defects have been derived from experimental excitation energies for many small molecules by Lindholm [15].

1.9 Population Analysis

It can be helpful in interpreting a molecular wave function to partition the electronic population, either from the total wave function or a spin orbital, between the various atoms in the molecule. In this report the scheme due to Mulliken [16] will be used. The gross atomic population of atom a, consisting of a sum of contributions from each spin orbital, is defined as

$$q_a = \sum_i q_a^i = \sum_i N_i \sum_\mu \{C_{\mu i}^2 + \sum_\upsilon C_{\mu i} C_{\upsilon i} S_{\mu\upsilon}\} \qquad [1.21]$$

Where N_i is the number of electrons on orbital i, the sums over μ and υ are sums over basis functions, with μ on atom a and υ on all other atoms on the molecule. $S\mu\upsilon$ is the overlap integral between basis functions μ and υ and C_{ni} is the coefficient of the n'th basis function in the i'th orbital.

1.10 Localized orbitals [17]

Hartree Fock canonical molecular orbitals often extend over the whole molecule and thus bear little relation to the conventional picture of specific bonds. However the electron distribution is related to the square of the wave function rather

than to individual spin orbitals, and while a given set of spin orbitals will determine a wave function, the converse is not true. A new set of normalized orthogonalized orbitals may be generated from the canonical orbitals, without change in the wavefunction, by means of an unitary transformation. However there are an infinite number of possible transformations and so an infinite number of possible orbitals. Just as the Hartree Fock canonical orbitals are appropriate for interpretation of the photoelectron spectrum other orbitals may be useful for different interpretative purposes.

The method of Edmiston and Rūdenberg [17] for the generation of localized orbitals is based upon the minimization of inter orbit interactions. When this is minimized the charge density of different orbitals must be separated as much as possible. This means that, as far as is consistent with the wave function the orbitals are localized as much as possible. Conversely, this means that the total intraorbital Coulomb energy is maximized. When localized orbitals are generated using this method the resulting orbitals bear a close resemblance to the conventional picture of molecular charge distribution arising from lone pair and bonding orbitals.

1.11 The Xα Approximation

The Hartree Fock pseudo eigenvalue equations contain different exchange terms for each of the Hartree Fock orbitals. Slater [18] suggested replacing each of these different terms by a weighted mean. When this weighted mean is calculated for a free electron gas the result is

$$[V_{xhf\uparrow}(1)]av = -3[\frac{3}{4\pi}\rho_{\uparrow}(1)]^{\frac{1}{3}} = V_{x\alpha\uparrow}(1) \qquad [1.22]$$

where

$$\rho_{\uparrow}(1) = \sum_{i\uparrow}[n_i\Phi_i^*(1)\Phi_i(1)] \qquad [1.23]$$

The expression was obtained by writing the wave functions as a Slater determinant, calculating the total energy for a wave function in this form, then the spin orbital Φ_i was varied so as to minimize the total energy, resulting in the Hartree Fock equations. The exchange term was then replaced by its average and this was replaced by its statistical equivalent. However the process of variation and replacement by the statistical average is not a commutative procedure. Gaspar, Kohm and Sham [19] made the replacement by the statistical approximation in the formulae for the total energy and then varied this to obtain the one electron equation. This resulted in a value for the exchange correlation only two thirds as big as that which Slater had obtained:

$$(V^{i\uparrow}_{xgks}(1)) = -2[\frac{3}{4\pi}\rho_{\uparrow}(1)]^{\frac{1}{3}} \qquad [1.24]$$

These discrepancies led to the introduction of a variable coefficient, α, in the approximate exchange term with $\alpha = 1$ being led to by Slater's calculation, and $\alpha = 2/3$ by the derivation of Gaspar, Kohm and Sham.

$$V_{x\alpha\uparrow} = -3\alpha[\frac{3}{4\pi}\rho_{\uparrow}(1)]^{\frac{1}{3}} \qquad [1.25]$$

As α originates in the introduction of an approximation into the one electron operator, and the energy expression explicitly contains α, α cannot be determined variationally. Such an attempt would in any case fail as the calculated total energy does not show a minimum with respect to α. The larger the value of α employed the lower the total energy. Hence an arbitrary criterion has to be found by which the value of α can be determined.

Schwarz [20,21] has performed a series of calculations in which two values of α have been found for isolated atoms. The first of these is α_{hf}, which is the value of α such that $\langle E_{x\alpha}\rangle$ is exactly equal to $\langle E_{HF}\rangle$.

The second of these values is α_{vt}. This is the value of α for which the Virial Theorem (V = —2T) is exactly satisfied when the $X\alpha$ spin orbitals calculated

using α_{vt} are substituted into the Hartree Fock expressions for the kinetic and potential energies. It may be seen from the values of α_{hf}, α_{vt} and $\partial(E_{X\alpha})/\partial\alpha$ given by Schwarz that the difference in $\langle E_{X\alpha}\rangle$ when α_{hf} and α_{vt} are used will be very small.

1.12 Significance of the $X\alpha$ One Electron Eigenvalue [22]

Hartree Fock eigenvalues are finite differences between the energy of the system with orbital i occupied and unoccupied, keeping all other orbitals unchanged. However using the $X\alpha$ approximation changes the meaning of the eigenvalues. The $X\alpha$ eigenvalues are no longer finite differences between the energies of two states but are found to be related to the total energy of the system by eqn 1.26b.

$$\epsilon_{ihf} = \langle E_{tot}(i=1)\rangle - \langle E_{tot}(i=0)\rangle \qquad [1.26a]$$

$$\epsilon_{iz\alpha} = \frac{\partial(E_{z\alpha})}{\partial n_i} \qquad [1.26b]$$

The i'th orbital eigenvalue within the $X\alpha$ scheme, $\epsilon_{iz\alpha}$, is thus the derivative

of the total energy with respect to the occupation number, n_i, of the i'th orbital.

This difference, arising from the approximation to the exchange integrals, explains the observation that the two sets of eigenvalues agree most closely if α is assumed to be unity, whereas the eigenfunctions agree most closely if α is smaller than unity but greater than two thirds.

1.13 The Slater Transition State [22]

Owing to the difference in definition of the Hartree Fock and $X\alpha$ eigenvalues there is no equivalent to Koopman's theorem relating the $X\alpha$ orbital eigenvalues to the ionization potentials. Hence it would seem necessary to perform the $X\alpha$ equivalent of ΔSCF calculations in order to obtain ionization energies. This involves taking the difference of two large quantities in order to obtain a small quantity, a process which cannot be guaranteed to lead to high accuracy.

Slater suggested the transition state concept which overcomes this difficulty. Here the total energy is expanded in a Taylor series about a hypothetical state which has an occupation number of one half in the orbital, k, from which ionization is occuring. It is then found that the difference in energies between the ground and ionized states is approximately the negative of the k'th orbital

eigenvalue where orbital k has an occupation number half an electron less than it had in the ground state, the so called Slater Transition State.

$$I_k \simeq -\epsilon_k(1/2) \qquad [1.27]$$

Thus a transition state calculation will often give a better approximation to the orbital ionization potential than Koopman's Theorem, as the transition state allows the orbitals to change from the ground state, so that there is a relaxation effect included within the $X\alpha$ estimates of the ionization potentials.

1.14 The Scattered Wave Model [23]

The $X\alpha$ approximation as such only saves computational cost in the calculation of the exchange integrals. A far more approximate method, which includes the $X\alpha$ approximation is the multiple scattering model ($MSX\alpha$) [23]. In this model the molecule is divided into three different types of regions, atomic (Region 1), interatomic (Region 2) and extramolecular (Region 3), shown for a diatomic system in Figure 1.1 . Inside each region the one electron equation is solved;

$$[-\frac{\nabla^2}{2} + V(\hat{r})]\psi_i(\hat{r}) = \epsilon_i\psi_i(\hat{r}) \qquad [1.28]$$

The potential within each atomic region and the extramolecular region is expanded in a series of spherical harmonics

$$V^j(\hat{r}) = \sum_L V_L(\hat{r})Y_L(\hat{r}); \qquad L = (l,m) \ [1.29]$$

However the potential is then approximated to by the first term of the expansion, giving a spherically symmetric potential.

In the interatomic region the potential is generally set to a constant volume average.

The fact that there now exists a spherically symmetric potential in regions 1 and 3 means that the one electron equation can be rapidly solved within these regions. The constant potential within region 2 makes the solution especially simple here.

In both the atomic and extramolecular regions the solutions of the one electron equations consist of a set of radial functions and spherical harmonics, and such solutions can be found for any value of the one electron eigenvalue. How-

ever for localized orbitals the radial functions in the extramolecular region must decay exponentially at large distances from the molecule.

In the intersphere region, because of the constant potential, the solution of the one electron equation consists of a set of 'outgoing waves' from each atomic region and of 'incoming waves' from the extramolecular region. Again solutions may be found for any value of the one electron eigenvalue.

As a solution to the one electron equation in each of the regions may be found for any arbitrary value of the energy the orbital energies are found by requiring that the various wave functions and their derivatives match at each of the interfaces between the different regions of space. This results in a secular determinant, the zeros of which have to be found by numerical methods, giving the orbital eigenvalues.

This numerical evaluation of the determinant at a large number of points is one of the chief computational problems of this method. If the scanning points are not close enough it is possible to skip a root resulting in an excited state wave function. Whenever this happens serious numerical instability may result as the wave function oscillates from one configuration to another between iterations, and if convergence results, it is equally likely to be onto an excited state as onto the ground state. If, in order to avoid this problem the energy mesh is very fine, the time required for the calculation may become as great as

for an ab-initio calculation.

It has been found necessary to scan the converged molecular potential after the calculation has been completed using an exceedingly fine energy mesh to check that no eigenvalues have been missed.

1.15 Deficiences of the MSXα Method

It has been found that in a number of cases the MSXα method fails to give satisfactory results, e.g. molecular geometries. These deficiencies can be attributed to the muffin tin approximation rather than to the $X\alpha$ approximation. At the start of an iteration the potential, V_{ind}, is spherically symmetrical within each of the atomic spheres. After the iteration the final potential, V_{fin}, is not. This nonspherical potential is then spherically averaged to give V_{fin}^{sph} and is used on the succeeding iteration. So there is never true self consistency, rather the convergence criterion is that the averaged final potential be the same as the initial potential. It is in fact impossible for true self consistency to be achieved as the very nature of a chemical bond is a nonspherical electron distribution around a nucleus. So the muffin tin approximation basically ignores the existence of chemical bonds.

Thus the muffin tin approximation which is the chief simplification of the MSXα method is also its chief theoretical deficiency. Many attempts have been made to overcome this deficiency while retaining the essential features of the method but most have not developed owing to an increase in the complexity of the treatment required outweighing the proposed advantages.

Only two improvements have proved satisfactory. The actual nonspherical charge density of the system can be used in the energy equations instead of the averaged charge density [24]. This is a mathematically very complex procedure which produces good results, e.g. the equilibrium bond distance of N_2 is correctly predicted whereas the standard model predicts a value several times too large. However the computational complexity has led to this method being but seldom employed.

The alternative method involves simply permitting the touching spheres to overlap. Johnson [25] first gave a formal justification of the procedure for 'small overlap'. This allows the existing MSXα programmes to be used unchanged, merely a change in the input data is involved. Most of the intersphere charge is concentrated just outside the muffin tins and a slight increase in their size, giving sphere overlap, takes this charge within the spheres, where it is better treated. Slater [26] pointed out that the muffin tin approximation is reasonable, if each sphere contains enough electrons to neutralize the nucleus contained within.

This is precisely what the overlapping spheres method does. The charge within the overlap region is counted twice but, provided that this is not a large volume, the errors introduced are not large.

The problem then arises of assigning radii to the various spheres. By varying the sizes of the spheres individually it is possible to produce significant changes in the calculated quantities. This kind of totally arbitrary situation is unsatisfactory especially as the energy of the system continually decreases as the overlap increases. The criterion now used to determine the sphere radii is to vary the overlap until the virial theorem is satisfied.

The method of overlapping spheres is not necessarily as large an improvement as it may seem. Besides the above disadvantages it has a serious time penalty. If the calculation is carried out as originally suggested, several different ground state calculations are required until a set of sphere radii have been found, the corresponding wave function of which satisfies the virial theorem. This requires a great increase in computational effort. Furthermore as the overlap increases the time required to find the eigenvalues of the secular determinant increases. This may mean that the time required for an overlapping sphere calculation is greater than for a large scale LCAO calculation. Because of this time problem the practice has grown of performing only one calculation, with a sphere overlap of approximately 20%, an entirely arbitrary procedure, though

it is often found that overlaps in this region do provide the desired values of the sphere radii.

There is one final problem with the overlapping sphere method. Overlaps of this magnitude are not really allowable as being 'small overlaps' and the multiple scattering equations no longer really hold.

The $MSX\alpha$ method has two main advantages compared to the LCAO method. The first is its saving in computational time compared to the LCAO method in a given molecule. The second is that by use of the Slater transition state concept it is much easier to get estimates of ionization potentials containing some relaxation than from LCAO calculations. Once a converged ground state molecular potential has been calculated it takes few iterations to converge a transition state calculation. To converge a ΔSCF calculation can be a difficult task as, for all except the highest ionized states of a given symmetry, the wave function tends to fall through to the highest state.

Despite the theoretically unsatisfactory nature of the multiple scattering method it does provide answers to real problems without input of experimental parameters, answers which are often in better agreement with experiment than those produced by ab-initio methods.

1.16 REFERENCES

1. E.Steiner, *The Determination and Interpretation of Molecular Wave Functions*, (Cambridge University Press, 1976).

2. R.McWeeny and B.T.Sutcliffe, *Methods of Molecular Quantum Mechanics*, (Academic Press, 1969).

3. E.Schrödinger, *Ann. Physik*,**79**, 361 (1926).

4. M.Born and J.R.Oppenheimer, *Ann. Physik*, **79**, 361 (1926).

5. D.R.Hartree, *Proc. Chambridge Phil. Soc.*, **24**, 89 (1928).

6. V.Fock, *Z. Physik*, **61**, 126 (1930).

7. C.C.J.Roothaan, *Rev. Mod. Phys.*, **23**, 69 (1951).

8. G.Hall, *Proc. Roy. Soc.*, **A205**, 541 (1951).

9. J.C.Slater, *Phys. Rev.*, **36**, 57 (1930).

10. S.F.Boys, *Proc. Roy. Soc., (London)*, **A200**, 542 (1950).

11. J.C.Campbell, I.H.Hillier and V.R. Saunders, *J. Chem. Phys.*, **74**, 3971 (1981).

12. B.Roos, *Computational Techniques in Quantum Chemistry and Molecular Physics*, ed G.H.F. Diercksen, B.T. Sutcliffe, and A. Veillard, 251 (D.Reidl, 1975).

13. T.Koopman, *Physicia*, **1**, 104 (1933).

14. R.S.Mulliken, *J.Am. Chem. Soc.*, **86**, 3183 (1964).

15. E.Lindholm, *Arkiv Für Fysik*, **40**, 97.

16. R.S.MUlliken, *I. Chem, Phys.*, **23**, 1833 (1955).

17. C.Edmiston and K.Ruedenberg, *Rev. Mod. Phys.*, **35**, 457 (1963).

18. J.C.Slater, *Phys. Rev.*,**81**, 831 (1951).

19. W.Kohn and L.J.Sham, *Phys. Rev.*, **140**, A133 (1965).

20. K.Schwarz, *Phys. Rev.*, **B5**, 2466 (1972).

21. K.Schwarz, *Theor. Chim. Acta.*, **34**, 225 (1974).

22. J.C.Slater, *Advances in Quantum Chemistry*, **6**, 1

23. K.H.Johnson, *Advances in Quantum Chemistry*, **1**, 143

24. J.B.Danese and J.W.D.Connolly, *Int. J. Quant. Chem.*, **S7**, 279.

25. K.H.Johnson, *Int. J. Quant. Chem.*, **S4**, 153 (1971).

26. J.C.Slater, *Int. J. Quant. Chem.*, **S8**, 81 (1974).

27. S.Huzinaga, *J.Chem.Phys.*, **42**, 1293 (1965).

28. T.H.Dunnings, *J.Chem.Phys.*, **53**, 2823 (1970).

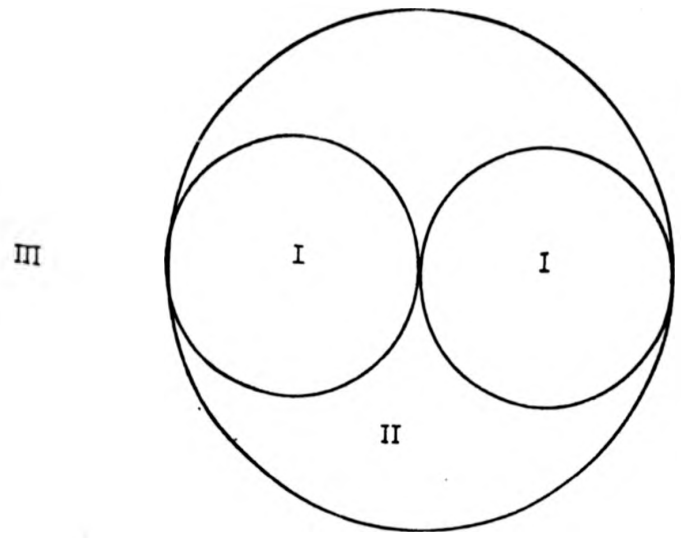

Fig. 1.1 Division of a molecular cluster into (I) atomic, (II) interatomic, and (III) extramolecular regions.

Chapter 2

Molecular Electronic Structure Calculations

In this chapter the results of two MO-SCF calculations on the MoO_4^{2-} ion will be compared. Both employ the same basis set but one involves the use of the core valence approximation scheme. The two sets of results will be shown to be in good agreement demonstrating the utility of the approximation. The results of an MSXα calculation upon this system will also be reported. Calculations are then reported, employing the core valence approximation upon the dirhodium tetraformate system. Finally MSXα calculations on the $CrCl_2$ and

$MnCl_2$ molecules are reported and used to interpret the photoelectron spectra of these systems.

2.1 Calculations on the Molybdate Ion

In the following sections ab initio MO SCF, core valence approximation MO SCF and Multiple Scattering $X\alpha$ calculations are presented for the molybdate anion. The core valence approximation MO SCF results will be shown to be in close agreement with the results of the ab initio MO SCF calculations. The MSXα calculations lead to the same ordering of the ground state orbitals as the ab initio calculations, and while there are slight differences in the ordering of the predicted ionization energies, both schemes yield a similar interpretation of the photoelectron spectra of the molybdate ion.

2.1.1 Ab Initio and Core Valence MO-SCF Calculations

The ground state wave function of the MoO_4^{2-} ion was computed within the restricted Hartree Fock scheme employing a (16s12p8d/6s3p2d) Gaussian basis set [1] on the molybdenum centre and a (9s5p/4s2p) Gaussian basis set [2] on the oxygen centres. The calculation was performed with the oxygen nuclei arranged

tetrahedrally around the molybdenum centre with an interatomic separation determined experimentally for the Na_2MoO_4 crystal (R_{Mo-O} = 1.97Å) [3]. The total energy and orbital eigenvalues of the outermost seven orbitals are presented in Table 2.1.

Also presented in Table 2.1 are the results of a calculation employing the core valence approximation. This calculation employed the same basis set and molecular geometry as the ab initio calculation. All contracted basis functions consisting entirely of Gaussian functions with exponents greater than 1.0 were treated as core type functions, giving 23 core basis functions and 42 valence basis functions. As shown in Table 2.1 the orbital eigenvalues of both the ab initio and core valence calculations are very similar and the total energies differ by only 0.07eV. The ab initio calculation required 367 seconds and the core valence 334 seconds for integral evaluation on a CDC 7600. The calculations required 5.8 and 5.9 seconds per SCF iteration respectively. Despite the slightly longer SCF time required for the core valence calculation, use of the approximation resulted in little loss of quality in the results and a small saving in the total calculation time.

Designating a further molybdenum s and three equivalent p functions as cores, giving in 27 core functions and 38 valence basis functions, results in a further reduction of the integral evaluation time to 326.9 seconds and the time

per SCF cycle is reduced to 5.5 seconds. This procedure is not justified as some of the exponents of the Gaussian functions involved are quite small ($\simeq 0.3$) and inaccuracies result. Not only is the resultant total energy in error by 0.3eV but the $7a_1$ orbital is now the highest occupied orbital instead of the $1t_1$. However the calculations show that for systems with a large number of core orbitals, significant savings may be made in the time required for integral evaluation.

Consideration of an isolated ionic system is unphysical as these systems exist in crystalline form, surrounded by other ions which provide a stabilizing electrostatic field. This stabilization is most important for the outer valence orbitals, which in the isolated ion calculations are bound by only 1.5eV. The electrostatic potential at the molybdenum and oxygen nuclei were calculated by a programme based on the formulae given by Tosi [4]. The charges on the molybdenum and oxygen centres were those given by the Mulliken population analysis of the wave function calculated for the isolated ion, $Q_{Mo} = +1.82947e$ and $Q_O = -0.95737e$. The resultant electrostatic potentials were reproduced by surrounding the molybdate system with point charges representing the surrounding sodium, molybdenum and oxygen atoms and by four supplementary charges which were chosen so that the potential at the central molybdenum and oxygen sites, on which the basis functions were placed, were the same as calculated for the molybdenum and oxygen site in the crystal. The orbital eigenvalues of the seven outermost orbitals of this calculation are given in Table 2.1, where

it may be seen that the surrounding charges stabilize each of the orbitals by almost the same amount.

While it is possible to compare the orbital eigenvalues directly with the photoelectron spectrum by use of Koopman's theorem, ΔSCF calculations have been carried out for the seven outermost orbitals so as to allow for electronic relaxation upon ionization. The calculated relaxation energies and ionization energies are presented in Table 2.2.

2.1.2 MSXα Calculations

For comparison purposes the results of an MSXα calculation are also given in Table 2.1. In this calculation each atomic centre was surrounded with a sphere which touched, but did not overlap, the sphere surrounding its nearest neighbour. A sphere also surrounded the entire system. The sphere radii were R_{Mo} = 2.6357au, R_O = 1.0907au and R_{outer} = 4.8171au, and were chosen from the ratio of Slaters atomic radii for molybdenum and oxygen. The α values of Schwarz were employed in the atomic spheres and a weighted average (α = 0.73606) in the intersphere and outer sphere. Partial waves up to l = 4 on the outer and molybdenum spheres and l = 2 on the oxygen sphere were employed.

This calculation yielded the same ground state configuration as the ab initio

calculation but the eigenvalues in Table 2.1 cannot be compared directly with the photoelectron spectrum. Slater Transition State calculations were carried out in order to obtain predictions of the ionization energies. As the transition state allows for orbital relaxation, these transition state energies, given in Table 2.2, are comparable with the ΔSCF ionization energies listed there.

2.1.3 Discussion

The X-ray photoelectron spectrum of Na_2MoO_4 measured by Calabrese and Hayes [5] is reproduced in Figure 2.1 . It consists of three peaks, centred at 1.0, 7.5 and 23.5eV binding energy. The first of these peaks, (I), is discounted by Calabrese and Hayes as arising from impurities in their samples. The experimental peak, [II], with a maximum at 7.5eV extends over 8eV and is skewed to low binding energy. This peak arises from the overlap of two peaks centred at 5.0 and 7.9eV binding energy.

Both the ΔSCF and MSXα calculations predict the appearance of three groupings of orbitals in the PES; a low binding energy grouping arising from the $1t_1$, $8t_2$, and $7a_1$ orbitals, another grouping arising from the 2e and $6t_2$ orbitals between two and five electron volts to higher binding energy, and a third group arising from the $6t_2$ and $6a_1$ orbitals to at least ten electron volts higher binding energy.

The most important result of this work is the demonstration of the accuracy of the core valence approximation in calculations involving large systems. This approximation will now be employed in the investigation of the $Rh_2(O_2CH)_4$ molecule, a much larger system in which the time saving owing to this approximation will be more significant.

2.2 Rhodium Tetraformate Calculations

Hartree Fock SCF MO calculations employing the core valence approximation were performed on $Rh_2(O_2CH)_4$ based upon the structural parameters determined by Cotton et al [6] for $Rh_2(O_2CCH_3)_4.2H_2O$ (R_{Rh-Rh} = 2.39Å, R_{C-O} = 1.27Å, R_{Rh-O} = 2.04Å and R_{C-H}= 1.08Å). The (17s11p8d/6s3p2d) basis of Huzinaga [1] was employed on the rhodium centres, the (7s3p/2s1p) basis on the oxygen and carbon centres, and a Slater type function (ξ = 1.2) expanded as four Gaussian type functions on the hydrogen centres. The basis functions corresponding to the carbon and oxygen 1s, rhodium 1-4s, 2p, 3p and 3d orbitals were treated as core functions. This resulted in 42 core basis functions and 72 valence basis functions. This calculation will be referred to as calculation A.

A second calculation, calculation B, employed the same basis set except for the functions corresponding to the rhodium 4d orbital. In calculation A

the three Gaussian basis functions comprising the 4d basis function (exponents 1.83, 0.71 and 0.25) had coefficients of 0.37, 0.51 and 0.29 respectively. These resulted from the minimization of the energy of an isolated rhodium atom. In calculation B the three exponents were unchanged but their coefficients were altered to 0.3, 0.3 and 0.3. This results in an extension of the 4d basis function further from the rhodium centre, so bonding between the metal and oxygen centres may be better described.

A third calculation, calculation C, in which the rhodium basis was as in calculation B was also performed. In this calculation each oxygen and carbon s basis function consisted of three Gaussian functions, and each p function of four Gaussian functions. These were obtained by least squares fitting of the best Slater type orbitals found for the isolated atoms. While this is expected to increase the total energy of the system as the oxygen and carbon 1s core orbitals are better described in the original basis (five Gaussians instead if three), bonding in the system may be better described, as the oxygen and carbon 2s and 2p basis functions consist of two and three Gaussian functions in calculation A and B, but consist of three and four functions in calculation C.

The current results are compared with those reported subsequently by Nakatsuji et al [7] , which employed a basis set in which each atomic orbital was represented by three Gaussian functions giving a (15s12p6d/5s4p2d) basis in the

rhodium centres, a (6s3p/2s1p) basis on the carbon and oxygen centres, and a contracted Gaussian type basis function consisting of three Gaussian type functions on the hydrogen centres. Comparison of this basis set with that employed in calculation C, which of the current series of calculations most closely approaches it, shows that calculation C employs a better basis set on all ligand centres. The quality of rhodium s and d basis functions in the current calculations is at least as good as that of Nakatsuji et al. However, a (12p/4p) contraction is employed by Nakatsuji et al on the rhodium centres whereas an (11p/3p) contraction is employed in the present calculations. As this is the sole point of superiority in the basis set of Nakatsuji et al, it is believed that the results of calculation C are of at least equal quality to those subsequently reported.

2.2.1 Computational Results

The total energies and charges on the various atomic centres given by Mulliken population analysis for each calculation are presented in Table 2.3. The small change in rhodium basis between calculations A and B yields a total energy lower by 0.23eV, confirming that basis B does permit a better description of the system. In calculation C the total energy increases very substantially, as expected, because the carbon and oxygen 1s basis functions are not of similar

quality to those employed in calculations A and B. In the minimal basis set calculations reported by Nakatsuji et al each basis function consisted of a contraction of three Gaussian type functions. As the core orbitals on the rhodium centres are better represented in the present calculations , it is thought that the total energy obtained by Nakatsuji et al, which was not reported, is considerable more positive than even that of calculation C, which employs the basis set closest to that reported by Nakatsuji et al.

From Table 2.3 it is clear that the charge distribution obtained from the Mulliken population analysis is extremely sensitive to small changes in basis set. The small change in total energy between calculation A and B is accompanied by a decrease in charge on the rhodium centres of 20%. Moving from calculation B to C, in which the ligand valence orbitals are better described, the charges on the carbon and oxygen centres become more negative, whereas the charges on the rhodium and hydrogen centres, where the basis set has remained unchanged, become more positive. This indicates that the new ligand basis functions in calculation C are being used to a greater extent than those which they replace in calculation B, displacing rhodium basis functions in the process rather than necessarily providing a greatly improved description of the valence electron distribution. However, the increase in the positive charge on the rhodium centre is only 15% of the decrease in this charge obtained by employing the slightly modified 4d basis function in calculation B.

The orbital eigenvalues and percentage contribution of metal basis functions to each of the outer valence orbitals, obtained by Mulliken population analysis, are presented in Table 2.4 for calculation C, which should best describe these orbitals, and the metal bonding properties of all orbitals with more than 9% metal character is indicated. Five orbitals are metal dominated, giving, in order of increasing energy, $\delta^*\pi^*\pi\sigma\delta$, but metal character is spread through many other orbitals, including one σ orbital of 49% metal character.

The calculated orbital configuration is found to be sensitive to basis set change. Considering orbitals of more than 40% metal character calculation A gives a metal bonding configuration of $\delta^*\pi\pi^*\delta\sigma\sigma$ and calculations B and C $\delta^*\pi\pi^*\sigma\delta\sigma$. Despite the presence of two orbitals with σ bonding character in these configurations Boys localization reveals that there is actually only one bond between the two metal centres, which is of σ bonding character. All other orbitals localize on separate metal atoms to give atomic d like orbitals, indicating that there is no overall δ or π contribution to bonding.

The molecular orbital coefficients of the valence metal basis functions contributing to the $4a_{1g}$ and $5a_{1g}$ molecular orbitals in calculation C are presented in Table 2.5, where they are compared with the coefficients of the corresponding basis functions in the highest occupied molecular orbital in the calculation of Nakatsuji et al, which is the only molecular orbital of Rh-Rh σ bonding

character reported by these authors.

2.2.2 Discussion

Despite the short experimental distance between the rhodium atoms the current calculations agree with both MSXα [8] and other LCAO calculations in predicting the existence of only a single bond between the two rhodium centres. However the various calculations provide rather different descriptions of the electron distribution within the system.

The most striking illustration of these differences is the large difference in overall atomic charges between the calculations reported by Nakatsuji et al and the results of calculation C with which they are most comparable. The discrepancy is largest in the case of the hydrogen centres. The current calculations produce charges on the hydrogen centres between 400 and 500% greater than those quoted by Nakatsuji et al, whilst the largest difference between the two sets of calculations for the other atomic centres is in the region of 30%. The comparatively large difference in hydrogen centre charge between calculations A and B, where the only difference is a slight modification in the rhodium basis, indicates that differences in rhodium basis sets between the current series of calculations and those of Nakatsuji et al may account for the large differences in the respective hydrogen charges. Values are also given in Table 2.3 for

overall atomic charges given by the MSXα calculations of Norman and Kolari [8]. They have been obtained from the published charges in the various atomic spheres as well as in the intersphere and outer sphere regions, by allocating the intersphere and outer sphere charge to the various spheres in proportion to the charge contained in a given set of symmetry equivalent spheres. When this is done the charge on the rhodium centres is found to be of almost equal magnitude but opposite charge to that yielded by LCAO-MO calculations, implying a very different charge distribution indeed.

It is possible that the current calculations are not in fact comparable with those of Nakatsuji et al [7], who report that the optimum calculated bond length was 2.28Å, instead of the experimental value of 2.39Å employed in the current calculations. It is not clear from the report of Nakatsuji et al whether the reported results apply to calculations performed with a rhodium distance of 2.39Å or 2.28Å, and this alteration in the bond length could affect the calculated electronic structure.

From the report of Nakatsuji et al [7] it appears that their calculations resulted in a set of pure metal orbitals, with a bonding configuration $\pi\delta\pi^*\delta^*\sigma$, unlike the current results which yield two orbitals of metal σ bonding character. Nakatsuji et al report the coefficients of various basis functions in their sole σ bonding orbital, and it may be seen in Table 2.5 that neither of the two σ

bonding orbitals resulting from the current calculations are very similar to that reported by Nakatsuji et al, both having less metal character and correspondingly more ligand character than those reported by Nakatsuji et al. Furthermore the report of these authors includes an orbital energy diagram for the molecular orbitals pertinent to the metal-metal bond in which the five occupied orbitals have eigenvalues between –5 and –9eV, a situation which is not reported in the current calculations which yield orbital energies of less than –12.5eV for all occupied orbitals.

The MSXα calculations of Normal and Kolari yield eigenvalues of between –6 and –9.7eV for orbitals of large metal character, but these figures are not comparable to those yielded by the various LCAO-MO calculations owing to the rather different meanings of the orbital eigenvalues in the two computational schemes.

The spread of metal character in significant quantities through a large number of orbitals is a feature shared by the current results and those yielded by MSXα calculation. Indeed, if orbitals of 40or more metal character are included, the MSXα calculation yields a metal-metal bonding configuration of $\delta\sigma\pi\sigma\delta\pi^*\delta^*$, although when all the bonding and antibonding contributions are summed, the result is an excess of two metal-metal bonding electrons over antibonding electrons, both of σ character, as results from the LCAO-MO calculations.

The prediction of the existence of only a single bond between the metal centres leaves the short metal-metal distance in this complex somewhat puzzling. There may well be merit in the suggestion advanced by Norman and Kolari [8] that the bridging carboxylate ligands constrain the metal atoms to a shorter separation than they otherwise prefer, and that the weaker the metal-metal bond (in this case single) the more likely it is to be affected by ligand preferences.

While this investigation has demonstrated the utility of the core valence integral approximation scheme, and produced interesting results as to the order of the metal-metal bond, it has also shown the great sensitivity of the calculated electron distribution to small changes in basis set when a minimal basis is employed. Therefore a detailed description must await the results of calculations performed with a much larger and more flexible basis set.

2.3 Calculations on $MnCl_2$ and $CrCl_2$

The transition metal dihalides, MX_2 are amongst the simplest molecular systems in which d orbitals participate in the bonding, and are also amongst the simplest transition metal complexes to have been studied by photoelectron spectroscopy (PES) to date. In this section an attempt will be made to interpret the PES of $CrCl_2$ and $MnCl_2$ [9] by the use of spin unrestricted $X\alpha$ calculations. This is

found to be a far from straight forward task, and in order to arrive at a definitive interpretation it will be found necessary to compare the current results with the spin restricted and spin unrestricted $X\alpha$ results of Berkowitz et al [10] for $MnCl_2$, published while the present results were being prepared for publication, and the CI and ΔSCF results of Lee et al [9] for both $CrCl_2$ and $MnCl_2$.

Comparison of the spin unrestricted $X\alpha$ results reported here with the spin restricted results of Berkowitz et al will illustrate the great importance of the consideration of spin effects in molecules where several different spin states are expected to be close in energy. It will be shown that the spin unrestricted $X\alpha$ transition state calculations are of much better quality than the ΔSCF calculations but do not correlate as closely with the PES as the CI calculations reported by Lee et al. However both the CI and spin unrestricted $X\alpha$ calculations lead to the same interpretation of the PES whereas it is impossible to gain an understanding of the PES on the basis of the ΔSCF results.

The most important point to emerge from the present work is the extreme utility of the use of radiation sources of different energies in the measurement of PES. In the present case the availability of both He(I) and He(II) spectra shows which bands in the PES are associated with ionization from orbitals with metal character. This, in combination with calculations, leads to a correct interpretation of the PES. This interpretation is rather different to that offered

by Berkowitz et al for $MnCl_2$ on the basis of the He(I) PES alone.

2.3.1 MSXα Calculations

MSXα calculations of the ground state electronic structure of $MnCl_2$ and $CrCl_2$ were carried out employing muffin tin potentials together with calculations of the valence ionization potentials using the transition state method. The calculations were carried out using overlapping spheres with radii determined by the method suggested by Norman [11], which gave an increase of 28% over touching sphere radii in the case of $MnCl_2$ and 25% in the case of $CrCl_2$. The Mn-Cl bond length employed was 2.21Å[12] and the Cr-Cl bond length was 2.35Å, the value given by an ab-initio calculation on $CrCl_2$ [13].

In both cases the molecular symmetry employed was $D_{\infty h}$. The outer sphere was placed externally tangential to the two chlorine spheres. The calculated total energy for $MnCl_2$ was -2069.178au, with a virial theorem ratio of 0.999995, and for $CrCl_2$ -1962.576au, with a value of the virial theorem ratio of 1.000013. The atomic exchange parameters (α_{vt}) employed were those obtained by Schwarz. For the intersphere region a weighted average of the atomic exchange parameters was employed, the weights being the number of electrons in the neutral atoms. Spherical harmonics up to $l = 4$, 4, and 2 were employed on the outer, metal and chlorine spheres respectively. All calculations were carried

by Berkowitz et al for $MnCl_2$ on the basis of the He(I) PES alone.

2.3.1 MSXα Calculations

MSXα calculations of the ground state electronic structure of $MnCl_2$ and $CrCl_2$ were carried out employing muffin tin potentials together with calculations of the valence ionization potentials using the transition state method. The calculations were carried out using overlapping spheres with radii determined by the method suggested by Norman [11], which gave an increase of 28% over touching sphere radii in the case of $MnCl_2$ and 25% in the case of $CrCl_2$. The Mn-Cl bond length employed was 2.21Å[12] and the Cr-Cl bond length was 2.35Å, the value given by an ab-initio calculation on $CrCl_2$ [13].

In both cases the molecular symmetry employed was $D_{\infty h}$. The outer sphere was placed externally tangential to the two chlorine spheres. The calculated total energy for $MnCl_2$ was -2069.178au, with a virial theorem ratio of 0.999995, and for $CrCl_2$ -1962.576au, with a value of the virial theorem ratio of 1.000013. The atomic exchange parameters (α_{vt}) employed were those obtained by Schwarz. For the intersphere region a weighted average of the atomic exchange parameters was employed, the weights being the number of electrons in the neutral atoms. Spherical harmonics up to l = 4, 4, and 2 were employed on the outer, metal and chlorine spheres respectively. All calculations were carried

out within the spin unrestricted formalism. These spin unrestricted calculations resulted in the following ground state configurations for $MnCl_2$ and for $CrCl_2$:

$$MnCl_2 = \left|\text{core}.\, 8\sigma_g^1\uparrow\ 8\sigma_g^1\downarrow\ 2\pi_g^2\uparrow\ 7\sigma_u^1\uparrow\ 7\sigma_u^1\downarrow\ 1\delta_g^2\uparrow\ 2\pi_g^2\downarrow\ 4\pi_u^2\uparrow\ 4\pi_u^2\downarrow\ 9\sigma_g^1\uparrow\ 3\pi_g^2\uparrow\right|$$

$$CrCl_2 = \left|\text{core}.\, 8\sigma_g^1\uparrow\ 8\sigma_g^1\downarrow\ 7\sigma_u^1\uparrow\ 7\sigma_u^1\downarrow\ 2\pi_g^2\uparrow\ 2\pi_g^2\downarrow\ 4\pi_u^2\uparrow\ 4\pi_u^2\downarrow\ 1\delta_g^2\uparrow\ 3\pi_g^2\uparrow\right|$$

To examine the charge migration occurring upon ionization a population analysis of the MSXα orbitals resulting from the ground state and transition state calculations was carried out. The quantities $\dot{Q}^n(A)$ and QL^n [14] give respectively , the gross population associated with the group of symmetry equivalent atoms A in orbital n, and the corresponding charge loss occurring at atoms A accompanying ionization from orbital n. These values together with the calculated ionization energies arranged in order are given in Table 2.6 for $MnCl_2$ and Table 2.7 for $CrCl_2$.

2.3.2 Discussion

Four main regions are evident in the He(I) p.e. spectrum of $MnCl_2$ of which three show clearly in the He(II) p.e. spectrum (fig. 2.2). The position of the peak maxima and the relative intensities of the various peaks are given in Table 2.8. In the He(II) spectrum band C has increased greatly in intensity relative to band b, and band A has also increased, although to a much lesser extent.

It is known that the relative cross sections for metal 3d ionization compared to chlorine 3p ionization are greater for He(II) than for He(I) radiation. Thus the large increase in the intensity of band C relative to band B indicates that it arises from predominantly metal ionization. The increase in band A intensity also indicates some metal contribution to this band.

Spectra bearing marked similarities to those of $MnCl_2$ are obtained for $CrCl_2$ (fig. 2.3). Here only three main regions can be identified, the band corresponding to the relatively weak $MnCl_2$ peak D being either nonexistent or unresolved. The position of the peak maxima and relative intensities of the various bands are given in table 2.9. Here too, bands A and C increase in intensity relative to band B when comparing the He(I) and He(II) p.e. spectra. This increase affects bands A and C much more equally than the similar increases in the case of $MnCl_2$ and indicates that both bands again arise from predominantly metal ionization.

The results of the spin unrestricted MSXα calculation on the ground states of both $MnCl_2$ and $CrCl_2$ demonstrate spin splitting of considerable magnitude not only in the eigenvalues of the valence orbitals but also in their composition. These effects are also present in the transition state eigenvalues presented in tables 2.6 and 2.7, and are much more marked for gerade levels, to which contributions from metal s and d orbitals are possible than for ungerade lev-

els, which are mainly chlorine 3p composition. The spin restricted cellular $X\alpha$ calculation of Berkowitz et al for $MnCl_2$ yields a very different ground state to that produced by spin unrestricted calculations, one in which there is only one partly occupied level, the $3\pi_g$ level.

$$MnCl_2 = |\text{core}.8\sigma_g^2\, 7\sigma_u^2\, 2\pi_g^4\, 4\pi_u^4\, 1\delta_g^4\, 3\pi_g^1|$$

The current results for $MnCl_2$ clearly associate the first band in the p.e. spectrum with ionization from the $3\pi_g$ orbital, with the ionization from the $9\sigma_g$ orbital predicted to lie at 0.54eV higher binding energy. As the experimental separation between bands A and the first maximum in band B is only 0.76eV, assignment of the $9\sigma_g$ ionization to band B is possible. However, the $9\sigma_g$ orbital is mainly metal in character, even more so than the $3\pi_g$ orbital, and the low energy component of band B decreases slightly in intensity in the He(II) spectrum. This is contrary to the behaviour expected of the band contained a contribution from a mainly metal ionization at its low energy edge, so it is unlikely that ionization from the $9\sigma_g$ orbital is contained in this region of the spectrum. For this reason band A is assigned to ionization from both the $3\pi_g$ and $9\sigma_g$ orbitals.

The experimental results show a gap of 1.2eV between peaks B and C. No such gap is present in Table 2.6 owing to the large amount of spin splitting in the computational results. However, it is possible to interpret the experimental

results with the aid of the calculations. Peak C shows a large increase in intensity in the He(II) spectrum which can only be rationalised on the basis of the current results by including ionization from the $1\delta_g$ orbital under this peak. If the calculated ordering of the ionization energies is correct peak C must also include ionization from the $8\sigma_g$ orbital and from the $2\pi_g$ majority spin orbital component, while peak B must be assigned to ionization from the $2\pi_g$ minority spin, $4\pi_u$ and $7\sigma_u$ mainly chlorine orbitals.

This assignment has only been rendered unambiguous by the availability of both He(I) and He(II) p.e. spectra. If only He(I) spectra had been available it would have been possible to assign ionization from the $9\sigma_g$ majority spin orbital to peak B and very difficult, unarbitrarily, to decide where the division between ionizations which contributed to peaks B and C lay. Berkowitz et al [10] have also reported spin unrestricted transition state cellular MSXα calculations on the valence ionization energies of $MnCl_2$, which lead to the same orbital occupancies and ordering of binding energies as the present calculations, and to a much smaller interval between the calculated ionization energies of the $3\pi_g$ and $9\sigma_g$ majority spin orbitals (table 2.6). However, their assignment of the He(I) p.e. spectrum of this system was based on spin restricted transition state calculations. Thus peak A was assigned to ionization from the partly occupied $3\pi_g$ and fully occupied $1\delta_g$ levels, peak B to the $4\pi_u$, $2\pi_g$ and $7\sigma_u$ levels and peak C to ionization from the $8\sigma_g$ orbital. From the extra information supplied by the

He(II) p.e. spectrum it is clear that this is a most unsatisfactory interpretation.

The present results also provide a superior interpretation of the p.e. spectra than that provided by the LCAO-MO Koopman's theorem and ΔSCF calculations of Lee et al [9], which both predict that all predominantly metal ionizations have higher binding energy than ligand ionizations, although the gap is reduced in the ΔSCF calculation. Configuration interaction calculations reported by the same authors lead to an interpretation in which band A arises from ionization from the $3\pi_g$ orbital, band C from the $1\delta_g$ orbital and band B from all the ligand orbitals together with the $9\sigma_g$ orbital. However, consideration of all the experimental evidence leads to an assignment which is identical to that deduced above except for ionization from the $2\pi_g$ majority spin orbital. This is assigned to peak B instead of peak C as the degree of spin splitting in the CI calculation is much smaller than in the MSXα calculations reported here. Both the LCAO calculations and the MSXα calculations predict a large degree of orbital relaxation upon ionization from metal orbitals and the CI calculations predict a number of ionic states corresponding to ionization energies in the range 16–18eV, having contributions from the Koopman's theorem configuration arising from $1\delta_g$ ionization. For this reason Lee et al [9] have assigned peak D as satellite peak, an assignment followed here in place of the immediately obvious assignment of this peak to ionization from the $8\sigma_g$ majority spin orbital, which would leave three ionizations under peak C, in which there is indeed evidence of three separate

maxima.

Assignment of the p.e. spectra of $CrCl_2$ is not as easy. Corresponding to the low binding energy peak A, which on intensity grounds must contain ionization from a predominantly metal orbital, transition state calculations predict that the orbital with the lowest ionization potential is the $3\pi_g$ orbital, which is of high metal character. As there is an interval of 1.1eV between the calculated $3\pi_g$ i.p. and the next lowest calculated i.p., almost exactly the gap between the experimental peaks A and B, peak A is assigned to ionization from the 3π orbital alone.

The experimental results (Table 2.9) clearly demonstrate the presence of two separate peaks originating from metal ionization. As the $3\pi_g$ ionization has already been assigned to peak A, peak C must include ionization from the $1\delta_g$ orbital. This assignment is less satisfactory than in the case of $MnCl_2$ in which the calculated $1\delta_g$ ionization energy lies within 0.5eV of the first maximum in peak C. In the case of $CrCl_2$ the calculated $1\delta_g$ ionization energy at 11.1eV, is only 1.5eV higher in energy than the calculated $3\pi_g$ ionization energy, whereas the experimental separation between the two peaks containing metal ionizations is 4.1eV. Furthermore, the calculated $1\delta_g$ ionization energy lies to lower binding energy than the $7\sigma_u$ level, a level which is of predominantly ligand character. In the case of $MnCl_2$ the corresponding peak was assigned to ionization from

both $8\sigma_g$ spin orbitals as the peak displays three separate maxima and the orbitals concerned had substantial metal contributions. However, for $CrCl_2$, these orbitals are calculated to have smaller metal contributions, peak C shows only one maximum, is less intense than the ligand peak in the He(II) spectrum and is very similar in intensity to peak A in the He(II) spectrum. As peak A has already been assigned to ionization from a predominantly metal orbital containing two electrons, peak C is assigned to ionization from the $1\delta_g$ orbital alone and peak B to ionization from the remaining, predominantly ligand, orbitals.

As was the case for $MnCl_2$, the $X\alpha$ calculation, in placing several ligand levels between the calculated binding energies of the two mainly metal orbitals, provides a more plausible interpretation of the experimental results than either Koopman's theorem or ΔSCF calculations, which predict a low b.e. grouping of ligand ionizations and a higher b.e. grouping of ionizations from the mainly metal $3\pi_g$ and $1\delta_g$ levels. Configuration interaction calculations [9], although yielding a different ordering of calculated binding energies, yield results similar to those of the MSXα calculations: with the lowest calculated p.e. being that of the $3\pi_g$ majority spin orbital, and the calculated binding energy of the $1\delta_g$ orbital lying amongst various ligand levels; and lead to the same interpretation of the experimental spectra.

These calculations have permitted a plausible interpretation of the p.e. spec-

tra of both $CrCl_2$ and $MnCl_2$, elucidating the similarities between the spectra of the two molecules, and extending the series of transition metal dichlorides studied by Berkowitz et al [10], while correcting the unsatisfactory interpretation reported of the He(I) p.e. spectrum of $MnCl_2$ on the basis of spin restricted cellular $X\alpha$ calculations. The comparison of spin restricted and unrestricted calculations for $MnCl_2$ shows particularly clearly the importance of spin effects in such open shell molecules, and the unsatisfactory assignment of the p.e. spectrum proposed by Berkowitz et al [10], the dangers of relying excessively upon such calculations. Berkowitz et al report that the gerade ligand levels have nonvanishing metal d character which increases for the minority spin orbitals from $MnCl_2$ to $NiCl_2$, and decreases in that order for majority spin orbitals. The current calculations do not show that trend extending to $CrCl_2$.

The most important point illustrated by the current calculations is the extreme utility of the availability of p.e. spectra obtained at different photon energies, which provide an empirical but useful guide to the location of bands containing contributions from metal ionization in the p.e. spectrum. Without this empirical information an incorrect assignment would have resulted from calculations with the $1\delta_g$ ionization being assigned to band B in the p.e. spectra of both $CrCl_2$ and $MnCl_2$, a band which the intensity data reveal to be mainly ligand in character.

2.4 REFERENCES

1. S.Huzinag, *J.Chem. Phys.*,**66**, 4245 (1977).

2. T.H.Dunnings, *J. Chem. Phys.*,**53**, 2823 (1970).

3. R.W.G.Wyckoff, *Crystal Structures*,**3**, Interscience(New York).

4. M.P.Tosi, *Sol. State Phys.*,bf 16, 19 (1964).

5. A.Calabrese and R.G.Hayes, *Chem. Phys. Letts.*,**43**, 263 (1976).

6. F.A.Cotton, D.G.Deboer, M.D.La Prade, J.R.Pipaland and D.A.Ucko, *Acta. Crystallogr.*,**B27**, 1664 (197)

7. H.Nakatsuji, J.Ushio, K.Kanda, Y.Onishi, T.Kawamura and T.Yonezawa, *Chem. Phys. Letts.*,**79**, 299 (1981).

8. J.G.Norman and H.J.Kolari, *J. Am. Chem. Soc.*,ul 100, 791 (1978)

9. E.P.F.Lee, A.W.Potts, M.Doran, I.H.Hillier, J.J.Delaney, R.W.Hawksworth, and M.F.Guest, *J. Chem. Soc. Faraday II*,**70**, 1305 (1979).

10. J.Berkowitz, D.G.Streets and A.Garritz, *J. Chem. Phys.*,70, 1305 (1979).

11. J.G.Norman. Jr., *J. Chem. Phys.*,ul 61, 4630 (1974).

12. I.Hargittai and J. Tremmel, *Coord. Chem. Rev.*,**18**, 257 (1976).

13. C.D.Garner, I.H.Hillier and C.D.Wood, *Inorg. Chem.*,**17**, 168 (1978).

14. R.W.Hawksworth, *PhD. Thesis*,(1982).

Table 2.1

Orbital Energies(au) of the Outermost Molecular Orbitals of the MoO_4^{2-} Anion

orbital	isolated ion core valence approx	isolated ion ab initio	orbital energy (au) pseudo-lattice ab initio	MS-Xα
$6a_1$	–0.83561	–0.83558	–1.19500	–0.783
$6t_2$	–0.82528	–0.82525	–1.18502	–0.778
$7t_2$	–0.16068	–0.16069	–0.52034	–0.324
2e	–0.15292	–0.15290	–0.51128	–0.319
$7a_1$	–0.07657	–0.07609	–0.43225	–0.281
$8t_1$	–0.06725	–0.06719	–0.42829	–0.268
$1t_1$	–0.05183	–0.05204	–0.41534	–0.25
	E=–4273.52315au	E=–4273.53061au		

Table 2.2

Calculated Ionization Energies for the MoO_4^{2-} Anion

	ΔSCF pseudo-lattice calc		MS-Xα calc
	B.E.(eV)	ΔE relax(eV)	Transn state energy(eV)
$1t_1$	10.71	0.59	9.82
$8t_2$	11.06	0.59	10.29
$7a_1$	10.77	0.99	10.66
2e	13.40	0.51	15.31
$7t_2$	13.51	0.65	13.02
$6t_2$	31.63	0.62	24.23
$6a_1$	31.90	0.62	24.35

Table 2.1

Orbital Energies(au) of the Outermost Molecular Orbitals of the MoO_4^{2-} Anion

orbital	isolated ion core valence approx	isolated ion ab initio	orbital energy (au) pseudo-lattice ab initio	MS-Xα
$6a_1$	–0.83561	–0.83558	–1.19500	–0.783
$6t_2$	–0.82528	–0.82525	–1.18502	–0.778
$7t_2$	–0.16068	–0.16069	–0.52034	–0.324
2e	–0.15292	–0.15290	–0.51128	–0.319
$7a_1$	–0.07657	–0.07609	–0.43225	–0.281
$8t_1$	–0.06725	–0.06719	–0.42829	–0.268
$1t_1$	–0.05183	–0.05204	–0.41534	–0.25
	E=–4273.52315au	E=–4273.53061au		

Table 2.2

Calculated Ionization Energies for the MoO_4^{2-} Anion

	ΔSCF pseudo-lattice calc B.E.(eV)	ΔE relax(eV)	MS-Xα calc Transn state energy(eV)
$1t_1$	10.71	0.59	9.82
$8t_2$	11.06	0.59	10.29
$7a_1$	10.77	0.99	10.66
2e	13.40	0.51	15.31
$7t_2$	13.51	0.65	13.02
$6t_2$	31.63	0.62	24.23
$6a_1$	31.90	0.62	24.35

Table 2.3

Calculated Total Energy and Charge Distribution in $Rh_2(O_2CH)_4$

Calc	Energy(au)	Rh	O	C	H	$\epsilon_i^{HF}(Ox_{1g}^{a_1})$(au)
A	-10118.0575050	+1.0258	-0.5009	+0.2741	+0.1715	-20.5089
B	-10118.0659941	+0.8086	-0.4583	+0.2901	+0.2222	-20.5324
C	-10112.1092152	+0.8374	-0.4744	+0.2740	+0.2560	-20.2668
LCAO [7]		0.70	-0.36 to -0.37	+0.30	+0.05 to +0.07	
MSXα [8]	-10127.0066	-0.73	-0.17	+0.67	+0.04	

Table 2.4

Calculated orbital eigenvalues and metal contributions in $Rh_2(O_2CH)_4$

Orbital	*Orbital energy au*	*metal contribution* (%)	*metal – metal bonding character*
$2a_{1g}$	−0.9068	5.3	
$2b_{1g}$	−0.9016	8.8	
$2e_u$	−0.8816		
$3e_u$	−0.7674	27.9	π^*
$3a_{1g}$	−0.7575	4.9	
$2b_{2u}$	−0.7496	24	$\delta^*_{x^2-y^2}$
$2a_{2u}$	−0.74601	16.6	σ^*
$3b_{1g}$	−0.74597	2.2	
$1b_{2g}$	−0.7423	33.3	δ_{xy}
$2e_g$	−0.6824	13	π
$4e_u$	−0.6819	7	
$1b_{1u}$	−0.6733	83.3	δ^*_{xy}
$1a_{2g}$	−0.6570		
$5e_u$	−0.6529	62.8	π^*
$3e_g$	−0.6198	77.7	π
$4a_{1g}$	−0.6084	57.8	σ
$2b_{2g}$	−0.6063	60.4	δ_{xy}
$4b_{1g}$	−0.5985	28.6	$\delta_{x^2-y^2}$
$3a_{2u}$	−0.5427	9.5	σ^*
$3b_{2u}$	−0.5388	6.2	
$5a_{1g}$	−0.5096	48.6	σ
$4e_g$	−0.4981	5.3	
$5e_g$	−0.4843	3.5	
$6e_u$	−0.4791	2.0	
$1a_{1u}$	−0.4683		
$2b_{1u}$	−0.4651	16.7	δ^*_{xy}

Table 2.5

MO coefficients of metal-metal σ bonding orbitals of $Rh_2(O_2CH)_4$ obtained from MO-SCF calculations.

		Present Results		Ref 7
		$4a_{1g}$	$5a_{1g}$	
Rh	$4d_{z^2}$	0.520	0.398	0.644
	5s	0.012	0.238	0.284
	$4p_z$	0.044	0.066	−0.121 ($5p_z$)
Max Coeff in carboxylate		0.167	0.224	0.071

Table 2.6

Electronic structure and ionization energies of $MnCl_2$ calculated by the MS-Xα method.

orbital	$IP_{calc}(eV)$	$\bar{Q}^n(Mn)$	$\bar{Q}^n(Cl)$	$QL^n(Mn)$	$QL^n(Cl)$	$IP^a(eV)$
$3\pi_g \uparrow$	10.3	40	60	28	72	10.6
$9\sigma_g \uparrow$	10.9	80	20	52	48	10.6
$4\pi_u \downarrow$	10.9	3	97	9	91	11.3
$4\pi_u \uparrow$	11.1	3	97	12	80	11.3
$2\pi_g \downarrow$	11.1	7	93	13	87	11.6
$7\sigma_u \downarrow$	12.2	17	83	21	79	11.9
$7\sigma_u \uparrow$	12.7	19	81	24	76	12.2
$1\delta_g \uparrow$	13.1	100	0	53	47	12.9
$8\sigma_j \downarrow$	13.3	27	73	28	71	13.6
$2\pi_g \uparrow$	13.4	66	34	51	49	13.3
$8\sigma_j \uparrow$	15.0	44	56	38	62	15.0

[a] IPs calculated by transition state cellular MS-Xα method [10].

Table 2.7

Electronic structure and ionisation energies of $CrCl_2$ calculated by the MS-Xα method.

orbital	$IP_{calc}(eV)$	$\bar{Q}^n(Cr)$	$\bar{Q}^n(Cl)$	$QL^n(Mn)$	$QL^n(Cl)$
$3\pi_g \uparrow$	9.6	73	27	26	74
$4\pi_u \downarrow$	10.7	2	98	9	91
$4\pi_u \uparrow$	10.8	2	98	8	92
$2\pi_g \downarrow$	10.9	6	94	11	89
$1\delta_g \uparrow$	11.1	100	0	41	59
$2\pi_g \uparrow$	11.5	30	70	23	77
$7\sigma_u \downarrow$	11.6	13	87	18	82
$7\sigma_u \uparrow$	11.9	15	85	16	84
$8\sigma_g \downarrow$	12.7	23	77	21	79
$8\sigma_g \uparrow$	13.7	35	65	23	77

Table 2.8

Experimental vertical ionization potentials on $MnCl_2$

	observed IP	Relative Intensity		Ref 10
	eV	He(I)	He(II)	
A	11.03	22	39	11.06
B	11.79	100	100	11.85
	12.05			12.06
	12.36			12.37
C	13.58 (13.79)	16	117	13.61
	13.95			
D	14.46	7	7	not present

Table 2.9

Experimental vertical ionization potentials of $CrCl_2$

	observed IP eV	Relative Intensity He(I)	He(II)
A	9.97	15	47
B	11.09	100	100
	11.79		
	12.14		
	12.75		
	13.27		
C	14.07	25	52

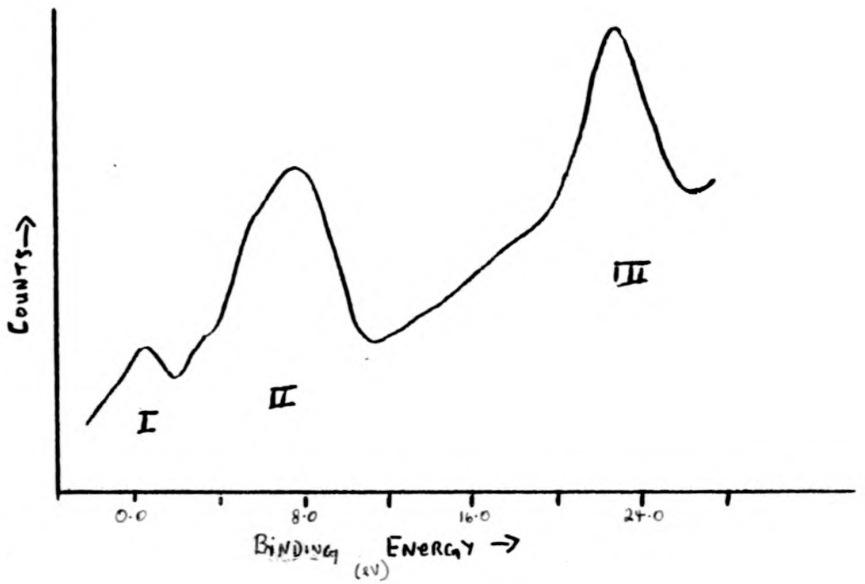

Fig. 2.1

XPS of Na_2MoO_4 [3]

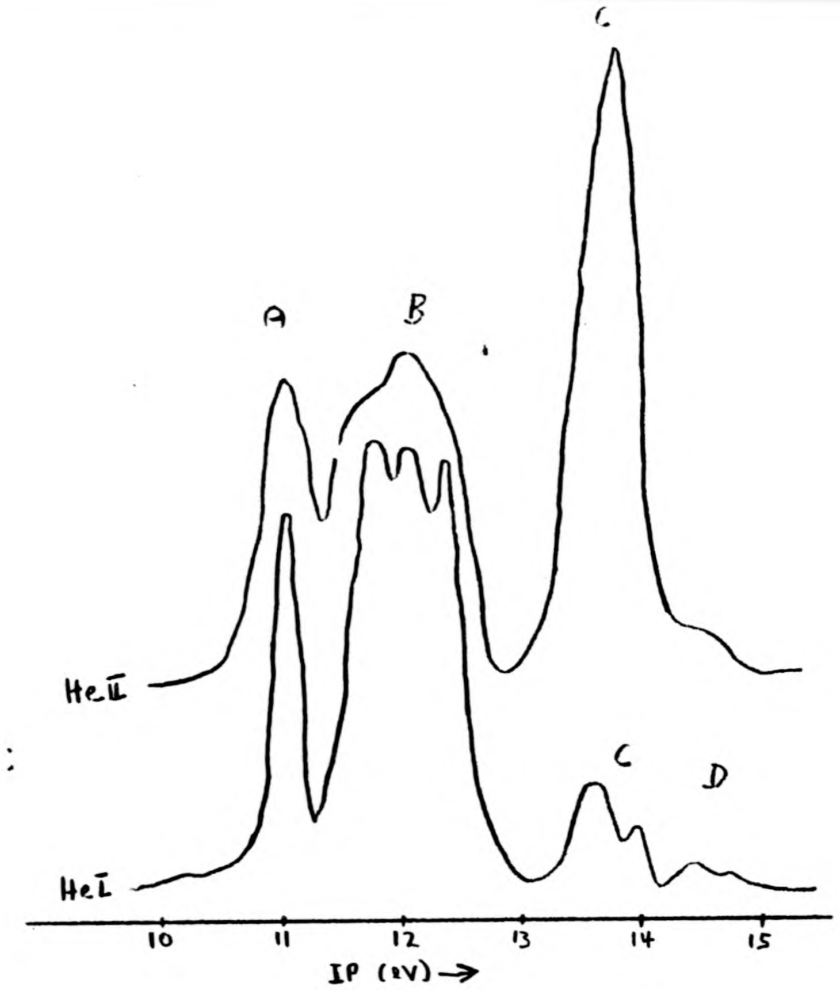

Fig. 2.2

UPS of $MnCl_2$ [9]

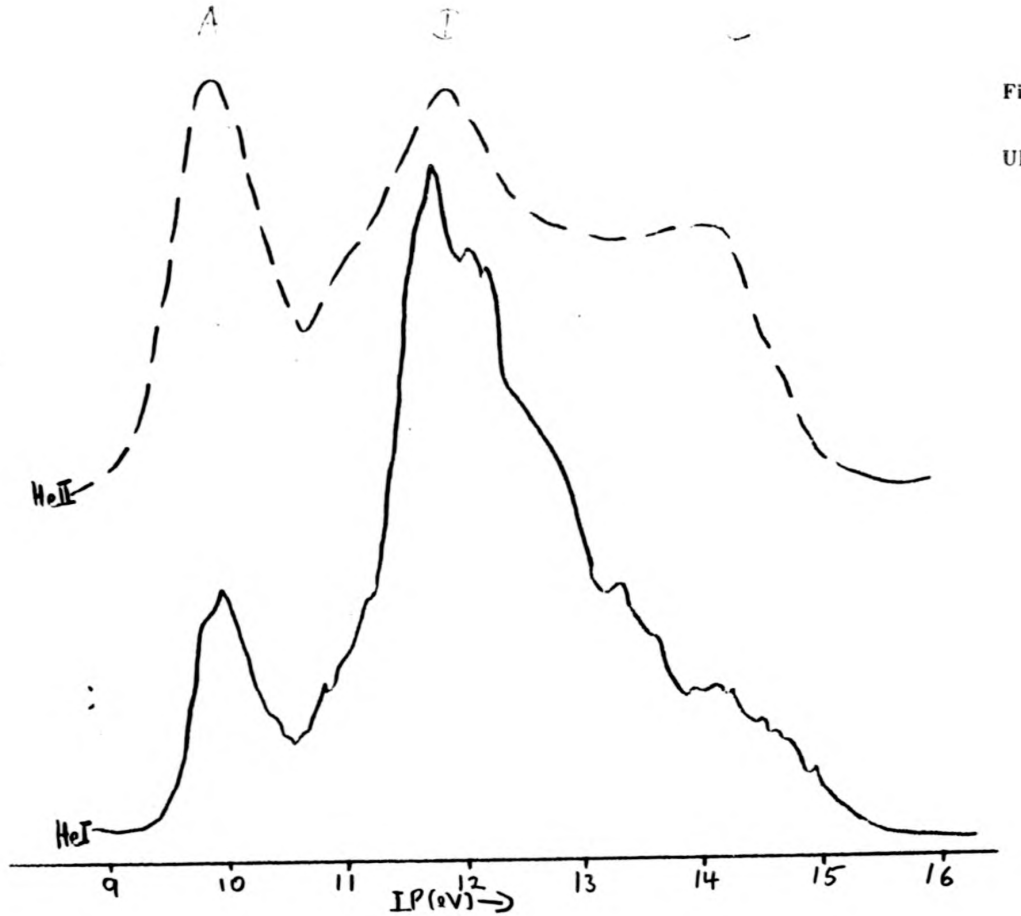

Fig. 2.3

UPS of $CrCl_2$ [9]

Chapter 3

The Calculation of Photoionization Cross Sections

In the previous chapter the variation in intensity of various bands with the energy of the ionizing radiation in the PES of $MnCl_2$ and $CrCl_2$ has provided information which proved critical to the correct assignment of the origin of the bands in the PES. It is clear that if it were possible to calculate the intensities

of various band in a PES from ab-initio principles a very useful criteria for verifying assignments based upon the calculated binding energies of the various molecular orbitals would be available. The fact that these intensities vary with the energy of the ionizing radiation would then also provide an additional check upon these assignments.

The degree of interaction between an electronic system and electromagnetic radiation of a given energy, E, is expressed by a cross section, σ(E). There are different cross sections for different processes e.g. for photoabsorption and photoionization. This report will only be concerned with photoionization cross sections. Again there are various kinds of photoionization cross section; σ_{tot}(E) measures the total cross-sectional area presented by the system to electromagnetic radiation of energy E for all processes leading to photoionization. A knowledge of σ_{tot}(E), together with the branching ratios for production of the molecular ion in its various electronic states, leads to the cross sections for production of the various ionic states of the molecule. These are known as partial photoionization cross sections. In the course of calculation these partial cross sections may be built up from contributions from various all electron states, of different angular momenta which all leave the molecular ion in the same state e.g. an electron may leave a π orbital as a σ, π or δ wave.

The calculation of photoionization cross sections is a very difficult compu-

tational problem, as the integrals involved require not only the ground state wavefunction but a wavefunction for all the electrons on the ionized state. The inclusion of the continuum photoelectron in the final state wavefunction, which gives rise to the computational difficulties, has encouraged the development of various approximate schemes for the calculation of photoionization cross sections. Crude approximations such as assumimg that the molecular photoionization cross section may be approximated to by the sum of atomic contributions [1], or that the continuum electron may be described as a plane wave have been employed [2]. While providing interesting results, especially at high photon energies, these methods are very inaccurate at low photon energies where many interesting effects arising from the molecular potential [3,4], and the interaction of the motion of the nuclear framework with the ejected electron [5,6], are observed. Two more sophisticated approximate methods for calculating photoionization cross sections, the MS-Xα [7] and Static Exchange Stieltjes-Tchebycheff moment imaging methods [8-11], have recently been developed and show great promise. The calculations reported in subsequent chapters were all performed within the Static Exchange Stieltjes Tchebycheff scheme and compared with MS-Xα results where these are available.

3.1 Oscillator Strengths and Photoionization cross sections [12,14]

Classically electrons were supposed to lie at equilibrium positions within electronic systems and to perform forced oscillations when exposed to electromagnetic radiation of the appropriate frequency. However electrons are statistically distributed, with a distribution given by $|\psi|^2$, rather than being fixed point charges, and it is this distribution which is distorted by electromagnetic radiation. To the various frequencies, w_i, which can cause distortion of the electronic distribution corresponds a portion of $|\psi|^2$, called the oscillator strength, f_i. In the continuous region of the spectrum, where all frequencies can interact to some extent with the electronic distribution, the spectral density of oscillator strength, $\frac{df}{dw}$, is used.

Consider a hypothetical one electron classical system, constrained so as to interact with electromagnetic radiation at only one frequency. At that frequency the oscillator strength will be unity. Such a one electron system, in reality, interacts with radiation over a wide spectrum of frequencies, but the total oscillator strength must still sum to unity. For a system with n electrons the total oscillator strength distribution, over all possible discrete transitions and over the continuous region of the spectrum, for all electrons, must sum to n, the number

of electrons. That is

$$\sum_j \left(\sum_i f_i + \int_{IP_j}^{\infty} \frac{df}{dw} \right) = n$$

(All channels j and all discrete transitions of channel j)

This is known as the Thomas-Reiche-Kuhn rule.

As the magnitude of the various discrete oscillator strengths is related to the strength of the interaction of electromagnetic radiation with the electronic system at different frequencies, the spectral density of oscillator strength in the continuous region of the spectrum is related to the photoionization cross section, which corresponds to the probability of ionization of the system by radiation of different frequencies. This relationship [13] is given by

$$\sigma(\omega) = 1.098 \times 10^{-16} \mathrm{cm}^2 \mathrm{eV} \frac{df}{dE}$$

The oscillator strength for a transition to an excited state, i, from the ground state, separated by an energy difference of E_i, is defined as

$$f_i = \frac{2}{3} E_i | < \Psi_i | \hat{\mu} | \Psi_o > |^2$$

where Ψ_i is the total electronic wavefunction for the i'th excited state

Ψ_o is the ground state electronic wavefunction,

μ is the dipole moment operator.

Alternative expressions for the oscillator strength, in terms of the matrix elements of the electron velocity and accelleration, exist [12]. However only the

dipole form will be employed in the results reported here.

The rotationally unresolved, fixed nuclei, photoionozation cross section for photoionization from the ground state, Ψ_0,is given by [14]

$$\sigma(E) = \frac{4\pi^2 E}{3h} | < \Psi_0 | \mu | \Psi_E > |^2$$

where Ψ_E includes a representation of the motion of the continuum electron with energy E. It is the difficulty of providing this representation which has caused the development of the various approximate schemes detailed below.

As with the oscillator strength alternative expressions exist for the photoionization cross section. If accurate wave functions are used for both the ground and final states, these expressions will lead to the same value of the cross section. However only approximate wave functions are available and thus these expressions lead to different values of the cross section [14]. All cross sections reported in this work were calculated using the dipole expression for the cross section.

3.2 Angular Effects in Photoelectron Spectra [15]

In general the strength of a peak in a photoelectron spectrum is not only dependent upon the energy of the exciting radiation but also upon the precise geometry of the spectrometer employed. This is because electrons do not emerge isotropically from the system but have an angular dependence given by

$$\frac{d\sigma_i(E)}{d\Omega} = \frac{\sigma_i(E)}{4\pi}[1 + \beta_i(E)P_2(\theta)]$$

for polarized light, where $d\sigma_i(E)$ is the cross section for emission from orbital i at photon energy E into the solid angle $d\Omega$. The asymmetry parameter $\beta_i(E)$ for the i'th molecular orbital is a function of photon energy only. The second order Legendre polynomial, $P_2(\theta)$, is given by

$$P_2(\theta) = 1/2(3\cos^2\theta - 1)$$

where θ is the angle between the plane of polarisation of the exciting radiation and direction of the photoelectron.

In order that the differential cross section, $d\sigma/d\Omega$, never be less than zero, β_i cannot lie outside the range $-1 \leq \beta \leq 2$. As the form of the asymmetry parameter may be different for different orbitals, i, it is clear that values of the ratios of the cross sections of different molecular orbitals, at a given photon

energy, obtained by comparing the areas of different photoelectron peaks for an arbitrary photoelectron spectrometer, may be completely false. However $P_2(\theta)$ is zero, thus eliminating the dependence upon the asymmetry parameter, for two magic angles, 54°44′ and 180°−54°44′. Results from spectrometers operating at these 'magic angles' permit the correct evaluation of the relative intensities of different peaks in the spectrum. Such geometries have not been standard in the past, so many experimental results are not useful in the investigation of the variation in intensity of photoelectron peaks with photon energy.

3.3 Factors affecting photoionization cross sections

Three main factors produce strong effects upon the form of the various cross section vs. energy curves considered in this thesis. These are Autoionization effects, Shape Resonance effects and Nuclear Motion effects.

3.3.1 Autoionization [3,4,15]

There are two main processes which may lead to ionization from a system in its electronic ground upon absorption of a photon. The first, direct ionization, is

comparatively fast.

$$AB + h\upsilon \rightarrow AB^{+} + e^{-}(E, \vartheta)$$

Direct ionization can occur at all photon energies greater than the lowest ionization threshold.

The second, Autoionization, proceeds by way of absorption of a photon leading to an excited bound electronic state of the system, followed by emission of an electron. As the excited bound state has a finite lifetime autoionization takes substantially longer than direct ionization.

$$AB + h\upsilon \rightarrow AB^{*} \rightarrow AB^{+} + e^{-}(E, \vartheta)$$

Autoionization can only occur at photon energies which are equal to the difference in energies between one of the excited electronic bound states of the system and the initial state. At these energies the interaction between the two possible modes of photoionization can produce dramatic effects upon the various partial channel photoionization cross sections and upon the asymmetry parameters.

Various features in the partial channel photoelectron cross sections of the molecules considered on this thesis will be interpreted in terms of autoionization effects. These autoionizations will be ascribed mainly to the formation of an excited electronic state arising from promotion of an inner valence electron to a Rydberg orbital and subsequent decay of this Rydberg state to yield an ionized state with a vacancy in a higher orbital.

Autoionization may occur in any many electron system and cannot therefore be described as a molecular effect.

3.3.2 Shape Resonances[3,4,8-11]

Shape resonances occur when, owing to the shape of the molecular potential, an ejected electron is temporarily trapped in the vicinity of the molecule. The formation of such a 'quasi bound state' generally causes an increase in the photoionization cross section owing to the increased overlap of the ionized and the ground state wave function. As the effect arises from the shape of the molecular potential it is called a shape resonance.

An illustration of this effect, in which the potential barrier arises from the presence of a cage of nuclei, is to be found in the ionization of an electron from the sulphur 3s orbital in SF_6. A low energy photon may be of greater energy than the gap between the ground state of SF_6 and the $SF_6^+(3s^{-1})$ ion. However a photoelectron originating in the sulphur 3s orbital experiences a potential barrier as it escapes the sulphur centre owing to the fluorine cage, and the associated charge distribution, surrounding the sulphur centre. This potential barrier may be higher than the kinetic energy of the photoelectron. Thus for a range of low photon energies the photoelectron may be trapped in the vicinity of the molecule and so is subject to a time delay before leaking through the

potential barrier. This time delay alters the dipole matrix element between the ground state and the ionized state, and thus the partial photoionization cross section, relative to photon energies where the kinetic energy of the photoelectron is greater than the potential barrier.

In the above analysis the barrier giving rise to the resonance has a simple, readily appreciated physical cause. Such an explanation is not readily available for the many resonant phenomena which have been observed in the much smaller molecules considered in this report. However it has been shown that a potential barrier also explains these cases [3,4]. The outgoing wave associated with the photoelectron has contributions of high angular momenta for certain channels and energies. These high angular momentum components can add a centrifugal term to the effective potential acting on the photoelectron, which, together with the attractive term arising from the positively charged molecular ion, can give rise to a barrier in the effective potential. This barrier temporarily traps the photoelectron in the vicinity of the molecule and thus enhances the partial channel photoionization cross section at these photon energies [4]. This mode of analysis is naturally associated with MS-Xα type calculations, in which the photoelectron is represented by a set of partial waves of different angular momenta [7].

While this analysis provides a good explanation of the origin of shape res-

onances it is difficult to relate to the results of calculations employing finite square integrable basis sets, such as those reported in this thesis. Instead a paradigm, based upon the relevant methodology, has been developed. In this paradigm the photoionization cross section in the region of a shape resonance is enhanced by contributions from transitions to valence states which lie above the photoionization threshold. As the valence states are confined to the vicinity of the molecule their overlap with the ground state is large. Transitions between ground and valence states ofter have large oscillator strengths, larger than for those for transitions to Rydberg states. As the oscillator strength is related to photoionization cross sections this is enhanced over the range of photon energies for which the valence state can contribute.

It is clear that the correct location of the higher valence states of the molecule, either above or below the appropriate photoionization threshold, is of great importance both in the interpretation of the experimental measurements and for the accuracy of any attempt to calculate photoionization cross sections. In some cases this can cause severe problems. The static exchange calculation on the $(1\pi_u^{-1})$ channel of C_2H_2, reported in chapter 5, predicts a maximum in the $1\pi_u \rightarrow k\pi_g$ contributions, yielding a maximum in the calculated $(1\pi_u^{-1})$ photoionization cross section. This calculated maximum does not agree with the experimental measurements. Manual deletion of the contributions to the $1\pi_u \rightarrow k\pi_g$ pseudospectrum in the region of the spurious maximum resulted in

computational results which then agreed well with the experimental results.

Such problems have also been reported by other workers for $\pi \rightarrow \pi^*$ contributions. Meaningful results have been reported in these cases both by the rather ad hoc method of manually deleting pseudospectral contributions deemed spurious and by alteration of the operator over which the pseudospectrum is constructed so as to force all the spurious contributions to lie below threshold [16,17].

3.3.3 Nuclear Motion Effects [5,6]

In the calculation of the molecular wavefunctions reported in this work it was assumed that the positions of the nuclear centres were fixed in space. Such is not the case. Atomic nuclei in molecular systems are subject to continual vibrational motion. Clearly such motion must affect the details of the molecular potential from moment to moment. As shape resonances are dependent upon the molecular potential it would seem likely that nuclear motion might be a significant factor to be included in any attempt to calculate accurate partial channel photoionization cross sections.

Dehmer, Dill and Wallace [5], in calculations within the the MS-Xα scheme upon the $(3\sigma^{-1})X^2\Sigma_g^+$ channel of N_2^+, showed that both the position and max-

imum value of a shape resonance within the partial cross section of this channel could be strongly dependent upon the value of the internuclear separation used on the calculation. Thus, as different vibrational states sample internuclear distances, the forms of the various vibrationally resolved partial channel photoionization cross sections leading to a given final electronic state may be different.

The Franck Condon principle asserts that nuclear and electronic motions are independent and so may be treated separately. The Franck Condon factors, which describe the distribution of vibrational states in the molecular ion after photoionization are therefore constants rather than functions of photon energy. The above work suggested that this was not the case in the vicinity of a shape resonance, where the distribution of vibrational states in the molecular ion may differ dramatically from the Franck Condon distribution, so demonstrating the coupling of nuclear and electronic motions.

Experimental verification was swiftly found in the case of CO where the distribution of vibrational states did indeed diverge dramatically from the Franck Condon distribution in the vicinity of a shape resonance [6]. However when experimental data became available for the $(3\sigma_g^{-1})X^2\Sigma_g^+$ channel of N_2 it was found that the MS-Xα calculations had substantially overestimated the magnitude of the deviation.

The effects of variation of internuclear separation may be interpreted very simplistically in terms of the virtual orbital paradigm, employed above in the interpretation of shape resonances, by considering the effects of this variation upon the molecular orbitals formed by the interaction of two hydrogen atoms. At large distances there is comparatively little interaction between the two atoms so the resulting bonding and antibonding orbitals differ little in energy, neither between themselves nor with respect to the ls orbitals of atomic hydrogen.

As the internuclear distance decreases the degree of interaction increases and the difference in energy between the bonding and antibonding orbitals increases. Thus, the case of CO, where the resonance is ascribed to contributions from the σ antibonding valence virtual orbital, and where the MSXα calculations show that as the internuclear distance is decreased the resonance moves to higher photon energy, may also be understood within the virtual orbital paradigm.

3.3.4 Cooper Minima

Cooper minima occur when the radial matrix element connecting the ground state radial wavefunction and the continuum wavefunction changes sign, as to change sign it must go through a zero. As the energy of the continuum electron increases the nodes in its radial wavefunction become more closely spaced. If such an electron comes from an atomic orbital with at least one node, there

must exist an energy at which the radial matrix element changes sign and hence the partial channel photoionization cross section goes through a minimum. This is not a molecular effect as such, and as none of the systems investigated in this thesis are large enough to exhibit this feature, will not be further considered here.

3.4 Computational Methods

3.4.1 The Gelius Intensity Model [1]

This model assumes that at high enough photoelectron energies the interaction of a photoelectron with the molecular ions electric field can be ignored. At such energies the kinetic energy associated with ejected valence photoelectrons can be regarded as essentially constant so the dependence of the partial cross section upon photon energy in ignored. At such energies the de Broglie wavelength of the photoelectron is smaller than the average molecular orbital size, so the major contributions to the cross section arise from regions where the molecular orbital wavefunction is varying rapidly, i.e. in the vicinity of nuclei. This suggests that it should be possible to express molecular orbital photoionization cross sections

as a sum of atomic terms:

$$\sigma_i = \sum_a \sigma_{ai}$$

where i applies to molecular orbitals and a to atomic contributions. Gelius assumed that:

$$\sigma_{ai} = \sum_\nu P_{\nu i}\sigma_\nu$$

where the sum over ν runs over all atomic orbitals on atom a and $P_{\nu i}$ is the gross atomic orbital population of the atomic orbital ϕ_ν in the i'th molecular orbital. This leads to the equation:

$$\sigma_i = \sum_\nu P_{\nu i}\sigma_\nu$$

where the summation over runs all atomic orbitals on all centres and the σ_ν's come from experiment or calculation, and the $P_{\nu i}$ from Mulliken population analysis.

While this method can produce results useful at high photon energy its fundamental assumption that molecular effects can be ignored makes it useless at low photoelectron kinetic where features such as shape resonances occur.

3.4.2 Plane wave [2], Orthogonalised Plane Wave [2] and Coulomb Wave Models [17].

The most obvious method of attempting to calculate molecular partial photoionization cross sections, in which the outgoing electron is explicitly treated, is the plane wave model. In this model the photoelectron is described by a planewave, which is the solution of the Schrödinger equation for a free electron. A ground state wavefunction is constructed in which each electron is described by a one electron orbital. The final state wavefunction is constructed by replacing the orbital of interest with a plane wave while freezing all other orbitals in their ground state form. Thus photoionization cross sections calculated using this method take account neither of the field of the molecular ion in which the photoelectron is moving nor of the effects of relaxation of the ground state orbitals as the photoelectron escapes. The momentum form of the formula for the photoionization cross section is employed and, as the plane wave is an eigenfunction of the momentum operator, the integral reduces to an overlap integral between the plane wave and the initial molecular orbital which is comparatively easy to evaluate.

Such a plane wave is not necessarily orthogonal to any of the occupied orbitals. In the Orthogonalised Plane Wave Method (OPW) the overlap formula used for the photoionization cross section in the Plane Wave method is modi-

fied by the addition of terms which correct this nonorthogonality. At low energy the OPW correction to the cross section calculated by the Plane Wave Method can be very substantial, as great as an order of magnitude in the case of the $(1b_1^{-1})X^2\ B_1$ and $(3a_1^{-1})A^2\ A_1$ channels of H_2O at 16.75eV. As well as allowing for orthogonality the OPW method permits the calculation of asymmetry parameter, $\beta(E)$, which vary with the photon energy whereas the plane wave method yields a constant value of $\beta = 2$. However the OPW method requires greater computational expenditure than the PW method.

Both the PW and OPW methods produce results which are quantitatively inaccurate at low photon energies. In the case of the $(1b_1^{-1})\ X^2\ B_1$ channel of H_2O OPW calculations yield a partial photoionization cross section value of 1.28Mb at 21.2eV photon energy whereas (e,2e) measurements yield a value of 5.8.mB. It is generally the case that PW and OPW calculations result in photoionization cross section profiles which rise to a maximum at a photon energy between 1.5 and 2.5 times greater than the ionization threshold. This does not conform with the general form of experimental results.

A superior method, the Coulomb wave method [18], employs hydrogen like continuum functions to replace the ground state orbital from which ionization and occurred in the final state wavefunction. Thus the effect of the molecular ion resulting from the photoionization process and carrying a unit positive charge is

allowed for to some extent. Again different value of the calculated cross section are obtained dependent upon whether the Coulomb Wave is orthogonalised to the occupied molecular orbitals or not. At high energies the results of Coulomb wave calculations approach those of Plane Wave calculations. However at low photon energies both orthogonalised and nonorthogonalised Coulomb wave calculations yield results in significantly better agreement with experiment than PW and OPW calculations. In the case of the $(1b_1^{-1})X^2\ B_1$ channel of H_2O orthogonalised coulomb wave calculations yield a maximum of 4 MB at 16eV, of same the order and at similar photon energy to the experimental results, unlike the OPW calculations.

3.4.3 The MSXα Method

The MSXα method for calculating bound state wavefunctions has been extended by Dill and Dehmer [7] to treat unbound electronic states of molecules in the independent electron approximation. The advantage of this method is that the 'Muffin Tin Potential', with a local approximation to the exchange potential, can be readily solved to give photoionization cross sections for any given photoelectron kinetic energy. Calculations have also been reported [19] in which the ground state potential is generated by a standard Hartree Fock LCAO-MO calculation, and is then employed in the construction of the final state multi-

ple scattering continuum functions. These calculations are open to the same objections as the bound state MSXα method; arbitrary choice of sphere radii, unphysical potentials and truncation of the number of partial waves in which the wavefunction is expanded, although this truncation is reported not to be a serious problem [20]. The photoionization cross sections calculated by this method, while permitting interpretation of experimental results, have proven not to be in as good agreement with the form or the magnitude of the experimental results as those obtained by the Stieltjes-Tchebycheff moment theory technique. However, because of its computational cheapness, this method has permitted detailed exploration of the coupling of nuclear and electronic motions in the vicinity of a shape resonance [5,6], and while again not in good agreement with experiment as to magnitude , has predicted and explained experimental effects not previously described. This method also has the considerable advantage of permitting the calculation of the various molecular asymmetry parameters, $\beta_i(E)$, with more accuracy than the calculated cross sections, whereas the methods employed to obtain the results presented in this thesis, at present, permit no calculation of the asymmetry parameters.

3.4.4 The TDHF or RPA Method

Effects such as channel interaction cannot be accounted for by simple Hartree Fock type approaches, although these do include exchange terms. An approach which can represent such effects is the Random Phase Approximation (RPA) or Time Dependent Hartree Fock Approach (TDHF), in which solutions of the time dependent Schrödinger equation are approximated. Such calculations have been reported, in combination with the Stieltjes-Tchebycheff moment theory analysis, outlined below, for N_2 [21] and H_2O [22] by Langhoff and coworkers. One problem with this method is that the resulting excitation energies and oscillator strengths generally do not correspond to a single final state configuration with a unique photoionization channel. Williams and Langhoff [22] have reported techniques for determining partial channel photoionization cross sections from TDHF spectra by removal of channel interaction terms. This calculation [22] employed a small basis set and yet produced results, which, while not in as good agreement with experiment as the calculations on H_2O reported in chapter 5, are somewhat similar in form and magnitude.

3.4.5 The Iterative Schwinger Method

Lucchese, Watson and McKoy [23] have recently reported calculations in which the static exchange equation for the final state wavefunction has been solved by use of a combination of numerical single centre expansion and variational basis set techniques. This method can be used iteratively to improve the quality of the calculated photoionization cross sections. This method appears to be that which currently most closely approaches the exact solution of the Schrödinger equation for the continuum case. It is therefore encouraging that the results reported in this thesis agree very closely with those of Lynch et al [24], calculated using an iterative Schwinger technique, for the $2\sigma_u \rightarrow k\sigma_g$ photoionization cross section contribution of C_2H_2, both showing two separate resonance features, whereas those of Machado et al [25], employing a smaller basis set, show no such structures.

3.5 The Static Exchange Method

Use of the independent particle model with exchange (the Hartree Fock method) is well established in bound state calculations. It is natural to seek a means of employing the same methods and programmes in photoionization calculations. Such calculations using the Hartree Fock potential are termed Static Exchange

calculations, as the potential contains both a static or local potential, and an exchange or nonlocal potential. It will be seen in chapters 4 and 5 that the use of converged ground state HF potentials, constructed with a good quality basis set, to generate IVO's using a large supplementary basis set, without iteration, as the ground state orbitals are frozen and the potential modified only by removal of an electron from the appropriate orbital, leads to good estimates of the difference in energies between the various excited states.

These IVO's, ϕ_i^Γ, where Γ labels the channel under consideration, are obtained by solution of a one electron equation of the form

$$(h_\Gamma - \epsilon_i^\Gamma)\phi_i^\Gamma = 0$$

where the ϵ_i^Γ correspond to the discrete energies for excitation and

$$h_\Gamma = T + V + V_\Gamma$$

is the static exchange Hamiltonian. Here T and V are the kinetic and nuclear potential operators and V_Γ is the appropriate non-local channel potential. This is written in the form

$$V_\Gamma = \sum_i (2a_i^\Gamma J_i - b_i^\Gamma K_i)$$

where J_i and K_i are the usual Coulomb and exchange operators and the summation over i runs over the occupied orbitals in the ground state.

The calculation of the appropriate potentials, determined by the set of $(a_i;b_i)$

over which the IVO's are canonicalized , so that there is no interaction between the various excited wavefunctions constructed by including one of the IVO's in the place of a ground state orbital, is often a difficult problem for molecules of high symmetry. Such potentials have been published for closed shell linear molecules and for the open shell molecule O_2 [26].

Such potentials were calculated for the various excited states ($^2\Sigma^+, ^2\Sigma^-, ^2\Pi, ^2\Delta$) and possible excitations to these states (ground state orbital $\rightarrow k\sigma, k\pi, k\delta$) for NO. This necessitates the expression of these states in terms of complex orbitals before producing potentials in terms of real orbitals, in which the relationship, derived from the work of Rose and McKoy [28] is useful.

$$< \pi_+\pi_+|\pi_+\pi_+ > = < \pi_+\pi_+|\pi_-\pi_- > + 2 < \pi_+\pi_-|\pi_+\pi_- >$$

The ground state HF potential can be generated using a much smaller basis set than is required to represent the excited orbitals, as the description of such orbitals requires large numbers of very diffuse basis functions. Hence it is only necessary to introduce the diffuse functions of the supplementary basis set when the IVO's are being constructed. The MO coefficients of these diffuse basis functions in the occupied orbitals, from which the Coulomb and exchange operators are constructed, are zero. Thus the only new two electron integrals which have to be calculated are those involving two or three of the old basis functions and one or two of the supplementary diffuse basis functions.

Although the impression is gained from the calculated excitation energies ε_i^Γ, reported below, that this method leads to good absolute values of the excitation energies, this is not the case. The often excellent agreement between the calculated and experimental excitation energies is due to the use of the experimental ionization potential ϵ^Γ, rather than the calculated ionization potential, in producing excitation energies from the orbital eigenvalues. ϵ_i^Γ.

$$\varepsilon_i^\Gamma = \epsilon^\Gamma + \epsilon_i^\Gamma$$

Such calculations, as well as producing bound Rydberg orbitals, produce orbitals canonicalized over the same operator with positive eigenvalues, known as pseudostates. Unfortunately these cannot be linked with continuum orbitals of the same energy as these IVO's are square integrable (L^2), and Kronecker delta function normalized. Continuum orbitals are not square integrable and are Dirac delta function normalized in the energy coordinate.

It is however possible, in principle, to obtain approximate moments of the oscillator strength distribution, $S(-k)$, using only the above pseudostates to calculate the oscillator strengths [28,9-11].

$$f_i^\Gamma = \frac{2}{3}\varepsilon_i^\Gamma | < \phi_i^\Gamma | \mu | \phi^\Gamma > |^2$$

$$\bar{S}(-k) = \sum_i (\varepsilon_i^\Gamma)^{-k} f_i^\Gamma$$

The dipole moment integrals required to calculate such oscillator strengths may

be read from the dump tape of the ATMOL programme used in the current calculations.

While, in the limit of a complete basis set, these moments converge onto the exact moments, basis sets are not in fact complete and it will be seen in the calculation reported below for O_2, H_2O and C_2H_2 that inadequacies in the ground state and supplementary basis set do affect the calculated cross sections.

3.6 Principal Representations [9,10].

If reasonable approximations to the moments of the oscillator strength distribution can be calculated then the problem of extracting the photoionization cross section is basically that of extracting a weight function, p(x), from its first 2n moments ν^k:

$$\nu^k = \int_a^b p(x)x^k dx$$

Approximating to these integrals by a numerical quadrature gives

$$\nu^0 = \int_a^b p(x)dx = \sum_{i=1}^{n}(A_i^p x_0)$$

$$\nu^1 = \int_a^b p(x)x\,dx = \sum_{i=1}^{n}(A_i^p x_i)$$

$$\nu^{2n-1} = \int_a^b p(x)x^{2n-1}\,dx = \sum_{i=1}^{n}(A_i^p x_i^{2n-1})$$

where the x_i and A_i^p are the Gaussian quadrature points and weights associated with the function p(x) and are said to provide a principal representation of the defining moments [29].

It is also useful to consider representations in which one quadrature point is fixed at a specified point, b. As this point is fixed an additional set of n points and weights are required in order to solve the 2n moment equations giving $n+1$ quadrature weights and points.

$$\nu^k = \sum_{i=0}^{n} (A_i(b) x_i(b))$$

and $x_o(b) = b$.

The dependence $A_i(b)$ and $x_i(b)$ does not mean that the A_i and x_i are actually functions of the prespecified point, a, but rather imply that they are dependent on where b is placed.

3.7 Stieltjes Histograms [29].

Solving the set of 2n linear equations directly is extremely difficult but it is possible to find the x_i and $x_i(b)$ by use of the properties of polynomials whose roots are at these points, and such methods are outlined in the next section. Thus far an n point approximant to the ν^k, which in the case under consideration

are already approximate coming from an N point pseudospectrum, has been described.

The advantage of the principal representations is that, if the approximate p^k are reasonably close to the exact ν^k it is possible to obtain estimates of the values of the function p(x) at a number of points as follows. Given the A_i and x_i then

$$\nu^0 = \int_c^d p(x)\,dx = \sum_{i=1}^{n}(A_i^p)$$

Then it is reasonable to suppose that

$$\int_c^y p(x)\,dx \simeq \sum_{i=1}^{n*}(A_i^p)$$

where $c \leq y < d$ and $x_{n*} < y < x_{n*+1}$

Thus it is possible to construct a histogram representation of the integral, known as the Stieltjes histogram, for which the midpoint at each point of increase, $\frac{1}{2}\left[\sum_1^{n^*} A_i^p + \sum_1^{n^*+1} A_i^p\right]$ give good approximations to the integral at the points of increase x_i. Hence it is possible to obtain an approximation to p(x) either by interpolating the midpoints with a smooth analytical fit and differentiating as

$$\frac{d}{dy}\int_0^y p(x)\,dx = p(y)$$

or in histogram form, from the slopes of the straight line segments joining suc-

cessive midpoints of the vertical steps of $\int p(x)dx$.

$$p(x) = \frac{1}{2}\frac{A^p_{i+1} + A^p_i}{x_{i+1} - x_i} \qquad x_{i+1} > x > x_i$$

$$p(x) = 0 \qquad 0 < x < x_1$$

$$p(x) = 0 \qquad x_n < x$$

In the current case the number of quadrature weights and points, or the order of the principle representation, must be less than the number of pseudostates defining the approximate spectral moments. As the order of the representation increases, the distribution of weights and points comes to resemble the original pseudospectrum of excitation energies and oscillator strengths.

Machado et al [25] have published the discrete pseudospectrum obtained for the $1\pi_u \rightarrow n\delta_g/k\delta_g$ excitation/ionization of C_2H_2, together with the 6th, 9th and 12th order energies and oscillator strengths, being the principal representations, at these orders, of the approximate spectral moments generated from the discrete pseudospectrum. They are reproduced in Table 3.1. The 6 and 9 point representations are quite smooth but the 12 point fit includes some of the irregularities of the original pseudospectrum of oscillator strengths.

The corresponding 9 point histogram representation of the integral of the spectral density of oscillator strength is reproduced in Fig. 3.1a, and a graph of the derivative of the polynomial, fitting the midpoints of the steps of this

histogram, in Fig. 3.1b. It may be seen in Fig. 3.1a that the midpoints of the steps of the Stieltjes histograms of orders 3 to 8 also lie on, or close to, the polynominal fitting the midpoints of the steps of the 9 point histogram.

The Stieltjes data points obtained by finite differencing of the cumulative histograms of order 3 to 9 are also shown in Fig. 3.1b and fit the polynominal derivative well, illustrating the stability of the method, which smoothes the pseudospectra, provided it is not taken to too high order.

3.8 The Stieltjes Imaging Procedure [8]

The method of obtaining the quadrature points and weights of the Stieltjes histogram are now outlined.

It is assumed that the basis set is large enough so that the first 2n moments of the photoionization cross section can be determined accurately from the pseudospectrum, where n is very much smaller than the number of pseudostates N,

$$\tilde{\nu}_k \simeq \nu_k = \int_{E_0}^{\infty} \sigma(E) E^{-k}\, dE \qquad k = 0, 2n-1$$

Transforming to the inverse energy coordinate gives

$$\omega = E^{-1}$$

$$dE = -d\omega/E^{-2} = -d\omega/\omega^2 = -\omega^{-2}d\omega$$

$$\nu_k = \int_{\omega_0}^{0} \sigma(\omega)\omega^k\omega^{-2}\,d\omega = \int_{0}^{\omega_0} (\sigma(\omega)\omega^{-2})\omega^k\,d\omega$$

In order to invert these moments to give $\sigma(E)$ the gaussian quadrature points and weights ω_i, A_i associated with the positive definite kernel $\sigma(\omega)\omega^{-2}$are required, and are defined by the moments ν_k.

It is known that the ω_i are the roots of the n'th order polynomial in ω, $P_n(\omega)$, which is orthogonal over the kernel defined above [8]. Any three consecutive $P_n(\omega)$ are related by the recursion relations

$$P_m(\omega) = (\omega - \beta_m)P_{m-1}(\omega) - \gamma_m P_{m-2}(\omega)$$

and

$$P_1(\omega) = \omega - \beta_1$$

$$P_0(\omega) = 1$$

As any polynomial of degree m, with only positive exponents, can be expressed as a sum of the $P_n(\omega)$, and as $P_n(\omega)$ is orthogonal over the kernel to all $P_i(\omega)$ where i is less than n, then $P_n(\omega)$ must be orthogonal over the kernel to all polynomials with only positive exponents of lesser degree. So

$$\int (\sigma(\omega)\omega^{-2})\omega^{m-2}P_m(\omega)\,d\omega = 0$$

Use of the recursion relation gives

$$\int (\sigma(\omega)\omega^{-2})\omega^{m-1}P_{m-1}(\omega)\,d\omega - \gamma_m \int (\sigma(\omega)\omega^{-2})\omega^{m-2}P_{m-2}(\omega)\,d\omega = 0$$

using the above metioned orthogonality to remove the term in β_m

Let

$$I_{kl} = \int (\sigma(\omega)\omega^{-2})\omega^k P_l(\omega)\,d\omega$$

Then

$$I_{m-1,m-1} - \gamma_m I_{m-2,m-2} = 0$$

therefore

$$\gamma_m = \frac{I_{m-1,m-1}}{I_{m-2m-2}}$$

also

$$I_{m-1,m} = 0 = I_{m,m-1} - \beta_m I_{m-1,m-1} - \gamma_m I_{m-1,m-2}$$

$$\therefore \beta_m = \frac{I_{m,m-1}}{I_{m-1,m-1}} - \gamma_m \frac{I_{m-1,m-2}}{I_{m-1,m-1}} = \frac{I_{m,m-1}}{I_{m-1,m-1}} - \frac{I_{m-1,m-2}}{I_{m-2,m-2}}$$

The recursion relationship also gives

$$I_{k,m} = I_{k+1,m-1} - \beta_m I_{k,m-1} - \gamma_m I_{k,m-2} \qquad k = m, 2n-1-m$$

and

$$I_{k,0} = C_k$$

$$I_{k,1} = C_{k+1} - \beta_1 C_k$$

$$\beta_1 = \frac{C_1}{C_0}$$

With these relationships it is possible to solve for γ_2 and β_2, allowing computation of $I_{k,2}$ and so on. Hence the values of $P_m(\omega)$ may be obtained. The values of $\frac{dP_m(\omega)}{d\omega}$ may be computed from the recursion relationship [8]

$$P'_m(\omega) = P_{m-1}(\omega) + (\omega - \beta_m)P'_{m-1}(\omega) - \gamma_m P'_{m-2}(\omega)$$

The ability to calculate $P_m(\omega)$ and $P'_m(\omega)$ for any value of ω allows the roots of $P_m(\omega)$ to be found by a Newton Raphson iterative numerical procedure, where the position of a root may be calculated to any desired accuracy. The correspondency weights are then [8]

$$A_i = \frac{I_{n-1,n-1}}{P'_n(\omega_i)P_{n-1}(\omega_i))}$$

These may then be converted back from the inverse energy coordinate to yield the weight and energies, (A_i, E_i), from which the Stieltjes values of the photoionization cross section may be computed.

3.8.1 The Tchebycheff Imaging Procedure [8]

As detailed above it is also possible to construct representations in which one point, b, is preset. This is termed Tchebycheff imaging. As well as the weight at the fixed point, b, the other weights and quadrature points have to be determined. These, for the desired order fit, are given as the zeros of the polynomial orthogonal over the kernel $(\sigma(\omega)\omega^{-2}(\omega - \omega_b))$. A similar development to the

above is follwed using the new kernel and modified moments computed as

$$d_k = C_{k+1} - \omega_b C_k$$

The weights are then given as [8]

$$A_i = \frac{I_{n-2,n-2}}{P'_{n-1}(\omega_i)P_{n-2}(\omega_i)(\omega_i - \omega_b)}$$

The weight associated with the predetermined point b is given for an n point Tchebycheff fit, as

$$A_b = C_0 - \sum_{i=1}^{n-1} A_i$$

where

$$A_b = A_n$$

The Tchebycheff value for the photoionization cross section is then

$$\sigma(E_b) = \sum_{i(E_i<E_b)} \frac{\partial A_i}{\partial E_b} + \frac{1}{2}\frac{\partial A_b}{\partial E_b} = \frac{1}{2}\sum_{i(E_i<E_b)} \frac{\partial A_i}{\partial E_b} - \frac{1}{2}\sum_{i(E_i>E_b)} \frac{\partial A_i}{\partial E_b}$$

The results presented in this thesis used these formulae, implemented by the method of finite differencing, in a programme made available by V.R.Saunders.

It should be noted that the results of an n point Stieltjes procedure are equivalent to the results of an n+1 point Tchebycheff procedure, as one point in the Tchebycheff procedure is predetermined.

3.9 Overview

The appropriately constructed discrete pseudospectrum of excitation energies and oscillator strengths coming from an L^2 calculation contains information about continuum states of the molecular system. This information cannot be extracted directly, but is obtained via a smoothing process, Stieltjes-Tchebycheff moment imaging, through the properties of the principal pseudostates. This is illustrated in Fig. 3.2, taken from Ref. 29. In Figs. 3.2a and 3.2b oscillator strengths which might arise from two independent calculations on the same system are shown. Also shown is the curve of the "actual" continuum oscillator strength for this system. The distributions in Figs. 3.2a and 3.2b show no relationship to one another or to the cross section. However, calculation of the principle pseudostates results in smooth distribution, shown in Fig. 3.2c, which is much more closely related to the actual oscillator strength. The actual values of the oscillator strength distribution may then be obtained by Stieltjes imaging.

3.10 REFERENCES

1. G.Gelius, C.J.Allan, G.Johansson, H.Siegbahn, D.A.Allison, and K.Siegbahn, *Physica Scripta*, **3**, 237 (1971).

2. F.O.Ellison, *J. Chem. Phys.*, **61**, 507 (1974).

3. M.A.Biondi, A.Herzenberg, and C.E.Kuyatt, *Physics Today*, **44**, October 1979.

4. R.P.Madden and A.G.Parr, *Applied Optics*, **21**, 179 (1982).

5. J.L.Dehmer, D.Dill, and S.Wallace, *Phys. Rev. Letts.*, **43**, 1005 (1979).

6. J.B.West, A.C.Parr, B.E.Cole, D.L.Ederer, R.G.Stockbauer, and J.L.Dehmer, *J. Phys. B*, **13**, L105 (1980).

7. D.Dill and J.L.Dehmer, *J.Chem. Phys.*, **61**, 2421 (1976).

8. J.J.Delaney, V.R.Saunders, and I.H.Hillier, *J. Phys. B*, bf 14,819,1981.

9. P.W.Langhoff in *Electron & Photon Molecule Collisions*, ed. T.N.Rescigno, B.V.McKoy, B.Scneider (Plenum, New York 1979).

10. P.Langhoff in, *Proc. Int. Conf. Moment Methods in Many Fermion Systems*, ed. B.J.Dalton, S.M.Grimms, J.P.Varv, S.A.Williams, 191 (Plenum, New York, 1980).

11. P.W.Langhoff, N.Papal, G.C.Sanak, T.N.Rescigno, and B.V.McKoy, *Int. J. Quant. Chem.*, **514**, 285 (1980).

12. U.Fano and J.W.Cooper, *Rev. Mod. Phys.*, **40**, 441(1968).

13. C.E.Brion and K.A.Tan, *Chemical Physics*, **34**, 141 (1978).

14. B.V.McKoy, D.Lynch, and R.R.Lucchese, *Int. J. Quant. Chem.*, **517**, 89 (1983).

15. R.E.Ballard, *Photoelectron Spectroscopy and Molecular Orbital Theory*, (Adam Hilger Ltd, Bristol 1978).

16. T.N.Rescigno, A.Gerwer, B.V.McKoy, and P.W.Langhoff, *Chem. Phys. Letts.*, **66**, 116 (1979).

17. N.Padial, G.Csanak, B.V.McKoy, and P.W.Langhoff, *Phys. Rev. A*, **23**, 218 (1981).

18. S.Iwata, and S.Nagakura, *Mol. Phys.*, **27**, 425 (1974).

19. W.Thiel, *Chem. Phys.*, **57**, 227 (1981).

20. F.A.Grimm, T.A.Carlson, J.D.Thomson, and J.W.Davenport, *J. Chem. Phys.*, **72**, 304 (1980).

21. G.R.J.Williams and P.W.Langhoff, *Chem. Phys. Letts.*, **78**, 21 (1981).

22. G.R.J.Williams and P.W.Langhoff, *Chem. Phys. Letts.*, **60**, 201 (1979).

23. R.R.Lucchese, D.K.Watson, and V.McKoy, *Phys. Rev. A*, **22**, 421 (1980).

24. D.Lynch, M.T.Lee, R.R.Lucchese, and V.McKoy *J. Chem. Phys*, **80**, 1907 (1984).

25. L.E.Machado, E.P.Leal, G.Csanak, B.V.McKoy, and P.W.Langhoff, *J. Elect. Spect.*, **25**, 1 (1982).

26. N.Padial, G.Csanak, B.V.McKoy, and P.W.Langhoff, *Phys. Rev. A*, **23**, 218 (1981).

27. A.Gerwer, C.Asaro, B.V.McKoy, and P.W.Langhoff, *J. Chem. Phys.*, **72**, 713, (1980).

28. J.B.Rose and B.V.McKoy, *J. Chem. Phys.*, **55**, 5435 (1971).

29. W.P.Reinhardt, *Computer Physics Comm.*, **17**, 1 (1979).

Table 3.1

VARIATIONAL AND MOMENT-THEORY SPECTRA FOR $1\pi_u \rightarrow n\delta_g/k\delta_g$ EXCITATION/IONIZATION OF C_2H_2

Variational spectrum[a] $\Delta\epsilon_i$(eV)/f_i	Moment-theory spectra[b] E_i(eV)/F_i		
	$n = 6$	$n = 9$	$n = 12$
9.91/0.1147	10.03/0.1756	9.92/0.1171	9.91/0.1148
10.55/0.0653	11.87/0.4983	10.71/0.1319	10.57/0.0776
10.86/0.0359	15.52/0.8242	11.76/0.2638	11.05/0.0897
11.06/0.0616	22.92/0.6744	13.73/0.5442	11.83/0.2327
11.82/0.2361	43.08/0.3994	18.05/0.7525	13.73/0.5398
13.72/0.5402	124.84/0.0960	27.02/0.4831	18.01/0.7471
17.98/0.7237		47.20/0.2686	22.55/0.0197
19.48/0.0337		93.07/0.0792	27.75/0.4733
27.56/0.4679		193.60/0.0275	47.26/0.2649
32.48/0.0193			79.01/0.0237
47.49/0.2616			101.38/0.0599
53.13/0.0028			198.84/0.0246
67.35/0.0003			
92.40/0.0613			
107.50/0.0173			
187.93/0.0189			
214.97/0.0071			
458.42/0.0000			

[a] Values in the static-exchange approximation

[b] Moment-theory spectra ... $n = 6$, 9, and 12.

Fig. 3.1

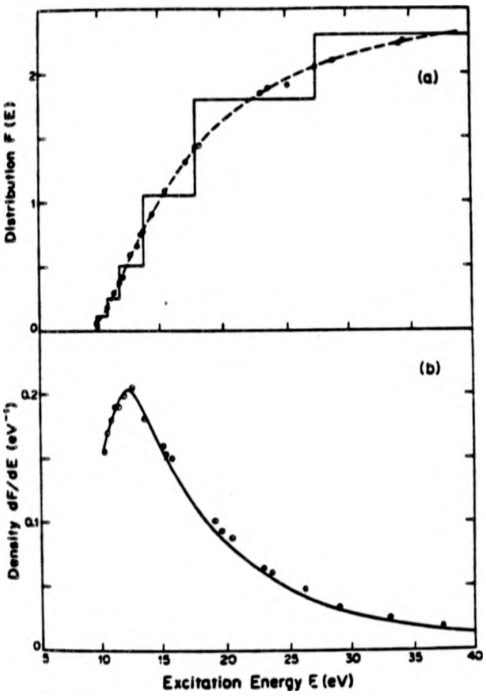

(a) Cumulative Stieltjes histograms for $1\pi_u \rightarrow k\delta_u$ photoionization of C_2H_2: ———, 9th-order histogram [illegible] obtained from [illegible] the calculated pseudo-spectrum of Table A1; ●, cumulative histogram midpoints [illegible] for $n = 3$—9; - - - - -, least-squares polynomial $(1/E)$ fit to histogram midpoints. (b) Stieltjes approximations to $1\pi_u \rightarrow k\delta_g$ photoionization of C_2H_2: ———, derivative dF/dE of cumulative fit shown in Fig. A1 (a); ●, Stieltjes data points obtained from finite-differences of cumulative histograms for $n = 3$—9.

Fig. 3.2

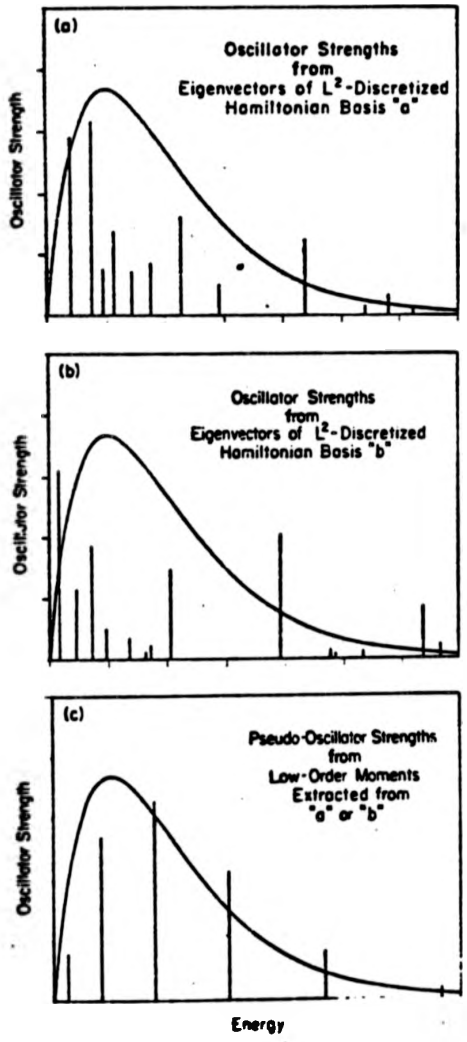
(a)
Oscillator Strengths
from
Eigenvectors of L²-Discretized
Hamiltonian Basis "a"
Oscillator Strength
(b)
Oscillator Strengths
from
Eigenvectors of L²-Discretized
Hamiltonian Basis "b"
Oscillator Strength
(c)
Pseudo-Oscillator Strengths
from
Low-Order Moments
Extracted from
"a" or "b"
Oscillator Strength
Energy

Chapter 4

Photoionization Cross Section Calculations for Open Shell Diatomic Systems

In this chapter the methods described in the previous chapter are applied to the open shell diatomic systems NO and O_2. Because of the outer open shell

these calculations are more complex and challenging than similar calculations for closed shell diatomic systems. It will be seen that the static exchange approximation coupled with the Stieltjes-Tchebycheff moment imaging technique provides results for these systems which are as encouraging as those obtained for closed shell molecules. No new method will be required to interpret the results obtained, which can be adequately understood in terms of contributions from atomic 3d pre-Rydberg orbitals, and of resonances arising from contributions from valence virtual orbitals, as were previous calculations [1].

A. Nitric Oxide Calculations [8]

4.1 Introduction

Many calculations have been reported for closed shell systems which have provided an understanding of the variation of partial channel photoionization cross sections with photon energy. Prior to the calculation reported in this section only one calculation employing the static exchange approximation together with the Stieltjes-Tchebycheff moment imaging technique had been reported for an open shell system; O_2 by Gerwer et al [2,3]. This calculation was suggested by reports of experimental measurements which showed strong structure in the

$(2\pi^{-1})X^1\Sigma^+$ and $(5\sigma^{-1})b^3\Pi$ partial channel photoionization cross sections of NO and by the desire to compare the calculated partial channel photoionization cross sections for the partially occupied outer π orbital of NO and O_2.

The different experimental measurements, both (e,2e) [4] and synchrotron [5,6] of the partial channel photoionization cross sections of NO agree substantially, and the various features in the experimental results can be understood in the light of the present results. The calculation will also be found to be useful in distinguishing between two sets of synchrotron measurements of the photoionization cross section of a photoelectron peak assigned to the $(4\sigma^{-1})c^3\Pi$ state [5,6], and in deciding which of these sets is more reliable.

In the case of NO, ionization from a closed shell orbital, because of the presence of an open shell, produces more than one ionic state of the molecular ion. For ionization from σ type molecular orbitals only two ionic states result, both of the same spatial symmetry but of different spin, which both require the same one electron operator in construction of the pseudospectra describing excitation and ionization. Ionization from a π type molecular orbital in general produces several molecular ionic states, of different spatial symmetry as well as of different spin. In the work of Gerwer et al on O_2 [2] a one electron operator averaged over all the possible excitations from the $1\pi_u$ orbital was employed in the investigation of ionization from this orbital. In this work the correct

operator will be employed for each of the NO $(1\pi^{-1})$ excitation series. It will be seen that these yield results which are very similar for each of the $(1\pi^{-1})$ ionic states, justifying the use of averaged operators in the O_2 calculation of Gerwer et al.

4.2 Theoretical and Computational Details

The ground state wavefunction of nitric oxide within the Hartree Fock approximation is:

$$\Psi = |1\sigma^2 2\sigma^2 3\sigma^2 4\sigma^2 1\pi^4 5\sigma^2 2\pi^1| X\,^2\Pi \tag{4.1}$$

Such a wavefunction was constructed with the Hartree Fock scheme employing the (9s5p/5s3p) Gaussian basis set of Dunning [7], supplemented with a d polarization function ($\xi = 0.8$) on each nucleus. The calculation was performed at the ground state internuclear separation (R_{NO} = 2.173au) [8]. This wavefunction yielded a ground state energy of -129.269au, to be compared with the best available Hartree Fock scheme value of -129.295au [9].

The separated channel approximation yields 18 distinct one electron dipole allowed series corresponding to individual excitation of the four highest lying

molecular orbitals. These series are designated:

$$
\begin{array}{cccc}
(2\pi^{-1}k\sigma)^2\Sigma^+ & & (2\pi^{-1}k\pi)^2\Pi & (2\pi^{-1}k\delta)^2\Delta \\
(5\sigma^{-1}k\pi)^2\Sigma^+ & (5\sigma^{-1}k\pi)^2\Sigma^- & (5\sigma^{-1}k\sigma)^2\Pi & (5\sigma^{-1}k\pi)^2\Delta \\
(1\pi^{-1}k\sigma)^2\Sigma^+ & (1\pi^{-1}k\sigma)^2\Sigma^- & & (1\pi^{-1}k\sigma)^2\Delta \\
 & & (1\pi^{-1}k\pi)^2\Pi & \\
(1\pi^{-1}k\delta)^2\Sigma^+ & (1\pi^{-1}k\delta)^2\Sigma^- & & (1\pi^{-1}k\delta)^2\Delta \\
(4\sigma^{-1}k\pi)^2\Sigma^+ & (4\sigma^{-1}k\pi)^2\Sigma^- & (4\sigma^{-1}k\sigma)^2\Pi & (4\sigma^{-1}k\pi)^2\Delta
\end{array}
\tag{4.2}
$$

Because of the open 2π shell in nitric oxide some of the above channels are comprised of two or more subchannels associated with various distinct molecular NO^+ ions. The construction of many electron pseudospectral wavefunctions and corresponding static-exchange potentials must be considered for the various subchannels.

For excitation and ionization from the singly occupied 2π molecular orbital the resulting core configuration can give rise to only the ground state of NO^+, ($^1\Sigma^+$), corresponding to an ionization energy of 9.27eV [15]. Consequently the construction of the excited kσ, kπ, and kδ molecular orbitals is relatively straight forward.

For excitation and ionization of the 5σ and 4σ molecular orbitals the remaining core gives rise to $^3\Pi$ and $^1\Pi$ molecular ionic states .Each of the doublet pseudospectral wavefunctions of different spatial were constructed so that the spin function associated with the 2π molecular orbital remained the same as in

the ground state wavefunction. In the static exchange approximation this doublet will carry all the intensity from the $^2\Pi$ ground state, and the other linearly independent doublet will have zero transition moment from the ground state.

For excitation and ionization from the 1π molecular orbital the remaining core gives rise to six ionic states, $^{1,3}\Sigma^+$, $^{1,3}\Sigma^-$, and $^{1,3}\Delta$ states. Each of the three core configurations of different spatial symmetry were coupled with virtual orbitals of σ, π, or δ symmetry to give the final doublet states of equation (4.2). Again the appropriate doublet state was constructed which contained the total intensity from the ground state.

It is important to note that elimination of the excited orbital from a symmetry adapted wavefunction describing one of the above channels does not lead to a pure ionic spin state, so the wavefunction implies a choice of static exchange potential and virtual orbitals appropriate to a core configuration consisting of an average of singlet and triplet states.

For each of the individual cases (equation 4.2), the appropriate virtual orbitals, Φ_i must be obtained from solution of the one electron equation of the form

$$(h_\Gamma - \epsilon_i^\Gamma)\phi_i^\Gamma = 0 \qquad (4.3)$$

where ϵ_i corresponds to the continuum or discrete energies for ionization and

excitation respectively and

$$h_\Gamma = T + V + V_\Gamma \tag{4.4}$$

is the static exchange Hamiltonian. Here T and V are the kinetic and nuclear potential operators, and V_Γ is the appropriate non-local channel potential. The latter are written in the form

$$V_\Gamma = \sum_i (2a_i^\Gamma J_i - b_i^\Gamma K_i) \tag{4.5}$$

where J_i and K_i are the usual Coulomb and exchange operators and the coefficients a_i, b_i must be determined for each case. These coefficients are chosen so that no interaction occurs within each class of doublet wavefunction (equation 4.2) which arise from the coupling of an ionic core configuration of a given spatial symmetry with a virtual orbital of a particular symmetry. The values of a_i and b_i used are listed in Table 4.1.

In the calculation of these virtual orbitals a large supplemental basis of Gaussian functions as well as the ground state basis was employed. The supplemental basis functions employed in the calculations reported here are given in Table 4.2. Several calculations were performed until the calculated $(2\pi^{-1})\,^1\Sigma^+$ partial cross section 9 point profile remained stable with respect to increase in the size of the supplemental basis, resulting in a basis which was very nearly linearly dependent.

For both the bound and continuum states, ϕ_i^Γ, transition energies ($\bar{\epsilon}_i^\Gamma$) and

oscillator strengths ($\tilde{f}_i^\Gamma$) were obtained from the pseudospectra of equation (4.3) and

$$\tilde{\epsilon}_i^\Gamma = \epsilon^\Gamma + \epsilon_i^\Gamma \tag{4.6}$$

$$\tilde{f}_i^\Gamma = {}^2/_3 \epsilon_i^\Gamma |(\phi_i^\Gamma | \underline{\mu} | \phi^\Gamma)|^2 \mu_i^\Gamma \tag{4.7}$$

Here the experimental ionization energy is used for ϵ^Γ, Φ^Γ is the occupied orbital of the active electron in the channel Γ, $\underline{\mu}$ is the dipole moment operator, and the values of μ_i^Γ are given in Table 4.1. For the continuum states the spectra of equations (4.4, 4.5) are then employed in the Tchebycheff technique in the construction of the photoionization cross sections.

Before discussion of the results it will be helpful to describe the various orbitals of the NO molecule [10]. The 1σ and 2σ orbitals are comprised of the oxygen and nitrogen 1s atomic orbitals respectively. The 3σ orbital is a bonding combination of 2s atomic orbitals with some p character and is centered towards the oxygen end of the molecule. The 4σ molecular orbital is a nonbonding combination of the nitrogen 2s atomic orbital and an oxygen sp hybrid. The 5σ molecular orbital is a weakly bonding combination of sp hybrids centered towards the nitrogen end of the molecule. The 1π molecular orbital consists of a bonding combination of $p\pi$ type atomic orbitals centered towards the oxygen end of the molecule, whereas the 2π molecular orbital is an antibonding combination of $p\pi$ type atomic orbitals shifted towards the nitrogen end of the molecule. The

6σ valence virtual orbital is a strongly antibonding combination of sp hybrid atomic orbitals with equal contributions from atomic orbitals centered on each nucleus. Transitions between each of the occupied ground state orbitals and the 6σ valence virtual orbital are dipole allowed and these transitions may appear either as interlopers in the calculated excitation series or above threshold giving rise to resonances. Strong contributions may also appear above threshold from transitions to atomic 3d pre-Rydberg orbitals.

4.3 Computational Results

4.3.1 2π Orbital IP = 9.27eV ($X^1\Sigma^+$) [15]

The static exchange excitation spectrum of the 2π orbital is presented along with quantum defect estimates [11] and the available experimental values [12] in Table 4.3. There is excellent agreement between the defect estimates and the experimental values except for the first members of each of the $2\pi \rightarrow k\sigma$ series and the $2\pi \rightarrow kp\pi$ series. In particular the quantum defect estimate of the energy of the $2\pi \rightarrow 3s\sigma$ excitation is 0.5eV greater than the experimental value whereas the calculated value is within 0.1eV. This suggests that the $3s\sigma$ orbital is not purely Rydberg in character but contains an admixture of the $6\sigma(p\sigma^*)$ valence virtual orbital. However the oscillator strength of this excitation is weak,

suggesting that the $2\pi \rightarrow 6\sigma(\sigma^*)$ intravalence excitation will also contribute above threshold. The deviation of the calculated $2\pi \rightarrow 3p\pi$ excitation energy from the experimental value is only noticeable because of the generally excellent agreement of the calculated values, defect estimates and experimental values, excluding the cases given above, demonstrating the Rydberg nature of these excitations.

The corresponding partial channel components are shown in Figure 4.1. Of these the $k\sigma$ component is weakest overall, being almost negligible except at low energies, where it possesses a weak maximum. This is assigned to contributions from the $6\sigma(p\sigma^*)$ valence virtual orbital lying 3eV above threshold. The shape of the $2\pi \rightarrow k\sigma$ component is very similar to that of the $1\pi_g \rightarrow k\sigma_u$, component although defining an area slightly less than half as great, in molecular oxygen [2], as is expected from the occupation numbers of the orbitals.

Both the $2\pi \rightarrow k\pi$ and $2\pi \rightarrow k\delta$ components display two maxima, the first narrow and at low energy, and the second, above 20eV, very broad and only decaying slowly towards high energies. The high energy features are similar to those which appear in the corresponding $1\pi_g \rightarrow k\pi_u$ and $1\pi_g \rightarrow k\delta_u$ channels in O_2, previously ascribed to contributions from relatively compact pre-Rydberg atomic 3p and 3d orbitals. The $(2\pi^{-1})\,^1\Sigma^+$ partial channel cross section is also shown in Figure 4.1. This also displays two separate maxima, the strongest cen-

tered at 13eV, arising from maxima in all three open channels, and the weaker, centered at 28eV, which is quite broad, arising from the $k\pi$ and $k\delta$ channels. Owing to the large number of pseudostates employed and the low order of the fitting parameter (6 in all cases) the features in Figure 4.1 are considered physically meaningful rather than artifacts of the imaging procedure. Furthermore the results presented here are the final results of a series of calculations in which the number of supplementary basis functions was progressively expanded until the $(2\pi^{-1})X\,^1\Sigma^+$ partial cross section was stable with respect to any further expansion of the basis set.

The (e,2e) data of Brion and Tan [4] is also presented in Figure 4.1. These results show a maximum centered at 28eV, as predicted by the calculation, but there is a substantial quantitative disagreement between the two curves in this region. At higher energies the calculation follows the form of the experimental results but always provides an underestimate of the magnitude of the partial cross section. It is possible that there is some channel coupling with 1π ionization in the resonant region since it will be shown that the calculation yields values for the various $(1\pi^{-1})$ partial cross sections which are greater than the experimental values in this region, and as a calculation employing a basis set of similar flexibility yields excellent agreement with experiment for the corresponding $(1\pi_g^{-1})X\,^2\Pi_g$ partial cross section in O_2.

In Figure 4.2 the computational results are presented for the more structured region of the partial cross section together with all the available experimental data, consisting of synchrotron measurements [5] and the (e,2e) data [4] previously mentioned. Of these only the (e,2e) measurements extend to energies above 32eV. All the experimental results agree as to the position and intensity of the maximum at 28eV. However the three lowest energy data points in the (e,2e) measurements are in substantial disagreement with the synchrotron measurements in the same energy region. Brion and Tan obtained absolute values for the partial cross sections by multiplying the total photoabsorption cross-section by the branching ratio for a given state at the various energy data points [4]. As mentioned in their paper this assumes that the ionization efficiency is unity. Since that assumption was believed to be questionable below 20eV photon energy two data points at which branching ratios and total photoabsorption cross-sections were measured did not have partial cross-sections tabulated. If partial cross-sections are calculated at these points (18eV and 19eV) assuming an ionization efficiency of unity, the resulting values are off the scale in Figure 4.2, whereas the synchrotron data at these energies show no such tendency, thus indicating that the ionization efficiency is indeed less than unity at these energies. The disagreement between both sets of synchrotron data and the (e,2e) data between 20eV and 22eV also suggests that the ionization efficiency may be significantly less than unity at energies up to 24eV.

Three calculated curves are plotted in Figure 4.2, obtained using 9 point (curve A), 6 point (B), and 4 point (C) imaging procedures. The 9 and 6 point curves are fairly similar, the 6 point curve being a flattened version of the 9 point, both displaying two maxima centered at the same energies, the second of which is in the same position but weaker than the experimental maximum. This near stability of the profiles, while changing the fitting parameter from 9 to 6, indicates that there may be a sufficiently large number of pseudostates present to justify the use of the 9 point imaging procedure, a situation which does not apply in some of the other calculations presented in this thesis (e.g., H_2O, Chapter 5). The 4 point fit completely smoothes the maximum at 29eV and instead has a weak maximum at 19eV, arising from the the two maxima present in both the 6 and 9 point fits. The smoothness and mutual agreement of the 6 and 9 point fits and their dissimilarity to the 4 point fit, together with the 4 point fit's removal of the high energy maximum present in the experimental data, indicates that the 4 point fit represents an over smoothing of the pseudospectral results.

The synchrotron data show a weak maximum at 18.5eV and a very sharp intense peak at 17eV [5]. The sharp maximum at 17eV is assigned to the autoionization of the $5\sigma \rightarrow 4p\sigma$ or $5\sigma \rightarrow 4p\pi$ excitations converging on the $B^1\Pi$ state of the ion. These are calculated to lie at 17.09eV and 17.06eV respectively and are experimentally located at 17.01eV and 17.06eV [12]. Since the present calculation employs the static exchange approximation, such effects cannot be

reproduced by it. The weak maximum near 19eV is also not reproduced in the present calculation (6 and 9 point). Several excited states arising from the 4σ orbital lie in this region [13] (Table 4.6) and autoionization from these states provides a possible explanation for this maximum. Unfortunately there are no measurements for photon energies lower than 16.5eV, so confirmation of the predicted low energy maximum must await further experimental work.

The results of an MSXα calculation of the outer valence partial photoionization cross sections of NO are also available [14]. For the $(2\pi^{-1})\,^1\Sigma^+$ channel, these show a gradual rise to a maximum at 19eV followed by a steady decline, very similar in form to the 4 point fit, though somewhat weaker. The maximum is attributed to a resonance in the σ channel, the magnitude of which is diminished by the effects of averaging over different values of the internuclear distance, thus allowing for the effects of vibrational motion. These results show no evidence of the broad experimental maximum at 29eV. In view of the excellent agreement between experiment and the present results above 20eV, and the position of the maximum in the kσ channel at 12eV photon energy, the interpretation of the maximum at 19eV suggested by the $X\alpha$ results appears somewhat dubious.

Calculations have recently been reported in which the photoionization cross section for this orbital has been obtained from the direct solution of the e +

NO^+ collisional equations at the static exchange level [26]. These have not shown the initial peaks reported here in the $2\pi \rightarrow k\pi$ and $2\pi \rightarrow k\delta$ profiles, nor the resulting initial peak in the partial channel cross section. They have however supported the presence of a broad shoulder between 20 and 30 eV reported here.

It has been suggested that these features at low photon energies in these profiles are spurious, arising from instabilities in the Tchebycheff imaging technique of deficiencies in the basis set. This does not appear to be the case. Calculations with different basis sets, performed during the current research, have all shown two separate structures in these profiles. Moreover, partial cross sections obtained using 4, 6, and 9 point fits (Fig. 4.2), all show an initial maximum. The effect of lowering the order of the fit, if these initial features were spurious and arose from too high an order fit, would be to remove these maxima. The opposite happens. It is the high energy shoulder that is diminished. This suggests that the initial maxima, proof of whose existence or nonexistence must await further experimental measurements, is a genuine feature of the partial channel cross section as calculated by the Tchebycheff technique.

4.3.2 5σ Orbital IP = 16.56eV ($b^3\Pi$) [15]

The static exchange excitation spectrum of the 5σ orbital for excitations leading to the $b^3\Pi$ state of the NO^+ ion, together with quantum defect estimates and

the available experimental values [12], is presented in Table 4.4. There is general accord between the various values for the $k\sigma$ excitations. The low values of the oscillator strength calculated for the $ks\sigma$ and $kd\sigma$ excitations, compared to those of $kp\sigma$ series, explains the experimental observation of only one $k\sigma$ Rydberg series, the $kp\sigma$ excitations. There is little evidence of contributions from the $6\sigma(\sigma^*)$ valence virtual orbital other than the strength of the $5\sigma \rightarrow 3p\sigma$ excitation, so a strong contribution from this excitation is expected above threshold.

Excitation of a σ electron to a $k\pi$ type Rydberg orbital can result in any one of three possible states of the excited system, $^2\Sigma^+$, $^2\Sigma^-$ and $^2\Delta$, as there are three ways in which the angular momentum of the excited electron may be coupled with that of the residual ion. Excitation to each of these three states is dipole allowed as the ground state of the molecule is of $^2\Pi$ symmetry. The canonicalization required for a $k\pi$ orbital is slightly different for each of these states. As a result corresponding orbitals belonging to each of these three different states have different eigenvalues and eigenvectors.

In Table 4.4 the three different calculated excitation energies and oscillator strengths for each $5\sigma \rightarrow k\pi$ excitations are listed. Except for the $5\sigma \rightarrow 3p\pi$ set of excitations, all the excitations of each set are calculated to lie extremely close together, and to have oscillator strength ratios of almost exactly 1:1:2. This

confirms that the excited orbitals in a given set are very similar, i.e. the excited electron does not couple strongly with the electrons in the residual molecular ion, and the oscillator strength ratios are to be expected from the multiplicity factors used (table 4.1). It is therefore unsurprising that the quantum defect estimates are in such good agreement with the calculated values. As the calculated values within a given set of excitations lie close together, it would appear that experimental resolution may not be fine enough to resolve the three cases even for the $5\sigma \rightarrow 3p\pi$ set. The $kd\pi$ excitations are much weaker than the $kp\pi$ excitations explaining the experimental observation of only the $kp\pi$ series.

The corresponding $k\sigma$ and $k\pi$ contributions to the $(5\sigma^{-1})b^3\Pi$ partial cross section are presented in Figure 4.3. As expected there is a strong resonance in the $k\sigma$ channel attributed to contributions from the $6\sigma(\sigma^*)$ valence virtual orbital. Above the resonance the $k\sigma$ contribution decays rapidly and makes little contribution compared to the $k\pi$ channel. The $k\pi$ channel, as expected form other studies, is weak compared to the resonant channel but is very broad, extending to high energies. The two contributions are combined to yield the $(5\pi^{-1})b^3\Pi$ partial cross section in Figure 4.4 which is presented along with the $(5\sigma^{-1})A^1\Pi$ partial cross section and the available experimental data for the $b^3\Pi$ ion.

The $k\sigma$ resonance is still clearly visible but the $k\pi$ contribution dominates at

high energies. The same canonicalizations are employed for construction of the pseudospectra regardless of whether the final state of the ion is singlet or triplet. A total $(5\sigma^{-1})^{1,3}\Pi$ partial cross section is constructed using the appropriate ionization energy (singlet or triplet) and this is then multiplied by one quarter to yield the $(5\sigma^{-1})A^1\Pi$, and by three quarters to yield the $(5\sigma^{-1})b^3\Pi$, partial channel cross sections. Thus it is not surprising that the calculated singlet and triplet partial cross sections presented in Figure 4.4 are identical in form, with the singlet shifted to higher energy because of its higher ionization energy and being one third as strong as the triplet.

Agreement between the calculated curve and the experimental results is excellent, especially at higher energies where the calculated curve follows the form of the experimental curve almost exactly, and lies just above the bounds on the error bars.

Similar calculations for ionization from the corresponding $3\sigma_g$ orbital in O_2 [2,3] have yielded $k\sigma_u$ and $k\pi_u$ contributions very similar in form to those presented here for the 5σ orbital in NO, predicting a resonance 3eV above threshold in the $k\sigma_u$ contribution. However the calculated cross section is substantially stronger than the experimental cross section, unlike the present case. As a result of this discrepancy, and the occurrence of the resonance near threshold, in the region of vibrational and autoionization structure, Gerwer et al. could

not claim full experimental verification. The present results lend support to the prediction of a resonance, and the better quality results obtained here are attributed to both superior ground state and supplemental basis sets.

The calculated curve for the $(5\sigma^{-1})b^3\Pi$ partial cross section gives an especially clear example of one of the less immediately evident properties of the imaging process. That is, at a given energy, the result obtained from the imaging of a set of pseudostates is not necessarily the same as the sum of the results of the imaging of two (or more) mutually exclusive but complete subsets of this set of pseudostates. In particular the calculation predicts that the resonance will show a sharp maximum followed by a narrow shoulder before the decline. [BHowever, summation of the $k\sigma$ and $k\pi$ contributions in Figure 4.3 does not yield the identical profile. For example, $\sigma\left[22\text{eV}, (5\sigma^{-1})b^3\Pi\right] = 9.0\text{Mb}$ by imaging all the pseudostates at once, but is 7.9Mb by separate imaging followed by summation of the $k\sigma$ and $k\pi$ contributions. At 25eV photon energy this ordering is reversed. However, the two different curves will both define the same area.

The $X\alpha$ calculation of Wallace et al [14] also predicts a resonance in this channel near 24eV, and has $k\sigma$ and $k\pi$ contributions similar to the present results. However, calculations at the equilibrium internuclear distance do not yield results as encouraging as those presented here, showing a very narrow

resonance with a maximum of 12Mb compared with an experimental maximum of 7.6Mb. Averaging over nuclear motion widens and diminishes this resonance yielding better results, though still not as good as those presented here, which were calculated at the equilibrium internuclear distance. From the results of this and other $X\alpha$ calculations it seems possible that the introduction of some form of averaging over nuclear motion would diminish the present, and already satisfactory, results and yield even better agreement with experiment.

Multiplet specific static exchange calculations have recently been reported for both ionic states arising from this orbital [24]. In these different potential operators were used for singlet and triplet states and so resonance peaks were calculated at different photoelectron kinetic energies in the two multiplet channels. The experimental confirmation [25] of this effect is somewhat unsatisfactory at present, as reported measurements of the cross sections for the v=0,1 vibrational states of the triplet and singlet ions were normalised upon the data of Southworth et al [5]. The data of Southworth et al contains the contributions of all vibrational states, yet the measurements of Morin et al [26],for only the first two vibrational levels of the triplet ion, are 2Mb greater at the resonance peak.

4.3.3 1π Orbital IP = 16.11eV ($a^3\Sigma^+$) [12,15]

Ionization of an electron from the 1π orbital can result in any one of six states of the NO^+ ion; $a\,^3\Sigma^+$, $w\,^3\Delta$, $b'\,^3\Sigma^-$, $A\,^1\Sigma^-$, $w\,^1\Delta$, and $B'\,^1\Sigma^+$. The calculated Rydberg series together with the quantum defect estimates and the available experimental data for excitations leading to the $w\,^3\Delta$ state of the ion are given in Table 4.5. As expected the calculated excitation series divide naturally into $s\sigma$, $p\sigma$, $d\sigma$, $p\pi$, $d\pi$ and $d\delta$ series. Unfortunately experimental values are only available for the $s\sigma$ series, but there is general agreement between the three sets of figures. The largest discrepancy is for the $1\pi \rightarrow 3s\sigma$ excitation, for which the calculated and experimental excitation energies are quite close together but there is a large discrepancy between the two values and the quantum defect estimate. This discrepancy together with the comparatively large oscillator strength suggests that this transition may be of mixed Rydberg/valence character, and could be better designated as $1\pi \rightarrow 3s\sigma/6\sigma(\sigma^*)$. The other excitation series show no sign of being anything other than purely Rydberg in character. Parallel excitation series leading to the other $(1\pi^{-1})$ ion states have been calculated and of these the $1\pi \rightarrow ks\sigma$ series are presented in Table 4.5.

The corresponding $k\sigma$, $k\pi$ and $k\delta$ contributions to the $w\,^3\Delta$ partial cross section together with the $(1\pi^{-1})w\,^3\Delta$ partial channel cross section are presented in Figure 4.5. The major contribution comes from the $k\delta$ profile while the $k\pi$

profile is broad and flat extending to high energy. The $k\sigma$ profile displays a monotonic decline giving no indication of the presence of a resonance in the channel. All profiles given on Figure 4.5 were obtained using a 6 point imaging procedure.

The effects of alteration of the fitting parameter are explored in Figure 4.6, where 9, 6, and 4 point profiles for the $(1\pi^{-1})w\,^3\Delta$ partial cross section are plotted. Both the 6 and 4 point fits are very similar in form and magnitude, whereas the 9 point fit displays series of oscillations. This is because too high a fitting parameter has been employed and the pseudospectrum is not adequately smoothed. This contrasts with the results for the $(2\pi^{-1})X\,^1\Sigma^+$ partial channel where the 9 and 6 point fits are in good agreement and the 4 point fit is over smoothed. Similar results have been obtained for all the other $(1\pi^{-1})$ channels. The 6 point profiles obtained for all the states which result from ionization from the 1π orbital are presented in Figure 4.7. Despite the different final states the form of all the curves is very similar. The same set of pseudostates were constructed for the $^3\Sigma^+$ and $^3\Sigma^-$ channels and the two profiles are almost identical. The $(1\pi^{-1})w\,^3\Delta$ profile, despite the pseudospectra for this channel being eigenfunctions of different operators than those of the $(1\pi^{-1})a\,^3\Sigma^+$ and $b'\,^3\Sigma^-$ channels, is almost identical to the $a\,^3\Sigma^+$ profile multiplied by two and shifted by the appropriate amount. The singlet profiles are just one third of the appropriate triplet profiles, again shifted by the difference in ionization energies.

All the $(1\pi^{-1})$ profiles have been summed to yield a total $(1\pi^{-1})$ photoionization cross section, presented in Figure 4.8, which shows a monotonic decline from an initial maximum. In both form and magnitude it is very similar to the $(1\pi_u^{-1})$ photoionization cross section in O_2, and is slightly less than twice as strong as the total $(5\sigma^{-1})$ photoionization cross section which has a binding energy in the same region.

Brion and Tan [4] have published (e,2e) measurements of the photoionization cross section for the sum of states whose ionization potential lies between 14 and 20 eV, i.e. all the states originating from 5σ ionization and all states originating from 1π ionization expect the $B'^1\Sigma^+$. The experimental data together with the calculated curve obtained by summation of the calculated partial channel cross section for each of these states is presented in Figure 4.9. Both the experimental and theoretical curves show an initial maximum near 22eV photon energy followed by a monotonic decline. The calculated initial maximum is greater than the experimental maximum by as much as 6Mb but because of its more rapid decline moves into better agreement at higher energies. However even at 31eV the calculated curve lies as much as 3Mb above the experimental curve.

Even though no experimental data is available for purely 1π derived states the fact that synchrotron measurements are available for the $(5\sigma^{-1})b^3\Pi$ state permits an estimate of the inaccuracy of the calculated 1π cross section below

38eV. From 23 to 32eV photon energy the $(5\sigma^{-1})b^3\Pi$ partial cross section is always less than 1Mb greater than the experimental data. It therefore seems reasonable to assign an error of no more than ½Mb to the $(5\sigma^{-1})$ $A^1\Pi$ partial cross section. Since the total cross section presented in Figure 4.9 is as much as 6Mb greater than the experimental results, it is clear that the various 1π derived cross sections are overestimates. Dividing the total overestimate among the various $(1\pi^{-1})$ states contributing to the profile in Figure 4.9 on the basis of their spin and symmetry degeneracies suggests that the magnitude of the overestimates for each of these partial channel may be bounded by the following limits: $a^3\Sigma^+$: 1Mb, $w^3\Delta$: 2Mb, $b'^3\Sigma^-$: 0.34 Mb and $W^1\Delta$: 0.67 Mb. On this basis it would seem reasonable to set a bound on the error in the $B'^1\Sigma^+$ profile, which is not included in the above estimates, of 0.33Mb.

While some of the overestimate may be accounted for by channel coupling it is clear that this cannot account for the total overestimate. The calculated $(2\pi^{-1})^1\Sigma^+$ photoionization cross section is 1½Mb less than the corresponding experimental measurements at 29eV photon energy, whereas the overestimate at this energy in Figure 4.9 is 5Mb. The overestimate may arise from the neglect of vibrational motion or from the neglect of electronic relaxation effects.

By the same argument the underestimate at high energies probably arises in the calculation of the $(1\pi^{-1})$ partial cross sections. While channel coupling

has been suggested as a contributor to the overestimate at low energies this suggestion cannot be advanced with regard to the $(2\pi^{-1})X\,^1\Sigma^+$ state at these energies, as the calculated total curves in Figures 4.1 and 4.9 are both underestimates at high energies. Here it is possible to deduce that the total $(1\pi^{-1})$ partial channel photoionization cross section in Figure 4.8 is too great at maximum and declines too rapidly to yield a slight underestimate at high photon energies.

4.3.4 4σ Orbital IP = 21.7eV ($c\,^3\Pi$) [15]

Ionization potentials for this orbital are still a matter of some controversy. Initially Edqvist et al [12] assigned the $(4\sigma^{-1})c\,^3\Pi$ ionization to a weak peak at 20.41eV and the $(4\sigma^{-1})B\,^1\Pi$ to a much stronger peak at 21.72eV. The triplet: singlet intensity ratio was measured as 0.1:1 instead of 3:1 as expected on the grounds of spin multiplicity. Both peaks showed little vibrational structure, whereas a weak peak centered at 23.3eV possessed a broad vibrational manifold and was assigned to the $(1\pi^{-1})B'\,^1\Sigma^+$ ionization. The anomalous intensity ratios led Lefebvre-Brion [16] to suggest that the $(4\sigma^{-1})c\,^3\Pi$ ionization corresponded to the narrow intense peak at 21.7eV and the $(4\sigma^{-1})B\,^1\Pi$ ionization was assigned to the broad manifold at 23.3eV. It was further suggested that the single configuration description was better for the triplet state than for the

singlet state, which was alleged to interact strongly with the $(5\sigma^1\ 1\pi^3\ 2\pi^2)$ configuration. It was then discovered that the line initially assigned to the triplet ionization was in fact spurious. In the resulting higher resolution spectrum the manifold at 23.3eV was resolved into a fairly regular vibrational progression, similar to those of the other $(1\pi^{-1})$ states, and the peak at 21.7eV was only partially resolved. It was then suggested that the 21.7eV peak resulted from ionization to both the $(4\sigma^{-1})c^3\Pi$ and $(4\sigma^{-1})B^1\Pi$ states lying very close together and an argument based on the intensity of the peaks was produced to support this view. [15]

The minimal basis set configuration interaction calculations of Thulstrup at al [17] yielded results which agreed with Edqvist at al [15] as to the ordering at the ionic states below 20eV. However no $(1\pi^{-1})\,^1\Sigma^+$ state was found and it was suggested that the peak at 23.3eV could arise from the $(4\sigma^{-1})B\,^1\Sigma^+$ state.

No Rydberg series leading to the 23.3eV peak have, as yet, been reported but Rydberg series leading to the 21.7eV peak have been reported by several authors [18,19]. Sasanuma et al [19] concluded that either the energy levels of the ionic states corresponding to the $B\,^1\Pi$ and $c^3\Pi$ states lie close together, within the 0.02eV limit of experimental resolution of their machines, or that Rydberg series converging on the $B\,^1\Pi$ state were too weak for them to observe. What is clear from the studies of the photoelectron spectra and Rydberg series, which all find

little vibrational structure, is that the 4σ orbital in NO is largely nonbonding in character.

Given that experimental data exists for the partial photoionization cross sections of both peaks between 20 and 24eV [5,6] and for the total photoionization cross section of these two peaks [4] it would seem that the present calculations have the potential to finally end the controversy surrounding the assignment. Unfortunately it will be seen that this not the case. Instead the limits of the current data and of the static exchange approximation will be highlighted.

All authors agree that the peak at 21.7eV includes the $(4\sigma^{-1})c^3\Pi$ state. Calculated, quantum defect estimates and experimental values for the excitation energies of the series leading to this state are given in Table 4.6. Agreement between all three sets of figures is quite satisfactory, although the oscillator strength distributions of the $4\sigma \rightarrow ks\sigma$ series is rather irregular. The strongest calculated series is the $kd\sigma$ series and there is little evidence of contributions from the 6σ valence orbital. No reliable experimental values are available for the $ks\sigma$ series, which is understandable upon comparison with the strength of the $kd\sigma$ series. The n'th member of the $s\sigma$ series is calculated to lie very close to the (n-1)'th member of the $kd\sigma$ series, which may also be a factor in the failure to locate this series experimentally.

The calculated $k\sigma$ and $k\pi$ contributions to the $(4\sigma^{-1})c^3\Pi$ partial cross sec-

tion are presented in Figure 4.10. The main feature is a resonance in the $k\sigma$ channel which is attributed to contributions from the $6\sigma(\sigma^*)$ orbital above threshold. At higher energies the $k\pi$ contribution dominates, as is usual in the partial cross section of σ type orbitals which possess a resonance in the $k\sigma$ channel [1]. Also given in Figure 4.10 is the $(4\sigma^{-1})c^3\Pi$ partial cross section and a total $(4\sigma^{-1})$ triplet plus singlet cross section calculated assuming both states have the same ionization energy, together with the two sets of synchrotron measurements for the peak at 21.7eV binding energy. The measurements of Gustafsson and Levinson [6] are more than 50% greater than those of Southworth et al [5], but both sets of data are in reasonable agreement as to the presence of a resonance.

The agreement between the calculated curves and the two sets of experimental data as to the position of the resonance is quite encouraging. There is good agreement between the calculated $(4\sigma^{-1})c^3\Pi$ curve and the experimental measurements of Southworth et al, but is also reasonable agreement between the calculated total $(4\sigma^{-1})$ curve and the measurements of Gustafsson and Levinson. Since both experimental measurements refer to the same peak, this does not permit assignment of the states contributing to the peak. The (e,2e) measurements of Brion and Tan [4] for the cross section of both the 21.7 and 23.3eV peaks are presented in Figure 4.11, and compared with a calculated curve obtained by assigning both 4σ derived states to the 21.7eV peak and the $(1\pi^{-1})B'^1\Sigma^+$state to the 23.3eV peak. Both the experimental curve and the

theoretical curve have maxima very close together but the theoretical curve is substantially stronger than the experimental curve. Referring back to Figure 4.10 it can be seen that the measurements of Gustafsson and Levinson for the strength of a single peak are stronger than those of Brion and Tan for the intensity of two peaks. The results of Brion and Tan are therefore incompatible with those of Gustafsson and Levinson, but compatible with those of Southworth et al. In view of this it seems probable that the results of Southworth et al and of Brion and Tan for the peak at 21.7eV binding energy are reasonably accurate and those of Gustafsson and Levinson unreliable.

The experimental measurements of Gustafsson and Levinson for the 23.3eV peak are presented in Figure 4.12, together with the partial cross section, for the $(4\sigma^{-1})B\,^1\Pi$ and $(1\pi^{-1})B'\,^1\Sigma^+$ states, calculated assuming that they have an ionization potential of 23.3eV. There is a maximum in both calculated curves in the same region as the experimental maximum. Superficially, the experimental results appear to be in much better agreement with the $(1\pi^{-1})B'\,^1\Sigma^+$ profile than with the $(4\sigma^{-1})B\,^1\Pi$ profile. However it has been shown that Gustafsson and Levinson's results are not reliable for the peak at 21.7eV and it seems doubtful that they are any more reliable for the 23.33V peak. For the 21.7eV peak the experimental results were as much as 60% greater than the apparently reliable results of Southworth et al in the resonance region. If the results of Gustafsson and Levinson were also too great by a factor of 60% in the case of the

23.3eV peak then the true experimental values would be scattered inconclusively in the region between the two calculated curves. A further three 'experimental' points are plotted in Figure 4.12. These were obtained by subtractions of the measurements of Southworth et al for the photoionization cross section of the 21.7eV peak from the measurements of Brion and Tan for the photoionization cross section of the 21.7 and 23.3eV peaks. These three points lie suggestively close to the $(4\sigma^{-1})B\,^1\Pi$ curve. However manipulation of the data in this manner is not strictly justified as errors must be treated as cumulative, and no error bars are given in the data of Brion and Tan. Furthermore, it was previously estimated that the calculated $(1\pi^{-1})B'\,^1\Sigma^+$ partial cross section could be as much as 1/3Mb greater than the physical cross section. This would place the $(1\pi^{-1})B'\,^1\Pi^+$ profile very close to the $(4\sigma^{-1})B\,^1\Pi$ profile.

Certain approximations which may not be justified have been made in calculating these cross sections. Firstly the calculations have been performed at the ground state internuclear separation. It has been shown that in $X\alpha$ calculations the intensity of a calculated resonance in the σ channel is often greatly reduced by inclusion of the effects of vibrational motion, e.g. the ionization from the 5σ orbital in the present case. No such investigation have as yet been carried out within the static exchange Stieltjes Tchebycheff scheme. However in view of the consistently good agreement between calculation and experiment for the cross section of outer valence σ type orbitals it is expected that these effects

will probably be weaker than is the case in $X\alpha$ calculations.

These calculations have also employed the frozen core approximation. This approximation is not necessarily justified, especially for ionization from inner valence orbitals at low photoelectron kinetic energies. This effects of configuration interaction have also not been considered i.e. it has been assumed that photoionization of an electron from the 4σ orbital will result only in a Koopmans hole type singlet or triplet configuration. However it has been shown that in many molecules a large portion of the intensity in inner valence ionization is carried by states of the two hole one particle type. A broad structure is found in the 26 — 36eV binding energy region which is inexplicable in terms of a single configuration picture. The partial photoionization cross section of this structure has been measured by Brion and Tan and is very similar in form to the curve obtained for the $(c^3\Pi + B^1\Pi + B'^1\Sigma^+)$ partial cross section, suggesting that it contains significant contributions from ionization from the 4σ and/or 1π orbitals. Furthermore at high energy this peak is up to 50% as strong as the peaks assigned to the $(c^3\Pi + B^1\Pi + B'^1\Pi^+)$ states. It therefore seems unlikely that the inclusion of such effects would fail to have a strong impact on the calculated $(4\sigma^{-1})$ photoionization cross section. In Figure 4.11 a second set of data points, obtained by addition of the measurements of Brion and Tan for the intensity of this broad structure to the measured intensity of the $(c^3\Pi + B^1\Pi + B'^1\Pi^+)$ states is plotted. While better agreement between calculation and experiment is

now obtained below 44eV photon energy it is clear that the calculated curve is now an underestimate in the high energy region, where it has already been concluded that the calculated $(1\pi^{-1})$ profiles probably provide an underestimate.

Because of the reasons given above it does not seem that this calculation contributes significantly to the decision of the correct assignment of the two photoelectron peaks under consideration. However it does seem clear that the experimental data of Gustafsson and Levinson is unreliable. Definitive measurements of the partial cross section of the 23.3 and 21.7eV peaks at higher energies would be of great interest.

The rectification of the various computational inadequacies is expected to lower the intensity of the total $(4\sigma^{-1})\left[c^3\Pi + B'^1\Pi\right]$ curve in Figure 4.10, bringing it into reasonable agreement with the experimental data of Southworth et al [5]. If the experimental data of Gustafsson and Levinson [6] is in error for the 23.3eV peak by the same factor that it is for the 21.7 eV peak, and the above factors are taken into account it is expected that the $(1\pi^{-1})B'^1\Pi^+$ profile would be more closely in agreement with the correct experimental results than the $(4\pi^{-1})B^1\Pi$ profile. Thus the present results tend to be more compatible with the assignment of both 4π derived states to the same peak at 21.7eV binding energy and the $(1\pi^{-1})B'^1\Pi^+$ state to the peak at 23.3eV, rather than the assignment of the two 4σ derived states to different peaks in the photoelectron

spectrum.

4.3.5 Total Photoionisation Cross Section

The total calculated photoionization cross section of NO, obtained by direct summation of the various calculated partial cross sections is presented in Figure 4.13, along with the experimental measurements of Brion and Tan [4]. Both curves are of the same general form showing a flat maximum extending from 20 to 25eV photon energy followed by a slow decline. However the magnitude of the calculated maximum is substantially greater than that of the experimental maximum. There is some slight cancellation of errors taking place with the calculated 2π partial cross section being less than the corresponding experimental measurements, the $(5\sigma^{-1})b\,^3\Pi$ partial cross section very close to the available experimental measurements and the total $(4\sigma^{-1})\left[c\,^3\Pi + B\,^1\Pi\right] + (1\pi^{-1})B'\,^1\Sigma^+$ is at worst 1Mb greater than the experimental measurements below 30eV. It is clear from the preceding discussion that the overestimate of the total cross section near maximum must arise from an overestimate of the magnitude of the various 1π cross sections below 40eV.

Above 40eV the calculated total cross section is less than the experimental cross section. As the states resulting from ionization of the 3σ molecular orbital are not included in the calculation whereas they are included in the experiment

strictly similar quantities are not being compared. Therefore a second set of 'experimental' points are plotted in Figure 4.13, consisting of the measured total cross section of Brion and Tan less the measured intensity of the 3σ derived states. The calculated cross section is still less, by up to 2Mb, than the 'adjusted' experimental data. This underestimate has two major contributions. Firstly the underestimate at high energies of the total $(4\sigma^{-1})\left[c^{3}\Pi + B^{1}\Pi\right] + (1\pi^{-1})B'^{1}\Sigma^{+}$ intensity together with the associated many electron transition peaks. Secondly the underestimate at high energies of the total 5σ and 1π (14–20eV binding energy) peaks. From the behaviour of the $(5\sigma^{-1})b^{3}\Pi$ partial cross section in the region for which experimental data is available and from calculations for closed shell diatomic molecules it seems likely that the calculated cross sections of the 5σ derived states will continue in good agreement with experiment at high energies. Therefore the underestimate at high energies must arise chiefly in the various calculated 1π partial cross sections. There is also a smaller contribution from the underestimate of the $(2\pi^{-1})X^{1}\Sigma^{+}$ partial channel photoionization cross section. As a total is presented in Figure 4.13 in which the effects of channel coupling should cancel out, it is clear that the calculation is not by any means exact.

strictly similar quantities are not being compared. Therefore a second set of 'experimental' points are plotted in Figure 4.13, consisting of the measured total cross section of Brion and Tan less the measured intensity of the 3σ derived states. The calculated cross section is still less, by up to 2Mb, than the 'adjusted' experimental data. This underestimate has two major contributions. Firstly the underestimate at high energies of the total $(4\sigma^{-1})[c^3\Pi + B^1\Pi] + (1\pi^{-1})B'^1\Sigma^+$ intensity together with the associated many electron transition peaks. Secondly the underestimate at high energies of the total 5σ and 1π (14–20eV binding energy) peaks. From the behaviour of the $(5\sigma^{-1})b^3\Pi$ partial cross section in the region for which experimental data is available and from calculations for closed shell diatomic molecules it seems likely that the calculated cross sections of the 5σ derived states will continue in good agreement with experiment at high energies. Therefore the underestimate at high energies must arise chiefly in the various calculated 1π partial cross sections. There is also a smaller contribution from the underestimate of the $(2\pi^{-1})X^1\Sigma^+$ partial channel photoionization cross section. As a total is presented in Figure 4.13 in which the effects of channel coupling should cancel out, it is clear that the calculation is not by any means exact.

B Oxygen Calculations

4.4 Introduction

Molecular oxygen, like nitric oxide, has a partially filled outer orbital above a closed shell. Differing from nitric oxide by possessing an extra electron in the partially filled molecular orbital and by possessing a centre of inversion it is expected to display the same trends in its partial photoionization cross sections as can be seen in the shift from N_2 to NO.

The static exchange Stieltjes Tchebycheff calculation of Gerwer et al [2,3] of the various partial cross sections of molecular oxygen yielded results which were in quite reasonable agreement with the available (e,2e) measurements [20]. However the published profile for the $(1\pi^{-1})X^2\Pi_g$ partial channel photoionization cross section consists of a slow rise to a maximum followed by a monotonic decline, unlike the highly structured profile reported here for the corresponding $(2\pi^{-1})X^1\Sigma^+$ state of NO. This unstructured maximum is also present at the same energy in the (e,2e) measurements but is more than 30% stronger than the calculated maximum.

This lack of structure in the theoretical results has prompted the recalcula-

tion of the $(1\pi_g^{-1})X\,^2\Pi_g$ partial channel photoionization cross section of molecular oxygen employing a basis set of comparable flexibility to that employed in the calculations on nitric oxide.

4.5 Theoretical and Computational Details

The ground state wavefunction of molecular oxygen within the Hartree Fock approximation is

$$\Psi = |1\sigma_g^2\ 1\sigma_u^2\ 2\sigma_g^2\ 2\sigma_u^2\ 3\sigma_g^2\ 1\pi_u^4\ 1\pi_g^2|X\,^3\Sigma_g^- \tag{4.8}$$

Such a wavefunction was constructed within the Hartree Fock scheme employing the (9s5p/5s3p) Gaussian basis set of Dunning [7] supplemented with a polarization function (ξ = 0.97) on each atomic centre. The calculation was carried out at the ground state internuclear distance (R_{oo} = 2.282au) [2,3] and yielded a ground state energy of —149.6365au compared with the Hartree Fock limit of —149.666au [2,3]. This is somewhat lower than the energy of —149.634au obtained by Gerwer et al [2] employing the (10s5p1d/3s2p1d) basis of Dunning.

The separated channel approximation yields three distinct dipole allowed series corresponding to individual excitation of the $1\pi_g$ orbital. These series are

designated

$$(1\pi_g^{-1}k\sigma_u)^3\Pi_u, \quad (1\pi_g^{-1}k\pi_u)^3\Sigma_u^-, \quad (1\pi_g^{-1}k\delta_u)^3\Pi_u \tag{4.9}$$

The supplemental basis set used to describe the excited and continuum orbitals is given in Table 4.7, and allows the construction of $10\delta_u$, $19\pi_u$ and $25\sigma_u$ orbitals. This is somewhat larger set than that of Gerwer et al whose supplemental basis set permitted the construction of $9\delta_u$, $16\pi_u$ and $23\sigma_u$ orbitals.

For each of the individual cases (Equation 4.9) the appropriate virtual orbitals are obtained from solution of the one electron equation (Equation 4.3) using the formulae for the static exchange potentials derived by Gerwer et al [2]. These orbitals were then employed in the Tchebycheff imaging procedure to construct the $(1\pi_g^{-1})X^2\Pi_g$ partial channel photoionization cross section.

4.6 Computational results for the $1\pi_g$ orbital IP = 12.07eV [22]

The calculated $1\pi_g \rightarrow k\sigma_u$ and $k\delta_u$ excitation series are given in Table 4.8, where they are compared with quantum defect estimates and experimental values. The calculated excitation series and oscillator strengths are virtually identical with

those of Gerwer at al despite the difference in basis sets.

The corresponding contributions to the $(1\pi_g^{-1})X\,^2\Pi_g$ photoionization cross section, obtained using the 6 point fitting method are presented in Figure 4.14. The $k\sigma_u$ contribution is of similar magnitude and form to that obtained by Gerwer et al and is similar to the $2\pi \rightarrow k\sigma$ contribution in NO (Figure 4.1) but less than twice as great.

The $k\pi_u$ contribution displays two separate maxima, the lower energy maximum being weaker and narrower than that at higher energy. The high energy maximum is similar to the corresponding $2\pi \rightarrow k\pi$ profile in NO, being twice as strong as the corresponding NO contribution and shifted by 5eV to higher photon energy even though the difference in ionization energies is only 2.9eV. The lower energy maximum is shifted by 3.5eV to higher photon energy, is of similar intensity to the corresponding maximum in NO but has widened, substantially smoothing the minimum between the two maxima which is a much more prominent feature of the $2\pi \rightarrow k\pi$ contribution in NO.

The $k\delta_u$ contribution consists of a gradual rise to a very broad maximum. This is very similar to, but slightly stronger than, the corresponding profile in the results of Gerwer at al. This profile differs considerably from the corresponding $2\pi \rightarrow k\delta$ profile in NO in lacking a low energy maximum. The single maximum present is slightly more than twice as great but much broader than

the $2\pi \rightarrow k\delta$ contribution in NO. It is also shifted to lower energy compared to the high maximum in the corresponding NO contribution.

The three contributions have been combined to yield the $(1\pi_g^{-1})X\,^2\Pi_g$ partial channel photoionization cross section, which is compared with the calculation of Gerwer et al and the available experimental data [20,23] in Figure 4.14. Clearly the present results are in much better agreement with the experimental data and show much more structure than the results of Gerwer et al. The partial cross section is, as expected in the light of the above discussion, rather different from the corresponding $(2\pi^{-1})X\,^1\Sigma^+$ partial channel photoionization cross section in NO. Both display two maxima, a narrow low energy maximum and a broad high energy maximum. However in the case of NO the narrow low energy maximum, arising from contributions on the $k\pi$ and $k\delta$ contributions, is stronger than the higher energy maximum whereas in the case of O_2 the low energy maximum arising from $k\pi_u$ contributions is weaker than the high energy maximum.

Two sets of experimental data are presented in Figure 4.14; the (e,2e) measurements of Brion et al [20] and the synchrotron measurements of Gustafsson [23]. The (e,2e) coincidence measurements show an unstructured maximum with some scatter, whereas the synchrotron measurements show a more structured maximum, consisting of a maximum followed by a plateau, in the same

position as the maximum in the coincidence measurements. This structured maximum is almost exactly reproduced, both in position and intensity by the present calculation.

Comparison of the present results with those of Gerwer et al shows that the improvement in the present results originates in the greater strength of the $1\pi_g \rightarrow k\delta_u$, and more particularly the $1\pi_g \rightarrow k\pi_u$, contributions near 25eV photon energy. In view of the similarity of the δ_u supplemental basis in both calculations it is indicated that the rather more flexible valence basis set employed in the construction of the ground state wavefunction is a significant factor in the increased contributions to the partial channel cross section.

These results illustrate the need for sufficiently flexible valence and continuum basis sets to be employed in this type of calculations. The excellent agreement with experiment obtained in the present case indicates that in the case of the $1\pi_g$ ionization of O_2 the separated channel static exchange approximation does not lead to any appreciable error in the calculated photoionization cross section.

4.7 Discussion

The results presented in this chapter for molecular oxygen have demonstrated the great importance of the employment of very flexible ground state and supplemental basis sets in the calculation of photoionization cross sections. The employment of such a basis set has been shown to lead to extremely good agreement between the calculated partial channel cross section of the outermost $1\pi_g$ orbital of O_2 and the corresponding experimental results. The basis set employed in the NO calculation covers the same exponent range as that employed in the O_2 calculation but, because of the absence of a centre of inversion in the NO molecule, a much larger pseudospectrum is obtained. In the investigation of the effect of variation of basis set on the calculated partial channel cross section it was found that the calculated $(2\pi^{-1})X\,^1\Sigma^+$ cross section profile was extremely sensitive to the presence, or otherwise, of supplemental basis functions on each atomic centre with exponents ($\xi = 0.1$) which classify these functions as valence rather than Rydberg in nature. For this reason the results reported here for NO, which are the final results of a series of calculations, include in the supplemental set several basis functions with high exponents.

Because of the similarity of the basis sets employed in the NO and O_2 calculations, it would be expected that the results obtained in the NO calculations, at least for the outermost 2π orbital, would be as good as those obtained for

the $1\pi_g$ orbital of O_2. This is not the case. While qualitative agreement is obtained for the $(2\pi^{-1})X\,^1\Sigma^+$ partial cross section there are quite large quantitative disagreements between the calculated and experimental photoionization cross section. This implies that the approximations used in the calculation are not as valid for NO as for O_2. As it has been shown that the total 1π photoionization cross section is an overestimate at low photoelectron kinetic energies the possibility of some channel coupling is indicated.

Because of the partially filled outer shell in NO, ionization from the 1π molecular orbital leads not only to distinct spin states of the ion but to different symmetry states, unlike ionization from the σ molecular orbitals. Photoionization cross sections computed for each of these individual states were found to be very similar once allowance was made for the different ionization energies and for the spatial and spin degeneracies, thus justifying the use of an average operator by Gerwer et al in their calculations on the corresponding $1\pi_u$ orbital in O_2.

It is found that the main features of the 2π and 1π photoionization cross sections may be explained in terms of transitions to atomic 3d pre-Rydberg orbitals. While almost equal contributions to the $(2\pi^{-1})X\,^1\Sigma^+$ partial channel cross section come from $k\pi$ and $k\delta$ contributions, the $k\pi$ contribution to the various $(1\pi^{-1})$ partial cannel cross sections is negligible.

Excellent agreement between theory and experiment is found for the $(5\sigma^{-1})b\,^3\Pi$ channel, with a strong resonance in the $k\sigma$ contribution. A similar but weaker resonance is found in the $(4\sigma^{-1})c\,^3\Pi$ partial channel and is assigned to contributions from the 6σ valence virtual orbital. The $2\pi \rightarrow k\sigma$ and $1\pi \rightarrow k\sigma$ contributions are very much weaker than the $5\sigma \rightarrow k\sigma$ contributions. This is presumably because the 5σ and 6σ orbitals are localised in the same region of space. Investigation of the photoionization of the 4σ molecular orbital has not proved to be as satisfactory as would have been expected from the results obtained for the outer valence orbitals, suggesting that the approximations employed may not be as satisfactory for the inner valence orbitals as for the outer valence orbitals. In particular the description of inner valence ionization by a Koopmans hole type state is known to be unsatisfactory. Furthermore, strong relaxation effects are expected for inner valence ionization and so the static-exchange approximation may not be valid particularly near the threshold. MSXα calculations suggest that the effects of nuclear motion may be important, an effect which has been ignored in these calculations. However good results obtained in many static exchange type calculations with the internuclear separation fixed at r_e indicate that the neglect of nuclear motion effects may not be as important for calculations employing this methodology as for MSXα type calculations.

The excellent results reported here obtained employing the static-exchange approximation and the Stieltjes-Tchebycheff imaging procedure are very en-

couraging. Possibly the most important result of these calculations has been the demonstration of the superiority of the results obtained using this method,as opposed to those obtained by the use of the MSXα method. The most striking demonstration of this superiority is the $(2\pi^{-1})X\,^1\Sigma^+$ partial channel photoionization cross section, for which the present results explain the main features while the MS-Xα results do not resemble the experimental results at all.

4.8 REFERENCES

1. P.W.Langhoff, N.Padial, G.Csanak, T.N.Rescigno and B.V.McKoy, *Int. J. Quant. Chem.*, **S14**, 285 (1980).

2. A.Gerwer, C.Asaro, B.V.McKoy, and P.W.Langhoff, *J. Chem. Phys.*, **72**, 713 (1980).

3. P.W.Langhoff, A.Gerwer, C.Asaro and B.V.Mckoy, *Int. J. Quant. Chem.*, **S13**, 645 (1979).

4. C.E.Brion and K.H.Tan, *J. Elect. Spectros & Rel Phenom.*, **23**, 1 (1981).

5. S.Southworth, C.M.Truesdale, P.H.Kobrin, D.W.Lindle, W.D.Brewer, and D.A.Shirley, *J. Chem. Phys.*, **76**, 143 (1982).

6. T.Gustafsson and J.Levinson, *Chem. Phys. Letts.*, **78**, 28 (1981).

7. T.H.Dunnings Jr., *J. Chem., Phys.*, **53**, 2823 (1970).

8. J.J. Delaney, I.H.Hillier,and V.R.Saunders, *J. Phys. B.* **15**, 1477 (1982).

9. S.Green, *Chem. Phys. Letts.*, **13**, 552 (1972).

10. H.Brion and M.Yamazaki, *J. Chem. Phys.*, **30**, 673 (1959).

11. E.Lindholm, *Arkiv für Fysik*, **40**, 97 (1969).

12. O.Edquist, E.Lindholm, L.E.Selin, H.Sjögren and L.Åsbrink, *Arkiv für Fysik*, **40**, 439 (1969).

13. M.Sasanuma, Y.Morioka, E.Ishiguro and M.Nakamura, *J. Chem. Phys.*, **60**, 327 (1974).

14. S.Wallace, D.Dill and J.L.Dehmer, *J. Chem. Phys.*, **76**, 1217 (1982).

15. O.Edqvist, L.Åsbrink and E.Lindholm, *Z. Naturforsch*, **26A**, 1407 (1971).

16. J.Lefebvre Brion, *Chem. Phys. Letts.*, **9**, p463 (1971).

17. P.W.Thulstrup, E.W.Thulstrup, A.Anderson, and Y.Öhrn, *H. Chem. Phys.*, **60**, 3975 (1974).

18. B.Narayana and W.C.Price, *J. Phys. B.*, **5**, 1784 (1972).

19. M.Sasanuma, Y.Morioka, E.Ishiguro and M.Nakamura, *J. Chem. Phys.*, **60**, 327 (1974).

20. C.E.Brion, K.H.Tan, M.J.van der Wiel and Ph.E.van der Leeuw, *J. Elect. Spect.*, **17**, 101 (1979).

21. P.E.Cade and A.C.Wahl, *At. Data Nucl. Data Tables*,**13**, 339 (1974).

22. E.Lindholm, *Arkiv für Fysik*,**40**, 117 (1969).

23. T.Gustafsson, *Chem. Phys. Letts.*,**75**, 505 (1098).

24. M.R.Herman, S.R. Langhoff and P.W. Langhoff, *Chem. Phys Letts.*,**109**, 150 (1984).

25. P.Morin, M.Y.Adam, P.Lablanquie, I.Nenner, M.J.Hubin Franksin and J.Delwache. *Proceedings of the 7th International Congress on VUV Physics*, Jerusalem (1983).

26. M.E.Smith, R.R.Lucchese, and V.McKoy, *J. Chem. Phys.*.79, 1360 (1983)

Table 4.1

Static-exchange potentials and multiplicity factors on NO [a,b]

Core Ionic State	$\Gamma \setminus i$	4σ	$1\pi^x$	$1\pi^y$	5σ	$2\pi^x$	$2\pi^y$	μ_Γ^c
$^1\Sigma^+$	$2\pi^y \rightarrow k\sigma$	1/1	1/1	1/1	1/1	0/0	0/0	1
	$\rightarrow k\pi^y$	1/1	1/1	1/1	1/1	0/0	0/0	1
	$\rightarrow k\sigma^{xy}$	1/1	1/1	1/1	1/1	0/0	0/0	2
$^{1,3}\Pi$	$5\sigma \rightarrow k\sigma(^2\Pi)$	1/1	1/1	1/1	½/−1	¼/¼	¼/¼	2
	$\rightarrow k\pi^y(^2\Sigma^+)$	1/1	1/1	1/1	½/−1	−¼/½	¾/½	1
	$\rightarrow k\pi^y(^2\Sigma^-)$	1/1	1/1	1/1	½/−1	¾/½	−¼/−½	1
	$\rightarrow k\pi^y(+2\Delta)$	1/1	1/1	1/1	½/−1	¼/−½	¼/½	2
$^{1,3}\Sigma^+$, $^{1,3}\Sigma^-$	$1\pi^y \rightarrow k\sigma(^2\Sigma^+)$	1/1	¾/0	¾/0	1/1	¼/¼	¼/¼	1
	$\rightarrow k\pi^y(^2\Pi)$	1/1	¾/0	¾/0	1/1	¼/¼	¼/¼	1
	$\rightarrow k\delta^{xy}(^2\Delta)$	1/1	¾/0	¾/0	1/1	¼/¼	¼/¼	2
$^{1,3}\Delta$	$1\pi^y \rightarrow k\sigma(^2\Delta)$	1/1	¾/0	¾/0	1/1	¼/¼	¼/¼	2
	$\rightarrow k\pi^y(^2\Pi)$	1/1	¾/3	¾/−1	1/1	¼/1	¼/0	2
	$\rightarrow k\delta^{xy}(^2\Sigma^+)$	1/1	¾/3	¾/−1	1/1	¼/1	¼/0	2
	$\rightarrow k\delta^{xy}(^2\Sigma^-)$	1/1	¾/3	¾/−1	1/1	¼/1	¼/0	2

[a] Values of the coefficients a_i^Γ/b_i^Γ occuring in equation (4.5).

[b] The $1\sigma - 3\sigma$ orbitals remain doubly occupied, hence $a_c^\Gamma = b_c^\Gamma = 1$.

[c] Multiplicity factors in equation (4.7).

Table 4.1

Static-exchange potentials and multiplicity factors on NO [a,b]

Core Ionic State	$\Gamma \setminus i$	4σ	$1\pi^x$	$1\pi^y$	5σ	$2\pi^x$	$2\pi^y$	μ_Γ^c
$^1\Sigma^+$	$2\pi^y \rightarrow k\sigma$	1/1	1/1	1/1	1/1	0/0	0/0	1
	$\rightarrow k\pi^y$	1/1	1/1	1/1	1/1	0/0	0/0	1
	$\rightarrow k\sigma^{2y}$	1/1	1/1	1/1	1/1	0/0	0/0	2
$^{1,3}\Pi$	$5\sigma \rightarrow k\sigma(^2\Pi)$	1/1	1/1	1/1	½/−1	¼/¼	¼/¼	2
	$\rightarrow k\pi^y(^2\Sigma^+)$	1/1	1/1	1/1	½/−1	−¼/½	¾/½	1
	$\rightarrow k\pi^y(^2\Sigma^-)$	1/1	1/1	1/1	½/−1	¾/¾	−¼/−½	1
	$\rightarrow k\pi^y(+2\Delta)$	1/1	1/1	1/1	½/−1	¼/−½	¼/½	2
$^{1,3}\Sigma^+$, $^{1,3}\Sigma^-$	$1\pi^y \rightarrow k\sigma(^2\Sigma^+)$	1/1	¾/0	¾/0	1/1	¼/¼	¼/¼	1
	$\rightarrow k\pi^y(^2\Pi)$	1/1	¾/0	¾/0	1/1	¼/¼	¼/¼	1
	$\rightarrow k\delta^{xy}(^2\Delta)$	1/1	¾/0	¾/0	1/1	¼/¼	¼/¼	2
$^{1,3}\Delta$	$1\pi^y \rightarrow k\sigma(^2\Delta)$	1/1	¾/0	¾/0	1/1	¼/¼	¼/¼	2
	$\rightarrow k\pi^y(^2\Pi)$	1/1	¾/3	¾/−1	1/1	¼/1	¼/0	2
	$\rightarrow k\delta^{xy}(^2\Sigma^+)$	1/1	¾/3	¾/−1	1/1	¼/1	¼/0	2
	$\rightarrow k\delta^{xy}(^2\Sigma^-)$	1/1	¾/3	¾/−1	1/1	¼/1	¼/0	2

[a] Values of the coefficients a_i^Γ/b_i^Γ occuring in equation (4.5).

[b] The $1\sigma - 3\sigma$ orbitals remain doubly occupied, hence $a_c^\Gamma = b_c^\Gamma = 1$.

[c] Multiplicity factors in equation (4.7).

Table 4.2.

Supplemental Gaussian basis functions used in NO static exchange calculation.

Location	Type	Number	Exponent range[a]
Nitrogen	s	3	1.2—0.12
	p	2	0.96—0.16
	d	3	0.44—0.13
Oxygen	s	3	1.7—0.15
	p	3	1.3—0.11
	d	3	0.44—0.13
Center of Mass	s	11	0.44—0.001
	p	11	0.44—0.001
	d	11	0.44—0.001

[a] A geometric series variation is employed in the indicated ranges, except that for nitrogen and oxygen, the functions close to those already present in the ground state basis are not included.

Table 4.3
Calculated 2π Static Exchange Spectrum in NO: IP = 9.27 eV ($X^1\Sigma^+$) [15]

Calculated values $\epsilon_i(eV)$	f_i	Quantum Defect Estimates[a] $\epsilon_i(eV)$	Experimental Values[b] $\epsilon_i(eV)$	Assignments
	$2\pi \rightarrow Ks\sigma$ $^2\Pi \rightarrow {}^2\Sigma^+$ $\delta = 0.98$			
5.58	0.004014	5.97	5.48	$2\pi \rightarrow 3s\sigma$
7.82	0.000001	7.79	7.78	$2\pi \rightarrow 4s\sigma$
8.45	0.000002	8.43	8.43	$2\pi \rightarrow 5s\sigma$
8.74	0.000002	8.73		$2\pi \rightarrow 6s\sigma$
8.96	0.000134	8.90		$2\pi \rightarrow 7s\sigma$
9.03	0.000253	9.00		$2\pi \rightarrow 8s\sigma$
9.22	0.000496			
	$2\pi \rightarrow Kp\sigma$ $^2\Pi \rightarrow 2\Sigma^+$ $\delta = 0.69$			
6.67	0.003862	6.72	6.61	$2\pi \rightarrow 3p\sigma$
8.03	0.000792	8.03	8.02	$2\pi \rightarrow 4p\sigma$
8.54	0.000280	8.54	8.53	$2\pi \rightarrow 5p\sigma$
8.79	0.000139	8.79		$2\pi \rightarrow 6p\sigma$
	$2\pi \rightarrow Kd\sigma$ $^2\Pi \rightarrow {}^2\Sigma^+$ $\delta = 0.21$			
7.60	0.001861	7.52	7.55	$2\pi \rightarrow 3d\sigma$
8.35	0.000787	8.32	8.32	$2\pi \rightarrow 4d\sigma$
8.69	0.000398	8.68	8.68	$2\pi \rightarrow 5d\sigma$
8.89	0.000319	8.86		$2\pi \rightarrow 6d\sigma$
	$2\pi \rightarrow Kp\pi$ $^2\Pi \rightarrow {}^2\Pi$ $\delta = 0.75$			
6.62	0.005555	6.56	6.49	$2\pi \rightarrow 3p\pi$
8.01	0.001212	7.97	7.97	$2\pi \rightarrow 4p\pi$
8.53	0.000465	8.51	8.51	$2\pi \rightarrow 5p\pi$
8.79	0.000237	8.77		$2\pi \rightarrow 6p\pi$
9.03	0.000463			
9.26	0.000086			
	$2\pi \rightarrow Kd\pi$ $^2\Pi \rightarrow {}^2\Pi$ $\delta = 0.0$			
7.82	0.000069	7.78	7.78	$2\pi \rightarrow 3d\pi$
8.45	0.000043	8.43	8.43	$2\pi \rightarrow 4d\pi$
8.74	0.000028	8.73		$2\pi \rightarrow 5d\pi$
8.92	0.000028	8.89		$2\pi \rightarrow 6d\pi$
	$2\pi \rightarrow Kd\delta$ $^2\Pi \rightarrow {}^2\Delta$ $\delta = 0.08$			
7.73	0.001705	7.67	7.69	$2\pi \rightarrow 3d\delta$
8.40	0.000885	8.38	8.39	$2\pi \rightarrow 4d\delta$
8.72	0.000490	8.71	8.71	$2\pi \rightarrow 5d\delta$
8.90	0.000389	8.88		$2\pi \rightarrow 6d\delta$
9.19	0.001035			

a) Values of the quantum defects obtained from Ref. 11

b) Experimental values obtained from Ref. 12

Table 4.4
Calculated 5σ Static Exchange Excitation Spectrum in NO IP = 16.56eV ($b^3\Pi$) [15]

Calculated Values ϵ_i(eV)	f_i(eV)	Quantum Defect Estimate[a] ϵ_i(eV)	Experimental Values[b] ϵ_i(eV)	Assignments
		$5\sigma \rightarrow ns\sigma$ $^2\Pi \rightarrow {}^2\Pi$ $\delta = 0.87$		
18.18	0.000878	18.26		$5\sigma \rightarrow 3s\sigma$
16.14	0.000348	16.08		$5\sigma \rightarrow 4s\sigma$
15.75	0.000188	15.72		$5\sigma \rightarrow 5s\sigma$
16.04	0.000110	16.02		$5\sigma \rightarrow 6s\sigma$
16.27	0.000006			
		$5\sigma \rightarrow np\sigma$ $^2\Pi \rightarrow {}^2\Pi$ $\delta = 0.67$		
13.97	0.061365	14.08	14.00 /strong	$5\sigma \rightarrow 3p\sigma$
15.28	0.021286	15.28	15.32	$5\sigma \rightarrow 4p\sigma$
15.83	0.009909	15.88	15.92	$5\sigma \rightarrow 5p\sigma$
16.08	0.005462	16.08		$5\sigma \rightarrow 6p\sigma$
16.32	0.012812			
		$5\sigma \rightarrow nd\sigma$ $^2\Pi \rightarrow {}^2\Pi$ $\delta = 0.21$		
14.84	0.000815	14.81		$5\sigma \rightarrow 3d\sigma$
15.66	0.000312	15.61		$5\sigma \rightarrow 4d\sigma$
15.90	0.000808	15.97		$5\sigma \rightarrow 5d\sigma$
16.10	0.000002	16.15		$5\sigma \rightarrow 6d\sigma$
16.51	0.000878			
		$5\sigma \rightarrow np\pi$ $^2\Pi \rightarrow {}^2\Sigma^+, {}^2\Sigma^-, {}^2\Delta$ $\delta = 0.7$		
14.05	0.004278			
15.95	0.004875	15.90	15.92 /strong	$5\sigma \rightarrow 3p\pi$
15.96	0.000879			
15.24	0.001880			
15.21	0.001875	15.21	15.28	$5\sigma \rightarrow 4p\pi$
15.32	0.000272			
15.24	0.000706			
15.32	0.000717	15.32	15.32	$5\sigma \rightarrow 5p\pi$
15.32	0.001468			
16.00	0.000462			
16.08	0.000462	16.08		$5\sigma \rightarrow 6p\pi$
16.00	0.000828			
		$5\sigma \rightarrow nd\pi$ $^2\Pi \rightarrow {}^2\Sigma^+, {}^2\Sigma^-, {}^2\Delta$ $\delta = 0.0$		
15.11	0.000067			
15.06	0.000061	15.06		$5\sigma \rightarrow 3d\pi$
15.06	0.000021			
15.74	0.000068			
15.72	0.000061	15.71		$5\sigma \rightarrow 4d\pi$
15.72	0.000018			
16.08	0.000068			
16.02	0.000061	16.02		$5\sigma \rightarrow 5d\pi$
16.05	0.000068			
16.21	0.000064			
16.21	0.000062	16.18		$5\sigma \rightarrow 6d\pi$
16.21	0.000068			
		$5\sigma \rightarrow np\sigma$ $^2\Pi \rightarrow {}^2\Pi(\rightarrow A^1\Pi)$ (IP=16.82eV) $\delta = 0.71$		
15.74	0.025868	15.72	15.64	$5\sigma \rightarrow 3p\sigma$
17.09	0.009844	17.06	17.06	$5\sigma \rightarrow 4p\sigma$
17.58	0.004128	17.58	17.58	$5\sigma \rightarrow 5p\sigma$
17.84	0.002256	17.88		$5\sigma \rightarrow 6p\sigma$
18.09	0.008116	17.98		$5\sigma \rightarrow 7p\sigma$
		$5\sigma \rightarrow np\pi$ $^2\Pi \rightarrow {}^2\Delta(\rightarrow A^1\Pi)$ $\delta = 0.78$		
15.72	0.004045	15.56	15.48	$5\sigma \rightarrow 3p\pi$
17.07	0.001268	17.01	17.01	$5\sigma \rightarrow 4p\pi$
17.58	0.000618	17.56	17.56	$5\sigma \rightarrow 5p\pi$
17.84	0.000346	17.82		$5\sigma \rightarrow 6p\pi$
18.08	0.000717	17.97		$5\sigma \rightarrow 7p\pi$

a) Quantum Defects from Ref. 11

b) Experimental Values from Ref. 12

Table 4.5
Calculated 1π static exchange excitation spectrum in NO IP = 17.337eV ($w^3\Delta$) [12,15]

Calculated Values $\epsilon_i(eV)$	f_i	Quantum Defect Estimates[11] $\epsilon_i(eV)$	Experimental Values[12] $\epsilon_i(eV)$	Assignments
		$1\pi \rightarrow ks\sigma$ $^2\Pi \rightarrow {}^2\Delta(\rightarrow {}^3\Delta)$ $\delta = 1.0$		
12.72	0.066818	13.94	13.82	$1\pi \rightarrow 2s\sigma$
15.80	0.001282	15.82	16.11	$1\pi \rightarrow 4s\sigma$
16.53	0.000492	16.48	16.46	$1\pi \rightarrow 5s\sigma$
16.82	0.000264	16.78		$1\pi \rightarrow 6s\sigma$
17.08	0.004141	16.96		$1\pi \rightarrow 7s\sigma$
		$1\pi \rightarrow kp\sigma$ $^2\Pi \rightarrow {}^2\Delta$ $\delta = 0.69$		
14.89	0.000080	14.78		$1\pi \rightarrow 3p\sigma$
16.14	0.000026	16.10		$1\pi \rightarrow 4p\sigma$
16.68	0.000011	16.60		$1\pi \rightarrow 5p\sigma$
16.87	0.000012	16.88		$1\pi \rightarrow 6p\sigma$
17.14	0.000266			
		$1\pi \rightarrow kd\sigma$ $^2\Pi \rightarrow {}^2\Delta$ $\delta = 0.21$		
15.68	0.0238666	15.58		$1\pi \rightarrow 3d\sigma$
16.42	0.000870	16.34		$1\pi \rightarrow 4d\sigma$
16.76	0.004824	16.74		$1\pi \rightarrow 5d\sigma$
16.96	0.002678	16.98		$1\pi \rightarrow 6d\sigma$
17.28	0.001678			
		$1\pi \rightarrow kp\pi$ $^2\Pi \rightarrow {}^2\Pi$ $\delta = 0.75$		
14.86	0.001021	15.54		$1\pi \rightarrow 3p\pi$
16.14	0.000331	16.04		$1\pi \rightarrow 4p\pi$
16.63	0.000148	16.58		$1\pi \rightarrow 5p\pi$
16.87	0.000084	16.84		$1\pi \rightarrow 6p\pi$
17.13	0.000218			
		$1\pi \rightarrow kd\pi$ $^2\Pi \rightarrow {}^2\Pi$ $\delta = 0.0$		
15.90	0.000454	15.82		$1\pi \rightarrow 3d\pi$
16.53	0.000238	16.48		$1\pi \rightarrow 4d\pi$
16.82	0.000184	16.79		$1\pi \rightarrow 5d\pi$
17.00	0.000127	16.96		$1\pi \rightarrow 6d\pi$
		$1\pi \rightarrow kd\delta$ $^2\Pi \rightarrow {}^2\Sigma^+, {}^2\Sigma^-$ $\delta = 0.06$		
15.56	0.025746	15.74		$1\pi \rightarrow 3d\delta$
16.46	0.014470	16.45		$1\pi \rightarrow 4d\delta$
16.78	0.008184	16.77		$1\pi \rightarrow 5d\delta$
16.96	0.006506	16.95		$1\pi \rightarrow 6d\delta$
17.26	0.018454			
	$1\pi \rightarrow ks\sigma$	$^2\Pi \rightarrow {}^2\Sigma^+(\rightarrow {}^3\Sigma^+)$ IP = 16.109eV $\delta = 1.0$		
12.57	0.030377	12.71	12.60	$1\pi \rightarrow 2s\sigma$
14.75	0.000571	14.60	14.72	$1\pi \rightarrow 4s\sigma$
15.37	0.000228	15.28		$1\pi \rightarrow 5s\sigma$
15.67	0.000123	15.56		$1\pi \rightarrow 6s\sigma$
15.88	0.001981	15.78		$1\pi \rightarrow 7s\sigma$
	$1\pi \rightarrow ks\sigma$	$^2\Pi \rightarrow {}^2\Sigma^-(\rightarrow {}^3\Sigma^-)$ $\delta = 1.0$ IP = 15.05eV		
14.43	0.034846	14.64	14.58	$1\pi \rightarrow 3s\sigma$
16.61	0.000648	16.58	17.08	$1\pi \rightarrow 4s\sigma$
17.24	0.000256	17.20	17.77	$1\pi \rightarrow 5s\sigma$
17.52	0.000138	17.50		$1\pi \rightarrow 6s\sigma$
17.74	0.002166	17.67		$1\pi \rightarrow 7s\sigma$
	$1\pi \rightarrow ks\sigma$	$^2\Pi \rightarrow {}^2\Sigma^-(\rightarrow {}^1\Sigma^-)$ $\delta = 1.0$ IP = 16.417eV		
14.80	0.035698	15.01		$1\pi \rightarrow 3s\sigma$
16.98	0.000657	16.90	16.98	$1\pi \rightarrow 4s\sigma$
17.61	0.000262	17.57		$1\pi \rightarrow 5s\sigma$
17.90	0.000140	17.87		$1\pi \rightarrow 6s\sigma$
18.11	0.002198	18.04		$1\pi \rightarrow 7s\sigma$
	$1\pi \rightarrow ks\sigma$	$^2\Pi \rightarrow {}^2\Delta(\rightarrow {}^1\Delta)$ $\delta = 1.0$ IP = 18.51eV		
14.89	0.072696	15.11	15.26	$1\pi \rightarrow 3s\sigma$
17.07	0.001552	17.00	17.14	$1\pi \rightarrow 4s\sigma$
17.70	0.000681	17.66		$1\pi \rightarrow 5s\sigma$
17.98	0.000286	17.97		$1\pi \rightarrow 6s\sigma$
18.20	0.004457	18.18		$1\pi \rightarrow 7s\sigma$

Table 4.6
Calculated 4σ Static Exchange Excitation Spectrum IP = 21.72eV (C $^3\Pi$) [15]

Calculated Values $\epsilon_i(eV)$	f_i	Quantum Defect Estimates[a] $\epsilon_i(eV)$	Experimental Values[b] $\epsilon_i(eV)$	Assignments
	$4\sigma \rightarrow 3s\sigma$ $^2\Pi \rightarrow {}^2\Pi$ $\delta = 0.97$			
18.20	0.000647	18.42	18.36[c]	$4\sigma \rightarrow 3s\sigma$
20.29	0.002188	20.22		$4\sigma \rightarrow 4s\sigma$
20.91	0.001128	20.90		$4\sigma \rightarrow 5s\sigma$
21.20	0.000627	21.19		$4\sigma \rightarrow 6s\sigma$
21.42	0.000388			
	$4\sigma \rightarrow 3p\sigma$ $^2\Pi \rightarrow {}^2\Pi$ $\delta = 0.68$			
19.27	0.000082	19.17	19.10	$4\sigma \rightarrow 3p\sigma$
20.54	0.000088	20.47	20.48	$4\sigma \rightarrow 4p\sigma$
21.02	0.000026	20.98	20.97	$4\sigma \rightarrow 5p\sigma$
21.26	0.000018	21.24		$4\sigma \rightarrow 6p\sigma$
21.52	0.000110			
	$4\sigma \rightarrow 3d\sigma$ $^2\Pi \rightarrow {}^2\Pi$ $\delta = 0.21$			
20.07	0.003652	19.97	20.00	$4\sigma \rightarrow 3d\sigma$
20.81	0.001812	20.77	20.78	$4\sigma \rightarrow 4d\sigma$
21.14	0.001029	21.13		$4\sigma \rightarrow 5d\sigma$
21.34	0.001299	21.31		$4\sigma \rightarrow 6d\sigma$
21.66	0.003896			
	$4\sigma \rightarrow 3p\pi$ $^2\Pi \rightarrow {}^2\Delta$ $\delta = 0.75$			
19.14	0.000066	19.08	18.96	$4\sigma \rightarrow 3p\pi$
20.48	0.000011	20.48	20.48	$4\sigma \rightarrow 4p\pi$
20.99	0.000004	20.97	20.97	$4\sigma \rightarrow 5p\pi$
21.24	0.000002	21.23		$4\sigma \rightarrow 6p\pi$
21.49	0.000001			
	$4\sigma \rightarrow 3d\pi$ $^2\Pi \rightarrow {}^2\Delta$ $\delta = 0.0$			
20.26	0.000360	20.21	20.21	$4\sigma \rightarrow 3d\pi$
20.89	0.000468	20.87	20.86	$4\sigma \rightarrow 4d\pi$
21.18	0.000261	21.19	21.16	$4\sigma \rightarrow 5d\pi$
21.37	0.000248	21.34	21.33	$4\sigma \rightarrow 6d\pi$
21.70	0.000774		21.44	

a) Values of the quantum defect from Ref.11
b) Experimental excitation energies from Ref.19
c) Single value given in Ref.12

Table 4.7

Supplemental Gaussian basis functions used in O_2 static exchange calculations.

Symmetry	Location	Type	Number	Exponent Range[a]
δ_u	0/0	d	9	0.53—0.005
σ_u/π_u	0/0	s	2	0.52—0.16
	0/0	p	2	0.39—0.12
	0/0	d	3	0.44—0.13
	c.m.	p	11	0.44—0.001

[a] A geometric-series variation is employed in the indicated ranges.

Table 4.8

Calculated $1\pi_g$ Excitation Spectrum in O_2 IP = 12.07eV

Calculated Values $\epsilon_i(eV)$	f_i	Quantum Defect Estimates[a] $\epsilon_i(eV)$	Experimenatel Values[b] $\epsilon_i(eV)$	Assignments
		$(1\pi_g)^3\Sigma_g^- \rightarrow (np\sigma_u)^3\Pi_u$		
8.55	0.00000	8.45		$1\pi_g \rightarrow 3p\sigma_u$
10.16	0.00844	10.50	9.97 /strong	$1\pi_g \rightarrow 4p\sigma_u$
11.00	0.00555	11.19	10.98	$1\pi_g \rightarrow 5p\sigma_u$
11.41	0.00288	11.51	11.36	$1\pi_g \rightarrow 6p\sigma_u$
11.63	0.00189	11.68	11.54	$1\pi_g \rightarrow 7p\sigma_u$
11.92	0.00483			
		$(1\pi_g)^3\Sigma_g^- \rightarrow (np\pi_u)^3\Sigma_u^-$		
9.42	0.00270	9.54	9.31/weak	$1\pi_g \rightarrow 3p\pi_u$
10.82	0.00076	10.84	10.46	$1\pi_g \rightarrow 4p\pi_u$
11.33	0.00032	11.34	11.36	$1\pi_g \rightarrow 5p\pi_u$
11.59	0.00017	11.59	11.54	$1\pi_g \rightarrow 6p\pi_u$
11.83	0.00034	11.73	11.62	
		$(1\pi_g)^3\Sigma_g^- \rightarrow (nf\delta_u)^3\Pi_u$		
11.22	0.00015	10.55		$1\pi_g \rightarrow 3f\delta_u$
11.63	0.00032	11.63		$1\pi_g \rightarrow 4f\delta_u$

a) Quantum Defects from Ref.11

b) Experimental Values from Ref. 22

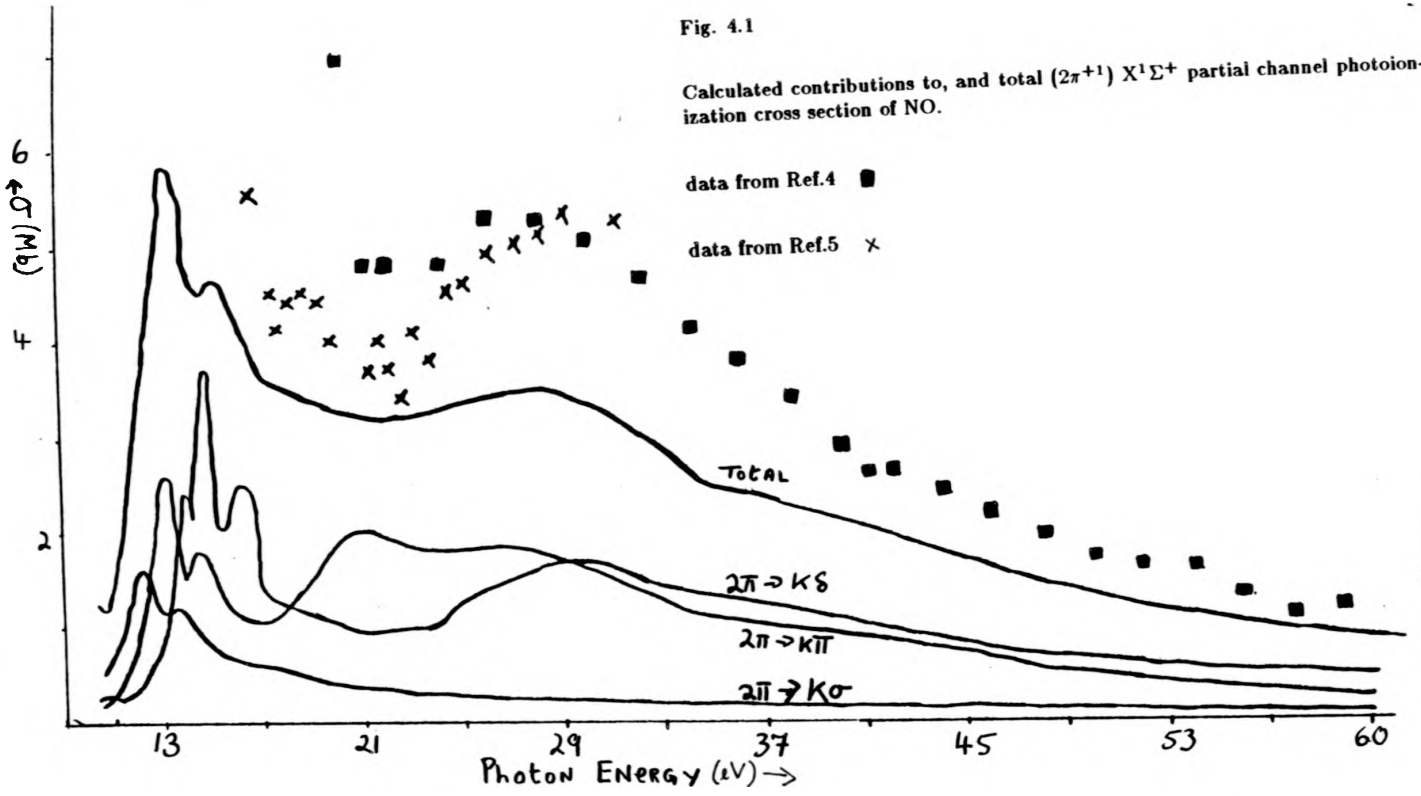

Fig. 4.1

Calculated contributions to, and total ($2\pi^{+1}$) $X^1\Sigma^+$ partial channel photoionization cross section of NO.

Fig. 4.2

Calculated 9, 6 and 4 point fits to the $(2\pi^{-1})X^1\Sigma^+$ partial channel photoionization cross section of NO.

data from Ref.4 ●

data from Ref.5 ⊥

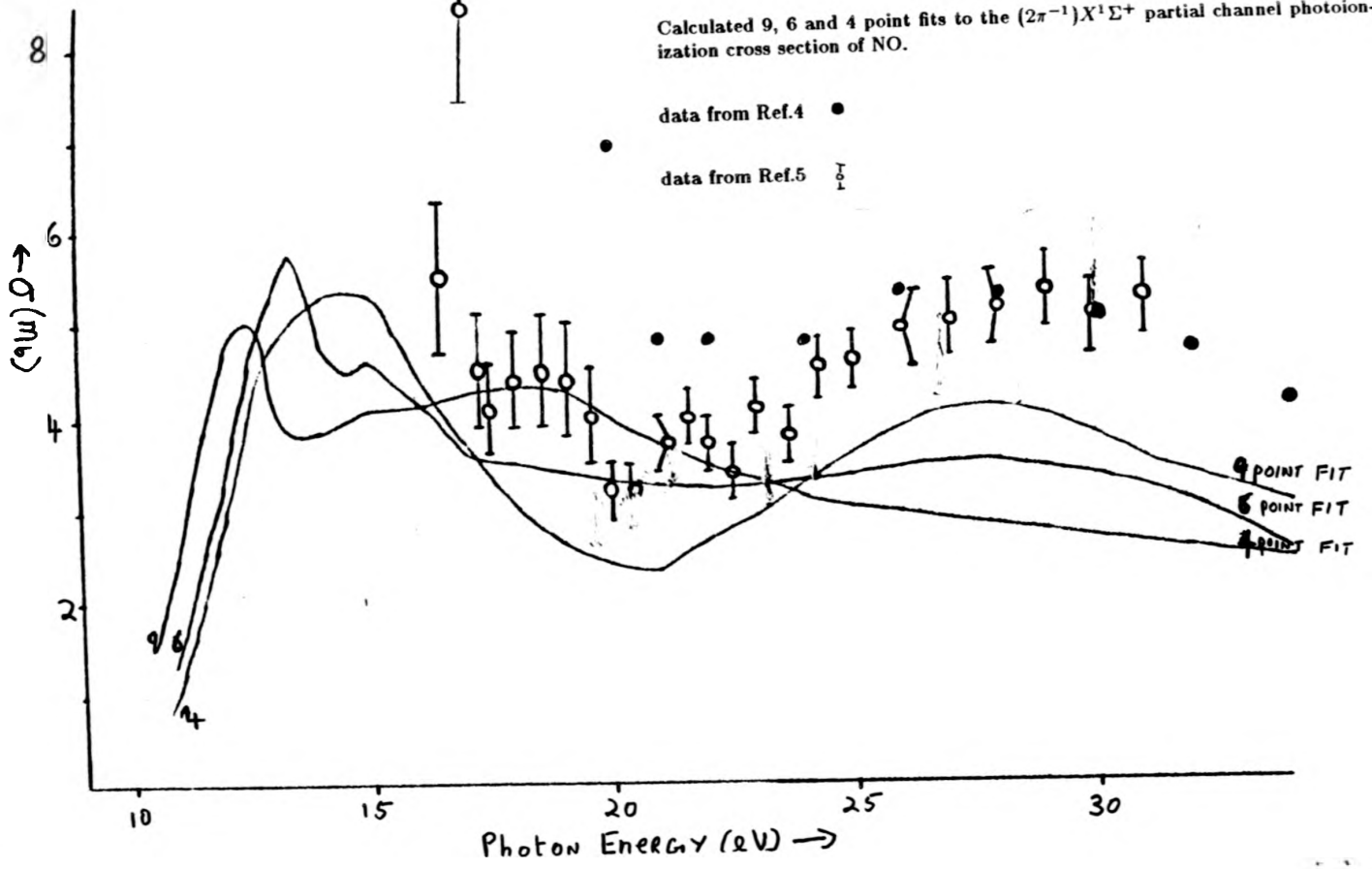

Fig. 4.3

Calculated contributions to the $(5\sigma^{-1})b^3\Pi$ partial channel cross section of NO.

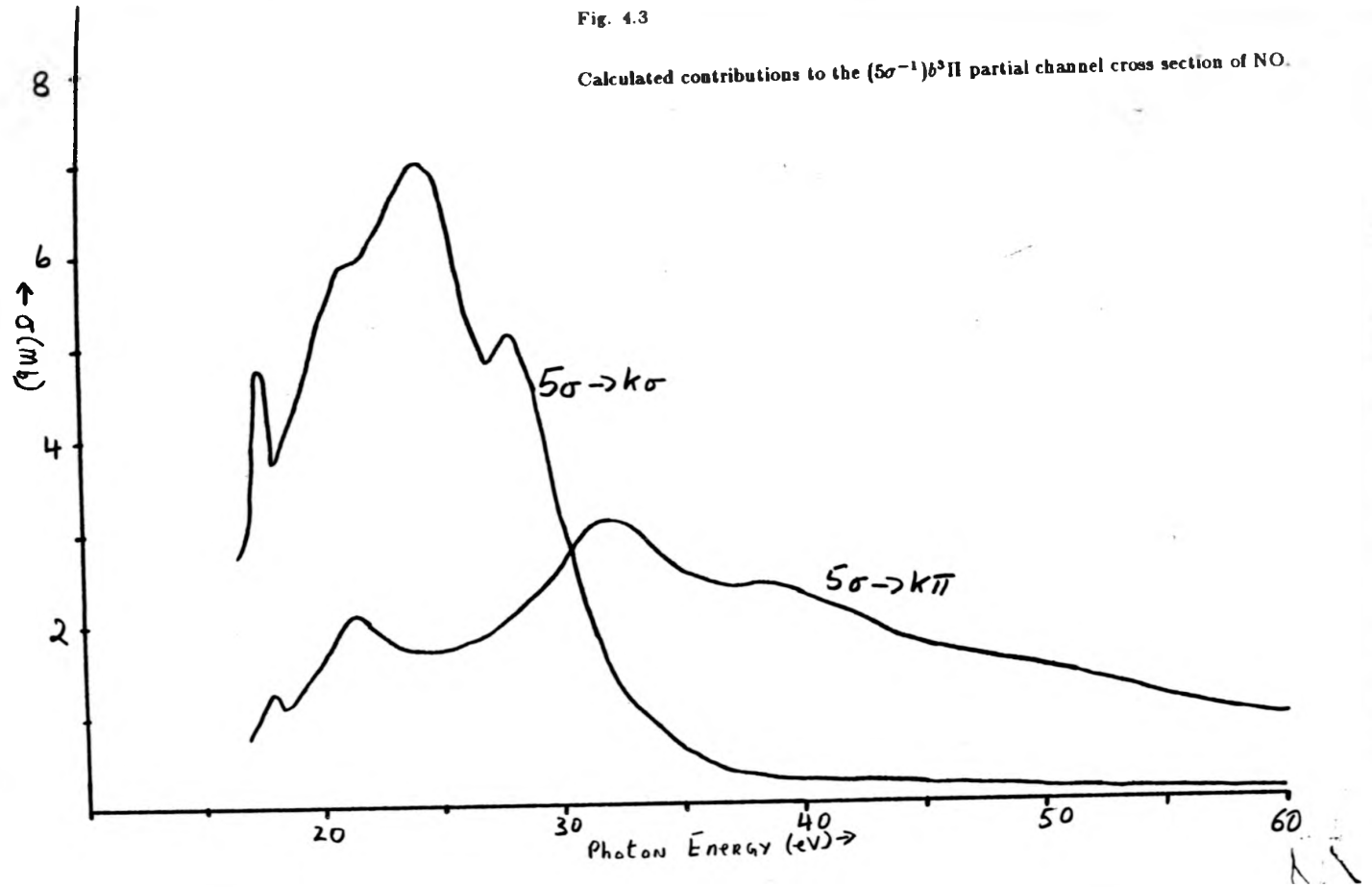

Fig. 4.4

Calculated $(5\sigma^{-1})b^3\Pi$ and $(5\sigma^{-1})*{}^1\Pi$ partial channel cross sections of NO.

data from Ref.5 ⊥

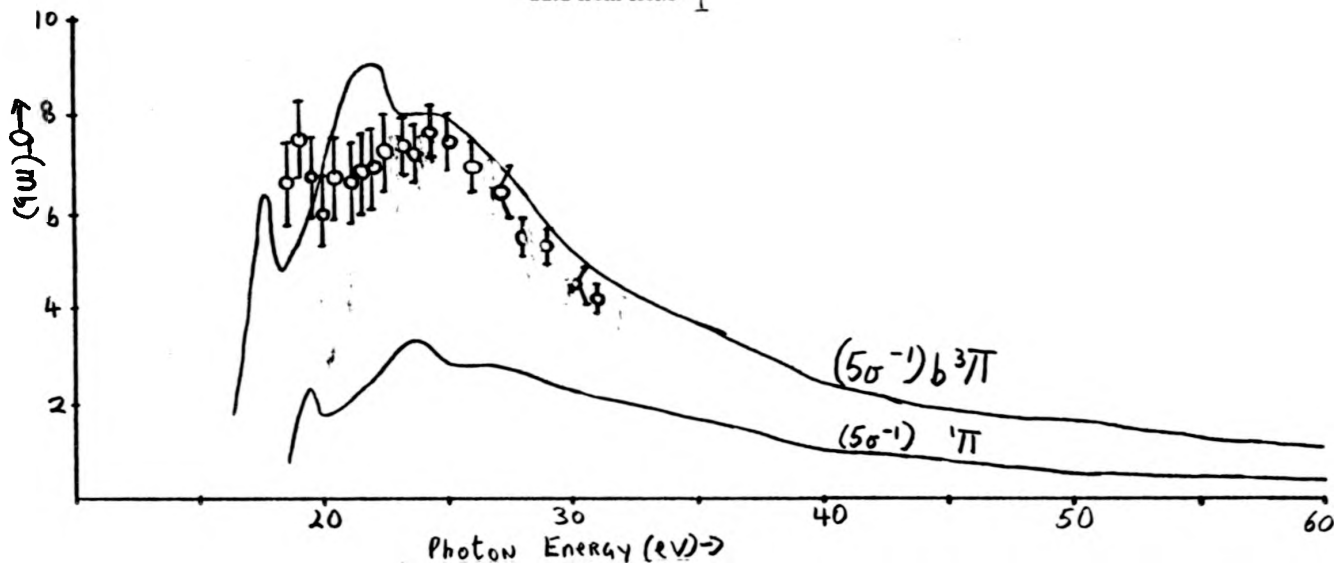

Fig. 1.6.

Calculated contributions to and total (10^{-18} cm^2) partial channel photoionization cross section of HCl

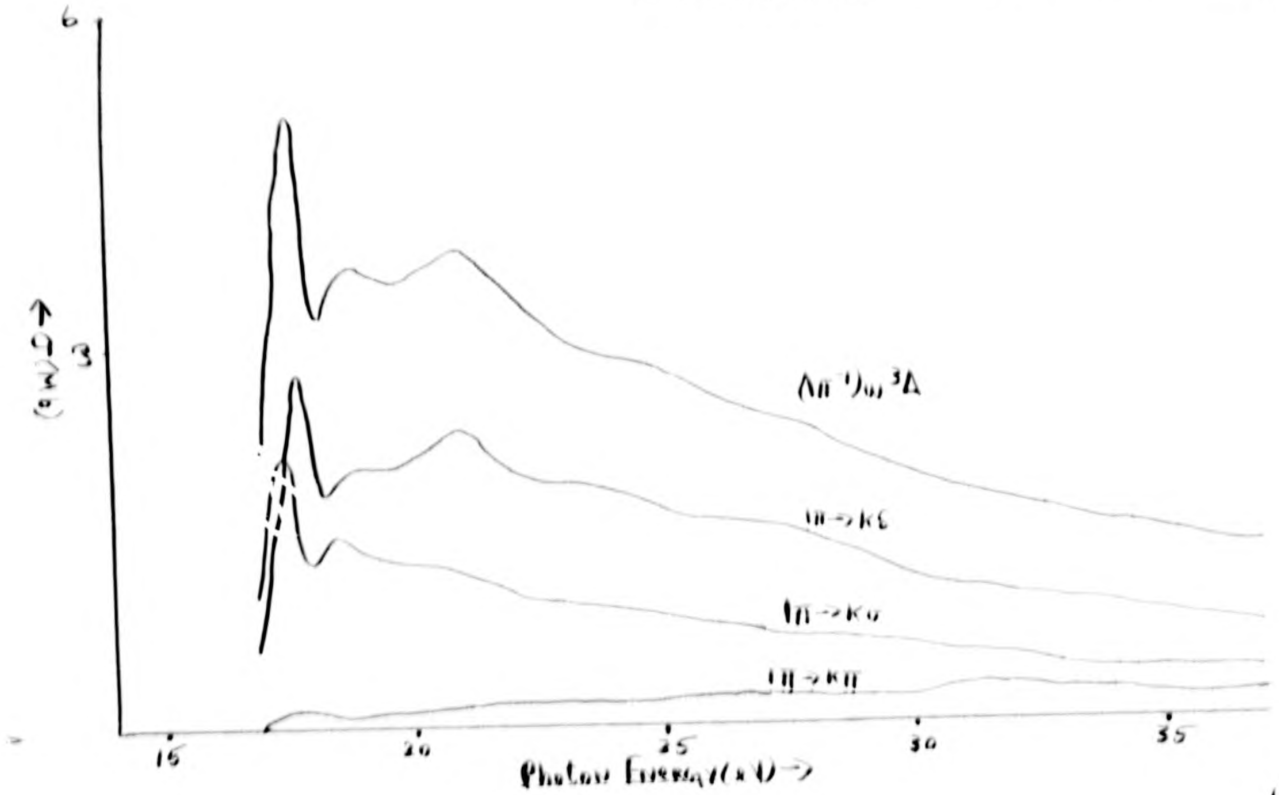

Fig. 4.5

Calculated contributions to, and total $(1\pi^{-1})w^3\Delta$ partial channel photoionization cross section of NO.

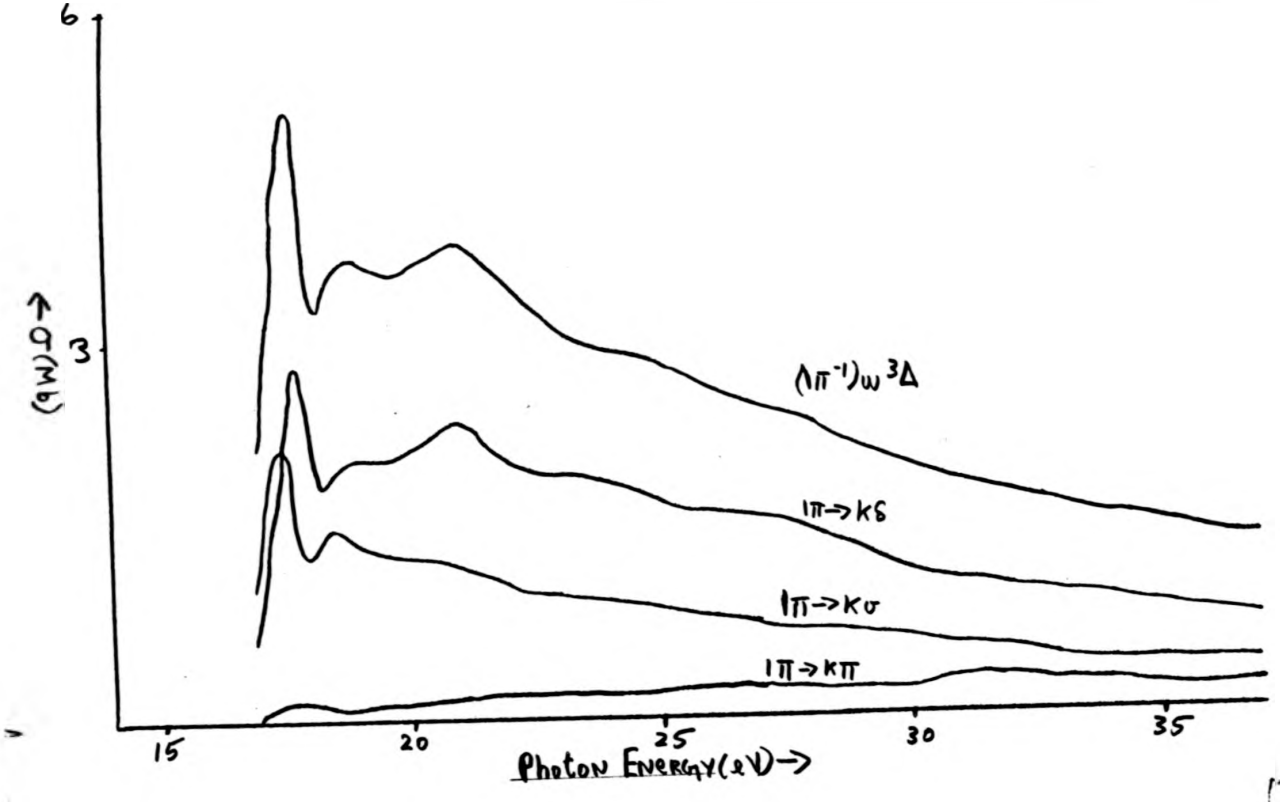

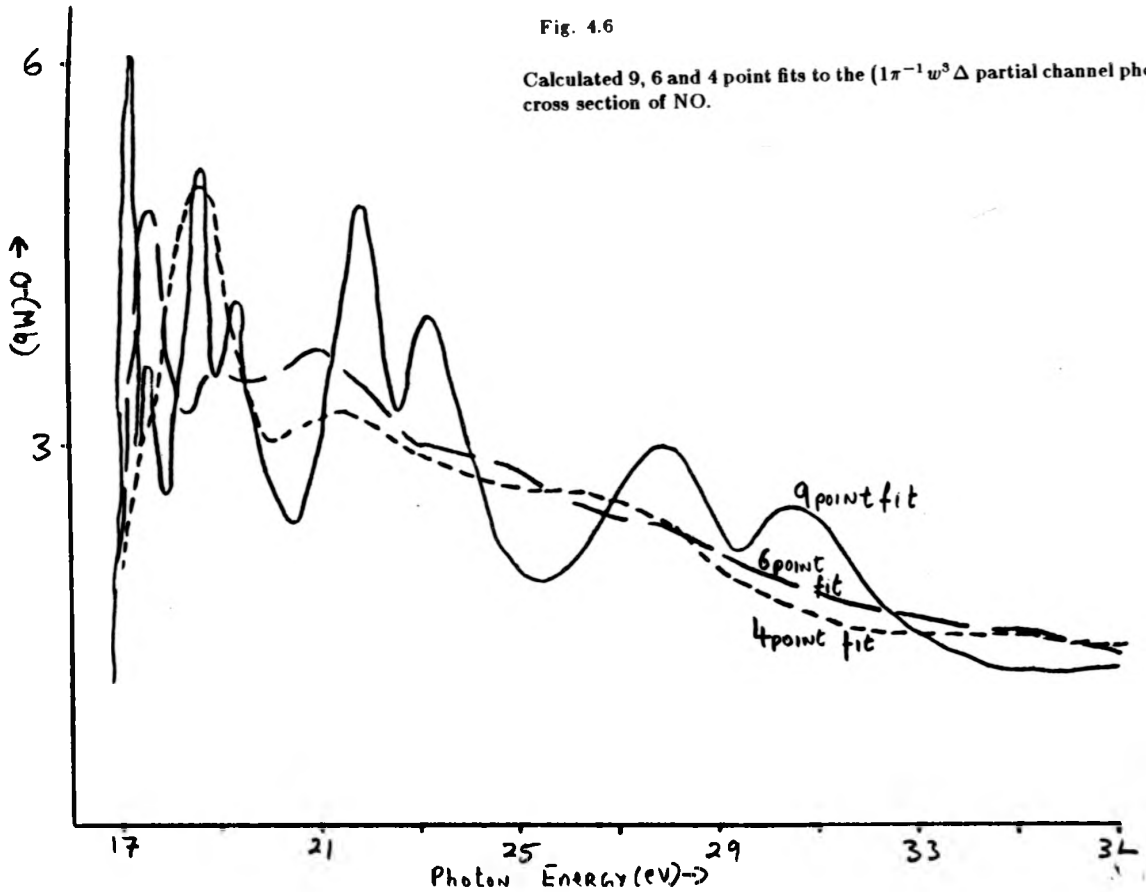

Fig. 4.6

Calculated 9, 6 and 4 point fits to the $(1\pi^{-1}w^3\Delta$ partial channel photoionization cross section of NO.

Fig. 4.7

Calculated partial channel photoionization cross sections of all ions produced by ionization from the 1π orbital of NO.

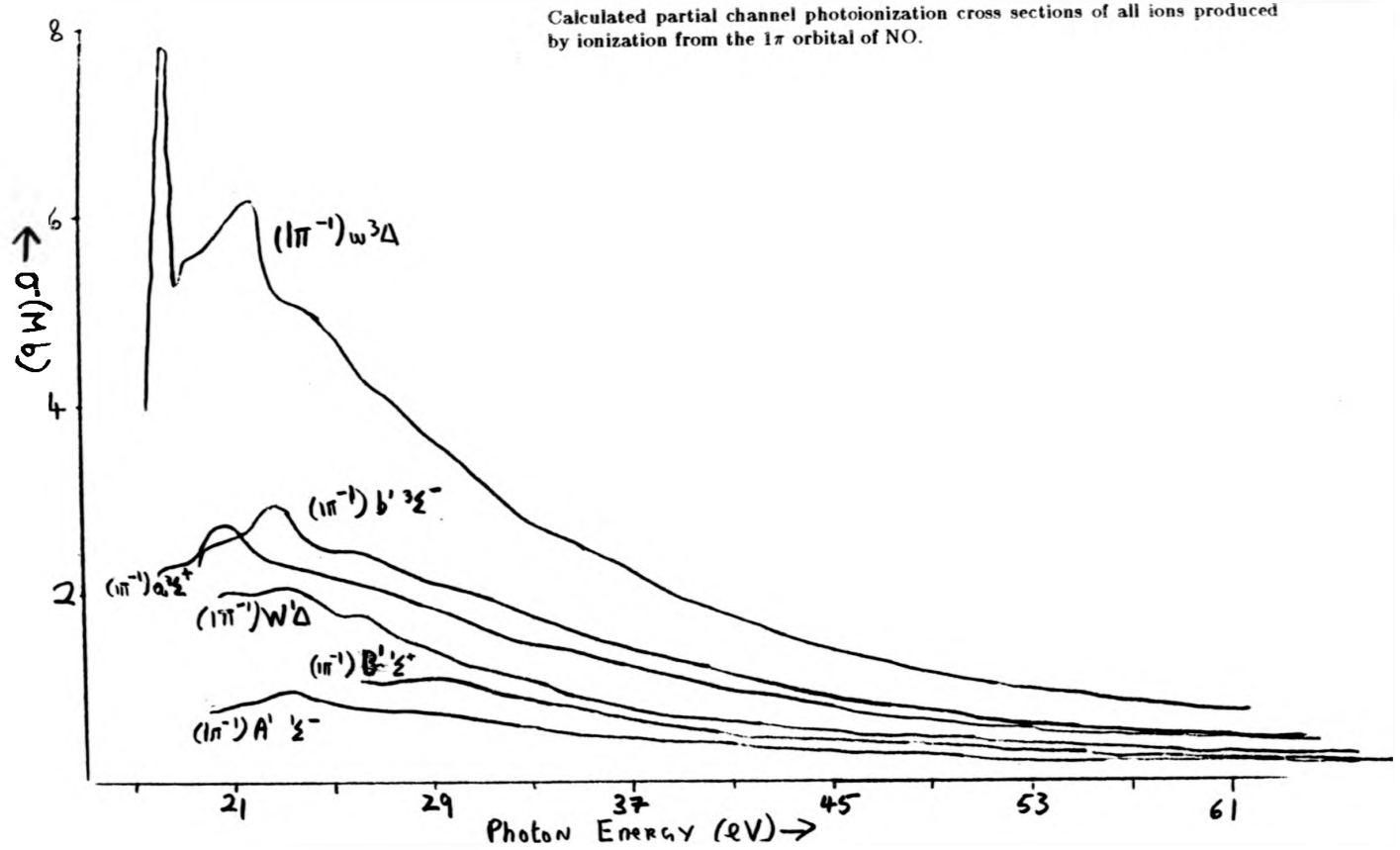

Fig. 4.8

Calculated total photoionizationcross section for ionization from the 1π orbital of NO.

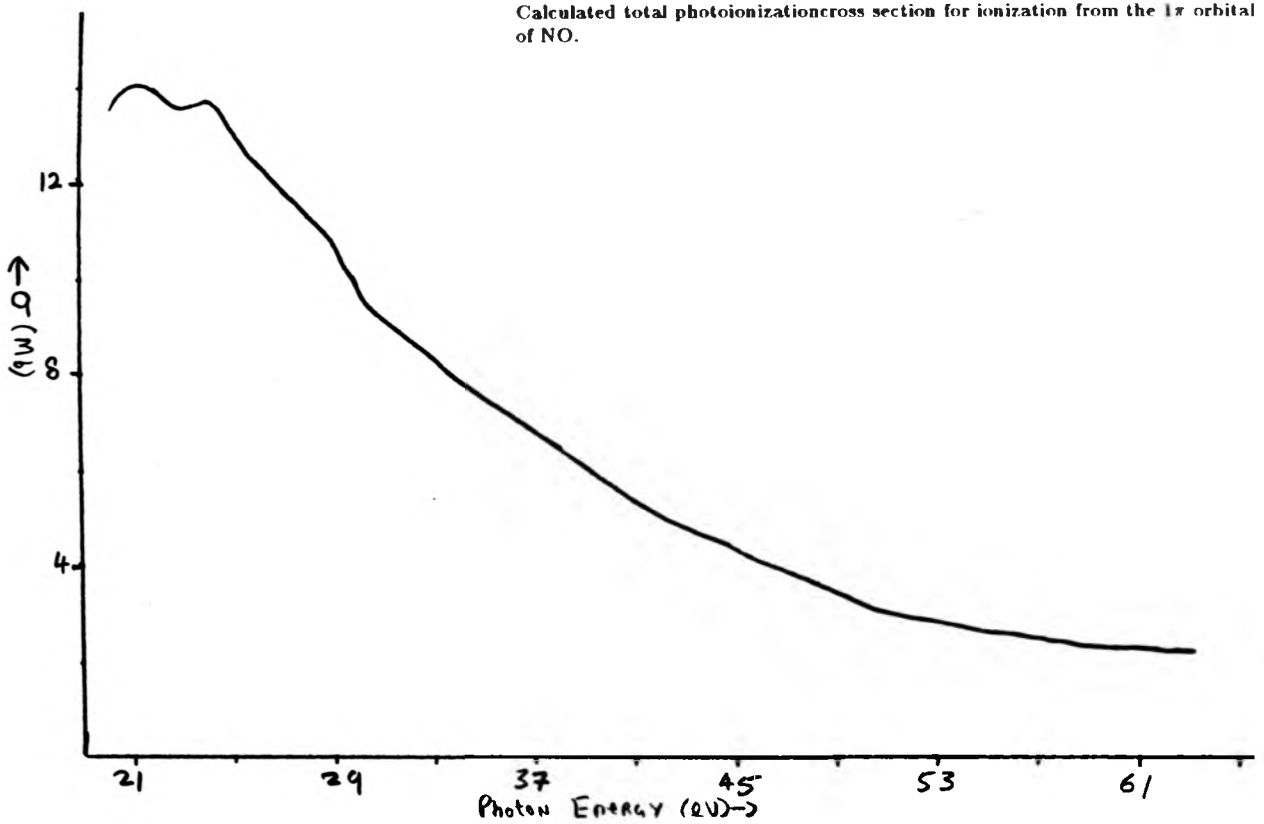

Fig. 4.9

Calculated photoionization cross section for all ionic states of NO with ionization energies between 14 and 20eV.

data from Ref.4 •

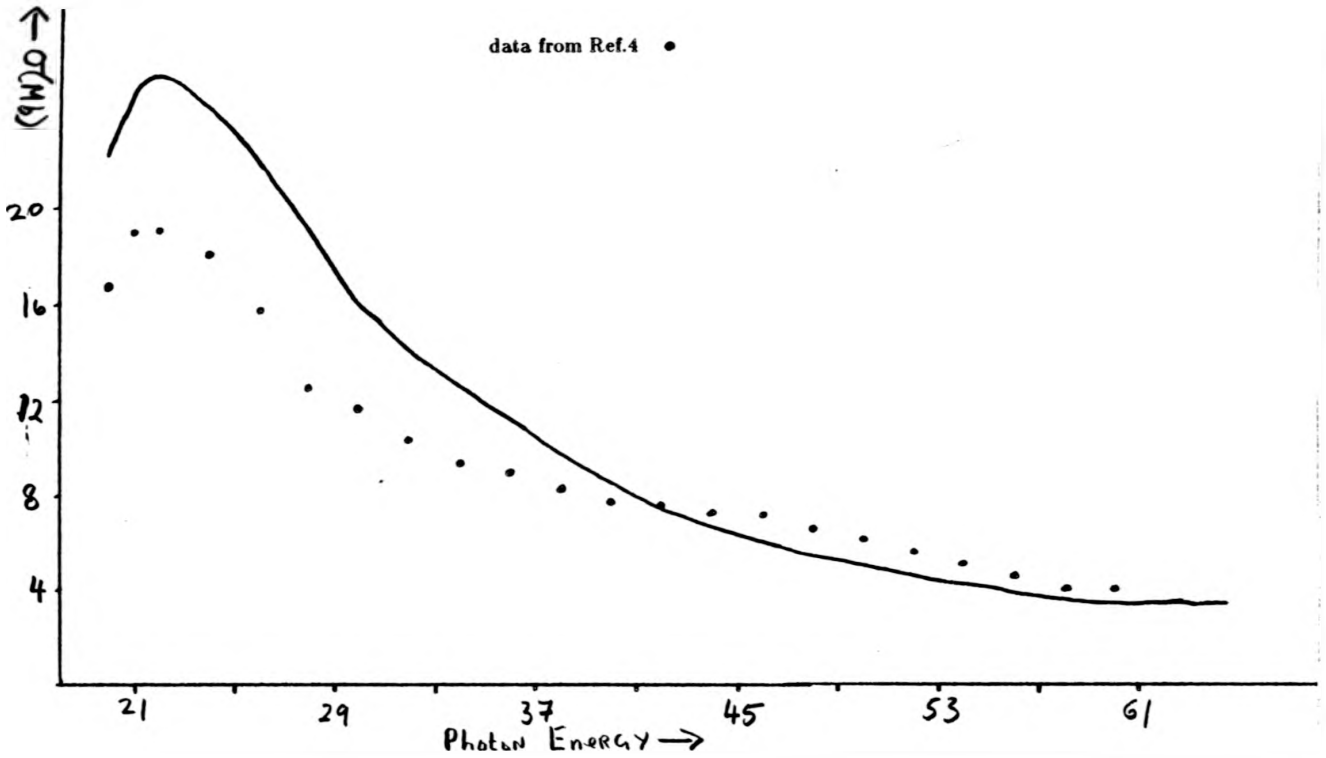

Fig. 4.10

Calculated contributions to, and $(4\sigma^{-1})c^3\Pi$ partial channel photoionization cross section of NO.

data from Ref.6 ■

data from Ref.5 ⊥

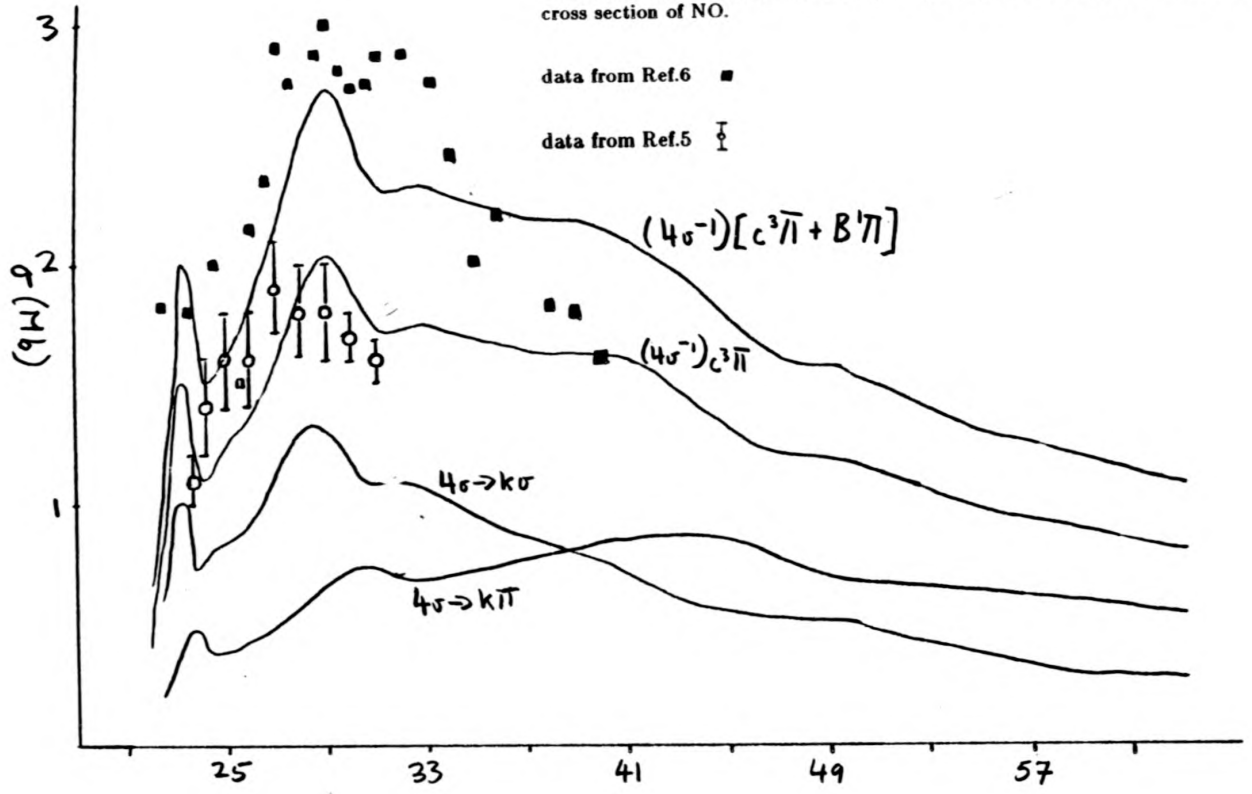

Fig. 4.11

Calculated photoionization cross sections for production of ionic states of NO^+ with ionization energies in the range 21-25 eV, obtained by summation of the calculated $(4\sigma^{-1})c^3\Pi$, $(4\sigma^{-1})B^1\Pi$ and $(1\pi^{-1})B'^1\Sigma^+$ partial channel photoionization cross sections.

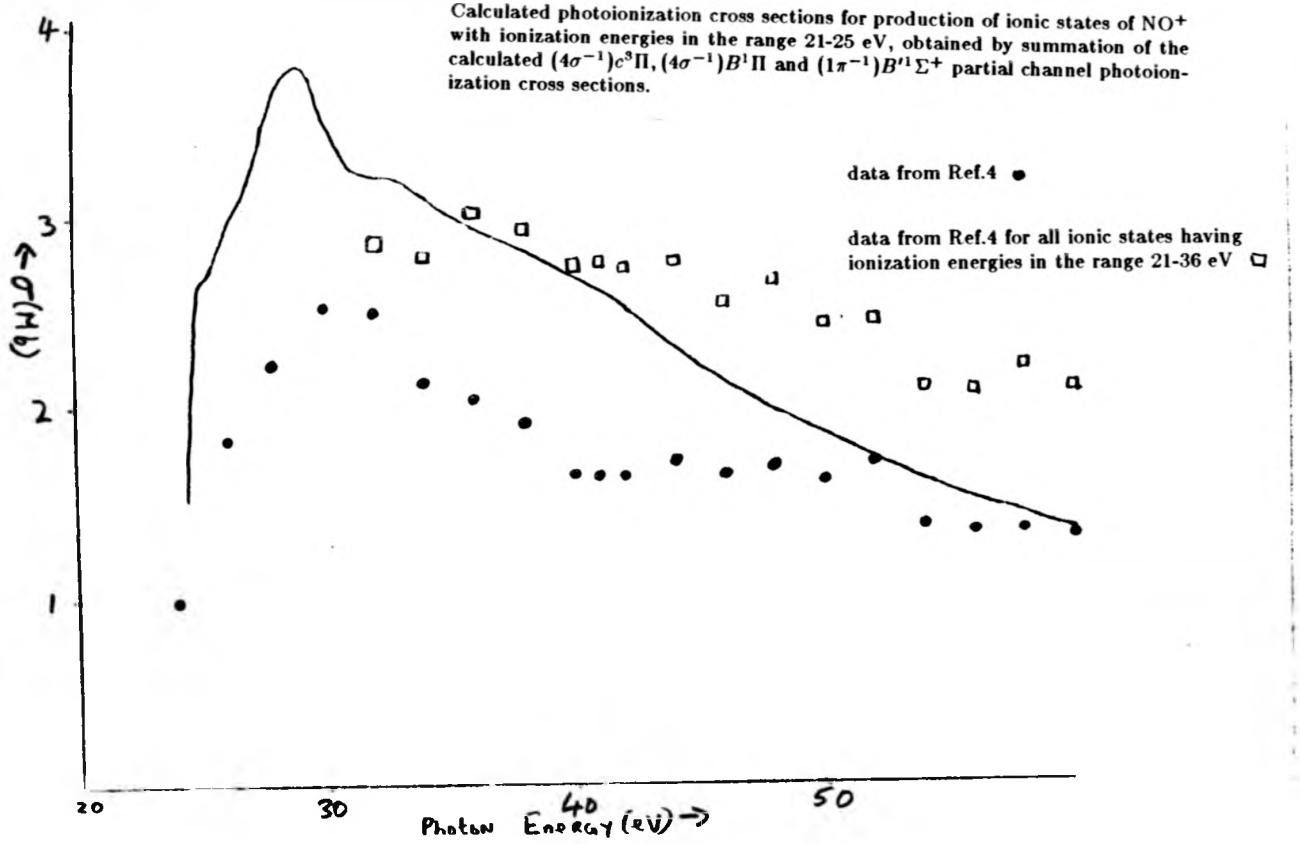

Fig. 4.12

Calculated partial channel photoionization cross section for production of ionic states of NO^+ with an IP of 23.3eV.

data from Ref.6 ■

values obtained from Refs.4 and 5 as detailed in section 4.3.3 o

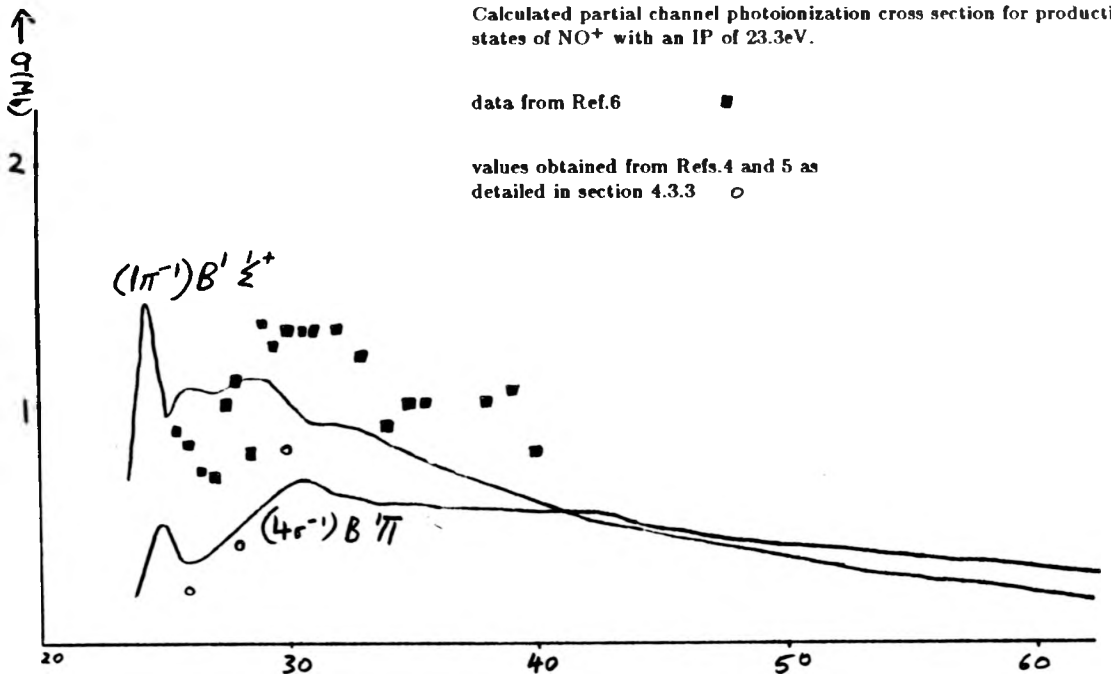

Fig. 4.13

Calculated valence shell photoionization cross section in NO.

data from Ref.4 •

data from Ref.4 with 3σ contributions removed □

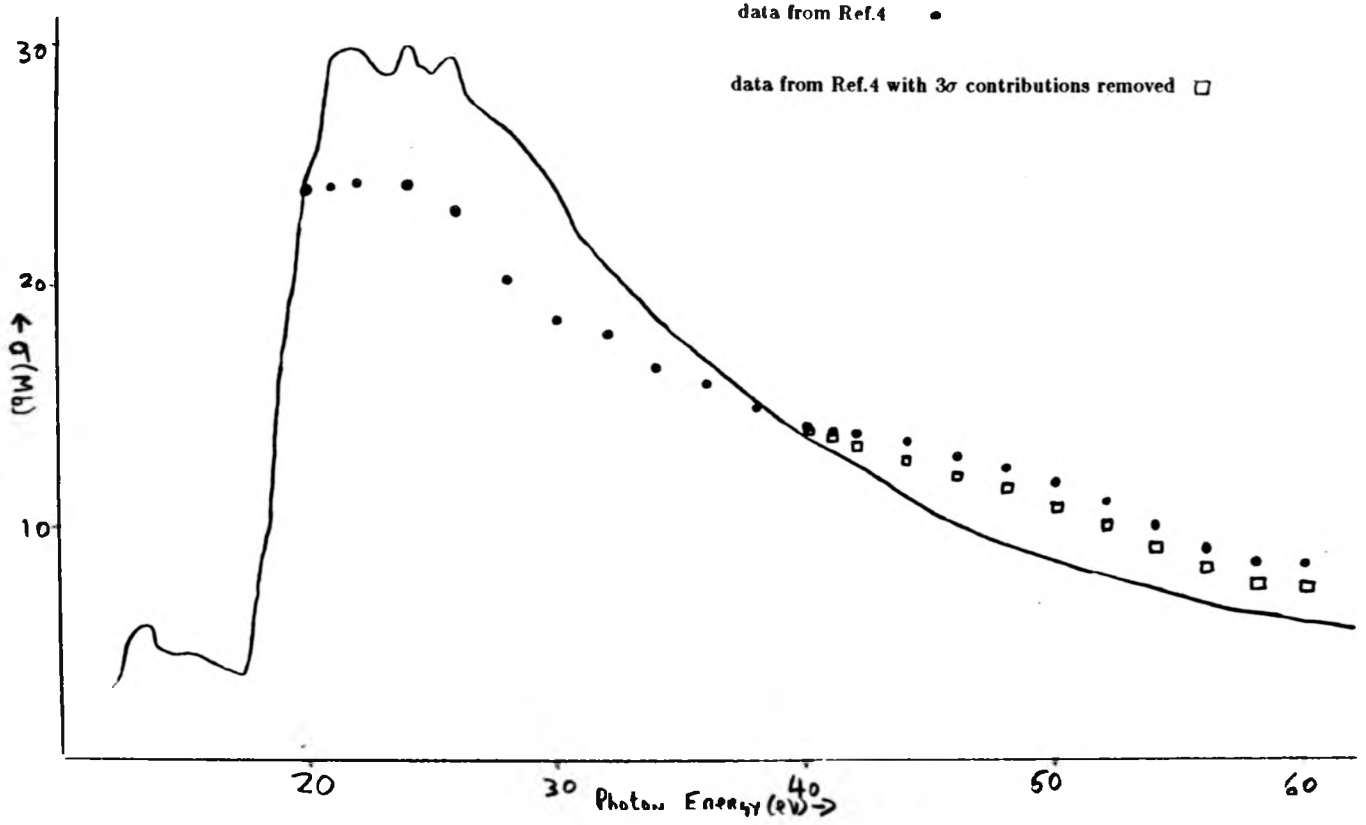

Fig. 4.14

Calculated contributions to, and $(1\pi_g^{-1})X^2\Pi_g$ partial channel photoionization cross section of NO.

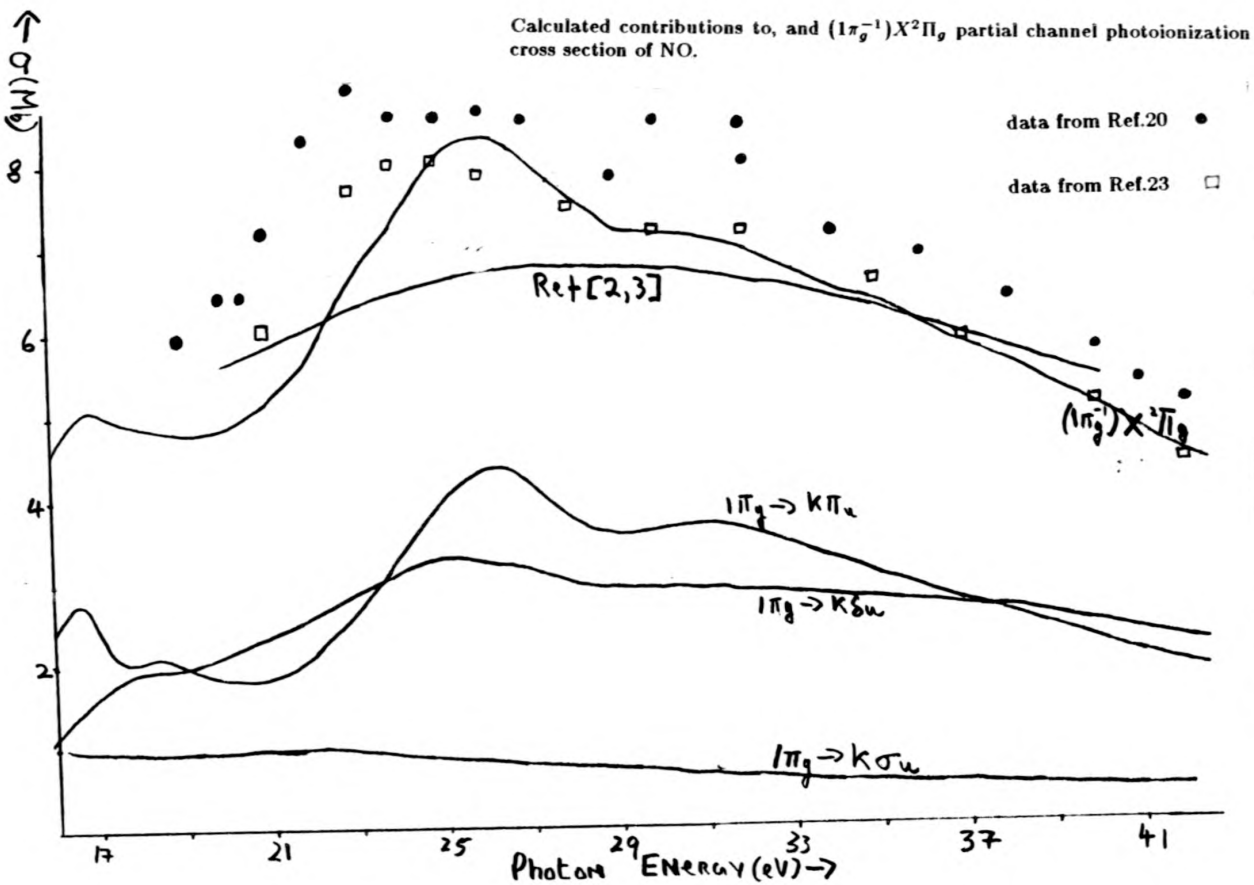

Chapter 5

The Calculation of the Partial Photoionization Cross Sections of Closed Shell Polyatomic Systems

In this chapter the results of a series of calculations on progressively larger polyatomic systems are reported. These comprise water, acetylene, and ni-

trous oxide. Comparison of the results of the first two molecules with subsequently published results clearly show the importance of employing a good quality supplemental basis set in the construction of the pseudospectra used in the Tchebycheff imaging procedure. The basis set employed in the nitrous oxide calculations, having been selected with the above results as a guide, is considered to be the best possible within the approximations used.

The results obtained for the outer valence orbitals indicate that the static exchange approximation leads to good results where the ionic state may be described by a single particle hole configuration, and where autoionization effects are not important. This calculation should encourage the application of these methods to large molecular systems and to those containing second row atoms.

A. H_2O Calculations

5.1 Introduction

The physical and chemical properties of the water molecule, being vital to life are topics of perennial scientific interest. A large amount of data concerning this molecule has recently become available [1-4]. Attempts have been made

to calculate the variation in intensity of the various photoelectron bands with photon energy, approximating the ejected electron with plane waves [5,6], plane wave orthogonalized to the occupied orbitals [5,6], and Coulomb waves [5,7]. Both the plane wave and the orthogonalized plane wave calculations yield results which are an order of magnitude too small, and while the results of the Coulomb wave calculation are in as good agreement with the experimental data near the threshold as the results presented here, at higher energies where the present results are in excellent agreement with experiment, the coulomb wave results are quite poor.

The availability of reliable experimental data and the failure of approximate methods to provide a good understanding of this data has stimulated attempts to apply more sophisticated theoretical techniques on this comparatively simple molecular system. The results of a TDHF calculation which employed a rather small basis set together with the Stieltjes-Tchebycheff imaging procedure have been reported by Williams and Langhoff [8]. This yielded surprisingly good results for the various partial cross sections, though yielding partial cross section components rather dissimilar to the present calculations, and yielded excitation series of much poorer quality than those reported here.

Subsequent to the publication of the present results [48], the results of a similar calculation by Diercksen et al employing a larger basis set became avail-

able [9]. Because of the larger basis set employed, that calculation is of a higher quality than the present results and so throws light upon basis set effects in such a small system. It should be noted that Diercksen et al performed four separate calculations and that only one of these was finally considered to contain a satisfactory a_1 basis. Finally an investigation employing the $X\alpha$ method has been undertaken by Roche et al [10] which produced results very similar to those for the corresponding orbitals in the atomic oxygen.

5.2 Theoretical and Computational Details

The ground state wavefunction of water within the Hartree-Fock approximation is:

$$|1a_1^2 2a_1^2 1b_2^2 3a_1^2 1b_1^2| X\,^1A_1 \tag{5.1}$$

Such a wavefunction was constructed within the Hartree-Fock scheme employing the (9s5p/5s3p) Gaussian basis of Dunning [11] supplemented with a d polarization function on the oxygen nucleus, and the (4s/3s) basis of the same author on the hydrogen centres. At the ground state internuclear separation (R(O-H) = 1.8089au, (HOH) = 104.52°) [12] this yielded an energy of −76.033au, to be compared with an estimated Hartree-Fock limit of -76.066 ± 0.003au [13].

The separated channel approximation yields twelve distinct one electron

dipole allowed series corresponding to individual excitations of the four highest lying filled molecular orbitals. These series are designated

$$\begin{array}{lll} (2a_1^{-1}kb_1)^1B_1 & (2a_1^{-1}kb_2)^1B_2 & (2a_1^{-1}ka_1)^1A_1 \\ (1b_2^{-1}ka_2)^1B_1 & (1b_2^{-1}ka_1)^1B_2 & (1b_2^{-1}kb_2)^1A_1 \\ (3a_1^{-1}kb_1)^1B_1 & (3a_1^{-1}kb_2)^1B_2 & (3a_1^{-1}ka_1)^1A_1 \\ (1b_1^{-1}ka_1)^1B_1 & (1b_1^{-1}ka_2)^1B_2 & (1b_1^{-1}kb_1)^1A_1 \end{array} \tag{5.2}$$

For each of these cases the singly excited orbital ϕ_i^Γ, constructed employing the large supplemental basis given in Table 5.1, is obtained from solution of the one electron equation of form

$$(h - \epsilon_i^\Gamma) = 0 \tag{5.3a}$$

where

$$h = T + V + \sum_{i \neq \Gamma}(2J_i - K_i + J_\Gamma + K_\Gamma) \tag{5.3b}$$

From this operator it is clear that when ionizing from a given molecular orbital all excited orbitals, regardless of symmetry, are constructed over the same operator. This is not the case with molecules of higher symmetry and is a consequence of the absence of any degenerate irreducible representations from the C_{2v} point group.

The excited orbitals so produced yield the pseudospectra employed in the Tchebycheff procedure to give the results detailed in the next section.

5.3 Computational Results

5.3.1 $1b_1$ Excitation I.P. = 12.61eV X^2B_1 [14]

The static exchange excitation series presented in Table 5.2 divide naturally into several different series. For the $1b_1 \rightarrow ka_1$ excitations there is reasonable agreement between the static exchange results, quantum defect estimates, and experimental results [3] for low quantum numbers. The $1b_1 \rightarrow 3sa_1$, is found to be the strongest of the discrete $1b_1$ excitations, as in other calculations. The results of the static exchange calculation of Diercksen et al [9], are in much better agreement with the quantum defect estimates for high quantum numbers, reflecting the much larger basis set used, though not in such good agreement with the two experimental values as those presented here. The results of the time-dependent Hartree-Fock calculation of Williams and Langhoff are in much poorer agreement with the experimental values than either of the static exchange calculations, reflecting the use of a very small basis set without truly diffuse functions suitable for describing Rydberg states. The oscillator strength distributions of both static exchange calculations agree reasonably well and the comparatively high oscillator strength of the $1b_1 \rightarrow 3sa_1$ transition has led Diercksen et al [9] to suggest that this transition has some intravalence $4a_1$ character.

Two further a_1 excitation series are given, kpd_1 and kda_1. Both these series are shorter than those of Diercksen et al, because of the larger basis set used, and as with the ksa_1 series, the early members are in good agreement with the experimental and defect estimate values. No TDHF results were presented for these or any of the remaining $1b_1$ excitation series.

The remaining excitation series, kpb_1, kdb_1, and kda_2, behave similarly to the kpa_1 and kda_1 series: having a first member in good agreement with experiment, whereas the remaining members are not in such good agreement with the experimental or defect estimate values. All the series are shorter than those of Diercksen et al., which overall are of rather better quality.

The three contributions to the $1b_1$ partial cross section are presented in Figure 5.1, and the partial cross section is compared with the available experimental data in Figure 5.2. The kb_1 and ka_2 profiles are almost identical, a result confirmed by Diercksen et al, and just over half as strong as the ka_1 profile, a ratio which may be rationalised by regarding the $1b_1$ orbital as a pure oxygen $2p_x$ orbital, with transitions to $d_{x^2-y^2}$ and $d_{z^2}a_1$, da_2 and db_1 orbitals. However at low energies, all the components are slightly greater in magnitude than those of Diercksen et al. The static exchange results present an interesting contrast to the TDHF results [8], where the maximum in the ka_1 profile is approximately 10% greater and considerably more peaked than the present results. Owing to

the small basis set used in the TDHF calculation it was impossible to image the kb_1 and kb_2 components separately, but a sum was obtained. This sum is considerably larger than that obtained in either of the static exchange calculations, but cancels the rapid decline in the ka_1 component to produce a partial cross section virtually identical to the present results above 40eV.

Several different sets of experimental data are presented in Figure 5.2: the (e,2e) measurements of Tan et al [2], which extend to high energy; and three sets of synchrotron measurements which are inconsistent at low energies [1,4,49]. At high energies the (e,2e) data and the calculation agree almost exactly, while at lower energies, the calculated partial cross section is significantly greater than the experimental curve. It is interesting to note that while the calculated curve of Diercksen et al is greater than the (e,2e) measurements at all except one experimental point, the discrepancy at low energies is less than that of the present results, yielding rather better overall agreement with the (e,2e) measurements. The synchrotron radiation measurements of Truesdale et al [1] are in good agreement with the coincidence measurements [2] above 26eV, as are the results of Thorntom et al.

Below this energy, they fill a gap in the coincidence data between 18 and 22eV. Despite some scatter in the synchrotron measurements of Truesdale et al, there is general agreement with the (e,2e) measurements between 22 and 26eV.

However, the two low energy (e,2e) data points, which show the presence of a maximum in the $(1b_1^{-1})\,^2B_1$ partial cross section disagree with the low energy synchrotron measurements of Truesdale et al which show no such maximum, while the results of Thornton et al, although also showing a maximum, disagree with both (e,2e) data and the synchrotron data of Truesdale et al as to the form and magnitude of the partial cross section curve in this region. Finally the low energy synchrotron data of Dutit et al [4] is shown. This data is not in good agreement with any of the other measurements; but as these are not magic angle results, and since angular effects are large for this orbital [10], these results may be discounted.

Both static exchange calculations agree as to the position of the maximum while differing by approximately 12% as to its magnitude; and as the calculation of Diercksen et al employs a larger basis set, it represents the results of the static exchange method more accurately. The TDHF calculation of Langhoff and Williams [8] also shows a maximum, arising mainly from the ka_1 profile, but to somewhat lower energy. The results of an $X\alpha$ calculation are also available[10]. This shows a monotonic decline from threshold with no maximum, and is only in the most general agreement with experiment even at high energies.

5.3.2 $3a_1$ Excitation I.P. = 14.73eV $^2A_1$[14]

The static exchange excitation series for this orbital are given in Table 5.3. These series, as in the case of the $1b_1$ orbital, are shorter than those of Diercksen et al [9], and while the early members of each series are in general agreement with the experiment and the defect estimates, later members are not in such good agreement as those of Diercksen et al.

Most of these series are clearly Rydberg in nature although Diercksen et al have assigned some intravalence character to the $3a_1 \rightarrow 3sa_1$ transition on the basis of its high oscillator strength. The only other candidate for intravalence character on the basis of the present results is the $3a_1 \rightarrow 3pb_2$ transition, which is the second strongest calculated excitation from this orbital, and the differences between the calculated, defect estimate and experimental value of this excitation appear to suggest some intravalence character. It is interesting to note that while both static exchange calculations are in better overall agreement with the experimental results than the TDHF calculation of Langhoff and Williams [8], the static exchange calculations predict that the $3a_1 \rightarrow 3pb_2$ excitation will be stronger than the $3a_1 \rightarrow 4pb_2$ excitation, whereas the TDHF calculation predicts the opposite result and hence is in better agreement with the experimental results on this point.

The ka_1, kb_1 and kb_2 contributions to the partial cross section are given in Figure 5.3. Of these, the ka_1 profile is the largest component of the partial cross section at energies above its maximum in both static exchange results, although somewhat stronger in the present calculation. The TDHF calculation has its ka_1 maximum at a higher energy, near 28eV, and is somewhat stronger than either of the static exchange results, by a factor of as much as 2 at high energies where it is the only important contributor to the partial cross section in the TDHF calculation. The kb_1 contribution has a maximum to slightly higher energy than the ka_1, and becomes the second most important contribution to the partial cross section at high energy in both static exchange calculations. This profile is somewhat more irregular than that of Diercksen et al, presumably as a consequence of the larger supplementary basis set yielding more pseudostates for the imaging process.

The TDHF results [8] are in complete disagreement with the static exchange results for this component, yielding a completely negligible contribution at higher energies. As noted by Diercksen et al [9] the $3a_1 \rightarrow ka_1$ and $3a_1 \rightarrow 3kb_1$ profiles are virtually identical to the corresponding $1b_1$ profiles as a result of the mainly oxygen 2p nature of both orbitals. This is not the case for the kb_2 component, which has a maximum, assigned by Diercksen et al to the presence of the $2b_2(\sigma^*)$ valence orbital, near 17eV in both static exchange calculations. At high energies this component makes the smallest though not

negligible contribution to the partial cross section. This is not the case with the TDHF calculation where the $1b_2$ component shows a steady decline from the threshold and makes a negligible contribution at high energies.

The three components are combined in Figure 5.4 to yield the $(3a_1^{-1})^2A_1$ partial cross section which is compared to the same sets of experimental data as the previous orbital. The coincidence data of Tan et al [2], while in good agreement with the calculated curve at high energy, is, as in the case of the $1b_1$ partial cross section, exceeded by the calculated curve at low energies. The synchrotron data of Truesdale et al [1] is in reasonable agreement with the (e,2e) measurements, though showing some scatter, and displays a minimum at 20eV not reproduced by the calculation. The measurements of Thornton et al [49] are in agreement with the other experimental results at higher energies. The measurements of Dutit et al [4] are greater than those of Truesdale et al, presumably owing to angular effects, but also show a minimum at 20eV. Two low energy coincidence points lie on the calculated curve near the predicted maximum . The maximum in the calculation of Diercksen et al, while in the same position, is approximately 12% lower bringing better overall agreement with the mass of the experimental data.

At higher energy the present results are slightly less than the (e,2e) measurements while those of Diercksen et al are slightly greater. The corresponding

TDHF partial cross section is almost identical to the present results except that the maximum is shifted to 2eV lower photon energy. The MSXα [10] result is almost identical to the MSXα result for the $(1b_1^{-1})^2B_1$ partial cross section, shows no maximum, and is considerably weaker than the present result, especially at higher energies.

5.3.3 $1b_2$ Ionization I.P. = 18.55eV B $^2B_2$ [14]

The calculated static exchange excitation spectrum of the $1b_2$ orbital is given in Table 5.4.

The $1b_2 \rightarrow 3sa_1/4a_1$ excitation is the strongest calculated excitation for the molecule and would appear to have some intravalence character on the basis of its strength. All the other series appear to be wholly Rydberg in nature with the possible exception of the $1b_2 \rightarrow 3pb_2$ excitation which has been suggested to have some intravalence character by Diercksen et al [9] because of the discrepancy between the calculated value and the defect estimate, a discrepancy which also exists in the present calculation.

As in the previously discussed cases these series are shorter than those of Diercksen et al, and are not in such good agreement with the defect estimates for the higher members of each excitation series, again illustrating the effects of

an improved basis set.

The three components of the partial cross section are shown in Figure 4.5 and are very similar to the results of Diercksen et al [9] , except for the ka_1 component, which shows a maximum in the present results instead of a monotonic decline.

The TDHF calculation [8] produces components very different to the static exchange calculations, with the ka_1 component dominating at high energies and the sum of the kb_2 and ka_2 components decaying monotonically from threshold.

The three components contributing to the partial cross section are combined to yield the partial cross section for the $(1b_2^{-1})\,^2B_2$ channel, presented in Figure 5.6. The calculated cross section shows an initial maximum which is approximately 80% greater than the experimental data before decaying very rapidly to yield good agreement with the experimental data above 30eV. Unlike the previously discussed channels the various sets of experimental data are in quite good agreement, except for one data point of Thornton et al [49]. Interestingly the synchrotron data of Dutit et al [4] fits quite smoothly with the trends shown in the other experimental data. The MSXα calculation [10] predicts a very low asymmetry parameter for this channel near threshold, so angular effects are not expected to be as large as for other channels.

This smooth joining of the data of Dutit et al and the other experimental data, which is not repeated in the case of the $(3a_1^{-1})^2A_1$ and $(1b_1^{-1})^2B_1$ channels, where the asymmetry parameter is predicted to be larger near threshold [10], confirms that the results of Dutit et al contain angular effects.

The calculation of Diercksen et al [9] shows no maximum in the $1b_2$ partial cross section but a steep decline from the 22eV moving into close agreement with experiment above 30eV. The TDHF calculation for this channel is also greater than the experimental data near threshold but is less at high energies. This is the channel for which the MSXα calculation produces the best results showing a maximum just above threshold in good agreement with experiment and is also in good agreement with experiment at high energies.

Diercksen et al [9] have suggested that there is channel coupling between the $(1b_2^{-1})^2B_2$ and the $(1b_1^{-1})^2B_1$ channels to account for the maximum between 18eV and 20eV in the $(1b_1^{-1})X^2B_1$ partial cross section data of Dutit et al [4]. As this maximum is not shown in more recent experimental measurements this suggestion is not confirmed. As all the calculated partial cross sections are greater than experiment near threshold it is not possible to account for the larger discrepancy between calculation and experiment for the $(1b_2^{-1})^2B_2$ cross section on this basis.

5.3.4 $2a_1$ Excitation IP = 32.3eV $^2A_1$[14]

The $2a_1$ excitation series are presented in Table 5.5, and can be seen to be in reasonable accord with the defect estimates, being generally weak and showing little evidence of any intravalence character. Again these series are slightly shorter and not in such good agreement with the defect estimates as those of Diercksen et al [9].

The three contributions to the $(2a_1^{-1})^2A_1$ partial cross section are shown in Figure 5.7. All are broad and unstructured, and are very similar to the results of Diercksen et al. The components are combined to yield the $(2a_1^{-1})^2A_1$ partial cross section which is compared with the available experimental data [2] in Figure 5.8. General accord is evidently achieved between the two sets of results.

MSXα calculations yield results for this channel which are virtually identical to those for the atomic oxygen 2s orbital [10], and which are very similar to, though somewhat weaker than, the present results.

5.3.5 Total Valence Photoionization Cross section

The calculated total valence photoionization cross section is compared with the available experimental results in Figure 5.9 .

The large discrepancy between calculation and experiment at low energy arises from the overestimate of all the partial channel cross sections in this energy range. It has its most significant contribution from the large overestimate of the $(1b_2^{-1})^2B_2$ partial cross section. The results of the static exchange calculation of Diercksen et al [9] are very similar to the present calculations, though in slightly better agreement at low energies, and the overestimate of the valence photoionization cross section again arises mainly from the $(1b_2^{-1})^2B_2$ partial channel.

The TDHF calculation of Langhoff and Williams [8] produces the best agreement between calculation and experiment at low energies, although an overestimate arising from the $(1b_2^{-1})^2B_2$ partial channel is again present. However, at high energies this calculation produces a comparatively large underestimate, arising from the same channel.

5.4 Discussion

The calculated excitation series divide naturally into ka_1, ka_2, kb_1 and kb_2 series, subdivided into s, p and d type series in accord with experimental results [3]. The excitation energies are in general accord with experimental values, but in some cases the high calculated oscillator strengths and the discrepancy

between the calculated, quantum defect and experimental excitation energies suggest that there may be contributions from the virtual valence $4a_1$ and $2b_2$ orbitals. The outer valence partial cross sections also display maxima near threshold arising from the ka_1 and kb_2 contributions which may also contain contributions from these valence virtual orbitals.

The effects of changing the order of the fit in the Tchebycheff imaging procedure have been explored and 6 and 9 point fits are presented, along with stick representations of the discrete pseudospectra, for the three outer valence orbitals in Figures 5.10 to 5.12. The 9 point fits are more irregular than the 6 point fits, showing maxima where the density of pseudostates is greatest.

The main feature of each partial cross section in the 6 point fits, a maximum several electron volts from threshold followed by a decline, is also present, though somewhat more irregularly, in the 9 point fits. The close relationship between the details of the profiles obtained from the 9 point imaging technique and the density of the pseudostates indicates that the results obtained employing 9 points are not smoothed adequately.

These results have been confirmed by the recent calculation of Diercksen et al [9], where a larger basis set was employed. As a result of the use of a larger basis set, the main deficiency of this calculation, the large overestimate of the magnitudes of the respective maxima, has been partially remedied. The extent

of the remaining discrepancy in the $(1b_1^{-1})^2B_1$ channel is unclear as there is a conflict between the (e,2e) data and the latest synchrotron data in the 16eV to 19eV energy range (Figures 5.2 and 5.4) for the $(1b_1^{-1})^2B_1$ and $(3a_1^{-1})^2A_1$ channels.

A large discrepancy remains in the larger calculation in the $(1b_2^{-1})^2B_2$ channel, which has been suggested to arise from coupling with the $(1b_1^{-1})^2B_1$ channel. The present results do not lend support to this suggestion.

It is interesting to note that the TDHF calculations of Langhoff and Williams [8], while yielding reasonable agreement with experiment at low energies for the $(1b_1^{-1})^2B_1$ and $(3a_1^{-1})^2A_1$ channels also overestimate the magnitude of the initial maximum in the $(1b_2^{-1})^2B_2$ channel. Furthermore, the partial channel cross section components given by the TDHF calculations are not, in general, very similar to those given by the static exchange calculations.

As the TDHF calculation used a very small basis, a close comparison of the results of the two methods is precluded. However, the initial results of the TDHF calculation are in as good overall agreement with experiment as the static exchange results.

The MSXα calculations [10] have yielded results, which, at energies greater than 10eV above the appropriate threshold, are in almost as good an agreement

with experiment as the present results, as well as yielding asymmetry parameters for each channel. No initial maxima are present in the $(1b_1^{-1})\,^2B_1$ or $(3a_1^{-1})\,^2A_1$ partial cross sections, whereas these are the main features in the experimental results and, although somewhat overestimated, are present in all the Stieltjes-Tchebycheff results. The present results lend themselves to interpretation in terms of contributions from the valence virtual orbitals falling in the discrete spectral interval, while the MSXα results lead to an interpretation of the results as those of a perturbed oxygen atom.

C_2H_2 Calculations

5.5 Introduction

As the simplest alkyne, the photoabsorption, photoexcitation of acetylene has been a topic of interest for many years. Its bonding was discussed by Mulliken in 1935 [16], and many early LCAO-MO-SCF calculations were carried out on it [17,18].

Experimentally a number of measurements of photoionization efficiencies [19-21] and of total [22,23] and partial channel [24] photoionization cross sections

have been reported at low energies. These measurements have indicated the presence of a double peaked structure in the total photoionization cross section in the region of 15eV, arising from ionization from the $1\pi_u$ orbital. Quantum defects for the Rydberg series have been published by Lindholm [25].

There have been several ab-initio investigations into the excited electronic states of acetylene which have located the $^1\Sigma_u^+$ state formed by excitation of a $1\pi_u$ electron to the $1\pi_g$ valence virtual orbital above the ionization threshold of the $1\pi_u$ orbital [26,27]. Semiempirical calculations have placed this state just below the ionization threshold [31].

Much new data has become available recently. The photoelectron spectrum of acetylene has been remeasured, using four different types of radiation, and the relative partial cross sections at these energies measured and calculated by Cavell and Allison [28]. Ionization potentials from their work will be used in these calculations and it should be noted that these differ slightly from the employed in the calculations of Langhoff et al [24,29].

The many-body calculations of Cederbaum et al [30] indicate that the independent particle picture is a good paradigm for the outer valence orbitals of acetylene.

Unwin and co workers [32] have investigated the changes in the intensities of

the various vibrational transitions accompanying ionization of a $1\pi_u$ electron as the photon energy changes. These intensities have also been measured by Kreile et al [33] at a number of points, as well as β paramaters for the various final vibrational states at these energies. Langhoff and co workers have published experimental and theoretical partial cross sections for the valence orbitals of acetylene, calculated within the static exchange approximation [24,29].

Results are presented for the four outermost orbitals of acetylene, obtained by the Stieltjes-Tchebycheff imaging technique within the static exchange approximation. These results are very similar to those of Langhoff et al. However, it will be suggested that despite the seeming plethora of results, both experimental and theoretical, definitive measurements have not yet been made and further calculations are required before a good understanding of the photoionization dynamics of acetylene is achieved.

5.6 Theoretical and Computational Details

The ground state wavefunction of acetylene within the Hartree-Fock approximation is:

$$|1\sigma_g^2 1\sigma_u^2 2\sigma_g^2 2\sigma_u^2 3\sigma_g^2 1\pi_u^4|\,^1\Sigma_g^+ \qquad [5.4]$$

Such a wavefunction was constructed within the Hartree-Fock scheme employing the (9s5p/5s3p) Gaussian basis set of Dunnings [11] on each carbon nucleus, supplemented with a d polarization function (ξ = 0.8,GTF), and the (4s/3s) basis of the same author, supplemented with a p polarization function (ξ = 0.4,GTF) on each hydrogen centre, at the ground state internuclear separation (R_{CC} = 1.204Å, R_{CH} = 1.058Å) [12].

This wavefunction yielded a ground state energy of -76.8379au, to be compared with a near Hartree-Fock limit value of -76.8450au [34]. A large supplemental basis set, given in Table 5.6, was used to construct virtual orbitals to describe photoexcitation and ionization by solution of the static exchange Hamiltonian:

$$h_\Gamma = T + V + \sum_i (2a_i^\Gamma J_i - b_i^\Gamma K_i) \qquad [5.5]$$

The a_i^Γ and b_i^Γ are those previously published by Langhoff et al for closed shell molecules belonging to the point group $D_{\infty h}$ with minor corrections and are listed together with the multiplicity factors, μ_i^Γ, in Table 5.7.

The pseudospectrum of transition energies and oscillator strengths $(\tilde{\epsilon}_i, \tilde{f}_i)$ obtained from these orbitals is used in the Tchebycheff moment of analysis as previously described, to yield the partial channel cross sections of the orbitals under consideration.

It must be emphasised that the IP's used in the construction of the pseudospectra are taken from the spectra published by Cavell and Allison [28]. These are slightly different to the values employed in the previous work on acetylene using the Stieltjes-Tchebycheff moment imaging technique [24]. This is expected to change the position of the calculated Rydberg series slightly, but major differences can only arise from basis set differences.

Before discussing the results it will be helpful to describe the occupied valence orbitals and virtual valence orbitals.

The $2\sigma_g$ orbital is strongly carbon-carbon bonding, and is of mainly s character. The $2\sigma_u$ orbital is a carbon-carbon antibonding but strongly carbon - hydrogen bonding sp hybrid. The $3\sigma_g$ orbital is a carbon-carbon bonding orbital which is also carbon-hydrogen bonding and is of almost pure p character. The $1\pi_u$ orbital arises from a bonding combination of carbon 2p atomic orbitals. The valence virtual orbitals consist of the $1\pi_g$, $3\sigma_u$, $4\sigma_g$, and $4\sigma_u$ orbitals. The $1\pi_g(\pi^*)$ orbital is an antibonding combination of carbon 2p atomic orbitals. The $3\sigma_u$ orbital is both carbon-carbon and carbon-hydrogen antibonding, and is of mainly carbon s character, whereas the $4\sigma_g$, and $4\sigma_u$ orbitals are sp hybrids, the first of which is mainly carbon-hydrogen antibonding , whereas the second is mainly carbon-carbon antibonding [17].

The dipole selection rules allow transitions of the type $g \leftrightarrow u$ in a molecule

It must be emphasised that the IP's used in the construction of the pseudospectra are taken from the spectra published by Cavell and Allison [28]. These are slightly different to the values employed in the previous work on acetylene using the Stieltjes-Tchebycheff moment imaging technique [24]. This is expected to change the position of the calculated Rydberg series slightly, but major differences can only arise from basis set differences.

Before discussing the results it will be helpful to describe the occupied valence orbitals and virtual valence orbitals.

The $2\sigma_g$ orbital is strongly carbon-carbon bonding, and is of mainly s character. The $2\sigma_u$ orbital is a carbon-carbon antibonding but strongly carbon - hydrogen bonding sp hybrid. The $3\sigma_g$ orbital is a carbon-carbon bonding orbital which is also carbon-hydrogen bonding and is of almost pure p character. The $1\pi_u$ orbital arises from a bonding combination of carbon 2p atomic orbitals. The valence virtual orbitals consist of the $1\pi_g$, $3\sigma_u$, $4\sigma_g$, and $4\sigma_u$ orbitals. The $1\pi_g(\pi^*)$ orbital is an antibonding combination of carbon 2p atomic orbitals. The $3\sigma_u$ orbital is both carbon-carbon and carbon-hydrogen antibonding, and is of mainly carbon s character, whereas the $4\sigma_g$, and $4\sigma_u$ orbitals are sp hybrids, the first of which is mainly carbon-hydrogen antibonding , whereas the second is mainly carbon-carbon antibonding [17].

The dipole selection rules allow transitions of the type $g \leftrightarrow u$ in a molecule

of $D_{\infty h}$ symmetry. While there will be strong transitions from the $2\sigma_u$ and $1\pi_u$ orbitals to the $1\pi_g$ valence virtual orbital, which may fall either in the discrete spectral interval or the continuum, no such transition is possible for the $2\sigma_g$ or $3\sigma_g$ orbitals.

The $1\pi_g$ virtual orbital as the lowest lying of the valence virtual orbitals, and in molecular nitrogen and carbon monoxide lies in the discrete spectral interval. In these cases its presence perturbs the $k\pi$ continuum profiles, leading to unphysical results unless special procedures are used [35,36].

As the position of the $1\pi_u \rightarrow 1\pi_g(\pi \rightarrow \pi^*)$ transition is not yet certain, difficulties arise which will be discussed under the appropriate heading.

At this stage it can be said that strong contributions are expected, in the Rydberg series or partial cross sections of all orbitals, in the $k\sigma$ channels , as valence virtual orbitals exist of the appropriate symmetry types (g and u) for dipole allowed transitions from the occupied orbitals. These orbitals are calculated to lie above the π^* virtual orbital [17].

5.7 Computational Results

5.7.1 $2\sigma_g$ orbital I.P. = 23.65eV [28]

The calculated discrete excitation energies and oscillator strengths for this orbital are given in Table 5.8 along with quantum defect estimates. There is good agreement between both sets of excitation energies except for the first member of the $p\pi_u$ series.

The oscillator strengths are weak and there is no evidence of the appearance of any intravalence transitions in the discrete spectral interval. In this context it should be noted that the results of Machado et al [29], while agreeing with regard to the excitation energies once allowance is made for the difference in ionization potential used, show a very different pattern of oscillator strengths. The results given here for the $p\sigma_u$ oscillator strengths are an order of magnitude less then those of Machado et al, thus lending little support to their suggestion of contributions from the $3\sigma_u(\sigma^*)$ to the discrete interval. The calculated oscillator strengths for the $p\pi_u$ series are approximately twice as great as those of Machado et al, illustrating the great sensitivity of the calculated oscillator strengths to small changes in the basis set.

As no indication of intravalence character has been found in the discrete

excitation series, it is expected that a resonance or resonances, shall appear in the $2\sigma_g \rightarrow k\sigma_u$ profile, owing to contributions from the $3\sigma_u$ and $4\sigma_u$ valence virtual orbitals in the continuum. The $2\sigma_g \rightarrow k\sigma_u$ and $2\sigma_g \rightarrow k\pi_u$ profiles are shown in Figure 5.13. The $k\sigma_u$ profile shows two maxima, one approximately 6eV above threshold and the stronger approximately 18eV above threshold.

The minimal basis set calculations of McLean [17] yield a difference of 23eV in the eigenvalues of the $3\sigma_u$ and $4\sigma_u$ orbitals, suggesting that these two orbitals could give rise to two distinct features in the partial photoionization cross section. The energy separation between the two maxima shown here is 13eV suggesting that the first of these maxima be tentatively attributed to the $3\sigma_u$ and the second to the $4\sigma_u$ valence virtual orbitals lying in the photoionization continuum. However, the results of Machado et al quoted above lend no support to this assignment.

While the form of $k\pi_u$ components in the present results and those of Machado et al [29] are fairly similar, the reported $k\sigma_u$ component is much smoother, rising very rapidly to a broad maximum extending from 30eV to 40eV. In general, the lower the number of spectral moments used in the imaging process, the smoother the resulting profile. A six point fit was used for the three profiles obtained for this channel. There are enough pseudostates to justify this choice, but it seems that those of Machado et al [29] may have been

obtained using a lower order fit. The $2\sigma_g \rightarrow k\pi_u$ profile is, as expected, weak and flat, extending to high energies where it dominates the partial cross section.

The two components are combined in Figure 5.14 to yield the partial cross section for the $2\sigma_g$ channel. This still shows clearly the two maxima arising from the σ_u virtual orbitals. Again the results of Machado et al are smoother and the comments made above about the order of the fit apply.

The recently published results of Lynch et al [52], obtained by solving the static exchange Hamiltonian (eq. 5.5) using scattering functions, without any smoothing techniques, produces a photoionization cross section profile for this ionization very similar in form to the current results. This confirms the presence of separate contributions from the $3\sigma_u$ and $4\sigma_u$ valence virtual orbitals, and demonstrates that the use of the 6 point Tchebycheff procedure is fully justified. It is therefore suggested that the results of Machado et al [24,29] for this ionization show no structure either because of over smoothing, due to too low an order fit, or because the various ground and supplemental basis set deficiencies have stronger effects for this ionization than for any of the others presented here.

At present no experimental data are available for this channel, and according to the results of Cederbaum et al [30], the 23.65eV line carries only 60% of the total intensity involved in the $2\sigma_g$ ionization. A further 25% is calculated to

manifest itself in a satellite peak at 28.9ev, shown quite clearly in the results of Cavell and Allison [28].

5.7.2 $2\sigma_u$ orbital I.P. = 18.75eV $B\,^2\Sigma_u$[28]

The calculated discrete excitation energies and oscillator strengths for this orbital are given in Table 5.9, along with quantum defect estimates. It can be seen that there is only moderate agreement between the two sets of figures, which suggests some perturbation owing to intravalence contributions.

The oscillator strengths are moderately strong for the two d series, but weak for the $s\sigma_g$ series. There is little evidence of the appearance of a transition to the $4\sigma_g(n/\sigma^*)$ valence virtual orbital in the oscillator strength distributions of either of the two σ series, but the $2\sigma_u \rightarrow 1\pi_g$ transition appears below the commencement of the $d\pi_g$ Rydberg series with a very high oscillator strength. This suggests that a shape resonance can be expected near threshold in the $2\sigma_u \rightarrow k\sigma_g$ channel.

It is instructive to compare the excitation energies with those of the published static exchange calculation on acetylene [24,29]. The $d\pi_g$ series are in reasonable agreement both with regard to position and intensity, although disagreeing by 0.13eV as to the position of the $2\sigma_u \rightarrow 1\pi_g(\pi^*)$ intervalence transi-

manifest itself in a satellite peak at 28.9ev, shown quite clearly in the results of Cavell and Allison [28].

5.7.2 $2\sigma_u$ orbital I.P. = 18.75eV $B\,^2\Sigma_u$[28]

The calculated discrete excitation energies and oscillator strengths for this orbital are given in Table 5.9, along with quantum defect estimates. It can be seen that there is only moderate agreement between the two sets of figures, which suggests some perturbation owing to intravalence contributions.

The oscillator strengths are moderately strong for the two d series, but weak for the $s\sigma_g$ series. There is little evidence of the appearance of a transition to the $4\sigma_g(n/\sigma^*)$ valence virtual orbital in the oscillator strength distributions of either of the two σ series, but the $2\sigma_u \rightarrow 1\pi_g$ transition appears below the commencement of the $d\pi_g$ Rydberg series with a very high oscillator strength. This suggests that a shape resonance can be expected near threshold in the $2\sigma_u \rightarrow k\sigma_g$ channel.

It is instructive to compare the excitation energies with those of the published static exchange calculation on acetylene [24,29]. The $d\pi_g$ series are in reasonable agreement both with regard to position and intensity, although disagreeing by 0.13eV as to the position of the $2\sigma_u \rightarrow 1\pi_g(\pi^*)$ intervalence transi-

tion, which Langhoff et al place at 15.54eV [24].

The recent calculations of Hayaishi et al [21], placed the $2\sigma_u \rightarrow 1\pi_g$ excitation at 16eV with an oscillator strength of 0.429. Their measurements of the photoionization efficiency led them to suggest that this excitation autoionizes strongly into the $(1\pi_u^{-1})X^2\Pi_u$ channel. More interesting at this point are the two Rydberg σ_g series, $s\sigma_g$ and$d\sigma_g$.

Langhoff et al report only an $s\sigma_g$ Rydberg series, as their supplemental basis does not contain any $d\sigma_g$ type basis functions. They find an intravalence interloper at 17.7eV with an oscillator strength of 0.1551, which is assigned to the $4\sigma_g(n/\sigma^*)$ valence virtual orbital. No such interloper is present in the results presented here.

In the published calculation, the supplemental basis set contained $23\sigma_g$ basis functions, whereas the calculations reported here have $37\sigma_g$ pseudostates, both of s and d type, and the ground state basis is larger, so the interloper can be dismissed as a spurious artifact of a poor basis. However the discrepancies between the quantum defect estimates and the static exchange results are very similar to those in the results of Langhoff et al.

The corresponding static exchange profiles are shown in Figure 5.15. The $k\sigma_g$ profile has a maximum just above threshold which is attributed to contributions

from of the $4\sigma_g$ valence virtual orbital, and decays quite rapidly. The $k\pi_g$ profile is has a minimum near threshold, and, compared to the $k\sigma_g$ profile, is weak and flat, extending to high energy where its contribution dominates. The two components are combined in Fig. 5.16 to yield the calculated partial cross section of the $2\sigma_u$ orbital. The initial maximum due to contributions from the $4\sigma_g(n/\sigma^*)$ orbital is still present. These results are in no better agreement with experiment than those of Langhoff et al [24,29].

An explanation of the discrepancy must be sought. It is clear that the error must originate in the $k\sigma_g$ component as this dominates the partial cross section at low energies. Langhoff et al have suggested that this discrepancy may arise from spurious contributions to the threshold $2\sigma_u \rightarrow k\sigma_g$ cross section from the $4\sigma_g(n/\sigma^*)$ valence virtual orbital [24] which, within the static exchange approximation at the ground state internuclear distance, lies in the discrete spectral interval. In view of the failure of this calculation to locate this transition in the discrete spectral interval, this suggestion is no longer tenable.

It is instead suggested that there may be significant coupling between the nuclear and electronic motion at low kinetic energies for $2\sigma_u$ ionization. This has been found to be a common effect of shape resonances and produces non Franck-Condon distributions among the final vibrational states of the ion over a comparatively wide energy range. For the $3\sigma_g \rightarrow k\sigma_u$ channel of N_2, Dehmer

et al [37,38] have shown that the position of the σ_u shape resonance is very sensitive to the internuclear separation. At shorter internuclear distances the shape resonance moves to higher energy, is broadened and weakened. At longer internuclear distances the resonance moves to lower energy, becomes considerably more intense, but is very narrow. This change in the resonance position may be rationalised by consideration of the nature of the $\sigma_u(\sigma^*)$ orbital in N_2.

As the internuclear distance decreases, the energy of the antibonding σ_u orbital increases because of the increased internuclear repulsion, whereas as the internuclear distance increases, the energy of the orbital decreases. The effects of the variation of the internuclear distance upon the energy of a virtual σ_g orbital would be expected to be the reverse of that for a σ_u virtual orbital.

As the $2\sigma_u$ orbital is carbon-carbon antibonding, removal of an electron from it results in a shortening of the carbon-carbon internuclear distance. If this lowered the energy of the resonance slightly, it would be removed from the continuum. This would result in a diminishment of the $k\sigma_g$ contribution near threshold while leaving this channel unchanged at higher energies.

An alternative explanation involves coupling between the $2\sigma_u \rightarrow k\sigma_g$ and $1\pi_u \rightarrow k\pi_g$ channel. In the $1\pi_u$ partial cross section is an interval between 19eV and 24eV where the calculated partial cross section is less than the experimental results. The calculated $2\sigma_u$ partial cross section is greater by approximately the

same amount within the same energy range.

5.7.3 $3\sigma_g$ orbital IP = 16.75eV A $^2\Sigma_g^+$[28]

The calculated excitation spectrum of the $3\sigma_g$ orbital is given in table 5.10 along with quantum defect estimates, with which the calculated values are in general agreement, and some recent experimental values. The calculated values are very similar to those published by Langhoff et al [24] once allowance is made for their use of the adiabatic ionization potential instead of the vertical ionization potential, which shifts all the excitation energies by 0.35eV to higher energy.

It should be noted that the $np\sigma_u$ series is moderately strong and the $np\pi_u$ series is weak, and that, because of a common quantum defect, estimates have both series overlapping. The experimental excitation energies are taken from the recent photoionization efficiency measurements of Hayaishi et al [21]. These measurements show a series of small sharp peaks owing to the autoionization of these Rydberg states into the $(1\pi_u^{-1})X^2\Pi_u$ channel. There is only one series, some of whose states show some vibrational resolution into a $v' = m$ and a $v' = m + 1$ peak, confirming that the defect estimates are correct in predicting common excitation energies for both Rydberg series, indeed the calculated values presented here for both series are very close except for the n = 3 members. The oscillator strengths presented alongside the experimental values are

those calculated by Hayaishi at al and confirm the trends in oscillator strength distributions shown in the present results.

The experimental values are not at first sight in good agreement with the calculated excitation energies. However the two values available for the $v' = m+1$ series are in much better agreement with the calculation. The difference between the experimental values of the $v' = m$ series and the calculated values are of the some order as the difference between the adiabatic and vertical ionization potentials. However the $v' = m$ series is much stronger than the $v' = m+1$ series, which is not what would be expected if the $v' = m$ series was converging on the adiabatic threshold and the $m+1$ series on the vertical threshold.

The corresponding profiles are presented in Figure 5.17. There is evidence of a shape resonance just above threshold arising from the $3\sigma_u$ orbital, but, as noted by Langhoff et al [24] there is no evidence of a separate feature arising from the $4\sigma_u$ orbital, contrary to the $2\sigma_g$ results. It has been suggested [24,29] that the $4\sigma_u(\sigma^*)$ virtual orbital is too oscillatory to result in a separate discernible feature in the partial cross section, but this objection also applies in the case of the $2\sigma_g$ orbital. The $k\pi_u$ profile extends to high energy where it dominates the partial cross section but its large contribution near threshold is somewhat unusual.

The two components are combined in Figure 5.18 to yield the $3\sigma_g$ partial

cross section which is compared with the available experimental results. While there is general agreement in the form of the results, there are large discrepancies at high energies, which suggests that the $k\pi_u$ profile is an overestimate, as the calculated cross section is greater than the experimental values at all energies.

This partial cross section is much stronger than the corresponding results for the $3\sigma_g$ and 5σ orbitals in N_2 [39] and CO [40]. In both cases the $d\sigma$ component and the partial cross section have a maximum several electron volts away from threshold whereas here there is steady decay away from the maximum at threshold.

5.7.4 $1\pi_u$ orbital IP = 11.43eV $X^2\Pi_u$[28]

The calculated $1\pi_u$ static exchange excitation spectrum is given in table 5.11 along with the available experimental data and quantum defect estimates. There are two $k\sigma_g$ Rydberg series, an s and a d series, both moderately strong and both in general agreement with the defect estimates. There is no evidence of the presence of any intravalence transitions. This is in conflict with the results of Langhoff et al, who, as in the case of the $2\sigma_u$ orbital, report the presence of an interloper at 10.4eV, assigned to the $1\pi_u \rightarrow 4\sigma_g(\sigma^*)$ transition. This is again assigned to deficiencies in their basis set.

Particularly noteworthy is the total absence of the $1\pi_u \rightarrow 1\pi_g(\pi^*)$ intravalence transition. This type of transition is well known from previous calculations as being somewhat of a problem in the static exchange method. These have often placed the corresponding transition in the continuum whereas experiment has shown it to lie in the discrete spectral interval. In these cases it has been comparatively easy to remove the spurious contribution in the $k\pi$ photoionization channel and to achieve physically meaningful results. However the excitation spectrum of acetylene is very complex and a full assignment is not yet available. In particular the position of the $^1\Sigma_g^+ \rightarrow {}^1\Sigma_u^+(\pi \rightarrow \pi^*)$ peak has not yet been experimentally resolved.

The configuration interaction calculations of Kammer [26] have yielded an excitation energy greater than 13eV for this transition and also for the corresponding non linear states, as have those of Buenker and Peymerimhoff [276]. A different conclusion is reached by the HAM/3 semi-empirical calculations of Åsbrink et al [31], which yield an excitation energy of 10eV. The authors suggest that this corresponds to a very strong experimental band at 9eV, to which a number of dipole forbidden transitions have been assigned. The static exchange results for the $2\sigma_u$ orbital, in which the transition to the $1\pi_g$ orbital lies 3eV below the ionization threshold suggests that the HAM/3 assignment may be correct.

Perhaps the best evidence is the data presented in Figure 5.19. Here two partial cross sections are presented for the $1\pi_u$ orbital. The larger of these has been obtained directly from the static exchange results whereas the smaller has had contributions from the $1\pi_u \rightarrow 1\pi_g(\pi^*)$ transition removed. It can be seen that the smaller is in much better agreement with the experimental data than the larger, indicating that the $^1\Sigma_u^+$ valence state does indeed lie below threshold. However this inference depends upon the reliability of the experimental results of Langhoff et al [24], who report that their measurements were taken close to the magic angle, and claim that their partial cross section measurements are accurate to within 10%. However earlier experimental results, while showing the same general form as those of ref. 24 have yielded $1\pi_u$ partial cross sections approximately twice as large in magnitude, which would agree well with the unaltered static exchange results [23]. Unfortunately these earlier measurements do not seem to be magic angle results, and the calculations of Kreile, Schweig and Theil [33] indicate that these effects are non negligible at all energies.

In Figure 5.20 the cross sections of the three channels, $k\sigma$, $k\pi$, $k\delta$ contributing to the $1\pi_u$ partial cross sections are shown. The $k\pi$ profile has been obtained by deleting all spurious contributions from the $^1\Sigma_g^+ \rightarrow {}^1\Sigma_u^+(\pi \rightarrow \pi^*)$ transition and is negligible at all energies compared to the $k\delta$ contribution to the partial cross section. The $k\sigma_g$ channel contribution shows evidence of the appearance of the $4\sigma_g(\sigma^*)$ valence virtual orbital just above threshold, and even at high en-

ergies makes a significant contribution to the partial cross section. The partial cross section is dominated at all energies shown by the $k\delta_g$ component which has a maximum just above threshold before decaying rapidly.

In figure 5.21 the modified static exchange partial cross section is shown, along with the experimental data, on a larger scale so as to permit more detailed comparison of the two sets of results. At energies greater than 17eV there is reasonable agreement between the two sets of results. However between 19.5 and 23eV the experimental measurements are an almost constant 2mB greater than calculation. This has already been suggested to arise from coupling with the $2\sigma_u$ channel.

Below 17eV photon energy the partial cross section displays its most interesting structure, a deep minimum followed by a maximum. As the minimum is so deep compared with the partial cross section, whatever process is taking place must be of the same overall symmetry as the $d\delta_g$ channel, i.e. $^2\Pi_u$. Machado et al [29] have published the $1\pi_u \rightarrow k\delta_g$ pseudospectrum obtained on their calculations on acetylene. As their supplemental δ_g basis is larger than that used here, resulting in 18 pseudostates instead of 14, it is expected that if the present basis is deficient rather different results would be produced by using these results in the Tchebycheff analysis. Figure 5.9 also shows the curve obtained using the $k\delta_g$ pseudospectrum of Machado et al together with the present $k\sigma_g$ pseudospectra

in the Tchebycheff analysis. The two sets of results are virtually identical.

All results presented for this orbital were obtained using the 6 point Tchebycheff procedure. Four and five fits have also been obtained, and while there are differences in detail they are in essential agreement with the six point results. Attempts to obtain higher order results have not been successful, resulting in a series of very rapid oscillations even at high energies. This is a result of an insufficient number of pseudostates. The maximum order fit that can be used in a given case depends on the number of pseudostates, and, in any case should be much less than half the number of pseudostates. In this case a 6 point fit is the highest order fit which gives converged results. However the imaging process is, in essence, a smoothing process, and especially at low order, tends to smooth away all detail.

While it seems unlikely that these features arise by direct photoionization the possibility cannot be dismissed. In this context it is interesting to note that the static exchange results, combined with the 6 point Tchebycheff imaging procedure, which has proved of the greatest utility in similar investigations, represents an almost exact smoothing of the experimental results between 13 and 17eV. That is, the area defined by the calculated curve and the experimental minimum is almost equal to that defined by the calculated curve and the experimental maximum.

Various attempts have been made to rationalise the observed features in terms of autoionizations. Langhoff et al suggest two plausible candidates for the observed maximum, the $2\sigma_u \rightarrow 1\pi_g(\pi^*)$ transition at 15.54eV and the $2\sigma_u \rightarrow 4\sigma_g(n/\sigma^*)$ transition at 17.68eV [24]. This work has shown that the second of these is a spurious artifact of the basis set while leaving the $\sigma \rightarrow \pi^*$ transition, with an oscillator strength of 0.792, directly under the observed maximum, and this transition is of the correct symmetry to interact with the $1\pi_u \rightarrow k\sigma_g$ and $1\pi_u \rightarrow k\delta_g$ channels. This suggestion has been repeated by Hayaishi at al [21] as an explanation of the increase in the photoionization efficiency in this energy range, and their calculations yielded an oscillator strength of 0.429 for the $2\sigma_u \rightarrow 1\pi_g$ excitation. Indeed this autoionization does give a very plausible explanation of the greater magnitude of the experimental results compared to the static exchange results in the 15.5 –17eV region. However, if this explanation is used an explanation must be sought for the deep minimum.

Various reports [50,51] have appeared to suggest that the direct partial photoionization of the $1\pi_u$ orbital, without any autoionization effects, if such a quantity were considered physically meaningful, would have the magnitude of the experimental partial cross section at the deepest point of the minimum, and that the two maxima on either side of the minimum arise entirely from autoionization effects. That this is not the case is suggested by the static exchange cross section which closes the top of the minimum.

Kreile et al [33] have published the results of MSXα calculations for the $^2\Pi_u$ ionization. These also show no minimum near 14eV and, contrary to the present results, are dominated by contributions from the $1\pi_u \rightarrow k\pi_g$ channel near threshold.

More sophisticated techniques are required to elucidate whether the experimental data can be understood in terms of the static exchange formulation, or whether improvements such as a one electron picture with relaxation are sufficient, or whether consideration of electron correlation will be required

5.7.5 Total Photoionisation Cross Section

The calculated total photoionization cross section of C_2H_2 obtained by the direct summation of the partial cross sections is given in Figure 5.22 where it is compared with the experimental data of Unwin et al [32]. The calculated results are in general agreement with the experimental data except in the 13–17eV region where the previously discussed features in the $(1\pi_u^{-1})X^2\Pi_u$ partial cross section contribute. The experimental measurements show a sharp peak corresponding to the opening of the $(3\sigma_g^{-1})A^2\Sigma_g^+$ channel in agreement with calculation, but only has a shoulder at the onset of the $(2\sigma_u^{-1})B^2\Sigma_u^+$ channel instead of a separate maximum as predicted in the static exchange results. At higher energies the experimental results fall away more rapidly than the

theoretical results, a detail which can be partially accounted for by the exclusion of the $2\sigma_g$ channel from the experimental results while the channel is included in the computational results. As the calculation is of the static exchange type autoionization effects have not been considered. These would be expected to smooth the sudden peaks caused by the opening of a new channel, in particular the $(2\sigma_u^{-1})B^2\Sigma_u^+$ channel, and have already been postulated as an explanation of the observed maximum at 15.5eV.

The experimental cross section measurements can be adequately understood on the basis of the static exchange results except in the energy range 14-17eV.

5.8 Conclusions

The partial cross sections of the outer and inner valence orbitals as well the total photoionization cross section of acetylene have been calculated and compared with the available experimental data. General agreement has been found although several problems remain. Shape resonances arising from σ type virtual orbitals embedded in the continuum have been found in the calculated cross sections of all the σ orbitals considered whereas the $1\pi_u$ partial cross section is dominated by the $k\delta_g$ channel at low energies. The calculated excitation energies have been in reasonable agreement with the available experimental values

and the oscillator strengths similar to the results of other calculations.

The static exchange calculation of Langhoff et al has found strong intravalence interlopers in the $k\sigma_g$ excitation series of the $2\sigma_u$ and $1\pi_u$ orbitals [24], and has suggested that the disagreement between theory and experiment in the case of the $(2\sigma_u^{-1})B\,^2\Sigma_u^+$ channel arises from spurious contributions from the $2\sigma_u \rightarrow 4\sigma_g$ excitation to the $2\sigma_u \rightarrow k\sigma_g$ partial channel near threshold. The present calculations, employing a more complete supplemental σ_g basis show no evidence of this interloper which appears to be an effect of a more contracted ground state basis, (10s,5p/4s)/[3s,2p/2s] instead of (9s,5p,1d/4s,1p)/[5s,3p,1d/3s,1p], and the smaller supplemental basis. However the calculated cross sections of the present calculations generally agree well with those of Langhoff et al [24,29], showing that once a reasonable supplemental basis set is employed the form of the resulting cross sections are fairly stable to increase in the basis set size, while the excitation series, which are important in the interpretation of these cross sections, are still very sensitive to basis set effects.

However, for the $(2\sigma_g^{-1})\,^2\Sigma_g^+$ channel the resulting partial cross section has been found to be similar in magnitude to the results of Langhoff at al [24] structure has been found in the present calculations, not present in the smooth profile reported by Langhoff et al, which is supported by recent calculations [52].

For the $(2\sigma_u^{-1})B\,^2\Sigma_u^+$ channel, a maximum in the theoretical results just above threshold attributed to the $4\sigma_g(n/\sigma^*)$ orbital has not been supported by the experimental results. These results show that previous suggestions that this excitation lies in the discrete spectral interval [24] are not tenable and it is instead suggested that the effects of vibrational motion may be very important in this channel. Here the results of Lynch et al [52] are ion close agreement with the various moment theory calculations of the partial photoionization cross section. However it should be noted that, while the results of Machado et al [24] show no minimum in the $k\pi_g$ contribution, the present results and those of Lynch et al are in agreement as to the form of this contribution.

The $(3\sigma_g^{-1})A\,^2\Sigma_u^+$ partial channel results show a shape resonance just above threshold arising from the $3\sigma_u(\sigma^*)$ orbital, a conclusion confirmed by the experimental measurements. The photoionization cross section profile of Lynch et al for this channel are similar to the various moment theory results.

The most interesting results are those for the $(1\pi_u^{-1})X\,^2\Pi_u$ channel. At high energies there is good agreement between theory and experiment, although a discrepancy of approximately 1.5Mb between 19 and 24eV suggests the possibility of some channel coupling. Below 19eV the experimental results show a deep minimum followed by a maximum, whereas the calculated curve follows an average path through these two features. On the basis of the present calculated

excitation series it is possible to assign the maximum to the autoionization the $(1\pi_g \leftarrow 2\sigma_u)^1\Pi_u$ state. The results of Lynch et al are similar in form to the present results for ionization from this orbital , indicating that the static exchange method does not lead to the interesting double peaked structure shown in the experimental results [24]. The report of these workers [52] also calls into question the location of the $1\pi_u \rightarrow 1\pi_g^*$ transition below the photoionization threshold suggesting that if the normalization of the experimental results of Langhoff et al [24] is incorrect, then curves calculated with the $1\pi_u \rightarrow 1\pi_g$ transition present above threshold become as accurate as the current results are compared to the currently available data. While it is possible to assign the maximum at 15.5eV to autoionization effects none of the present computational results rationalise the sharp minimum at 13.5eV.

Nitrous Oxide Calculations

Nitrous oxide, N_2O, is isoelectronic with carbon dioxide for which calculations of the partial channel photoionization cross sections have been reported [47]. Experimental studies of the total and partial channel photoionization cross sections of this molecule by (e,2e) spectroscopy [44] and by synchrotron radiation [59,60] suggest that it would be desirable to extend the series of theoretical studies of the photoionization processes of larger molecules. The measurements

of Carlson et al [60] extend to higher photon energy than those of Truesdale et al [59], and so are plotted upon the various graphs of calculated partial channel cross sections presented below. Carlson et al [60] also report MSXα calculations of these cross sections , which show different features depending upon whether the ground state or transition state potential is used.

5.9 Theoretical and Computational Details

Within the Hartree-Fock approximation the ground state of nitrous oxide is [45] is

$$(1\sigma^2 2\sigma^2 3\sigma^2 4\sigma^2 5\sigma^2 6\sigma^2 1\pi^4 7\sigma^2 2\pi^4) X^1\Sigma^+ \qquad (5.6)$$

The basis set employed was the (9s5p/5s3p) set of Dunnings [11], supplemented with additional d functions of exponent 0.8 on the nitrogen atoms and 0.97 on the oxygen atom. A Hartree-Fock wavefunction constructed using this basis set at the experimental equilibrium geometry (N-N length = 2.13 a.u., N-O length = 2.2378 a.u., NNO angle = 180 degrees) [12], yields a molecular energy of -183.7214au compared with a Hartree-Fock limit of approximately 183.7567au [45].

One-electron excitation and ionization of the outer valence electrons gives

many-electron eigenstates which can be written symbolically in the forms

$$\begin{aligned}
&(2\pi^{-1}k\sigma)^1\Pi,(2\pi^{-1}k\pi)^1\Sigma^+,(2\pi^{-1}k\delta)^1\Pi;\\
&\quad,(7\sigma^{-1}k\sigma)^1\Sigma^+,(7\sigma^{-1}k\pi)^1\Pi;\\
&(1\pi^{-1}k\sigma)^1\Pi,(1\pi^{-1}k\pi)^1\Sigma^+,(1\pi^{-1}k\delta)^1\Pi;\\
&\quad,(6\sigma^{-1}k\sigma)^1\Sigma^+,(6\sigma^{-1}k\pi)^1\Pi;
\end{aligned} \tag{5.7}$$

Within the static exchange and frozen core approximations these are the only states which have non-vanishing oscillator strengths from the $X^1\Sigma^+$ ground state of N_2O.

Virtual orbitals, Φ_i^Γ, are constructed for each of the individual channels of equation 5.7 by solution of the one-electron equation previously described, using the supplementary basis set of Table 5.13. The coefficients a_i/b_i have been published by Orel et al [46] and Padial et al[47] for the case of a molecule belonging to point group $D_{\infty h}$. The appropriate operators for a linear molecule without a centre of inversion ($C_{\infty v}$) may be easily derived from these values and for reference are given in Table 5.12.

A qualitative description of the orbitals whose cross sections are under consideration here will help clarify these photoionization cross sections. The 2π orbital is a non bonding orbital with little central atom character. It consists almost entirely of end atom p basis functions in an anti-bonding combination. The 7σ orbital is N-N bonding and N-O antibonding. It is composed of sp

hybrids mainly localized on the terminal nitrogen atom. The 1π orbital is a bonding orbital extending over the entire molecule. Finally the 6σ orbital is an anti bonding orbital extending over the entire molecule. The unoccupied virtual valence orbitals are the $3\pi(\pi^*)$, $8\sigma(\sigma^*)$, and $9\sigma(\sigma^*)$ orbitals [53].

It is helpful to interpret the pseudospectra in terms of transitions into compact intravalence states and more diffuse Rydberg states with a lower oscillator strength. The $3\pi(\pi^*)$ orbital is the lowest lying valence virtual orbital and so it is anticipated that it will contribute mainly to the discrete excitation series, whereas the 8σ and 9σ are higher lying. Therefore a large number of resonance-like features arising from transitions into $k\sigma$ orbitals which lie in the continuum are expected to appear in the partial channel photoionization cross sections of N_2O.

5.10 Theoretical Results

5.10.1 $2\pi(n)$ Orbital (IP = 12.9eV) [56]

The $2\pi \rightarrow k\sigma$ excitations of Table 5.14 form a weak Rydberg series which are in good accord with the experimental values [54] and defect estimates, except for the first members of the $2\pi \rightarrow ns\sigma$ and $2\pi \rightarrow np\sigma$ series. However the calculated

oscillator strengths of these transitions do not suggest contributions from the valence virtual σ^* orbitals. The quantum defects used have been obtained by fitting the experimental data so the exact agreement between experiment and defect estimates is hardly surprising.

The $2\pi \rightarrow k\sigma$ cross section (Fig. 5.23) commences with a broad maximum which may be due to the presence of the 8σ and $9\sigma(\sigma^*)$ virtual orbitals in the continuum rather than in the discrete series. The profile is very similar to the $1\pi_g \rightarrow k\sigma_u$ profile of CO_2 [47], though shifted to 2eV lower photon energy after allowing for the difference in ionization energy.

The $2\pi \rightarrow k\pi$ excitation series (Table 5.14) are expected to contain a strong $2\pi \rightarrow 3\pi(\pi^*)$ or $n \rightarrow \pi^*$ transition. It is known from previous static exchange calculations that such strong intervalence transitions can spuriously perturb the photoabsorption and ionization spectrum, cf N_2 [55], and CO_2 [47]. Several methods have been employed in the attempt to overcome this problem including altering the static exchange Hamiltonian so as to force the perturbing state to fall in the discrete region of the spectrum [55], orthogonalizing the basis set to the intervalence state [55] and manual deletion of the pseudostates carrying spurious intensity from the Tchebycheff imaging process.

The uncorrected results of the calculation are shown in Figure 5.24. The $2\pi \rightarrow n\pi$ profile is curve B and the total 2π profile is curve A. It can be

seen that the total profile is dominated by the $2\pi \rightarrow n\pi$ transitions at low energies leading to unphysical values of the total cross section at these energies. When the pseudostates carrying spurious intensity are deleted from the imaging process curve C results, also presented as in Figure 5.23, which is broadly similar to the $1\pi \rightarrow n\pi_u$ profile in CO_2 [47].

The $2\pi \rightarrow k\pi$ discrete excitation series of Table 5.14 form a Rydberg series perturbed by the $2\pi \rightarrow 3\pi$ transition whose intensity is distributed among several states some falling in the discrete region but most in the continuum. If all the intensity from this transition had appeared in the discrete region the expected $2\pi \rightarrow n\pi$ profile would be broad and flat extending to high energy, and this is indeed the result which is finally obtained. This profile is again very similar to the $1\pi_g \rightarrow n\pi_u$ profile though the maximum is shifted to substantially lower photon energy. This may well be inaccurate but is a consequence of the rather crude method of dealing with the intervalence transition.

The $2\pi \rightarrow n\delta$ discrete excitations of Table 5.14 form a weak Rydberg series in close agreement with the quantum defect estimates though no experimental assignments are available at present. The corresponding $2\pi \rightarrow n\delta$ continuum of Figure 5.23 contains a strong maximum which is approximately 75% greater than the corresponding $1\pi_g \rightarrow nf\delta_u$ profile of CO_2. This is presumably an effect owing to the removal of the centre of inversion. The maximum can be given a

$2p \rightarrow kd$ designation whereas in CO_2 the δ_u orbitals have a kf designation.

The three components of Figure 5.23 are combined in Figure 5.25 where the calculated vertical electronic $(2\pi^{-1})X^2\Pi$ partial channel cross section is compared with the available experimental results [44,60]. Evidently there is excellent quantitative agreement between theory and experiment at all energies. The maximum in the partial channel photoionization cross section from 18 to 21eV arises from the $2\pi \rightarrow n\delta$ channel.

MSXα calculations [60] do not agree as well with experiment below 45eV photon energy, as to form or magnitude, as the present results. They do, however, display an initial maximum about two thirds as great as the experimental maximum.

5.10.2 7σ Orbital (IP = 16.4eV [56])

The $7\sigma \rightarrow k\sigma$ discrete excitations of Table 5.15 form a weak Rydberg series in reasonable agreement with experiment and quantum defect estimates, except for the first member of the $ns\sigma$ series. Except for this transition there is no evidence of the appearance of transitions to 8σ or $9\sigma(\sigma^*)$ intervalence orbitals, so it is anticipated that these will fall above threshold, Figure 5.26, yielding an initial maximum in the $7\sigma \rightarrow k\sigma$ profile. This is indeed the case confirming

the appearance of the 8σ and 9σ states in the continuum. This profile is very similar to the $3\sigma_u \rightarrow k\sigma_g$ profile in CO_2 though the resonance is 75% greater and the profile decays much more rapidly.

The $7\sigma \rightarrow k\pi$ discrete transitions (Table 5.15) form a weak Rydberg series which, except for the first few members, are in good accord with both defect estimates and experiment. These members are perturbed by the $7\sigma \rightarrow 3\pi$ intervalence transition which appears at 10.4eV. Thus no special procedures were required in order to obtain a meaningful $7\sigma \rightarrow k\pi$ profile. As expected from the presence of this intervalence transition in the discrete excitation series this profile is broad and flat to high energy. This profile is almost identical to the $3\sigma_u \rightarrow k\pi_g$ profile of CO_2.

The two components of Figure 5.26 are combined in Figure 5.27 to yield the vertical electronic $(7\sigma^{-1})A^2\Sigma^+$ partial channel cross section which is compared with (e,2e)[44] and synchrotron [60] measurements. The theoretical and experimental results agree very well above 30eV, but at lower photon energies the calculated profile follows the shape of the (e,2e) results while being up to 30% less intense. A minimum in the synchrotron results at 25eV is not shown in either the (e,2e) results or the present calculations. MSXα calculations [60], however, placing the resonance in the kσ contribution above 30eV,do predict a minimum, although overall agreement with experiment is not as good as in the

present calculations.

5.10.3 1π Orbital (IP = 18.22eV [56])

The $1\pi \rightarrow k\sigma$ discrete excitations series of Table 5.16 is comprised of two weak series $(s\sigma, p\sigma)$ and a stronger series $(d\sigma)$. While the $d\sigma$ series is in good accord with the defect estimates, the $s\sigma$ and $p\sigma$ series are somewhat perturbed. A strong transition at the commencement of the $s\sigma$ series suggests the appearance of the 8σ valencelike orbital in the discrete interval rather than in the continuous area of the spectrum. The corresponding continuum profile in Figure 5.28 is weak extending to high energy with a very weak maximum at 22eV which may be attributed to the appearance of the $9\sigma(\sigma^*)$ orbital in the continuum. This maximum is approximately half as strong as the corresponding maximum appearing in the $2\pi \rightarrow k\sigma$ profile where both the 8σ and 9σ orbitals appear above threshold. The curve is slightly more intense than the $1\pi_u \rightarrow k\sigma_g$ in CO_2 where a similar intensity ratio between the $1\pi_g \rightarrow k\sigma_u$ and $1\pi_u \rightarrow k\pi_g$ curves is also observed.

The $1\pi \rightarrow k\pi$ discrete excitations (Table 5.16) are in reasonable accord with the defect estimates and there is no evidence of the appearance of the $1\pi \rightarrow 3\pi$ intervalence transition in this series. The corresponding cross section, Fig 5.28, obtained without the use of any special techniques, also shows no sign of the

presence of this transition unless the small maximum near threshold is attributed to it. However, in Figure 5.24 the presence of this transition in the $2\pi \rightarrow k\pi$ continuum results in an extremely large initial maximum of 70Mb, whereas the value of the maximum in this case is only 2Mb. Overall the cross section is negligible compared to the $1\pi \rightarrow k\delta$ sections in the range of energies considered. This is comparable to the case of CO_2 where the $1\pi_u \rightarrow k\pi_g$ cross section is also negligible unlike the $1\pi_g \rightarrow k\pi_u$ cross section. However no intervalence transition of the type $\pi \rightarrow \pi^*$ is possible for the $1\pi_u$ orbital as the $1\pi_u \rightarrow 2\pi_u$ transition is dipole forbidden owing to the higher symmetry of CO_2.

The $1\pi \rightarrow kd\delta$ discrete excitations form a moderately strong Rydberg series in reasonable agreement with the defect estimates. The corresponding cross section contribution, Fig. 5.28, displays a large initial maximum which dominates the partial cross section at all the energies under consideration, as is the case with CO_2.

The three components of Figure 5.28 are combined in Figure 5.29 to yield the vertical electronic $(1\pi^{-1})B^2\Pi$ partial channel cross section which is compared with the available experimental data. While there is reasonable agreement between the theoretical and experimental values at high energies there is a very large discrepancy at low energies, where the calculation overestimates the partial channel cross section.

There are two major sources of error in this calculations. Firstly, the separated channel approximation, which predicts a single photoelectron peak for each occupied orbital. In fact N_2O has a very rich photoelectron spectrum, with many bands above 20eV [44,56,57]. Of particular relevance are the satellite peak at 19.5eV detected in the high resolution work of Potts and Williams [55], and the weak peak centered at 24eV. The first of these, in the (e,2e) values quoted, is apparently included in the 6σ data, which may account for the small discrepancy between theory and experiment at all energies in the 6σ partial channel cross section. The calculations of Domcke et al [58] have assigned these peaks to many electron transitions involving the 1π orbital. In Figure 5.29, as well as the $(1\pi^{-1})B^2\Pi(e,2e)$ measurements the points corresponding to the sum of the $(1\pi^{-1})B^2\Pi$ intensity and the intensity of the 24eV satellite peak are plotted. As can be seen, the sum, except at the very lowest energies, is greater than the theoretical curve.

Secondly, the theoretical curve is the vertical partial channel cross section and the effects of vibration, in both the ground and final state, are ignored. This approximation may produce bad results for the 1π orbital as the photoelectron band arising from this orbital has the largest vibrational envelope. It has been shown in the case of N_2 [37,38], that averaging over various bond lengths, so allowing somewhat for the effects of vibration, instead of just using the ground state equilibrium bond length, can result in the removal of resonances while

leaving the partial channel cross section unchanged at other energies.

The MSXα results [60] are the reverse of the current results , underestimating the cross section between 23 and 48 eV. When the ground state potential is used, instead of the transition state potential, a minimum is produced at 30 eV. While neither the present nor the MSXα calculations agree well with experiment the present results are definitely superior above 30 eV.

5.10.4 6σ Orbital (IP = 20.1eV [56])

The $6\sigma \rightarrow k\sigma$ discrete excitation series of Table 5.17 form a weak Rydberg series in moderately good agreement with experiment and defect estimates, although the discrepancy between the defect estimate and the calculated value for the $6\sigma \rightarrow 3s\sigma$ excitation is suggestive of some intravalence contribution. However , contributions from the valence virtual σ orbitals are also expected above threshold so the corresponding cross section should have a large initial maximum owing to intervalence contributions above threshold. This is indeed the case (Figure 5.30), confirming the appearance of the 8σ and $9\sigma(\sigma^*)$ orbitals in the continuum with this static exchange potential.

It is interesting to compare this profile with the corresponding $4\sigma_g \rightarrow k\sigma_u$ profile in CO_2 [47]. There the resonance, arising from the $4\sigma_g \rightarrow 4\sigma_u$ transition,

is centered approximately 13eV above threshold, whereas in N_2O the resonance occurs just above threshold. This shift arises from the removal of the centre of inversion in N_2O. Here the 8σ and 9σ orbitals can have components of all angular momenta, whereas in CO_2, with respect to the centre of mass, the $5\sigma_g(\sigma^*)$ contains s and d contributions, and the $4\sigma_u(\sigma^*)$ orbital contains p and f contributions. A particular orbital in CO_2 can only have transitions to one of the σ^* valence like virtual orbitals, whereas in N_2O an electron in any orbital can be excited to either of the valence like 8σ or 9σ orbitals. Also, in CO_2, there is a separation of approximately 15eV between the $5\sigma_g$ orbital, which appears near threshold, and the $4\sigma_u$ orbital, which appears higher in the continuum. In N_2O the 8σ and 9σ orbitals occur close together, just above threshold. The result is that there is just one type of partial cross section profile possible for σ type orbitals in N_2O, an initial maximum at threshold, arising from $\sigma \rightarrow \sigma^*$ contributions, followed by a shoulder arising from increasing $\sigma \rightarrow \pi^*$ contributions, and then a monotonic decline. In CO_2 two profiles are possible, the one described above for σ_u type orbitals, and another, which is a maximum situated at about 15eV above threshold followed by a monotonic decline for σ_g type orbitals.

The $6\sigma \rightarrow k\pi$ discrete excitations (Table 5.17) form a weak Rydberg series perturbed by an intervalence transition, and so in only moderate agreement with experiment and defect estimates. This interloper is assigned to the $6\sigma \rightarrow 3\pi$

transition and the resulting $6\sigma \rightarrow k\pi$ continuum profile (Figure 5.30) is broad and weak, dominating the total cross section at high energy.

The two components of Figure 5.30 are combined in Figure 5.31 to yield the vertical $(6\sigma^{-1})C^2\Sigma^+$ partial channel cross section which is compared with (e,2e) [44] and synchrotron [60] measurements. Good agreement is obtained with the calculated curve. At lower photon energies the calculated curve almost exactly divides the two sets of experimental measurements.

MSXα calculations [60] place the resonance in the kσ contribution, resulting in a sharp peak in this contribution, at 35eV. This results in two minima, near 28 and 38eV photon energy. Below 55eV photon energy the MSXα results are always less than the experimental results. Thus the present results are considerably superior to the MSXα results.

5.10.5 Total Cross Section

The total photoionization cross section, obtained by summation of the partial cross sections, is displayed in Figure 5.32, where it is compared with the (e,2e) [44] measurements. While the theoretical curve is in qualitative agreement with the experimental measurements, there are substantial numerical discrepancies. At energies greater than 26eV the calculated values are smaller than the mea-

sured values. Potts and Williams [57] have assigned the 5σ and 4σ IP's values of 33.7 and 37.3eV respectively. As the calculations reported here are only concerned with the outer valence (6σ, 1π, 7σ, 2π) orbitals, it is expected that the sum of these partial cross sections, if exactly calculated, would fall below the actual value of the total cross section to the high energy side of 33eV.

Nitrous oxide has an extremely rich spectrum with a series of bands running almost continuously from 23 to 41eV [56]. The calculations of Domcke at al [58] reveal that several satellite peaks, involving the 4σ and 5σ orbitals, occur to the low energy side of the main 5σ band. The band centred at 28.7eV has been assigned to transitions involving the 4σ and 5σ orbitals and so the underestimate of the total cross section between 26 and 33eV may be understood as originating partially in the neglect of the inner valence orbitals in the calculation. There is another satellite peak centered at 24eV, of which the main component arises from the 1π orbital [58]. At the energy range in question the calculated 1π cross section is less than the experimental value for the $B^2\Pi$ state plus the intensity of the 24eV transition. Thus the neglect of the effect of the 4σ and 5σ orbitals combine with the underestimate of the 1π cross section to give an underestimate of the total cross section in the region 26 to 33eV.

It is evident from the graphs of the partial cross sections that the overestimate of the total cross section between 20 and 26eV originates with the

calculated 1π cross section, which, below 26eV very substantially overestimates the partial cross section. In this energy range all the other orbitals under consideration have calculated partial cross sections which are in very close agreement with experiment or slight underestimates. This results in a slight diminishment of the overestimate of the total cross section.

Overall the total cross section has a very simple structure. The calculation shows a rise to a maximum, arising from the superposition of the maxima of the various channels, followed by a monotonic decline where the declining tails of the various channels overlap. The experimental results do not extend to low enough energy to confirm the existence of an initial maximum. A shoulder experimental results, owing to the increased contributions of the various satellite peaks, is an effect which is not reflected in the theoretical results.

In these calculations the effects of autoionization from a discrete excitation series to an underlying continuum have been ignored. From the good agreement between the various calculated partial channel cross sections and experiment this does not seem to be a serious deficiency in these calculations.

MSXα calculations [60] upon this molecule have once again demonstrated the superior accuracy of the Stieltjes Tchebycheff moment imaging technique for calculating partial channel photoionization cross sections.

5.11 Conclusions

The Stieltjes Tchebycheff moment imaging technique, using the static exchange and frozen core approximations, permits the calculation of photoionization cross sections using conventional molecular orbital techniques. This means that it is possible to account for various prominent features in the partial cross sections in terms of contributions from valence virtual orbitals. In particular various resonances may be attributed to intervalence transitions, which lie in the continuum instead of the discrete spectral interval. Close agreement has generally been obtained between the theoretical partial channel cross sections and experimental result. The calculations reported here have demonstrated that the use of a large and flexible supplementary basis set, as well as a good ground state basis set, is of the greatest importance. In the case of C_2H_2 such basis set deficiencies let to the location of spurious intravalence transitions [24,29], which influenced the interpretation of the experimental results. Even when such dramatic results have not ensued, the values of the calculated cross sections have been affected by such deficiencies. Thus the computational cost of providing adequate basis sets would appear to be a major factor hindering the wider use of this technique.

The MSXα method has been widely used to calculate photoionization cross sections. While permitting interpretation of the experimental results, MSXα calculations generally are not in as close agreement with experimental mea-

surements as the moment imaging results. Such results are often very different in form to the experimental or moment theory partial channel photoionization cross sections.

While remaining useful in the exploration of the photoelectron dynamics of small molecules, it is, at present, difficult to forsee an extension of static exchange Stieltjes Tchebycheff moment imaging calculations, as reported in this thesis, to large molecules, as a result of the approximations employed.

Both the frozen core approximation, and the neglect of electron correlation effects, in the transition metal dihalide calculations reported in chapter 2,led to incorrect assignments of the photoelectron spectrum. It seems unlikely that these approximations could fail to introduce sufficient uncertainty into the calculated photoionization cross sections of large molecules, as to render assignments, based upon arguments arising from the detailed values of the calculated cross sections, dubious.

5.12 REFERENCES

1. C.M.Truesdale, S.Southworth, P.H.Kobrin, D.W.Lindle, G.Thornton and D.A.Shirley, *J. Chem. Phys.*, **76**, 860 (1978).

2. K.H.Tan, C.E.Brion, Ph.E.van der Leeuw and M.J.van der Wiel, *Chem. Phys.*, **29**, 299 (1978).

3. P.Gürtler, V.Saile and E.E.Koch, *Chem. Phys. Letts.*, **51**, 368 (1977).

4. O.Dutit, K.Ito, A.Tabche-Fouhaile, P.Morin, T.Baer, P.M.Guyon and I.Nenner, *Extended Abstracts of the Sixth International Conference on Vacumn Ultra Violet Radiation Physics*, (U.S. Naval Research Labratory, Washington, D.C. (1980) vol. 11-17).

5. J.Wayne Rabalais, T.P.Debies, J.L.Berkosky, J.T.J.Huang and F.O.Ellison, *J. Chem. Phys.*, **61**, 516 (1974).

6. T.P.Debies and J.W.Rabalais, *J. Am. Chem. Soc.*, **97**, 497 (1975).

7. S.Iwata and S.Nasakura, *Mol. Phys.*, **27**, 425 (1974).

8. G.R.Y.Williams and P.W.Langhoff, *Chem. Phys. Letts.*, **60**, 201 (1979).

9. G.H.F.Diercksen, W.P.Kramer, T.N.Rescigno, C.F.Bender, B.V.Mckoy, S.R.Langhoff and P.W.Langhoff, *J. Chem. Phys.*, **76**, 1043 (1982).

10. M.Roche, D.R.Sacahub and R.D.Messmer, *J. Elect. Spect. Rel. Phenom.*, **19**, 273 (1980).

11. T.H.Dunnings. Jr., *J. Chem. Phys.*, **53**, 2823 (1970).

12. Tables of interatomic distances and configurations in molecules and ions, *Special publication no.18*, The Chemical Society.

13. T.H.Dunnings,Jr., R.M.Pitzer and S.Aung, *J. Chem. Phys.*, **57**, 5044 (1972).

14. D.W.Turner, C.Baker, A.D.Baker and C.R.Brundle, *Molecular Photoionization Spectroscopy*, (Wiley New York 1970).

15. H.T.Wang, W.S.Felps and S.P.Mcglynn, *J. Chem. Phys.*, **67**, 2614 (1977).

16. R.S.Mulliken, *J. Chem. Phys.*, **3**, 517 (1938).

17. A.D.Mclean, J. Chem. Phys., **32**, 595 (1960).

18. A.D.Mclean, B.J.Ransil and R.S.Mulliken, *J. Chem. Phys.*, **32**, 1873 (1960).

19. P.H.Metzger and G.R.Cook, *J. Chem. Phys.*, **41**, 462 (1966).

20. R.Botter, V.F.Diebler, J.A.Walker and H.M.Rusenstock, *J. Chem. Phys.*, **44**, 1271 (1966).

21. T.Hayaishi, S.Iwata, M.Sasanuma, E.Ishiggro and Y.Morioka, *J. Phys. B*, **15**, 79 (1982).

22. W.C.Walker and G.L.Wiessler, *J. Chem. Phys.*, **23**, 1547 (1958).

23. R.I.Schoen, *J. Chem. Phys.*, **37**, 2032 (1962).

24. P.W.Langhoff, B.V.Mckoy, R.Unwin and A.M.Bradshaw, *Chem. Phys. Letts.*, **83**, 270 (1981).

25. E.Lindholm, *Arkiv För Fysik*, **40**, 97 (1969).

26. W.E.Krammer, *Chem. Letts.*, **6**, 529 (1970).

27. R.J.Buenker and S.D.Peymerimhoff, *J. Chem. Phys.*, **48**, 354 (1968).

28. R.G. Cavell and D.A.Allison, *J. Chem. Phys.*, **69**, 159 (1978).

29. L.E.Machado, E.P.Leal, G.Csanak, B.V.Mckoy and P.W.Langhoff, *J. Elect. Spect. Rel. Phenom.*, **25**, 1 (1982).

30. L.S.Cederbaum, W.Domcke, J.Schirmer, W.von Niessen, G.H.Diercksen and W.P.Kraemer, *J. Chem. Phys.*, **69**, 1591 (1976).

31. L.Åsbrink, C.Fridh and E.Lindholm, *Chem. Phys.*, **27**, 159 (1978).

32. R.Unwin, I.Khan, N.V.Richardson, A.M.Bradshaw, L.S.Cederbaum and W.Domcke, *Chem. Phys. Letts.*, **77**, 242 (1981).

33. J.Kreile, A.Schweig and W.Thiel, *Chem. Phys. Letts.*, **79**, 547 (1981).

34. A.D.Mclean and M.Yoshimne, *Supp. to IBM. J. Res. and Dev.*, (1967).

35. T.N.Rescigno, A.GErwer,B.V.Mckoy and P.W.Langhoff, *Chem. Phys. Letts.*, **66**, 116 (1974).

36. G.R.J.Williams and P.W.Langhoff, *Chem. Phys. Letts.*, **78**, 21 (1981).

37. J.L.Dehmer, D.Dill and S.Wallace, *Phys. Rev. Letts.*, **43**, 1005 (1979).

38. J.B.Weit, A.C.Parr, B.E.Cole, D.L.Ederer, R.Stockbauer and J.L.Dehmer, *J. Phys. B.*, **13**, L105 (1980).

39. T.N.Rescigno, C.F.Bender, B.V.Mckoy and P.W.Langhoff, *J. Chem. Phys.*, **68**, 970 (1978).

40. N.Padial, G.Csanak, B.V.Mckoy and P.W.Langhoff, *J. Chem. Phys.*, **69**, 2992 (1978).

41. R.Colin, M.Herman and I.Koop, in *'Communications Presentees au Colloque International d'Astrophysique, Liege 1977'*, no.21, 355.

42. M.Herman and R.Colin, *Physicia Scriptia*, **25**, 275 (1982).

43. G.Raseev, H.Le Rouzo and H.Lefebre-Brion, *J. Chem. Phys.*, **72**, 5701 (1980).

44. C.E.Brion and K.H.Tan, *Chem. Phys.*, **34**, 141 (1978).

45. M.Yoshimne and A.R.Mclean, *Int. J. Quant. Chem.*, **1S**, 313 (1967).

46. A.E.Orel, T.N.Rescigno, B.V.Mckoy and P.W.Langhoff, *J. Chem. Phys.*, **72**, 1265 (1980).

47. N.Padial, G.Csanak, B.V.Mckoy and P.W.Langhoff, *Phys. Rev. A*, **23**, 218 (1981).

48. J.J.Delaney, V.R.Saunders and I.H.Hillier, *J. Phys. B*, **14**, 819 (1981).

49. G.Thornton, S.H. Southworth ,R.A.Rosenberg, M.G.White and D.A.Shirley, Unpublished Results, (1980).

50. P.R.Keller, M.Mehaffy, J.W.Taylor, F.A. Grimm and T.A.Carlson, *J. Elect. Spect.*, **27**, 223 (1982).

51. A.C.Parr, D.L.Ederer, J.B.West, D.M.P.Holland and J.L. Dehmer, *J. Chem. Phys.*, **76**, 4349 (1982).

52. D.Lynch, M.T.Lee, R.R.Lucchese and V.McKoy, *J. Chem. Phys.*, **80**, 1907 (1984).

53. R.Mulliken, *J. Chem. Phys.*, **3**, 720 (1935).

54. E.Lindholm, *Arkiv För Fysik*, **40**, 129 (1969).

55. T.N.Rescigno, A.Gerwer, B.V.McKoy and P.W.Langhoff, *Chem. Phys. Letts.*, **66**, 116 (1979).

56. D.W.Turner, C.Baker, A.D.Baker and C.R.Brundle, in *Molecular Photoabsorption Spectroscopy* (Wiley, New York, 1970).

57. A.W.Potts and T.A.Williams, *J. Elect. Spect.*, **3**, 3 (1974).

58. W.Domcke, L.s.Cederbaum, J.Schirmer, W.Van Nieisen, C.E.Brion and K.H.Tan, *Chem. Phys.*, **40**, 171 (1979).

59. G.M.Truesdale, S.Southworth, P.H.Korbin, D.W.Lindle, and D.A.Shirley, *J. Chem. Phys.*, **78**, 7117 (1983).

60. T.A.Carlson, M.O.Krause, and F.A.Grimm, *J. Chem. Phys.*, **79**, 97 (1983).

Table 5.1

Supplemental Gaussian basis functions used in H_2O static-exchange calculations.

Location	Type	Number	Exponent Range[a]
Oxygen	s	7	1.6 – 0.00625
	p	6	1.6 – 0.0125
	d	5	0.2 – 0.0125
Hydrogen	s	6	1.6 – 0.0125
	p	6	0.4 – 0.0125

a) A geometric series variation was employed in the indicated range, but no exponent present in the ground state basis set is duplicated.

Table 5.1

Supplemental Gaussian basis functions used in H_2O static-exchange calculations.

Location	Type	Number	Exponent Range[a]
Oxygen	s	7	1.6 - 0.00625
	p	6	1.6 - 0.0125
	d	5	0.2 - 0.0125
Hydrogen	s	6	1.6 - 0.0125
	p	6	0.4 - 0.0125

a) A geometric series variation was employed in the indicated range, but no exponent present in the ground state basis set is duplicated.

Table 5.2

Calculated $1b_1$ Excitation Spectrum in H_2O

IP = 12.61eV [14]

Calculated Values		Quantum Defect Estimates[25]	Experimental Values[3]	Assignments
$\epsilon_i(eV)$	f_i	$\epsilon_i(eV)$	$\epsilon_i(eV)$	
$1b_1 \rightarrow nsa_1$				
7.44	0.02200	7.30	7.44/strong	$1b_1 \rightarrow 3sa_1$
10.60	0.00027	10.60	10.64/weak	$1b_1 \rightarrow 4sa_1$
11.65	0.00074	11.56		$1b_1 \rightarrow 5sa_1$
12.32	0.00854			
12.52	0.00096			
$1b_1 \rightarrow npa_1$				
9.95	0.00528	10.04	10.00	$1b_1 \rightarrow 3pa_1$
11.41	0.00216	11.36	11.37	$1b_1 \rightarrow 4pa_1$
12.10	0.00954	11.87	11.89	$1b_1 \rightarrow 5pa_1$
$1b_1 \rightarrow nda_1$				
11.04	0.00521	11.10	10.99	$1b_1 \rightarrow 3da_1$
11.16	0.00489		11.12	$3da_1$
11.90	0.00012	11.76	11.73	$1b_1 \rightarrow 4da_1$
11.98	0.00143			
$1b_1 \rightarrow npb_1$				
10.16	0.00073	10.04	10.17	$1b_1 \rightarrow 3pb_1$
11.61	0.00072	11.36	11.43	$1b_1 \rightarrow 4pb_1$
12.34	0.00964			
$1b_1 \rightarrow ndb_1$				
11.14	0.00390	11.10	11.06	$1b_1 \rightarrow 3db_1$
11.98	0.00023	11.76	11.77	$1b_1 \rightarrow 4db_1$
$1b_1 \rightarrow nda_2$				
11.08	0.00546	11.10	11.06	$1b_1 \rightarrow 3da_2$
11.91	0.00009	11.76		$1b_1 \rightarrow 4da_2$
12.21	0.01463			

Table 5.3

Calculated $3a_1$ Excitation Spectrum in H_2O

IP = 14.73eV [14]

Calculated Values		Defect Estimates[25]	Experimental Values[3]	Assignments
ϵ_i(eV)	f_i	ϵ_i(eV)	ϵ_i(eV)	
$3a_1 \rightarrow nsa_1$				
10.00	0.08603	9.42	9.85/0.09	$3a_1 \rightarrow 3sa_1$
12.82	0.01244	12.72	12.90/weak	$\rightarrow 4sa_1$
13.79	0.00538	13.68	14.2 /weak	$\rightarrow 5sa_1$
14.43	0.01048			
$3a_1 \rightarrow npa_1$				
12.25	0.00018	12.16		$3a_1 \rightarrow 3pa_1$
13.66	0.00116	13.48		$\rightarrow 4pa_1$
14.23	0.00359	13.99		$\rightarrow 5pa_1$
$3a_1 \rightarrow nda_1$				
13.16	0.00951	13.22		$3a_1 \rightarrow 3da_1$
13.27	0.00191			
14.01	0.00035	13.88		$\rightarrow 4da_1$
14.21	0.00359			
$3a_1 \rightarrow npb_1$				
12.12	0.00160	12.16		$3a_1 \rightarrow 3pb4_1$
13.62	0.00103	13.48		$\rightarrow 4pb_1$
14.44	0.01134			
$3a_1 \rightarrow ndb_1$				
13.27	0.00463	13.22		$3a_1 \rightarrow 3db_1$
14.10	0.00018	13.88		$\rightarrow 4db_1$
$3a_1 \rightarrow npb_2$				
11.52	0.03101	12.16	12.5/medium	$3a_1 \rightarrow 3pb_2$
13.36	0.00523	13.48	13.5/strong	$\rightarrow 4pb_2$
14.03	0.02275	13.99		$\rightarrow 5pb_2$
14.63	0.02652			
$3a_1 \rightarrow ndb_2$				
13.08	0.02985	13.22		$3a_1 \rightarrow 3db_2$
14.00	0.00026	13.88		$\rightarrow 4db_2$
14.17	0.00075	14.19		$\rightarrow 5db_2$

Table 5.4

Calculated $1b_2$ Excitation Spectrum in H_2O

IP = 18.55eV [14]

Calculated Values ϵ_i(eV)	f_i	Defect Estimates[25] $\epsilon_i(eV)$	Experimental Values[3] ϵ_i(eV)	Assignments
$1b_2 \rightarrow nsa_1$				
13.45	0.17112	13.24	13.8/strong	$1b_2 \rightarrow 3sa_1(4a_1)$
16.57	0.04559	16.54	16.9/medium	$4sa_1$
17.61	0.03090			$5sa_1$
18.30	0.00104			$6sa_1$
18.47	0.01443			
$1b_2 \rightarrow npa_1$				
15.97	0.01089	15.98		$1b_2 \rightarrow 3pa_1$
17.38	0.00084	17.30		$4pa_1$
18.05	0.01728			
$1b_2 \rightarrow nda_1$				
16.96	0.01125	17.04		$1b_2 \rightarrow 3da_1$
17.11	0.00000			
17.84	0.00091	17.70		$4da_1$
18.01	0.00549			
$1b_2 \rightarrow nda_2$				
17.01	0.00908	17.04		$1b_2 \rightarrow 3da_2$
17.84	0.00011	17.70		$4da_2$
18.13	0.01803			
$1b_2 \rightarrow npb_2$				
15.78	0.01250	15.98		$1b_2 \rightarrow 3pb_2$
17.34	0.00726	17.30		$4pb_2$
17.89	0.02290	17.81		$5pb_2$
18.01	0.00155			
$1b_2 \rightarrow ndb_2$				
16.95	0.02347	17.04		$1b_2 \rightarrow 3db_2$
17.82	0.00004	17.70		$4db_2$

Table 5.5

Calculated $2a_1$ Excitation Spectrum in H_2O

IP = 32.3eV $^2A_1$ [14]

Calculated Values ϵ_i(eV)	f_i	Defect Estimates[25] ϵ_i(eV)	Assignments
$2a_1 \rightarrow na_1$			
27.52	0.00523	26.89	$2a_1 \rightarrow 3sa_1$
30.29	0.00125	30.19	$2a_1 \rightarrow 4sa_1$
31.28	0.00021	31.15	$2a_1 \rightarrow 5sa_1$
31.91	0.00020	31.56	$2a_1 \rightarrow 6sa_1$
32.18	0.00239		
$2a_1 \rightarrow npa_1$			
29.58	0.00179	29.63	$2a_1 \rightarrow 3pa_1$
31.01	0.00131	30.95	$2a_1 \rightarrow 4pa_1$
31.66	0.00006	31.46	$2a_1 \rightarrow 5pa_1$
$2a_1 \rightarrow nda_1$			
30.59	0.00052	30.69	$2a_1 \rightarrow 3da_1$
30.73	0.00008		
31.48	0.00004	31.35	$2a_1 \rightarrow 4da_1$
31.64	0.00054		
$2a_1 \rightarrow npb_1$			
29.51	0.00222	29.63	$2a_1 \rightarrow 3pb_1$
31.05	0.00145	30.95	$2a_1 \rightarrow 4pb_1$
31.93	0.00026	31.46	$2a_1 \rightarrow 5pb_1$
$2a_1 \rightarrow ndb_1$			
30.76	0.00019	30.69	$2a_1 \rightarrow 3db_1$
31.54	0.00018	31.35	$2a_1 \rightarrow 4db_1$
$2a_1 \rightarrow npb_2$			
28.35	0.00696	29.63	$2a_1 \rightarrow 3pb_2$
30.79	0.00174	30.95	$2a_1 \rightarrow 4pb_2$
31.47	0.00000	31.46	$2a_1 \rightarrow 5pb_2$
31.98	0.00233	31.71	$2a_1 \rightarrow 6pb_2$
$2a_1 \rightarrow ndb_2$			
30.46	0.00125	30.69	$2a_1 \rightarrow 3db_2$
31.44	0.00038	31.35	$2a_1 \rightarrow 4db_2$
31.64	0.00023	31.66	$2a_1 \rightarrow 5db_2$

Table 5.6

Supplemental Gaussian basis furnctions used in C_2H_2

Static Exchange Calculations

Location	Type	Number	Exponent Range
Carbon Atoms	s	2	0.89 — 0.28
	p	2	0.64 — 0.21
	d	3	0.44 — 0.14
Hydrogen Atoms	s	1	0.34
	p	2	0.22 — 0.12
	d	3	0.44 — 0.14
Centre of mass	s	7	0.085 - 0.0025
	p	7	0.064 — 0.0018
	d	7	0.076 — 0.0023

Table 5.7

Static-exchange potentials and multiplicity factors in C_2H_2

Γ_i	$2\sigma_g$	$2\sigma_u$	$3\sigma_g$	$1\pi_u^x$	$1\pi_u^y$	μ_Γ
$1\pi_u^x \rightarrow k\sigma_g$	1/1	1/1	1/1	0.75/0	0.75/0	4
$1\pi_u^x \rightarrow k\pi_g^x$	1/1	1/1	1/1	0.25/ − 3	1.25/5	4
$1\pi_u^x \rightarrow k\delta_g^x$	1/1	1/1	1/1	0.75/1	0.75/1	8
$3\sigma_g \rightarrow k\sigma_u$	1/1	1/1	0.5/ − 1	1/1	1/1	2
$3\sigma_g \rightarrow k\pi_u^x$	1/1	1/1	0.5/ − 1	1/1	1/1	4
$2\sigma_u \rightarrow k\sigma_g$	1/1	0.5/ − 1	1/1	1/1	1/1	2
$2\sigma_u \rightarrow k\pi_g^x$	1/1	0.5/ − 1	1/1	1/1	1/1	4
$2\sigma_g \rightarrow k\sigma_u$	0.5/ − 1	1/1	1/1	1/1	1/1	2
$2\sigma_g \rightarrow k\pi_u^x$	0.5/ − 1	1/1	1/1	1/1	1/1	4

Table 5.8

$2\sigma_g$ Static Exchange Excitation Spectrum in C_2H_2

(IP= 23.65eV $^2\Sigma_g^+$)

Present Results ϵ_i(eV)	f_i	Assignments	Defect Estimates[25] ϵ_i(eV)
$(2\sigma_g^{-1})\,^1\Sigma_g^+ \rightarrow (np\sigma_u)\,^1\Sigma_u^+$			$\delta = 0.7$
21.10	0.00075	$2\sigma_g \rightarrow 3p\sigma_u$	21.08
22.43	0.00004	$2\sigma_g \rightarrow 4p\sigma_u$	22.40
22.93	0.0	$2\sigma_g \rightarrow 5p\sigma_u$	22.91
23.32	0.00002		
$(2\sigma_g^{-1})\,^1\Sigma_g^+ \rightarrow (np\pi_u)\,^1\Pi_u$			$\delta = 0.7$
21.32	0.00107	$2\sigma_g \rightarrow 3p\pi_u$	21.08
22.50	0.00054	$2\sigma_g \rightarrow 4p\pi_u$	22.40
22.96	0.00028	$2\sigma_g \rightarrow 5p\pi_u$	22.91
23.26	0.00038	$2\sigma_g \rightarrow 6p\pi_u$	23.17

Table 5.9

$2\sigma_u$ Static Exchange Excitation Spectrum in C_2H_2

(IP = 18.75eV $B\,^2\Sigma_u^+$)

Present Results $\epsilon_i(eV)$	f_i	*Assignments*	*Defect Estimates*[25] $\epsilon_i(eV)$
$(2\sigma_u^{-1})\,^1\Sigma_g^+ \rightarrow (ns\sigma_g)\,^1\Sigma_u^+$			$\delta = 0.95$
15.81	0.00691	$2\sigma_u \rightarrow 3s\sigma_g$	15.51
17.40	0.00355	$2\sigma_u \rightarrow 4s\sigma_g$	17.29
17.97	0.00172	$2\sigma_u \rightarrow 5s\sigma_g$	17.92
18.44	0.00195		
$(2\sigma_u^{-1})\,^1\Sigma_g^+ \rightarrow (nd\sigma_g)\,^1\Sigma_u^+$			$\delta = 0.50$
16.91	0.06865	$2\sigma_u \rightarrow 3d\sigma_g$	16.57
17.77	0.02542	$2\sigma_u \rightarrow 4d\sigma_g$	17.64
18.15	0.01412	$2\sigma_u \rightarrow 5d\sigma_g$	18.08
18.53	0.02518		
$(2\sigma_u^{-1})\,^1\Sigma_g^+ \rightarrow (nd\pi_g)\,^1\Pi_u$			$\delta = 0.06$
15.67	0.79206	$2\sigma_u \rightarrow 1\pi_g(\pi^*)$	
17.45	0.04191	$2\sigma_u \rightarrow 3d\pi_g$	17.18
18.00	0.01281	$2\sigma_u \rightarrow 4d\pi_g$	17.87
18.30	0.00958	$2\sigma_u \rightarrow 5d\pi_g$	18.19

Table 5.10

$3\sigma_g$ Static Exchange Excitation Spectrum in C_2H_2.

(IP = 16.75eV $A\,^2\Sigma_g^+$)

Present Results $\epsilon_i(eV)$	f_i	*Defect Estimates*[25] $\epsilon_i(eV)$	*Experimental Results*[41] $\epsilon_i(eV)$	*Assignments*
$(3\sigma_g^{-1})^1\Sigma_g^+ \rightarrow (np\sigma_u)^1\Sigma_u^+$		$\delta = 0.7$		
14.06	0.177017	14.18	-/0.1623	$3\sigma_g \rightarrow 3p\sigma_u$
15.49	0.069311	15.50	15.3/0.0514	$3\sigma_g \rightarrow 4p\sigma_u$
16.01	0.036342	16.01		$3\sigma_g \rightarrow 5p\sigma_u$
16.31	0.040345	16.27		$3\sigma_g \rightarrow 6p\sigma_u$
$(3\sigma_g^{-1})^1\Sigma_g^+ \rightarrow (np\pi_u)^1\Pi_u$		$\delta = 0.7$		
14.52	0.023214	14.18	(14.35)14.12/0.0104	$3\sigma_g \rightarrow 3p\pi_u$
15.63	0.008885	15.50	(15.28)15.28/0.0030	$3\sigma_g \rightarrow 4p\pi_u$
16.07	0.004307	16.01	15.74	$3\sigma_g \rightarrow 5p\pi_u$
16.38	0.005764	16.27	16.0	$3\sigma_g \rightarrow 6p\pi_u$

Table 5.11

$1\pi_u$ Excitation Spectrum in C_2H_2 (IP = 11.43eV $X^2\Pi_u$)

Present Results $\epsilon_i(eV)$	f_i	*Experimental Results*[41] $\epsilon_i(eV)$	*Assignments*	*Defect Estimates*[25] $\epsilon_i(eV)$
$(1\pi_u^{-1})^1\Sigma_g^+ \rightarrow (ns\sigma_g)^1\Pi_u$				$\delta = 0.95$
8.34	0.19226	8.16	$1\pi_u \rightarrow 3s\sigma_g$	8.19
10.04	0.03256	9.93	$1\pi_u \rightarrow 4s\sigma_g$	9.97
10.64	0.01343	10.57	$1\pi_u \rightarrow 5s\sigma_g$	10.60
11.08	0.04266	10.87	$1\pi_u \rightarrow 6s\sigma_g$	10.90
11.20	0.00243			
$(1\pi_u^{-1})^1\Sigma_g^+ \rightarrow (nd\sigma_g)^1\Pi_u$				$\delta = 0.50$
9.60	0.11298	9.24	$1\pi_u \rightarrow 3d\sigma_g$	9.25
10.45	0.03784	10.31	$1\pi_u \rightarrow 4d\sigma_g$	10.32
10.83	0.01588	10.74	$1\pi_u \rightarrow 5d\sigma_g$	10.76
$(1\pi_u^{-1})^1\Sigma_g^+ \rightarrow (nd\pi_g)^1\Sigma_u^+$				$\delta = 0.06$
9.84	0.14250	9.27	$1\pi_u \rightarrow 3d\pi_g$	9.86
10.54	0.07482	10.32	$1\pi_u \rightarrow 4d\pi_g$	10.55
10.88	0.05057	10.75	$1\pi_u \rightarrow 5d\pi_g$	10.87
11.26	0.11047	10.96		
$(1\pi_u^{-1})^1\Sigma_g^+ \rightarrow (nd\delta_g)^1\Pi_u$				$\delta = 0.0$
9.94	0.11806	9.98	$1\pi_u \rightarrow 3d\delta_g$	9.92
10.58	0.06685	10.59	$1\pi_u \rightarrow 4d\delta_g$	10.58
10.90	0.04872	10.88	$1\pi_u \rightarrow 5d\delta_g$	10.89
11.30	0.10945	11.06		

Table 5.12

Static-Exchange Potentials and Multiplicity Factors in N_2O[a,b]

Γ	6σ	$1\pi_x$	$1\pi_y$	7σ	$2\pi_x$	$2\pi_y$	μ_Γ
$6\sigma \rightarrow k\sigma$	1/−1	1/1	1/1	1/1	1/1	1/1	2
$6\sigma \rightarrow k\pi_x$	1/−1	1/1	1/1	1/1	1/1	1/1	4
$1\pi_x \rightarrow k\sigma$	1/1	0.75/0	0.75/0	1/1	1/1	1/1	4
$1\pi_x \rightarrow k\pi_x$	1/1	0.25/−3	1.25/5	1/1	1/1	1/1	4
$1\pi_x \rightarrow k\delta_{xy}$	1/1	0.75/−1	0.75/3	1/1	1/1	1/1	8
$7\sigma \rightarrow k\sigma$	1/1	1/1	1/1	1/−1	1/1	1/1	2
$7\sigma \rightarrow k\pi_x$	1/1	1/1	1/1	1/−1	1/1	1/1	4
$2\pi_x \rightarrow k\sigma$	1/1	1/1	1/1	1/1	0.75/0	0.75/0	4
$2\pi_x \rightarrow k\pi_x$	1/1	1/1	1/1	1/1	0.25/−3	1.25/5	4
$2\pi_x \rightarrow k\delta_{xy}$	1/1	1/1	1/1	1/1	0.75/−1	0.75/3	8

a) values of the coefficients a_i^Γ, b_i^Γ in eqn.(5.5) b) The $1\sigma - 5\sigma$ orbitals remain doubly occupied here $a_c^\Gamma = b_c^\Gamma = 1$

Table 5.13

Supplemental Gausian basis functions used in N_2O

Static Exchange Calculations

Location	Type	Number	Exponent Range[a]
Terminal	s	2	0.39 — 0.12
Nitrogen	p	2	0.30 — 0.09
	d	3	0.45 — 0.14
Central	s	10	0.39 — 0.001
Nitrogen	p	9	0.30 — 0.0016
	d	10	0.45 — 0.0024
Oxygen	s	3	0.53 — 0.09
	p	2	0.4 — 0.12
	d	3	0.54 — 0.17

a) A geometric Series variation is employed in the indicated ranges, but no oxponents already present in the ground state basis set is duplicated.

Table 5.14

2π Excitation Spectrum in N_2O (IP = 12.9eV)

Present Results $\epsilon_i(eV)$	f_i	Experimental Results[54] ϵ_i(eV)	Defect Estimates[54] ϵ_i(eV)
$(2\pi)^1\Sigma^+ \rightarrow (ns\sigma)^1\Pi$			
8.73	0.00440	9.50/strong	9.49
11.43	0.00002	11.38	11.38
12.06	0.00001	12.05	12.05
12.38	0.00001		12.36
12.79	0.00001		
$(2\pi)^1\Sigma^+ \rightarrow (np\sigma)^1\Pi$			
10.70	0.02596		10.37
11.80	0.01061		11.66
12.23	0.00529		12.17
12.47	0.00009		12.41
$(2\pi)^1\Sigma^+ \rightarrow (nd\sigma)^1\Pi$			
11.03	0.00209	10.97/weak	10.97
11.87	0.00117	11.88	11.88
12.25	0.00077		12.27
12.49	0.00660		12.48
$(2\pi)^1\Sigma^+ \rightarrow (np\pi)^1\Sigma^+$			
10.25	0.13554	10.54/strong	10.69
11.63	0.05578	11.77	11.78
12.15	0.02801	12.23	12.22
12.42	0.02057		12.45
12.83	0.06644		
$(2\pi)^1\Sigma^+ \rightarrow (nd\pi)^1\Sigma^+$			
11.47	0.00232	11.28/strong	11.28
12.09	0.00155		12.01
12.41	0.00314		12.33
$(2\pi)^1\Sigma^+ \rightarrow (nd\delta)^1\Pi$			
11.34	0.00237		11.39
12.02	0.00128		12.05
12.34	0.00092		12.36
12.76	0.00204		12.52

Table 5.15

7σ Excitation Spectrum in N_2O (IP = 16.4eV)

Present Results		Experimental Results [54]	Defect Estimates [54]
ϵ_i(eV)	f_i	ϵ_i(eV)	ϵ_i(eV)
$(7\sigma)^1\Sigma^+ \rightarrow (ns\sigma)^1\Sigma^+$			
12.41	0.06193	12.37/strong	13.00
15.03	0.02078	14.89	14.89
15.60	0.01201	15.53	15.55
15.89	0.00997		15.86
16.03	0.00224		16.02
16.30	0.02678		
$(7\sigma)^1\Sigma^+ \rightarrow (np\sigma)^1\Sigma^+$			
13.93	0.00189	13.90/medium	13.89
15.19	0.00000	15.16	15.17
15.67	0.00004	15.71	15.67
15.96	0.00340		15.92
$(7\sigma)^1\Sigma^+ \rightarrow (nd\sigma)^1\Sigma^+$			
14.72	0.01977	14.62/weak	14.64
15.47	0.00983	15.44	15.45
15.81	0.00511	15.80	15.80
$(7\sigma)^1\Sigma^+ \rightarrow (np\pi)^1\Pi$			
10.38	0.14842		
13.76	0.00466	14.02/medium	14.02
15.12	0.00304	15.16	15.22
15.64	0.00159	15.71	15.69
15.92	0.00010		15.93
16.31	0.00563		
$(7\sigma)^1\Sigma^+ \rightarrow (nd\pi)^1\Pi$			
15.01	0.00258	14.84/strong	14.84
15.59	0.00136	15.53	15.52
15.90	0.00223		15.84

Table 5.16

1π Excitation Spectrum in N_2O (IP = 18.22eV)

Present Results ϵ_i(eV)	f_i	Defect Estimates[54] ϵ_i(eV)
$(1\pi)^1\Sigma^+ \rightarrow (ns\sigma)^1\Pi$		
13.95	0.29598	14.82
16.77	0.00032	16.71
17.39	0.00002	17.37
17.71	0.00006	17.68
18.08	0.00016	
$(1\pi)^1\Sigma^+ \rightarrow (np\sigma)^1\Pi$		
16.07	0.00102	15.69
17.14	0.00085	16.99
17.57	0.00071	17.49
17.81	0.00327	17.72
$(1\pi)^1\Sigma^+ \rightarrow (nd\sigma)^1\Pi$		
16.35	0.05538	16.34
17.20	0.01439	17.22
17.59	0.00464	17.60
17.84	0.00025	17.80
$(1\pi)^1\Sigma^+ \rightarrow (np\pi)^1\Sigma^+$		
15.77	0.00025	15.90
17.04	0.00018	17.06
17.52	0.00015	17.52
17.79	0.00015	17.76
18.17	0.00933	
$(1\pi)^1\Sigma^+ \rightarrow (nd\pi)^1\Sigma^+$		
16.79	0.00104	16.65
17.42	0.00087	17.34
17.73	0.00118	17.66
$(1\pi)^1\Sigma^+ \rightarrow (nd\delta)^1\Pi$		
16.61	0.08816	16.71
17.33	0.04682	17.37
17.67	0.03142	17.68
18.06	0.06572	

Table 5.17

6σ Excitation Spectrum in N_2O (IP = 20.10eV)

Present Results ϵ_i(eV)	f_i	Experimental Results[54] ϵ_i(eV)	Defect Estimates[54] ϵ_i(eV)
$(6\sigma)^1\Sigma^+ \rightarrow (ns\sigma)^1\Sigma^+$			
15.89	0.06132		16.68
18.70	0.00889		18.57
19.30	0.00494		19.23
19.61	0.00434		19.54
20.03	0.01321		
$(6\sigma)^1\Sigma^+ \rightarrow (np\sigma)^1\Sigma^+$			
17.83	0.00123	17.56/weak	17.55
18.98	0.00004	18.87	18.85
19.43	0.0000	19.38	19.35
19.70	0.00370		19.60
$(6\sigma)^1\Sigma^+ \rightarrow (nd\sigma)^1\Sigma^+$			
18.30	0.01842	18.27/medium	18.20
19.12	0.00900	19.11	19.08
19.49	0.00481	19.49	19.46
19.72	0.00067		19.66
$(6\sigma)^1\Sigma^+ \rightarrow (np\pi)^1\Pi$			
15.45	0.40029		
17.56	0.00001	17.72/weak	17.76
18.87	0.00031	18.96	18.92
19.37	0.00022	19.42	19.38
19.65	0.00001		19.62
20.04	0.00336		
$(6\sigma)^1\Sigma^+ \rightarrow (nd\pi)^1\Pi$			
18.70	0.00597	18.55/strong	18.51
19.30	0.00250	19.25	19.20
19.61	0.00209	19.56	19.52

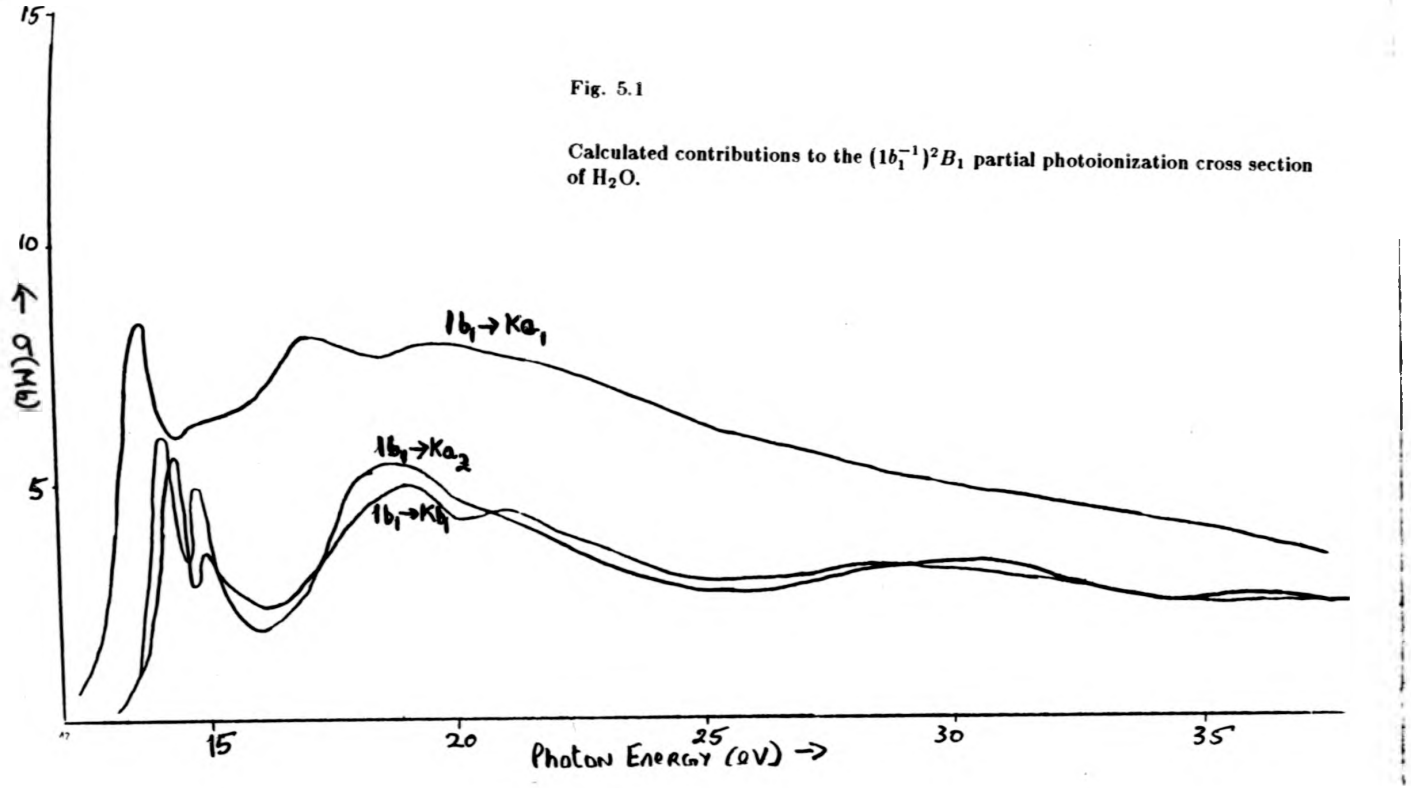

Fig. 5.1

Calculated contributions to the $(1b_1^{-1})^2B_1$ partial photoionization cross section of H_2O.

Fig. 5.2

Calculated $(1b_1^{-1})^2B_1$ partial channel photoionization cross section of H_2O.

data from Ref. 4 □

data from Ref. 2 ●

data from Ref. 1 ○

data from Ref.49 I

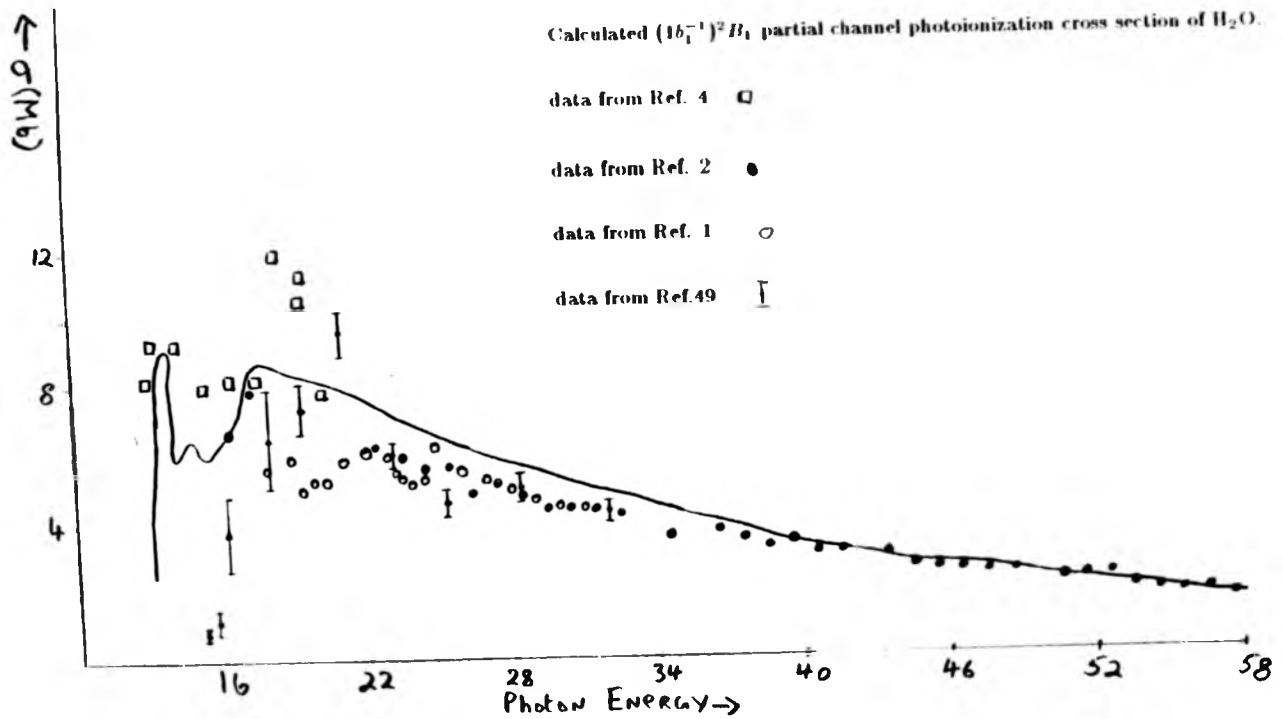

Fig. 5.3

Calculated contributions to the $(3a_1^{-1})^2 A_1$ partial channel photoionizattion cross section of H_2O.

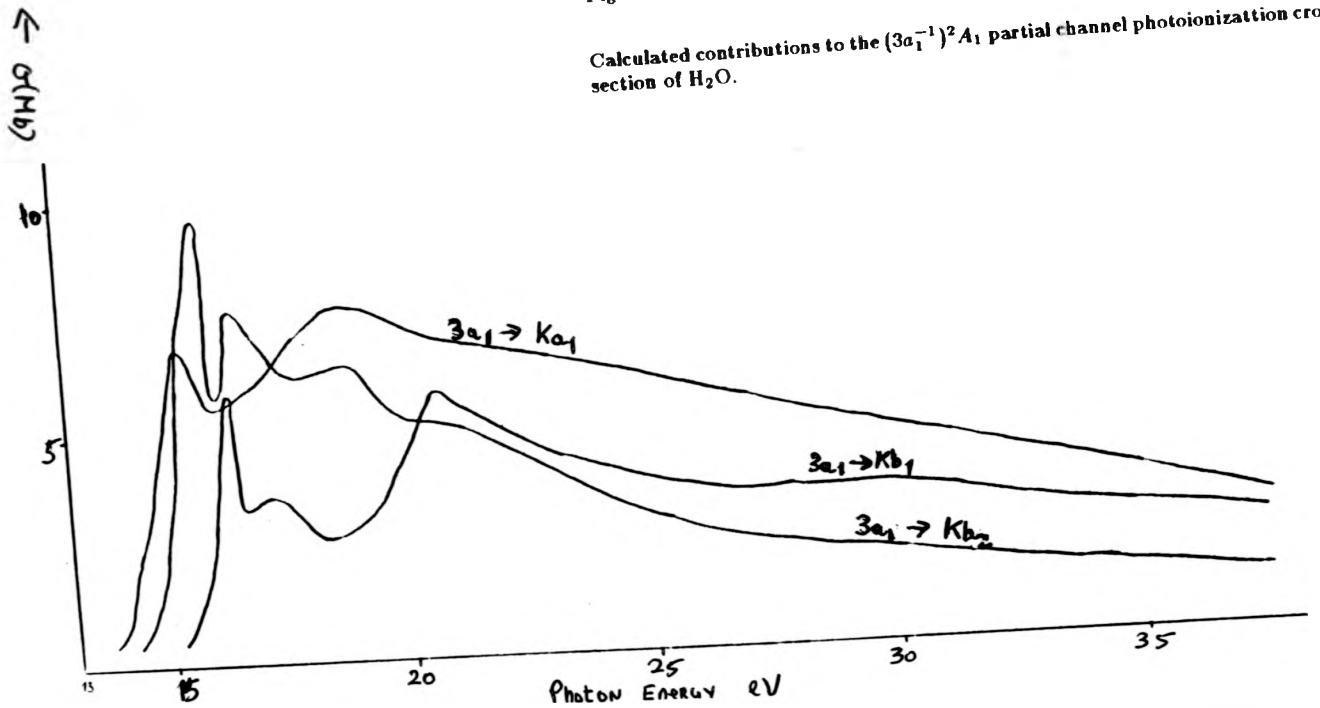

Fig. 5.4

Calculated $(3a_1^{-1})^2A_1$ partial channel photoionization cross section of H_2O.

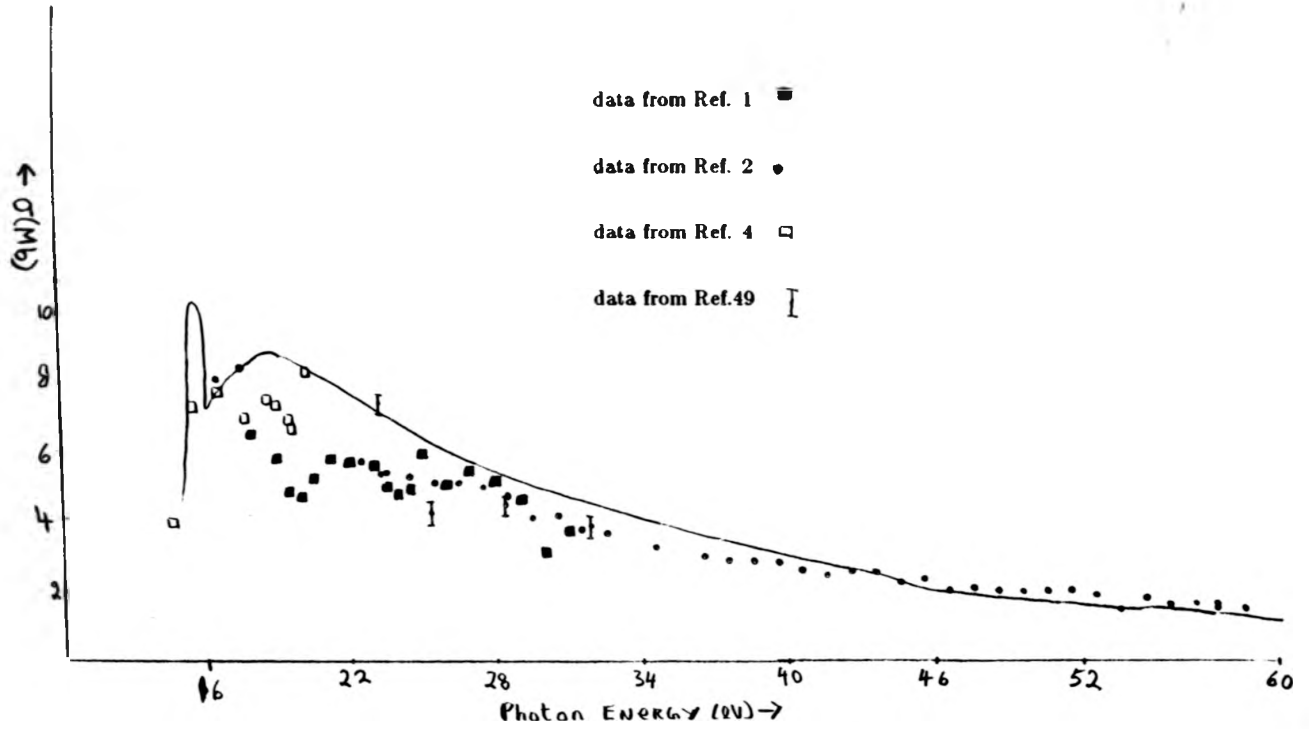

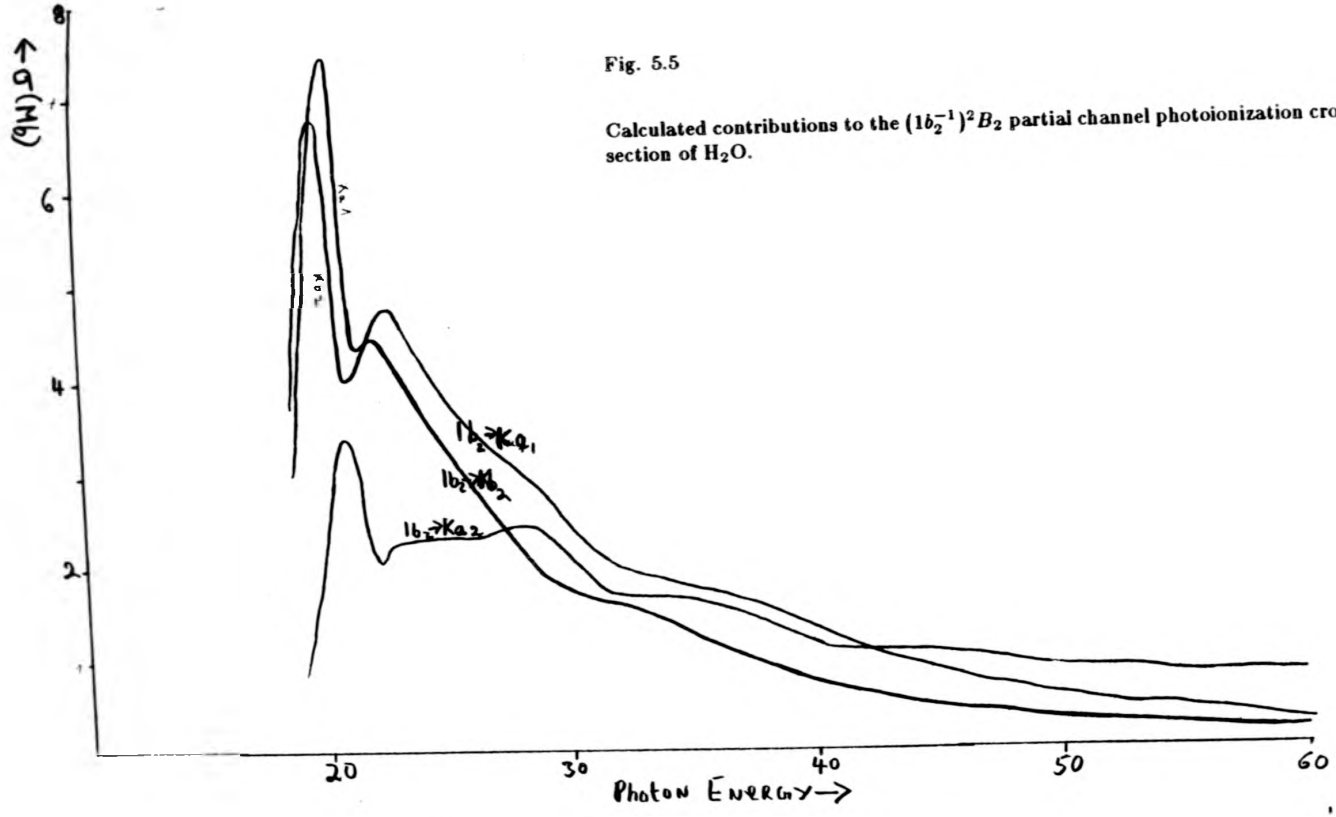

Fig. 5.5

Calculated contributions to the $(1b_2^{-1})^2B_2$ partial channel photoionization cross section of H_2O.

Fig. 5.6

Calculated $(1b_2^{-1})^2B_2$ partial channel photoionization cross section of H_2O.

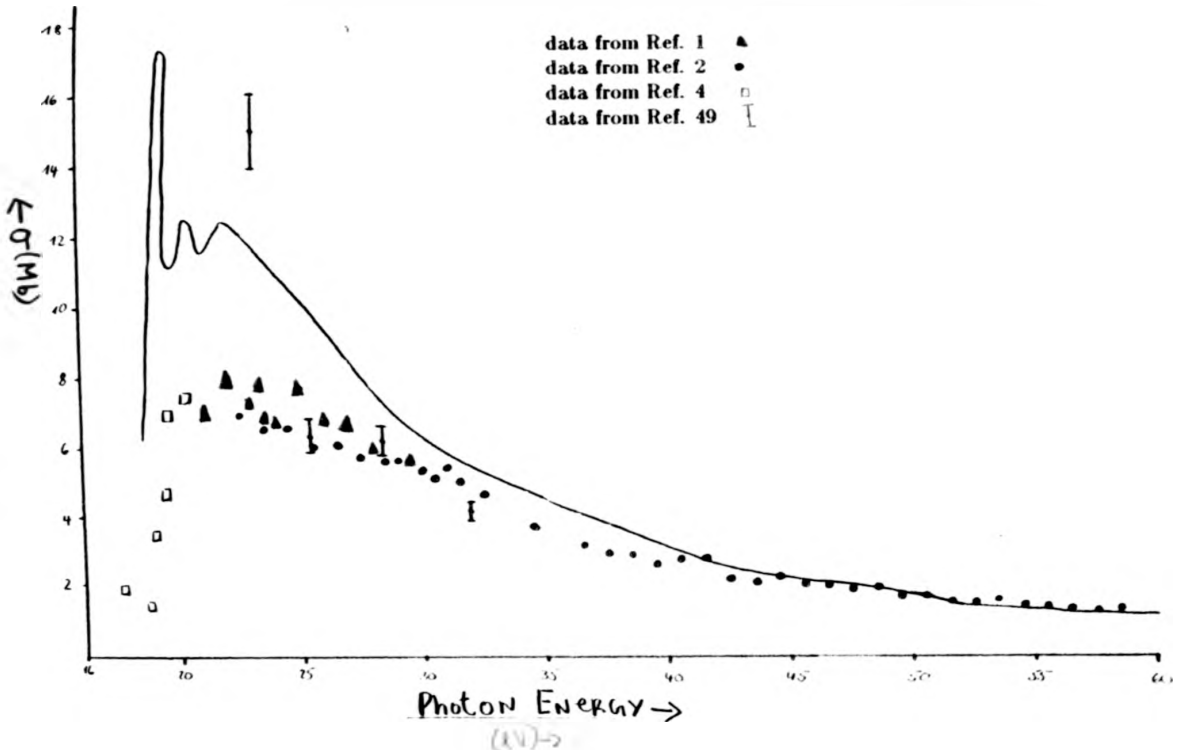

Fig. 5.7

Calculated contributions to the $(2a_1^{-1})^2A_1$ partial channel photoionization cross section of H_2O.

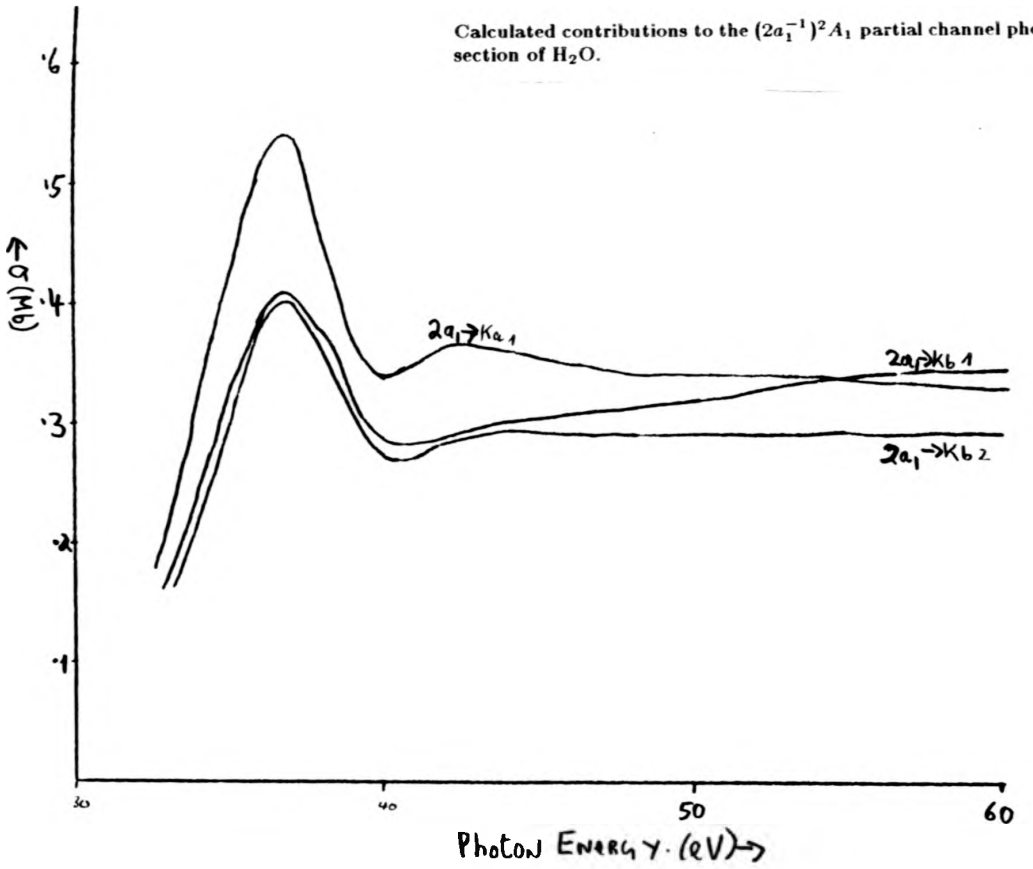

Fig. 5.8

Calculated $(2a_1^{-1})^2 A_1$ partial channel photoionization cross section of H_2O.

data of Ref. 2 •

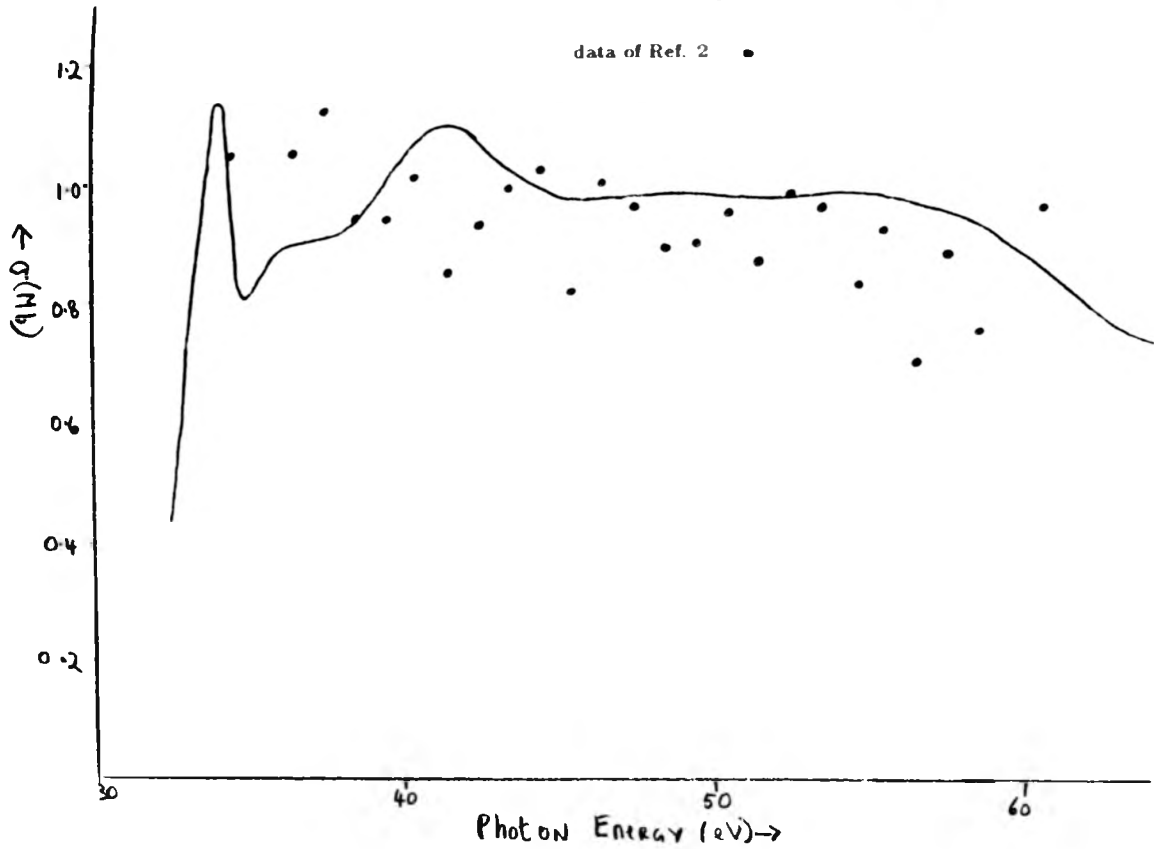

Fig. 5.9

Calculated total photoionization cross section of H_2O

data from Ref. 1 ■
data from Ref. 2 •
data from Ref.49 [

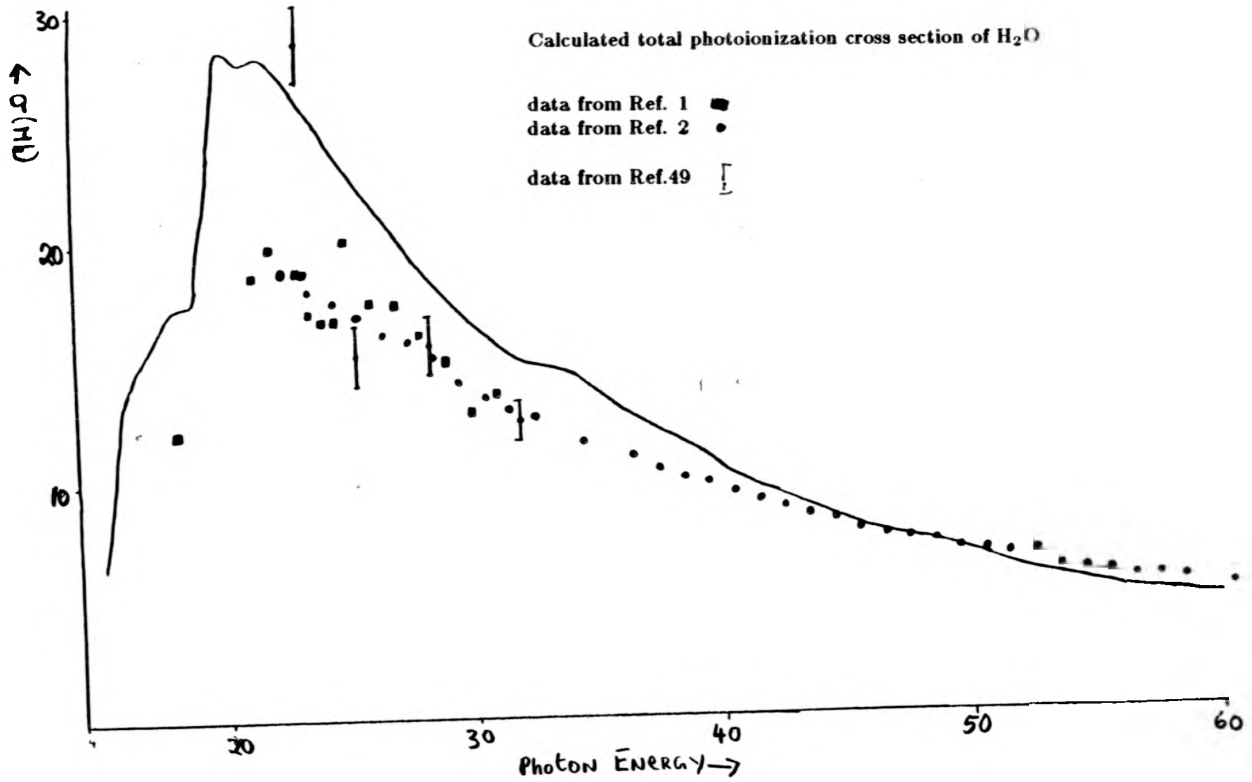

Fig. 5.10

Calculated pseudospectra, 9 and 6 point fits to the $(6a_1^{-1})^2B_1$ partial channel photoionization cross section of H_2O.

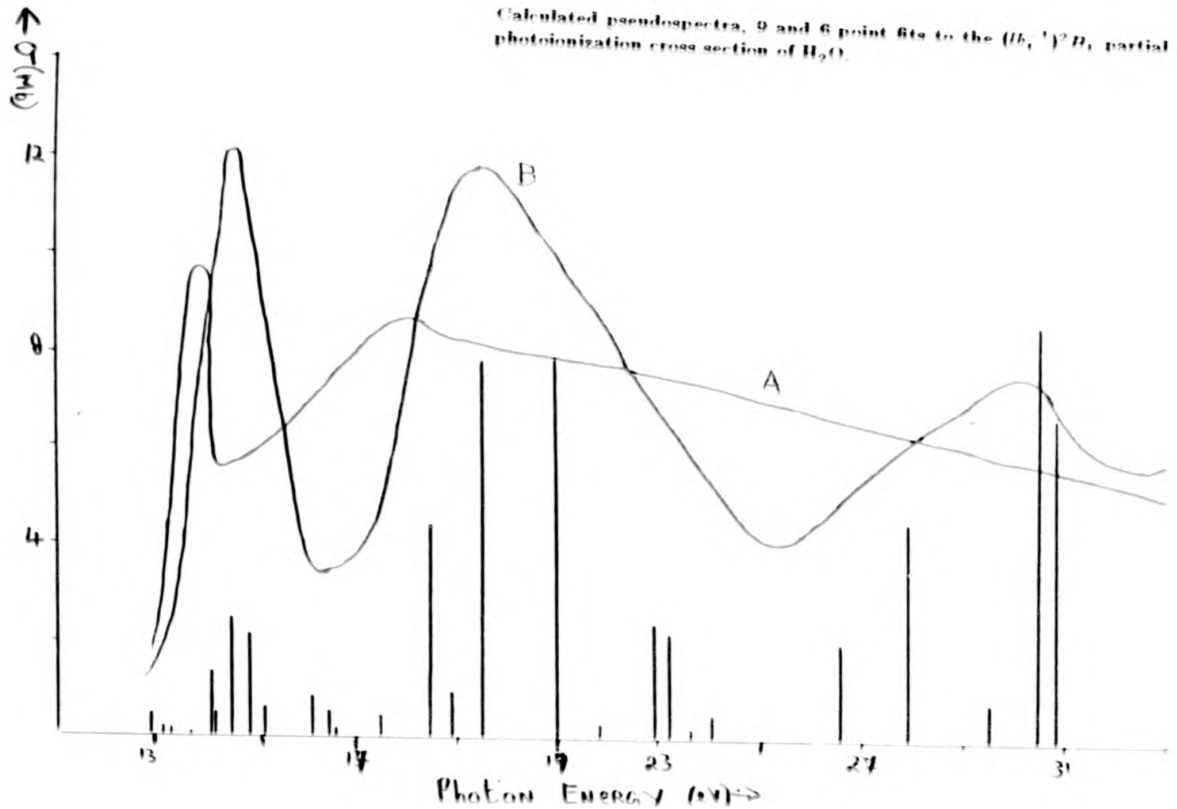

Fig. 5.11

Calculated pseuospectra, 9 and 6 point fits to the $(3a_1^{-1})^2A_1$ parial channel photoionization cross section of H_2O.

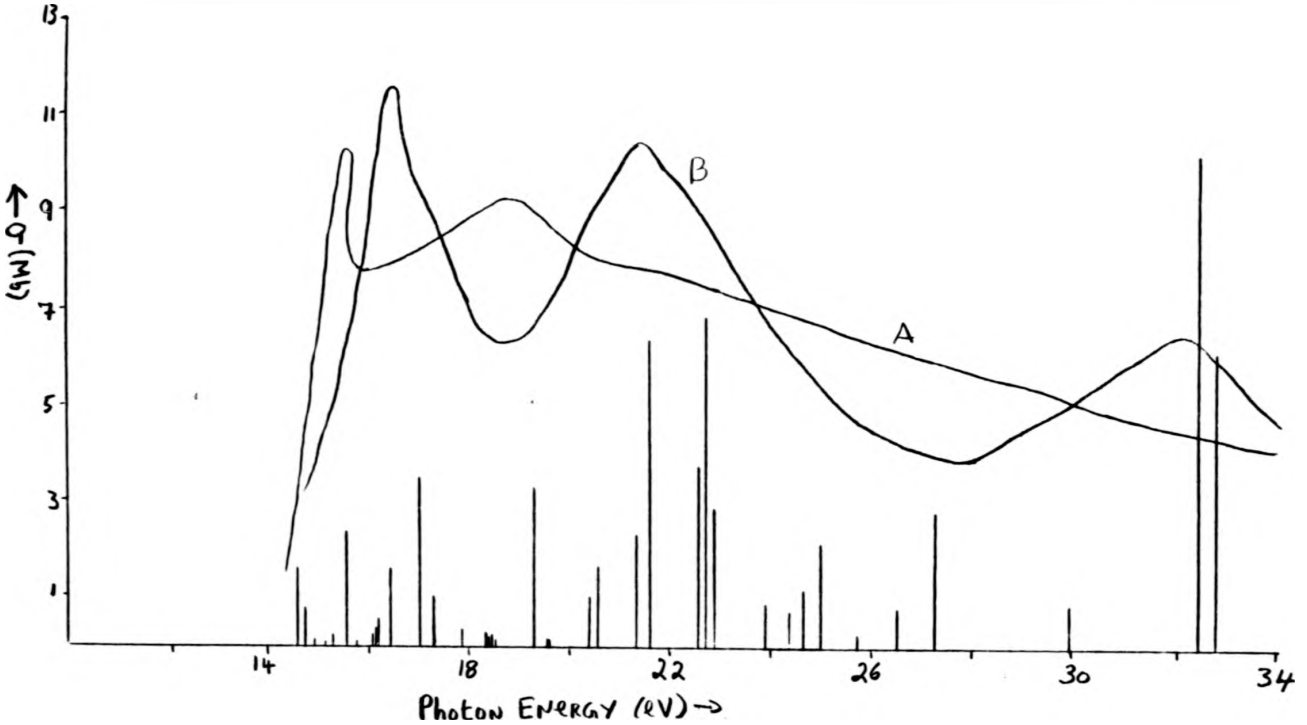

Fig. 5.12

Calculated pseudospectra, 9 and 6 point fits to the $(1b_2^{-1})^2B_2$ partial channel photoionization cross section of H_2O.

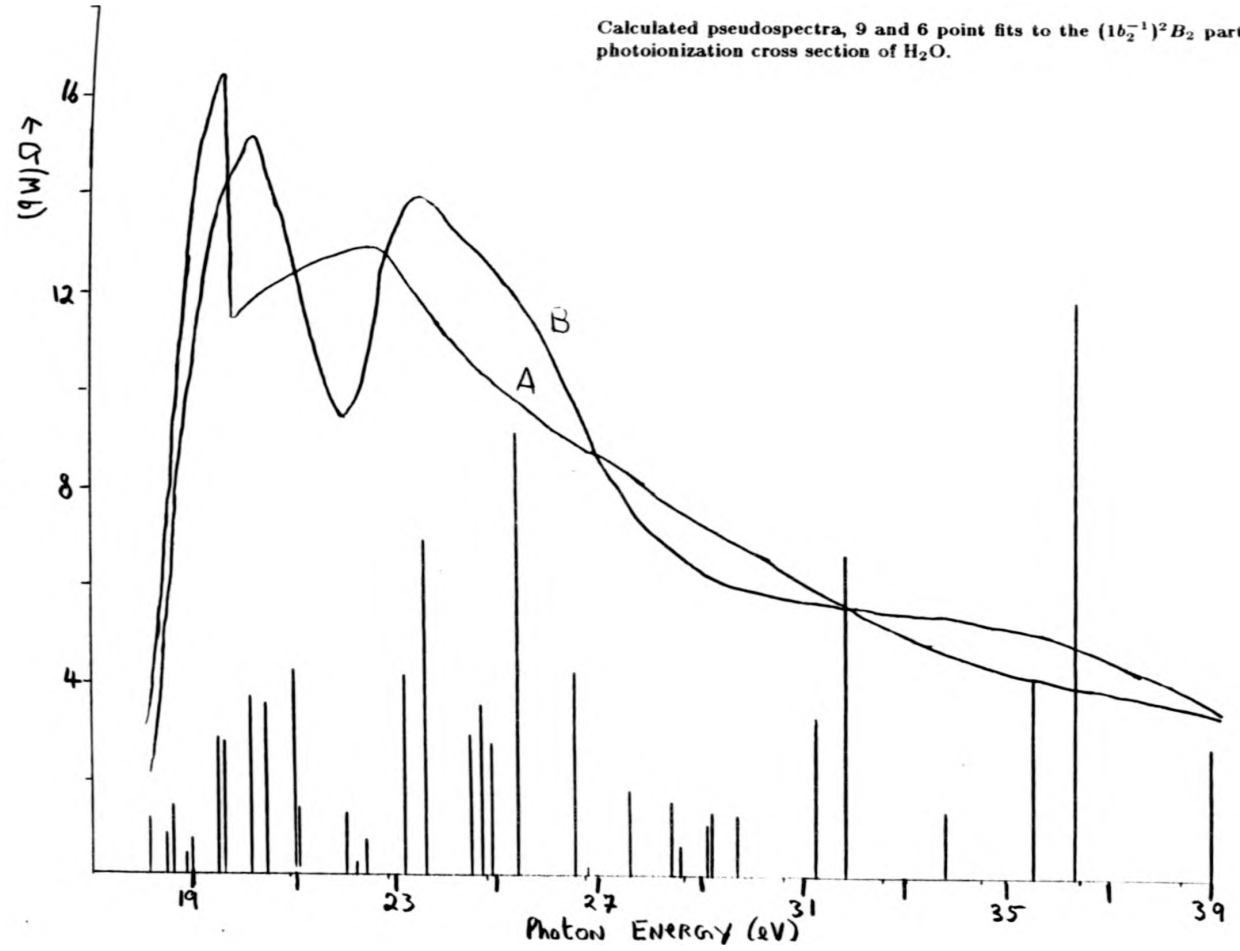

Fig. 5.13

Calculated contributions to the $(2\sigma_g^{-1})^2\Sigma^+$ partial channel photoionization cross section of C_2H

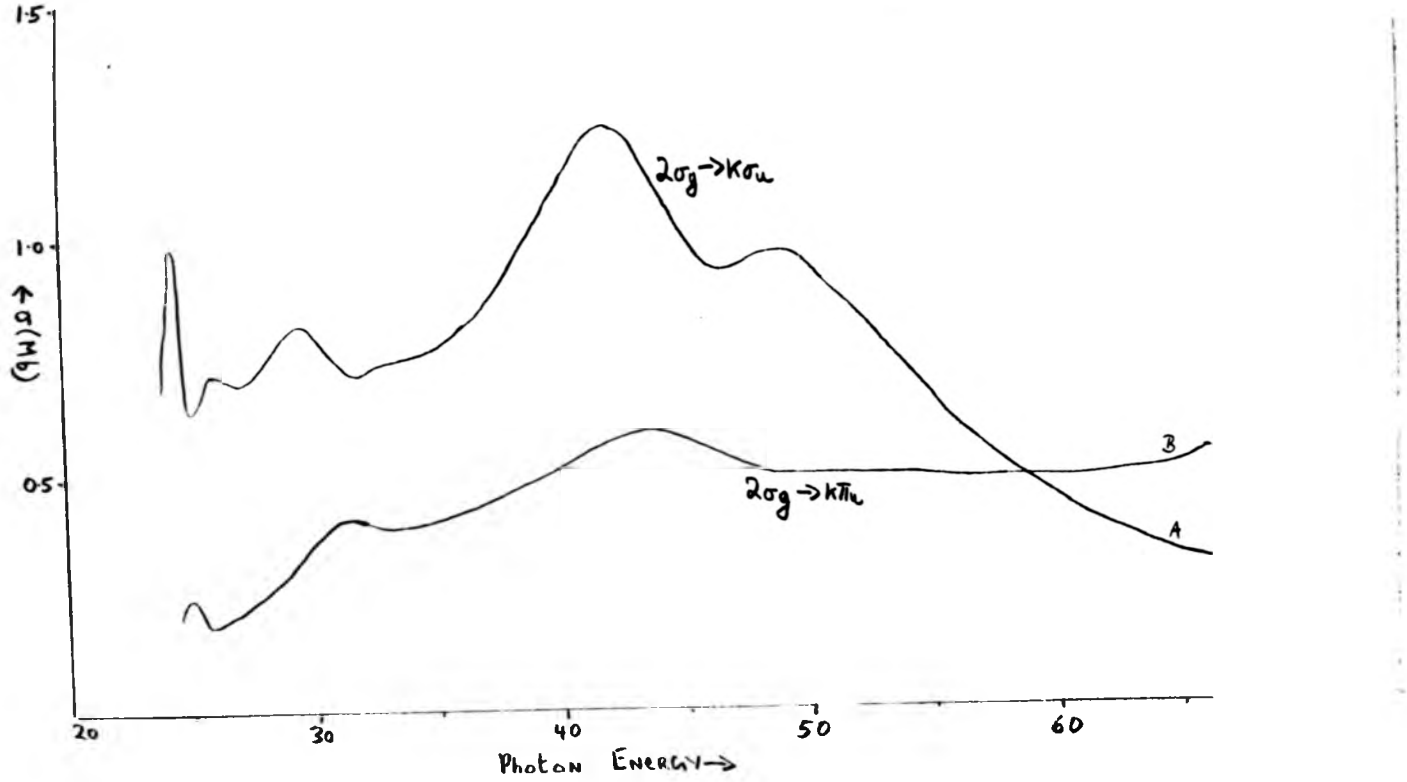

Fig. 5.14

Calculated $(2\sigma_g^{-1})^2\Sigma_g^+$ partial channel photoionization cross section in C_2H_2.

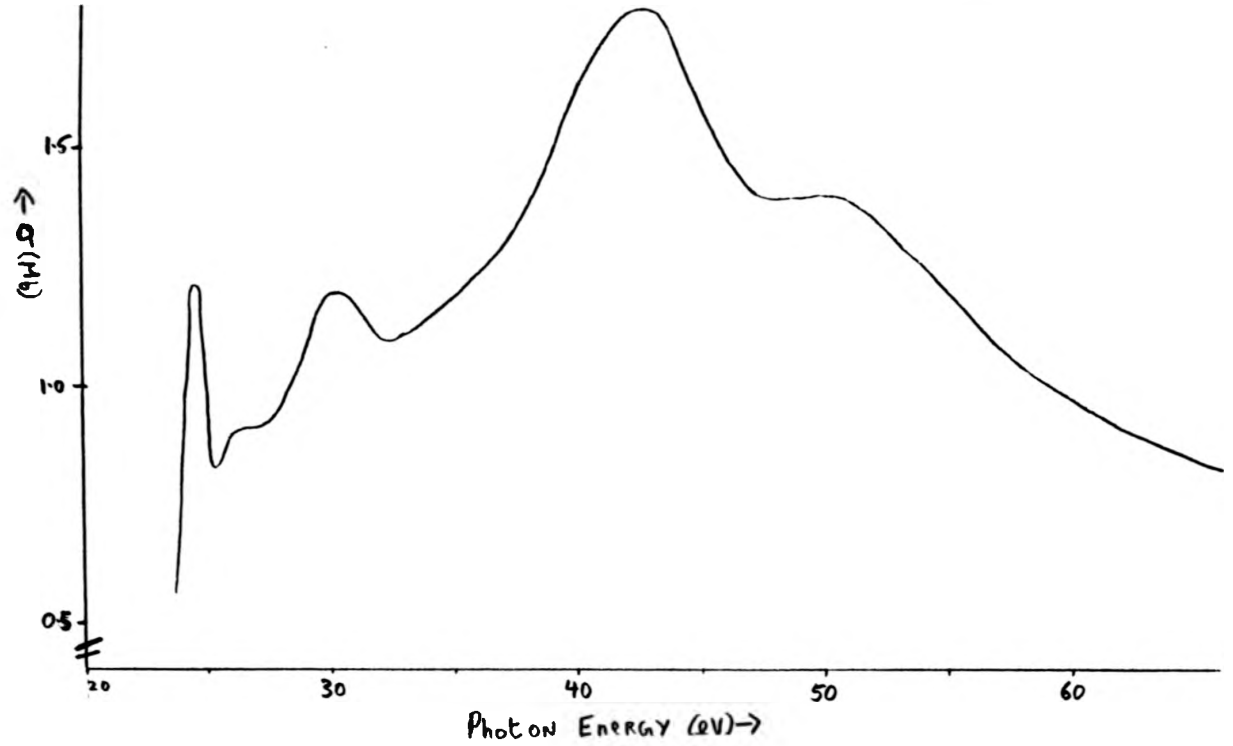

Fig. 5.15

Calculated contribution to the $(2\sigma_u^{-1})B^2\Sigma_u^+$ photoionization cross section of C_2H_2.

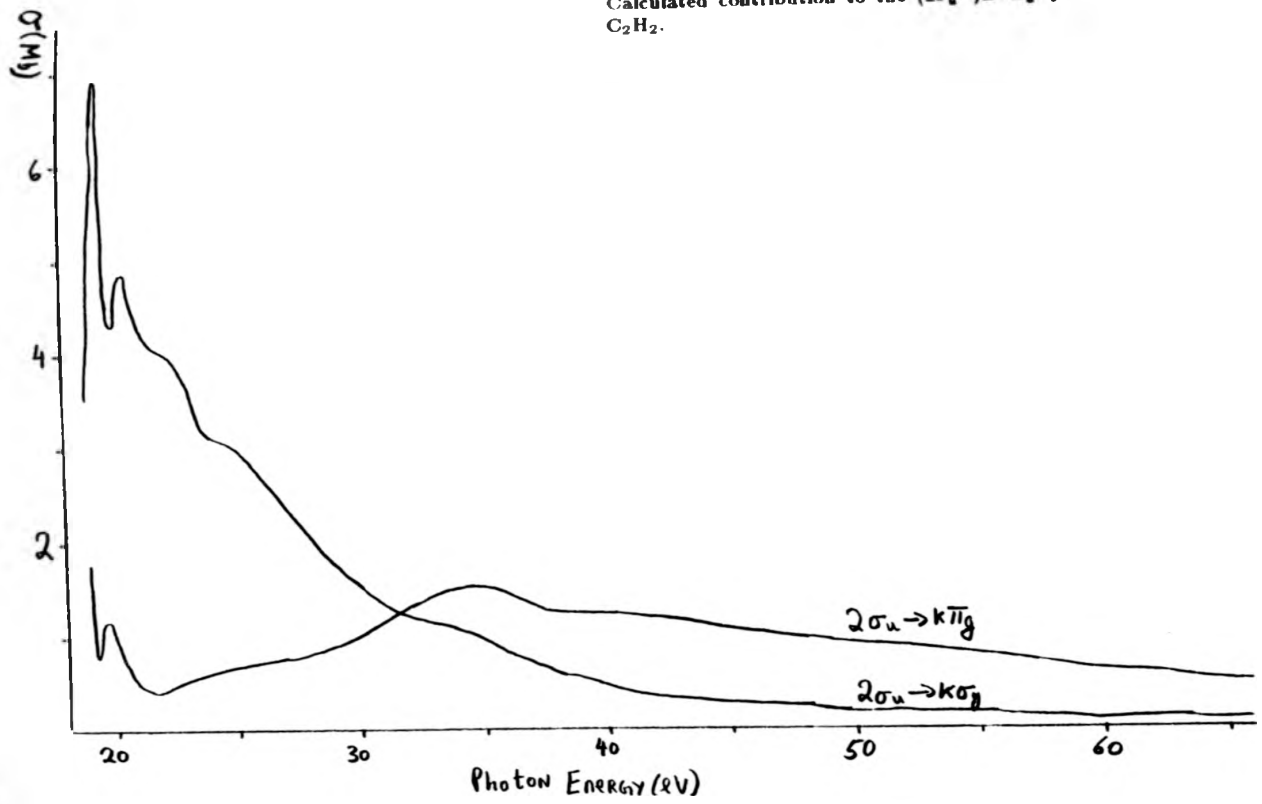

Fig. 5.16

Calculated $(2\sigma_u^{-1})B^2\Sigma_u^+$ photionization cross section of C_2H_2.

data from Ref.24 ×

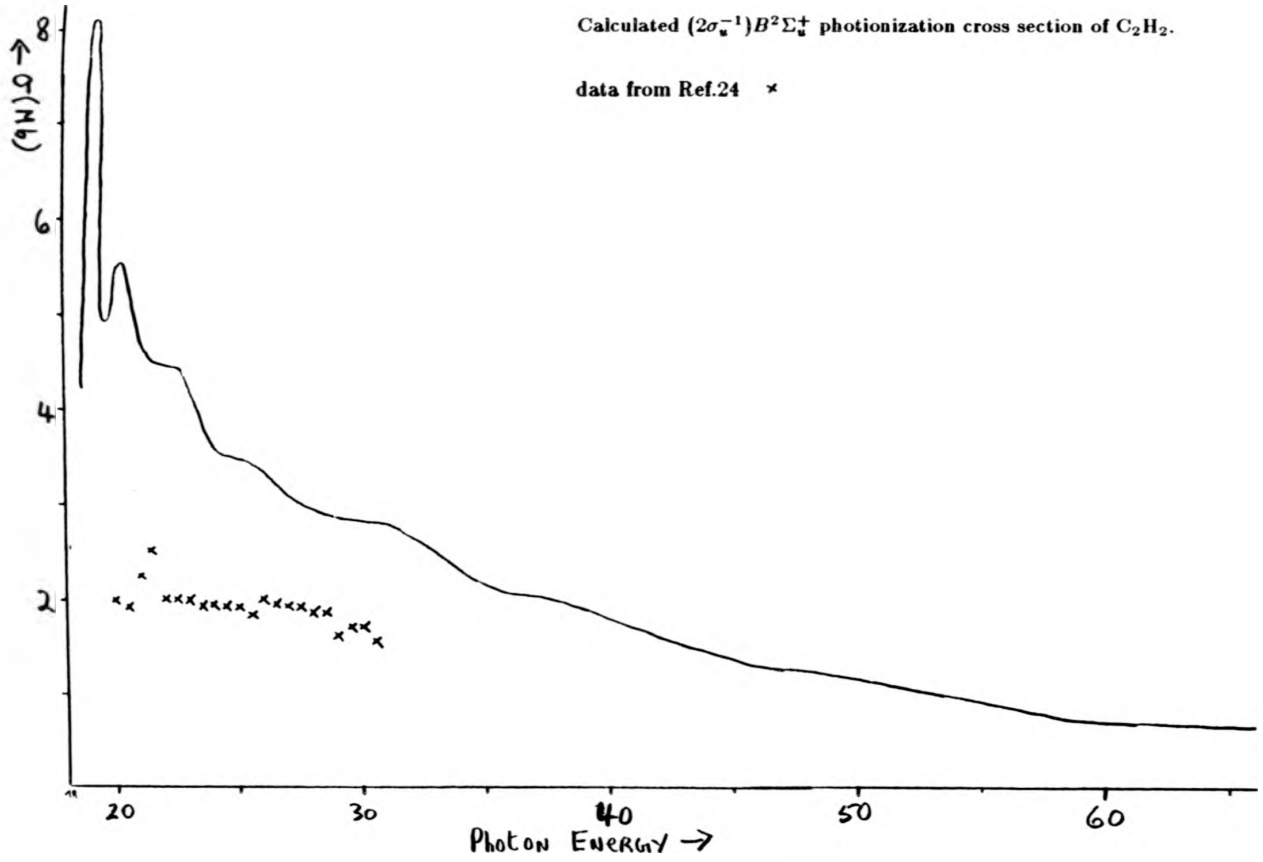

Fig. 5.17

Calculated contribution to the $(3\sigma_g^{-1})A^2\Sigma_g^+$ partial channel photoionization cross section in C_2H_2.

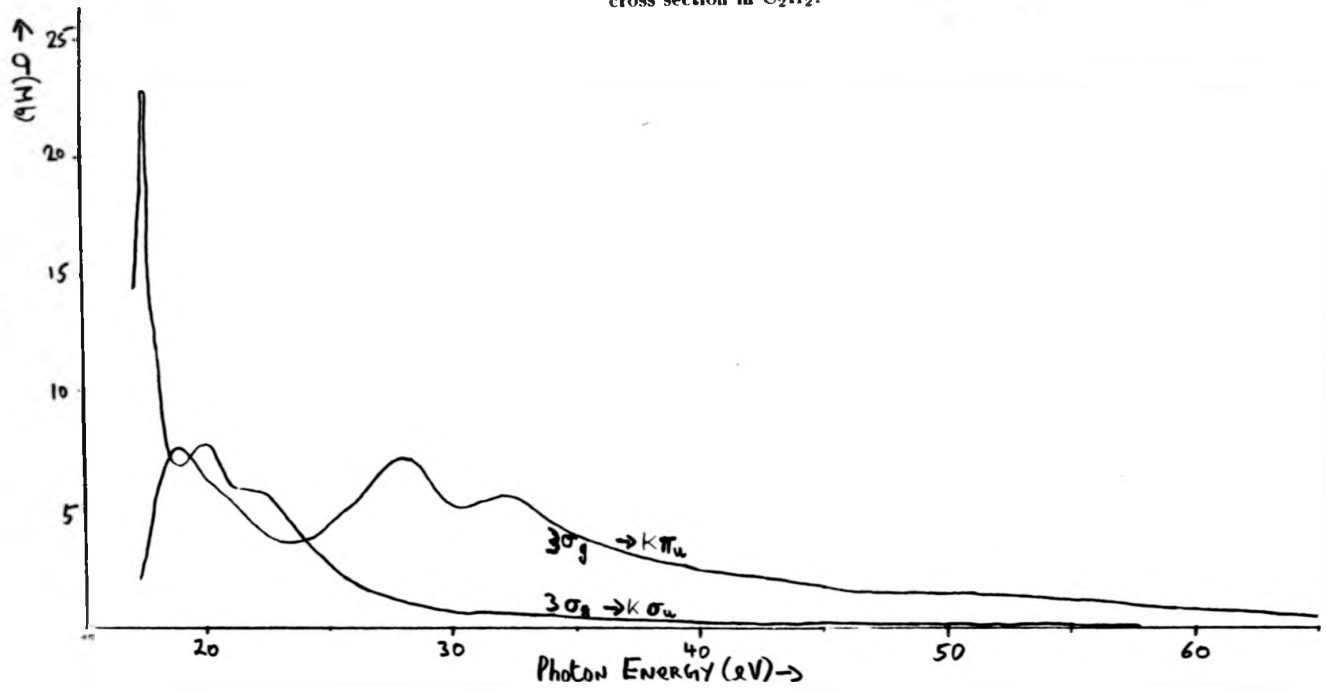

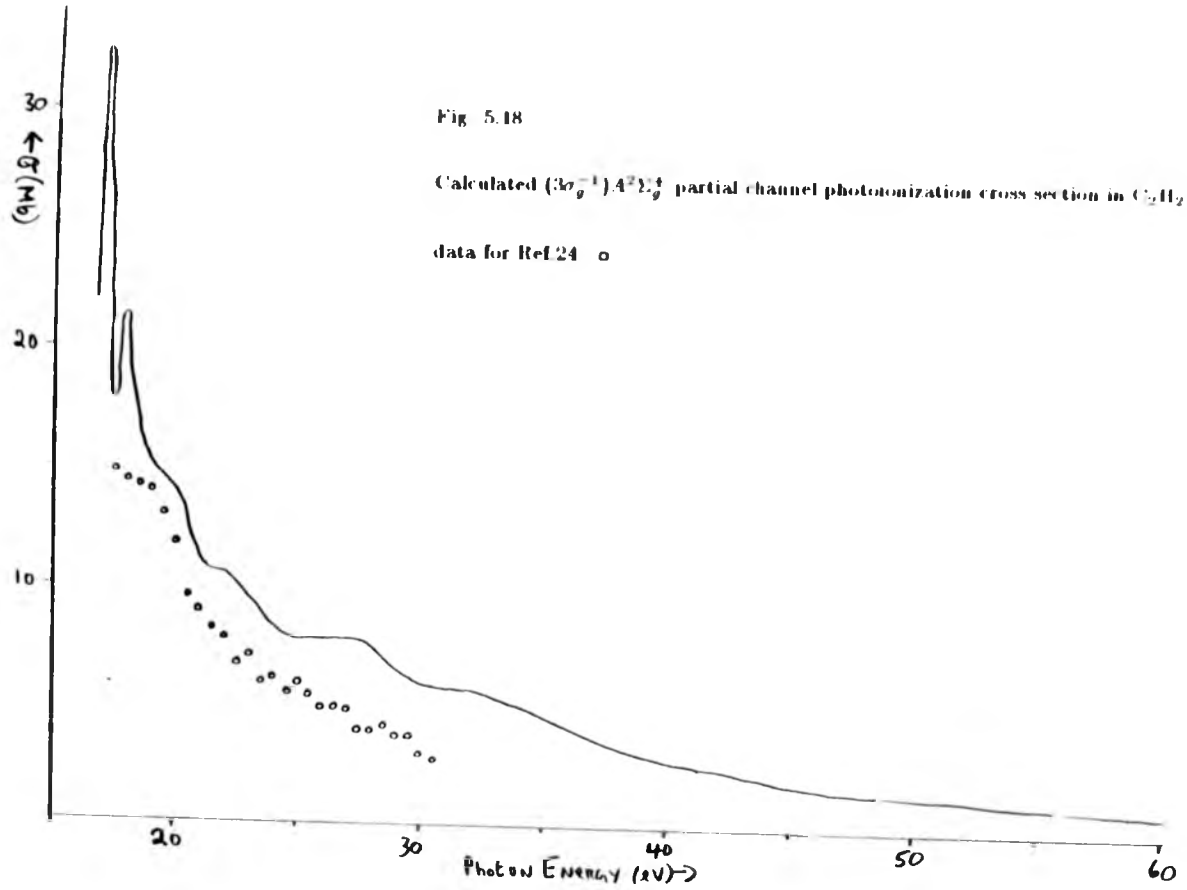

Fig 5.18

Calculated $(3\sigma_g^{-1})4^2\Sigma_g^+$ partial channel photoionization cross section in C_2H_2

data for Ref 24 o

Fig. 5.19

$1\pi_u^{-1})X^2\Pi_u$ partial channel photoionization cross sections of C_2H_2 calculated both and without spurious $1\pi_u \rightarrow k\pi_g$ contributions.

data from Ref.24 o

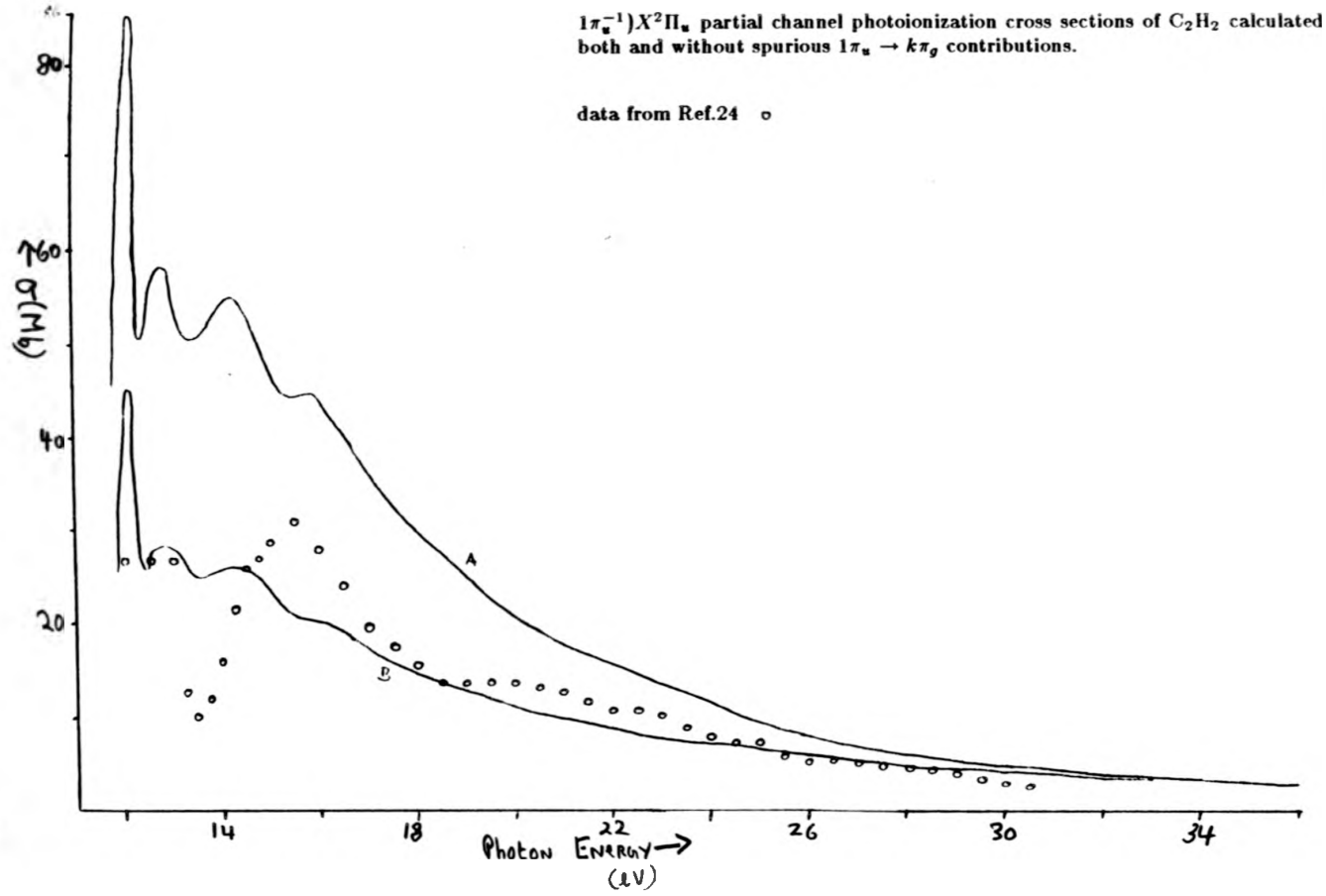

Fig. 5.20

Calculated contribution to the $(1\pi_u^{-1})X^2\Pi_u$ partial channel photoionization cross section of C_2H_2.

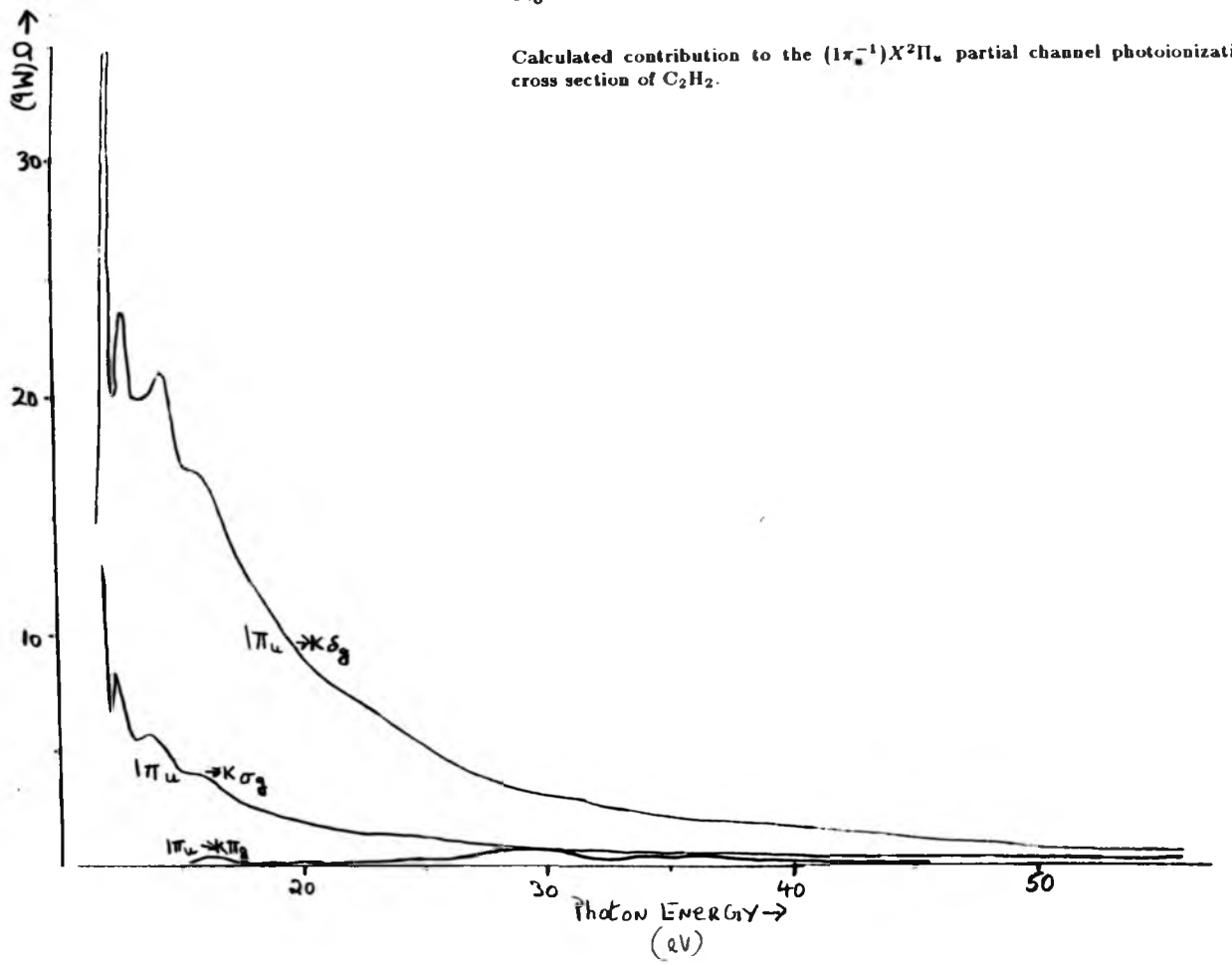

Fig. 5.21 Calculated 6 point $1\pi_u^{-1})X^2\Pi_u$ partial channel photoionization cross section in C_2H_2.

data from Ref. 24 Δ

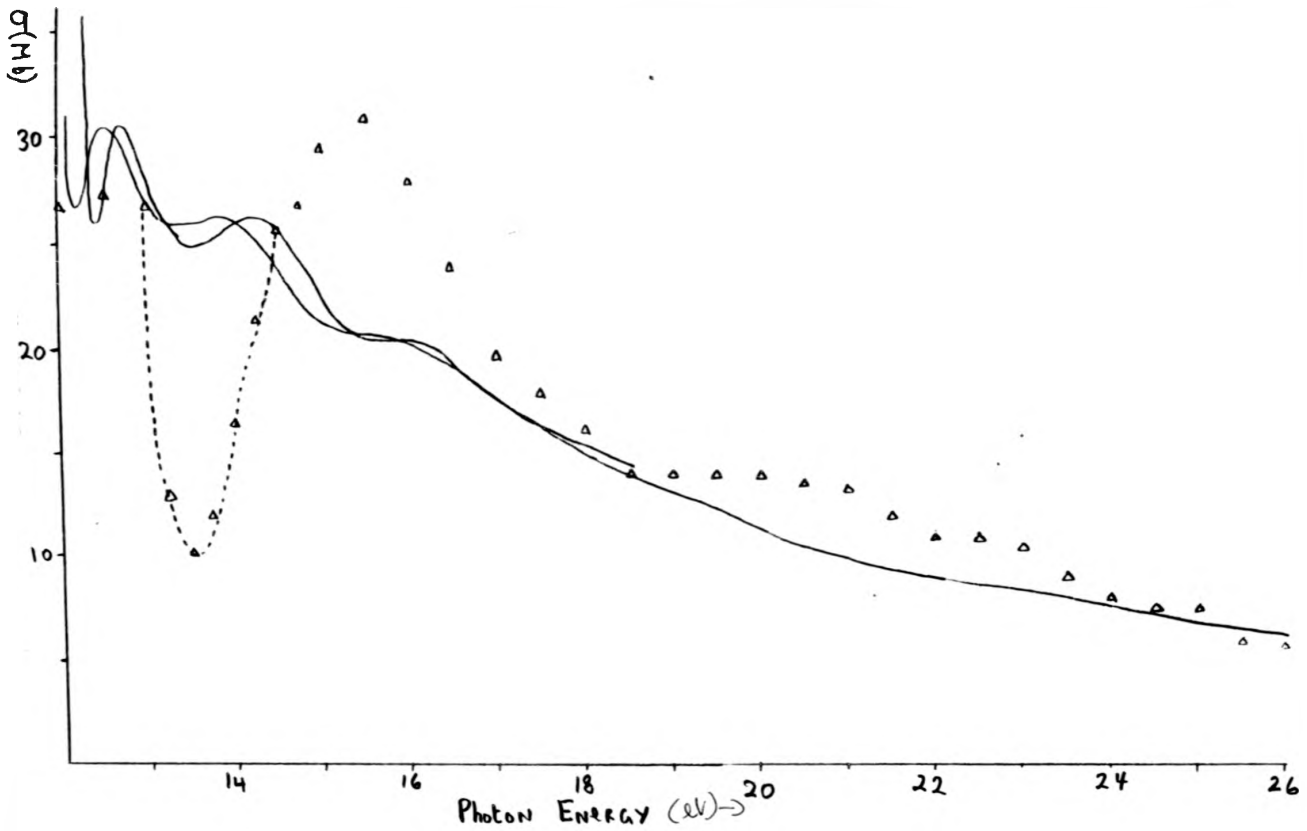

Fig. 5.22

Calculated total valence photoionization cross section of C_2H_2

data from Ref.24 o

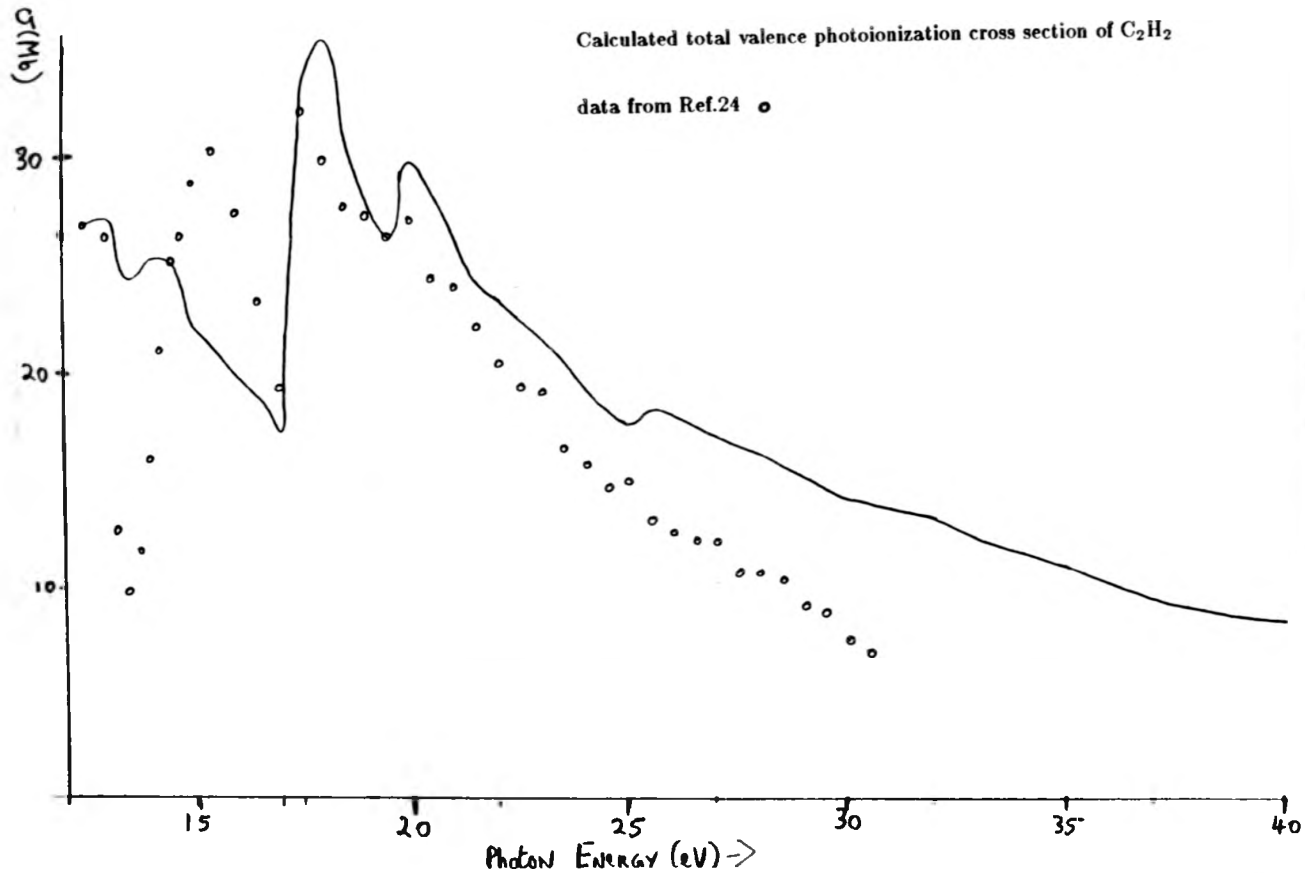

Fig. 5.23

Calculated contributions to the $(2\pi^{-1})X^2\Pi$ partial channel photoionization cross section in N_2O.

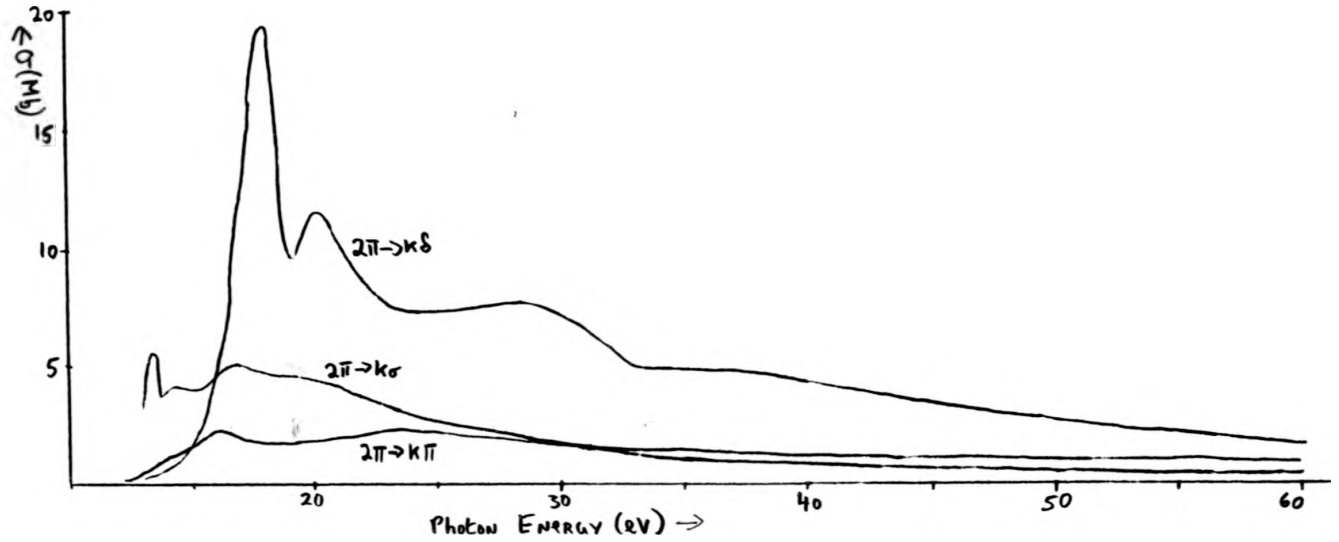

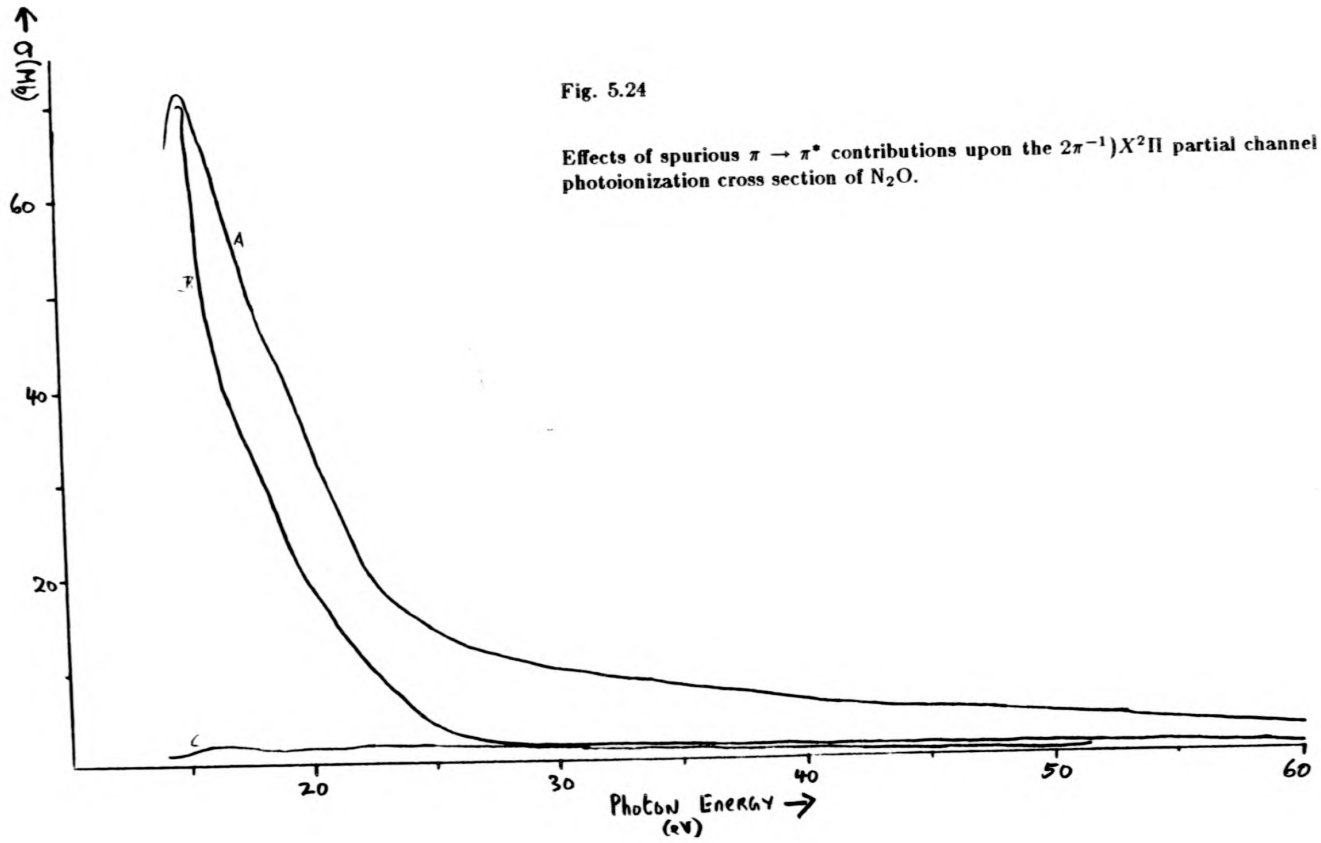

Fig. 5.24

Effects of spurious $\pi \rightarrow \pi^*$ contributions upon the $2\pi^{-1})X^2\Pi$ partial channel photoionization cross section of N_2O.

Fig. 5.25

Calculated partial channel photoionization cross section for ionization from the 2π orbital of N_2O.

data from Ref.44 •
data from Ref.60 ⊕

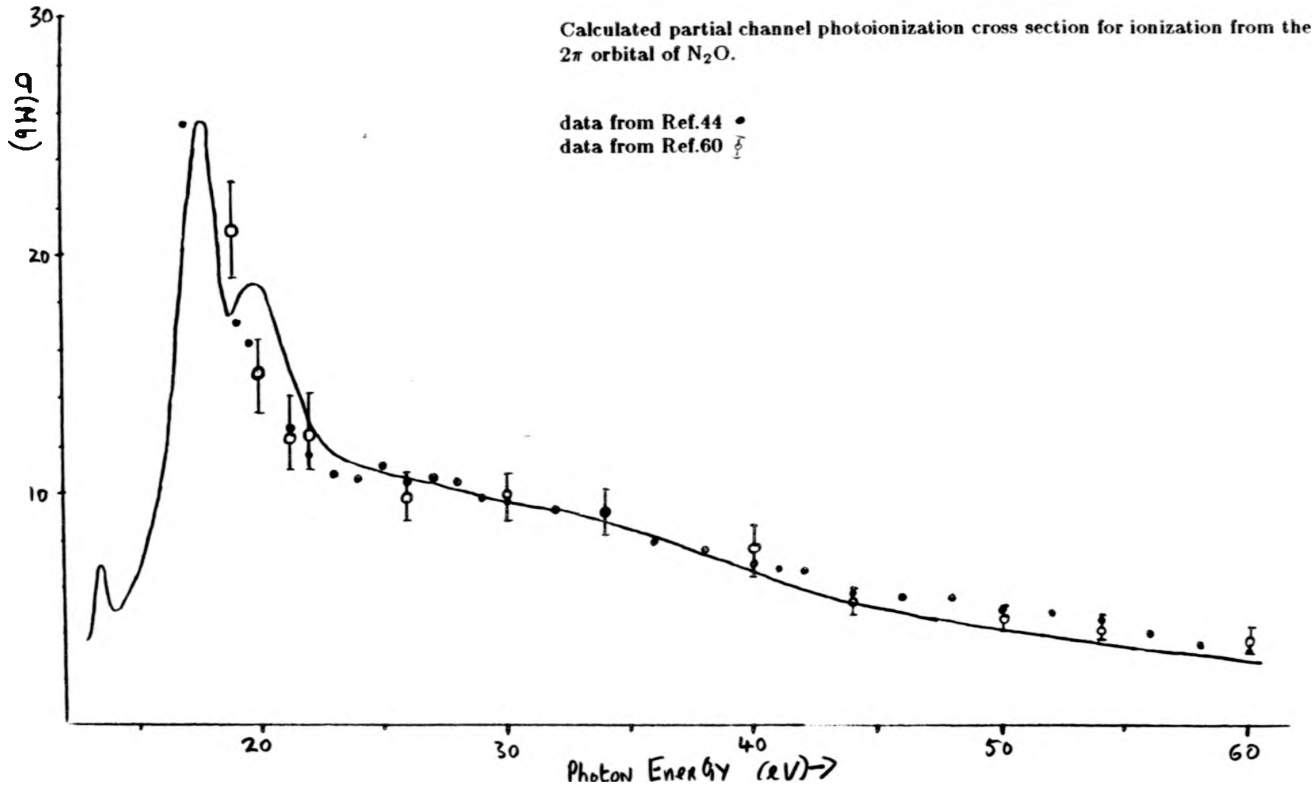

Fig. 5.26

Calculated contributions to the partial channel photoionization cross section for ionization from the 7σ orbital of N_2O.

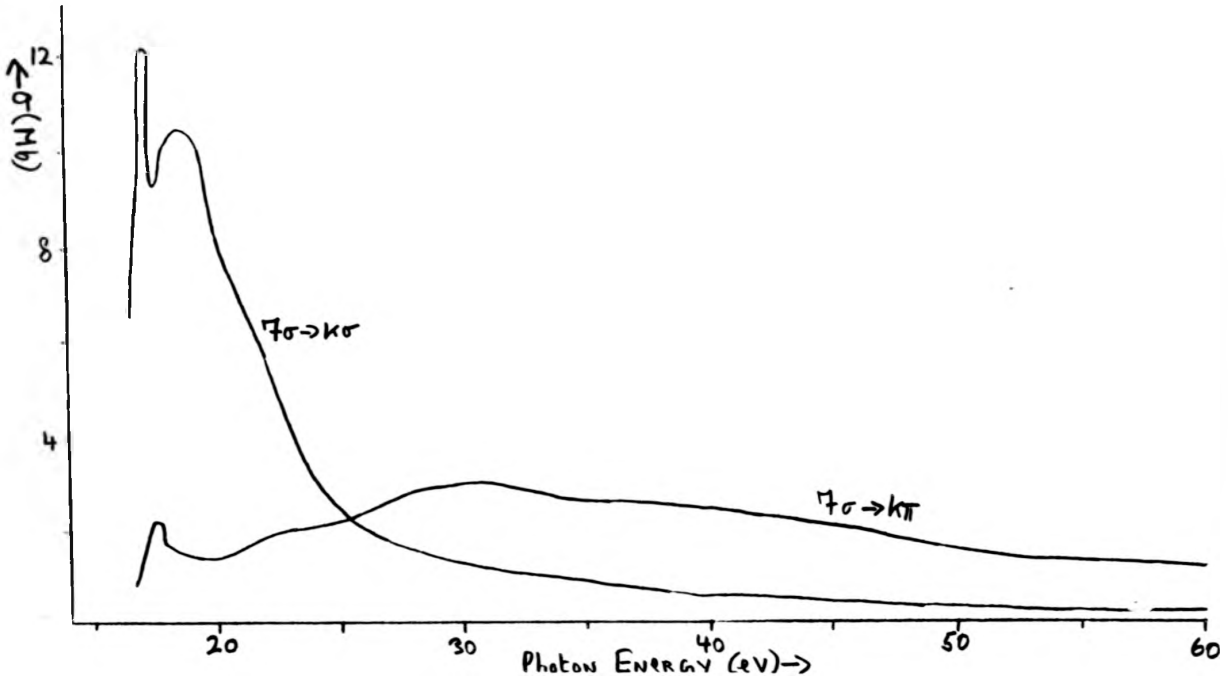

Fig. 5.27

Calculated partial channel photoionization cross section for ionization from the 7σ orbital of N_2O.

data from Ref.44 •
data from Ref.60 I

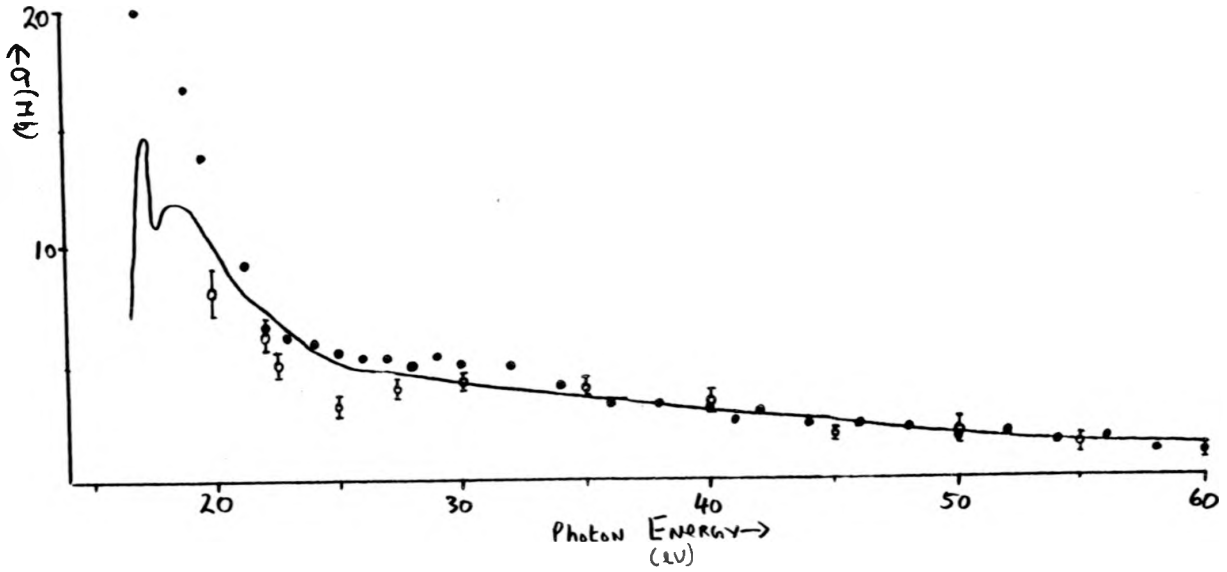

Fig. 5.28

Calculated contributions to the partial channel photoionization cross section for ionization from the 1π orbital of N_2O.

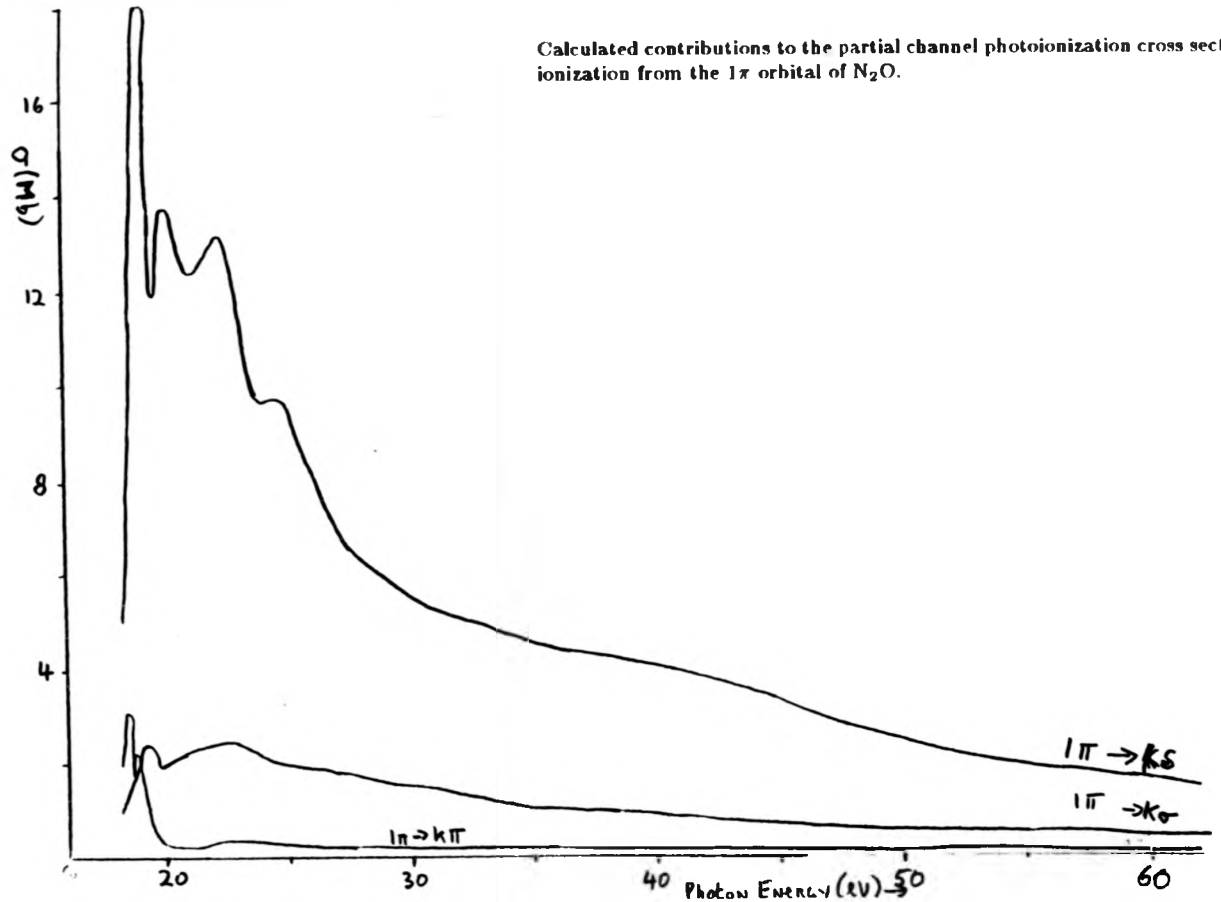

Fig. 5.29

Calculated partial channel photoionization cross section for ionization from the 1π orbital of N_2O.

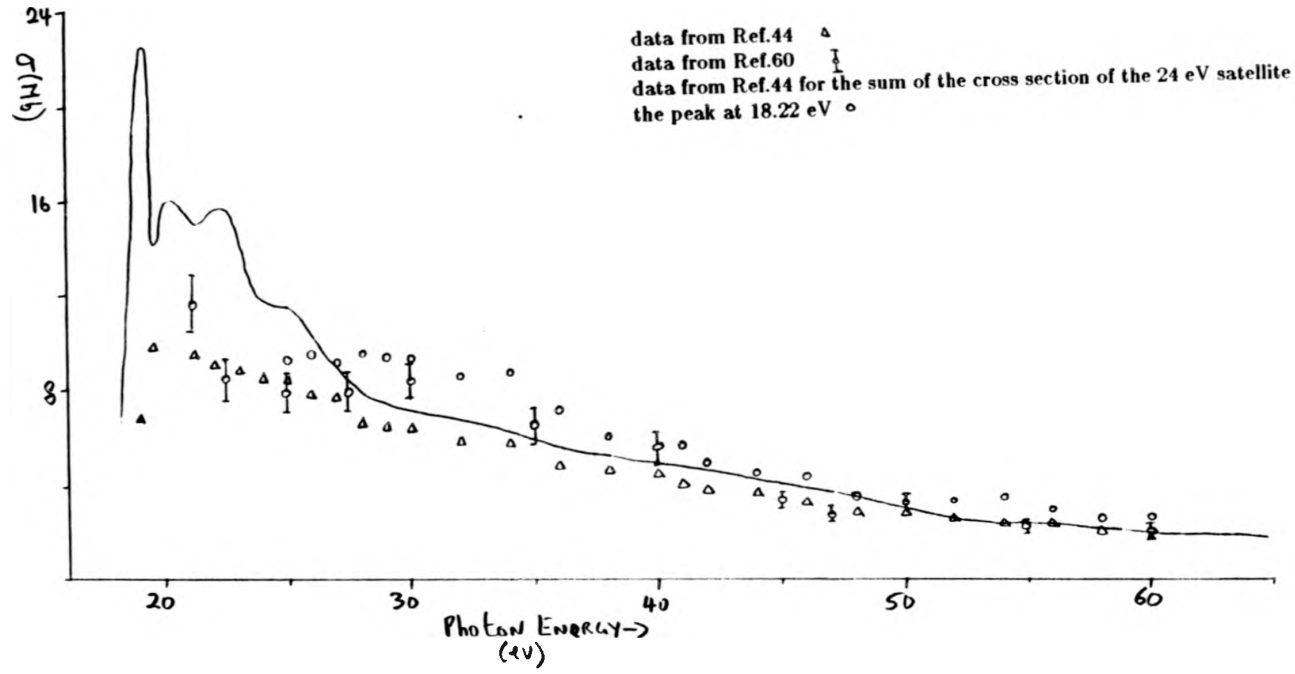

Fig. 5.30

Calculated contributions to the partial channel photoionization cross section for ionization from the 6σ orbital of N_2O.

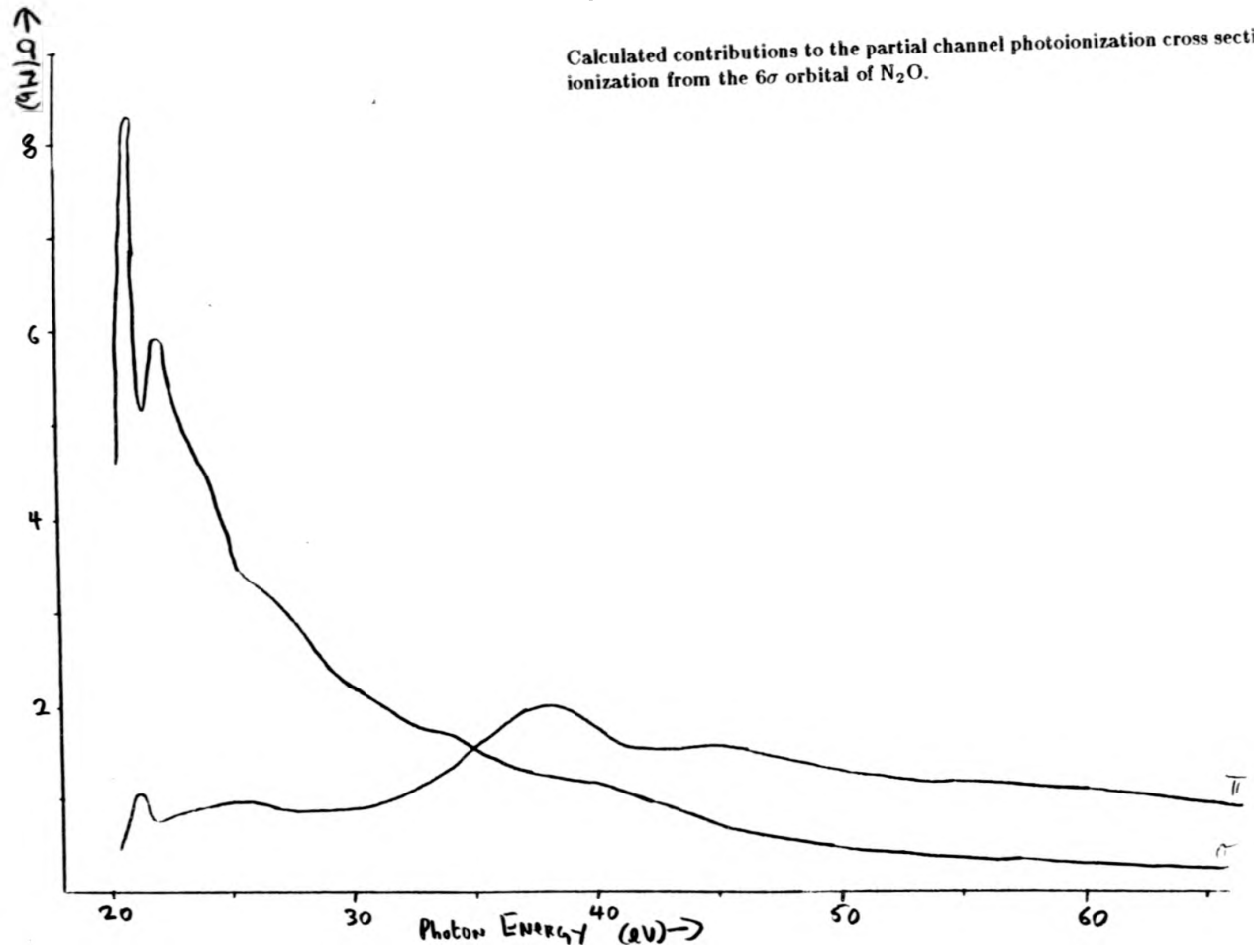

Fig. 5.31

Calculated partial channel cross section for ionization from the 6σ orbital of N_2O.

data from Ref.44 △
data from Ref.60 I

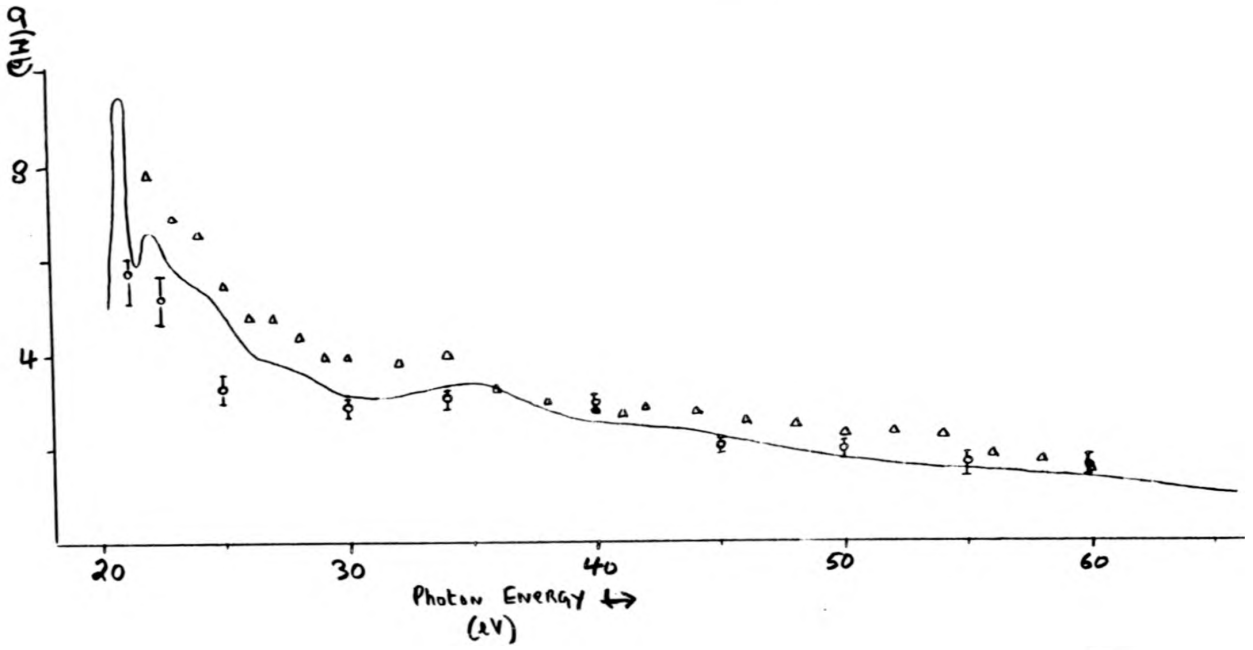

Fig. 5.32

Calculated total photoionization cross section of N_2O.

data from Ref.44 o